

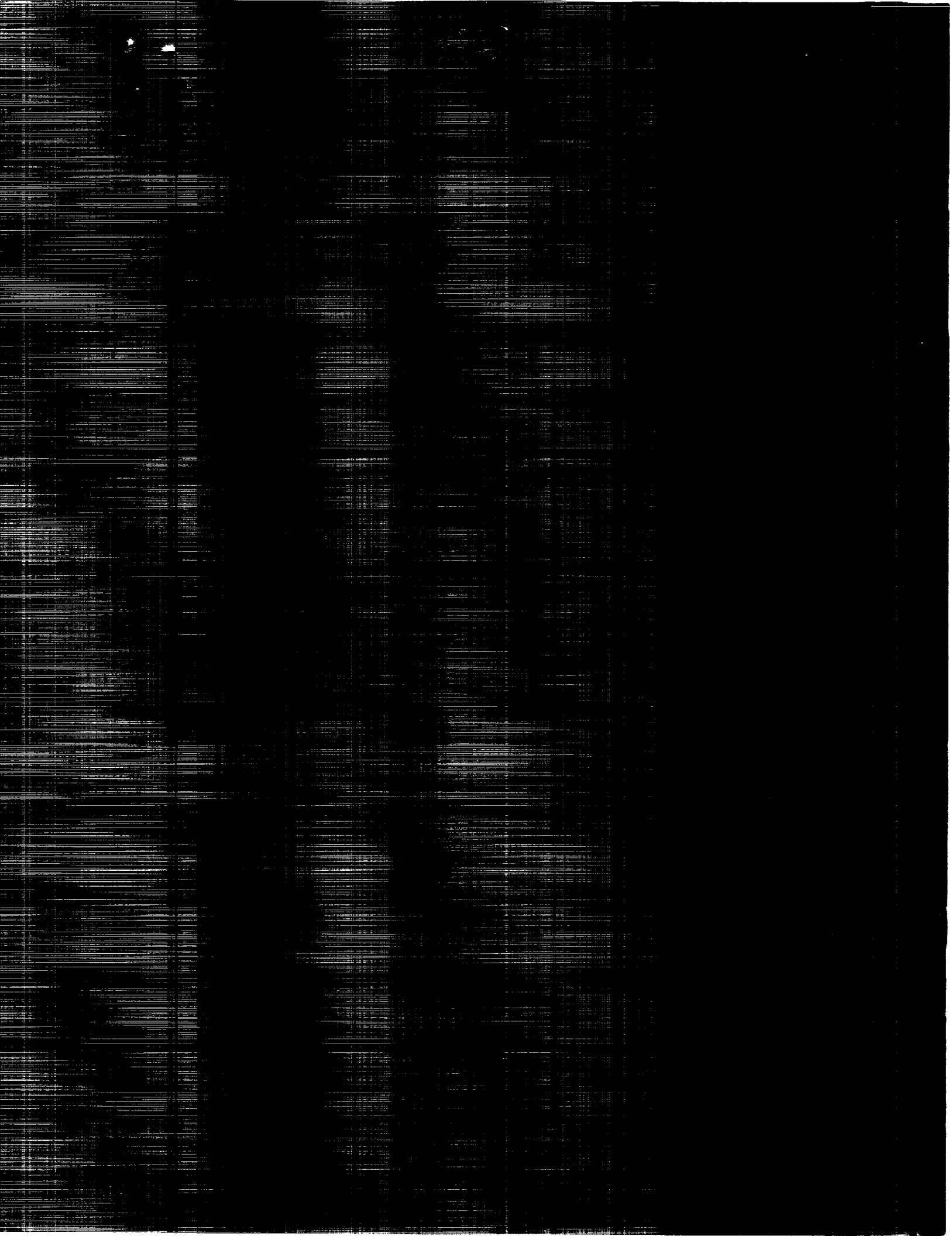
Wack
DIMENSIONAL SCALING FOR IMPACT CRATERING AND PERFORATION

(NASA-CR-188259) DIMENSIONAL
SCALING FOR IMPACT CRATERING AND
PERFORATION (POD Associates)
174 p

N94-10665

Unclas

G3/13 0132637



ACKNOWLEDGEMENTS

The authors gratefully acknowledge the technical comments and impact experiment data provided by Dr. Fred Hörz, and data provided by Dr. Eric Christiansen (both at NASA Johnson Space Center), and this project's technical monitor, Mr. Tom See (Lockheed Engineering and Sciences Company). The authors appreciate the support of the LDEF Project Office and the LDEF M&D SIG (specifically Dr. Bill Kinard [NASA Langley Research Center] and Dr. Mike Zolensky [NASA Johnson Space Center]) for this work. The authors also gratefully acknowledge the reports and data provided by Professor J.A.M. (Tony) McDonnell and Dr. Kenneth Sullivan (University of Kent at Canterbury, U.K.) and by Dr. William Schonberg and Mr. Roy Taylor (University of Alabama in Huntsville), whose reports are excerpted in Appendix B of this report.

The majority of the work reported here was performed under subcontract to Lockheed Engineering and Sciences Company under Purchase Order Number 02N0171219 and reported separately in a series of five reports. This compilation and the updates and extensions of the work were completed with POD Associates, Inc. Independent Research and Development funding under IRAD Project Number 069301. The authors are indebted to many other associates at POD Associates, Inc. for their outstanding efforts in making this project complete: Dr. Cassandra Coombs, Ms. Samantha Lapin and Mr. Jim Brandvold for their technical support and reviews, and Ms. Jean Mason and Ms. Denice Lucero for their administrative support. Without the support of this team, this report could not have been written.

TABLE OF CONTENTS

<u>Section</u>	<u>Page</u>
1.0 INTRODUCTION	1
1.1 Identification and Significance of the Problem	1
1.2 Background	2
1.3 Damage Modes	3
1.4 Issues	3
1.5 Technical Objectives	5
1.6 Technical Approach	5
2.0 PHYSICAL LOGIC	6
2.1 Hypervelocity Impact	6
2.2 Basic Phenomenology	6
2.3 Cratering Behavior	8
2.3.1 Melt Craters	8
2.3.2 Initial Approach - The "Energy Equation"	9
2.3.3 More General Approach	9
2.3.4 Caveats	12
2.3.5 Crater Diameter Versus Penetration Depth	14
2.3.6 Projectile Strength	16
2.3.7 Strength Effects at Low Impact Speeds	17
2.3.8 General Comments on Scaling (Similarity) Laws	19
2.3.9 Supralinearity	20
2.3.10 Brittle Material Response	23
2.3.11 Phase Changes and Momentum Enhancement	24
2.3.12 Dimensional Analysis	27
2.4 Perforation Behavior	28
2.4.1 Stress Wave Logic: The Ballistic Limit	29
2.4.2 Ultra-Thin Targets (Foil)	32
2.4.3 The Intermediate Case	33
2.4.4 Perforation Supralinearity	35
2.5 Oblique Impacts: Summary of Typical Behavior	35
2.5.1 Idealized Theory	35
2.5.2 The Ricochet Case	36
3.0 CTH HYDRODYNAMIC CALCULATIONS	39
3.1 Cratering in Aluminum	39
3.2 Cratering in TFE Teflon	41
3.3 Perforations in Aluminum	44
3.4 Perforations in TFE Teflon	46
3.5 Oblique Impacts into Aluminum	47

4.0	COMPARISONS WITH OTHER SCALING LAWS	49
4.1	Cratering in Aluminum	49
4.2	Cratering in TFE Teflon	50
4.3	Perforations in Aluminum	51
4.4	Perforations in Teflon	52
5.0	COMPARISONS WITH EXPERIMENTAL DATA	54
5.1	Cratering in Aluminum	54
5.2	Cratering in Teflon	55
5.3	Perforations in Aluminum	56
5.4	Perforations in Teflon	56
5.5	Oblique Impacts in Thick Aluminum	57
5.6	Oblique Impacts in Thin Aluminum	57
6.0	OTHER MATERIAL COMPARISONS	58
6.1	Copper Cratering	58
6.2	Lead Cratering	58
7.0	CONCLUSIONS	60
7.1	Cratering	60
7.2	Perforations	61
7.3	Oblique Impacts	62
7.4	Implications for LDEF	62
8.0	RECOMMENDATIONS FOR FUTURE WORK	64
	REFERENCES	66
	APPENDIX A - FIGURES	A-1
	APPENDIX B - OTHER SCALING LAWS	B-1

1.0 INTRODUCTION

1.1 Identification and Significance of the Problem

With the ever increasing use of space satellites, and the concomitant increase in the amount of man-made debris, the issue of accidental collisions with particles becomes more severe. While the natural micrometeoroid population (Cour-Palais, 1969) is unavoidable and assumed constant, continued launches of spacecraft steadily increase the amount of debris (Kessler, 1987 and 1990). The latter comprises items ranging from spent rocket cases, through defunct satellites, to the remains of bodies which have fragmented due to explosions or collisions. The result is a distribution of particles ranging in size from microns to meters. As with the micrometeoroids, the population of debris is greatest for the smaller particles, tending to decrease with an inverse power-law versus size.

To understand and model these environments, impact damage features (*i.e.*, craters and perforations) from returned spacecraft materials (*e.g.*, Long Duration Exposure Facility [LDEF], Solar Maximum Mission, etc.) must be analyzed in order to determine the impact parameters (*e.g.*, particle size, particle and target material, particle shape, relative impact speed, etc.) associated with each feature. Such analysis requires the use of generic analytic scaling laws which can adequately describe the impact effects. Currently, most existing analytic scaling laws are little more than curve-fits to limited data and are not based on physics, so are not generically applicable over a wide range of impact parameters. Therefore, generic physics-based analytic scaling laws still need to be developed.

The LDEF Meteoroid and Debris Special Investigation Group (M&D SIG) is chartered to collect and interpret the LDEF impact data and apply the interpretations to verify and update the environment and impact effects models. Since the largest sources of LDEF data are impacts into aluminum and FEP Teflon, the M&D SIG's efforts will be hampered without broadly applicable scaling laws. Consequently, the M&D SIG is supporting these POD Associates, Inc. (POD) efforts to develop new generic physics-based scaling laws. The results of these efforts are being presented in this report.

This report summarizes the development of two physics-based scaling laws for describing crater depths and diameters caused by normal incidence impacts into aluminum and TFE Teflon. The report then describes equations for perforations in aluminum and TFE Teflon for normal impacts. Lastly, this report also studies the effects of non-normal incidence on cratering and perforation.

Although FEP Teflon was flown on LDEF, TFE Teflon is studied instead since the available experimental data (Hörz, 1992) is for TFE Teflon and the material parameters provided in the literature (Harper, 1992; Moses, 1978; Dean, 1992; Rice, 1980) reveal some inconsistencies (some references even fail to distinguish between TFE and FEP Teflon, which have slightly different properties). However, it is expected that TFE and FEP Teflon will show similar responses under hypervelocity impact conditions.

1.2 Background

For bodies in low Earth orbit (LEO), whether orbital debris or antisatellite weapons, there is only a small change in speed versus altitude even out to 2000 km, and the average speed is about 7.7 km/s (e.g., at 500 km). However, because different bodies are in different orbits, collisions are possible with impact speeds between zero and about 15.4 km/s (average about 10 km/s), dependent upon the angle between the velocity vectors. The two speed limits for same-altitude bodies are for "tail-chasing" and "counter-orbital" conditions, respectively. These possible impact speeds are independent of particle size and mass.

Micrometeoroids orbit around the Sun rather than the Earth, but their orbits can intercept the Earth's. Since the Earth itself moves at about 30 km/s, while the micrometeoroids can have speeds of up to 42 km/s (for highly elliptic orbits) at the Earth's orbital radius from the Sun, the results can involve collisions with maximum impact speeds from about 12 to 72 km/s (for co-orbiting to counter-orbiting cases, respectively). For a space platform in orbit around the Earth (at 7.7 km/s), the additional effect of velocity vector summation results in micrometeoroid collisions with speeds from almost zero to 79 km/s. In reality, very few collisions occur at the highest speeds, and the average impact speed is about 19 km/s, with a meaningful population range from a few km/s to about 25 km/s (Zook, 1990). As with the debris, the impact speeds are independent of micrometeoroid sizes and masses.

While the debris is mostly concentrated in the higher inclination orbits (above 60 degrees), the micrometeoroids effectively arrive from all directions. In both cases, the effect of the spacecraft orbital motion always results in the highest flux (impacts per presented area per time) and highest impact speeds on the RAM surface, for which the surface normal points along the spacecraft velocity vector. Consequently, the RAM surface suffers the greatest degree of impact damage. The pseudo-circular orbits of the debris result in impacts on the spacecraft surfaces which are in the plane locally parallel to the Earth's surface below (i.e., RAM, SIDES and TRAIL), and the impact rate rapidly decreases as the TRAIL surface is approached, and there are very few collisions with the EARTH or SPACE facing surfaces. The micrometeoroids impact all surfaces, but for LEO, the Earth provides significant geometric shielding (a "shadow"), reducing the number of impacts on all faces except SPACE, but especially on the EARTH facing surface.

Note that, due to orbital mechanics and satellite geometries, very few of the impacts involve "normal" collisions (impact velocity along the normal to the target surface), and thus the hits occur with a large spread in impact angle. It is well known that the angle of approach modifies the resulting penetration (Christiansen, 1992c), hence the effect needs to be properly understood in order to correctly interpret the environment and the consequential impact effects. Likewise, the effects of density of both the impacting particle and the target must be known. Presently, it is assumed that most of the micrometeoroids have a density of about 0.5 g/cm^3 (Cour-Palais, 1969), while the debris value is about 4.7 g/cm^3 for small particles (less than 1 cm), and decreases with increase in particle size (Kessler, 1987) (since most large pieces are not chunky pseudo-spheres, but rather odd-shaped items which, on average behave as if partly porous).

Furthermore, the effects of impactor and target material properties (*i.e.*, yield, fracture strength, melt energy, etc.) must be understood.

1.3 Damage Modes

The impact damage ranges from simple pitting, erosion and cratering for impact into plastically yielding materials, through conchoidal and star cracking for brittle targets, to complete perforation, large-scale spallation/fragmentation, and material melting and vaporization. The data from LDEF indicates additional effects, such as delaminations of multilayered materials, and the generation of rings of ejected material, and/or permanently deformed material. These effects are in addition to thermal cycling, UV (ultraviolet light) embrittlement of plastics, and AO (atomic oxygen) erosion. All these effects can be synergistic. Impacts can modify material properties or morphologies, thereby altering the subsequent responses to UV, AO or thermal cycling. Likewise, thermal cycling, UV, and AO can alter properties such that the resultant impact cratering, cracking and perforations are modified. These various effects, and their synergies, are all being studied.

1.4 Issues

To correctly interpret the space environment, the resulting modes of impact damage, and the potential methods that may be employable to mitigate the effects, it is necessary to properly understand the "rules" of impact damage. Unfortunately, existing experimental facilities cannot replicate the complete range of conditions. Gas guns are limited to maximum speeds of about 8 km/s, electric guns have limitations due to sabot requirements, Van de Graaff accelerators can only be used with small charged particles, etc.. Further, many techniques have been developed primarily to accelerate flat plates to study planar, one dimensional (1-D) strain, impact effects. However, these approaches are not easily adapted to the problem of throwing chunky bodies. Consequently, only partial experimental testing can be done at present. In particular, there are no satisfactory means of replicating the high speed (above 15 km/s) impacts of the larger particles (above 0.1 mm diameter), of either metallic or (especially) non-metallic nature, in a well-controlled manner that also allows for non-normal impacts.

As a result, reliance must be put on either extrapolation of (limited) experimental data obtained at lower speeds, or with non-typical materials, or put on computational approaches. Although computational capabilities have increased dramatically during the last decade (more rigorous physical modeling, and much faster and more capable computers), the fact remains that properly calculating impact problems is time-consuming and costly. Furthermore, the accuracy of the calculation is limited by adequacy of known material properties and behavior, such as high pressure EOS (equation of state), rate-dependent yielding and fracturing, etc. Much of the experimental data needed is frequently obtained from 1-D experiments (plate slap). However, while this approach eases the interpretation of material responses, it does not necessarily provide all the required data. For example, 1-D strain is an irrotational flow problem, whereas cratering and penetration of one finite body into another clearly involves material rotational flow. Thus

computational techniques are usually best reserved for analysis of specific cases, and for identifying sensitivities to parameter uncertainties.

As a result, a need still exists for analytic scaling laws which can adequately describe the impact effects. Done properly, such laws are very useful for determining the "ball-park" of probable responses, which in turn allows attention to be applied to specific cases via the computer codes. These laws need not be perfect (10 percent accuracy is sufficient for many purposes), but they do need to be rational and based on physics, such that extrapolations to experimentally inaccessible conditions are credible and well-founded.

Unfortunately, many existing scaling laws are little more than curve-fits to limited data, and are usually derived by investigators who invariably fit only their own data. Accordingly, there are several such laws, and simple inspection reveals glaring discrepancies. For example, these laws rarely agree on such issues as the proper power-index to be applied to impact velocities or densities. Further, while some authors invoke material "hardness" numbers, others use yield strengths. However, invariably such parameters are applied to only the target materials, but not the impactors, despite the problem being one that deals with both bodies. Some laws fail to acknowledge the well-known "supralinearity" observed in cratering, wherein the crater size increases faster than the impactor size (all other factors remaining constant). Unfortunately, those laws that do incorporate this effect are themselves in violation of "dimensional analysis". Frequently, these formulations involve numerical "constants" that cannot be (!), since to adhere to physical principles they must have an inverse dimension to that "left hanging" within the equation. Further, while many such laws define an upper limit to validity (*e.g.*, in velocity), rarely is the corresponding lower limit given, despite the fact that the formulations are self-evidently incorrect for low velocity (or density, etc.).

Many other problems abound. For example, if material yield strength is invoked, the value used is the static one, whereas it is well known that many materials display considerable strain and strain-rate sensitivities, and can also suffer from thermal softening effects. Most investigators assume that the "cosine law" applies to impacts (*i.e.*, the penetration is a function of the normal component of the impact velocity). However, while this effect is observed for the lower impact speeds (indeed, ricochets can occur for angles of incidence greater than about 60 degrees from the surface normal), it is not necessarily true at the higher speeds. This arises because, at the lower velocities, the impact phenomenon is dominated by momentum, but as the velocity increases so the process becomes dominated by energy. Thus an impact by a small particle at very high velocity will behave very much like a surface explosion. Such explosions do not obey the cosine law. Also, few investigators explain what happened to the remaining component of the incident energy and momentum.

Impact events fall into three basic classes: flat plate (1-D) planar impacts, chunky (pseudo-spherical) impacts, and long rod impacts. For the smaller man-made space debris and micrometeoroids, it is reasonable to assume the particles are chunky. However, for the larger (and far more deadly) particles it is unlikely that they are spherical. Rather, the pieces will be parts of thin plates, or antenna booms (etc.). These impactors will produce results more typical

of those for flat plates or long-rod penetrators. Surprisingly, although many investigators have studied these responses independently, there have been few attempts to marry the results. Thus no analytic law presently exists that allows description of the gradual trend from flat plate through spherical shape to long rod impact. Consideration of this issue will be useful in its own right, since it allows a simple appreciation of the consequences of impactor changes in shape. Further, this approach immediately reveals the source of confusion in the multiple power-laws that exist.

1.5 Technical Objectives

The technical objective for this work is to develop a set of generic scaling laws that adequately describe the physics of impact events. This will include cratering, cracking and spalling, perforations, and melting/vaporization phenomena. The laws will take into account material properties, sizes, shapes, velocities and angles of incidence, and will logically extrapolate to both high velocity conditions presently inaccessible, and to (known) low velocity conditions.

Specifically, the objectives are to:

- (1) Study the responses of aluminum and Teflon (specifically TFE) for normal impacts by chunky bodies, developing a generic scaling law that describes cratering through perforation, and
- (2) Expand these studies to include non-normal impacts.

This report specifically studies the effects of both normal and oblique impacts into aluminum and Teflon targets, and also gives some data for other materials.

1.6 Technical Approach

POD has tackled the issue of impacts into aluminum and TFE Teflon via three approaches:

- (1) Application of physical logic in an attempt to determine which parameters should apply to the problem,
- (2) Application of hydrodynamic code calculations, using the CTH code (Bell, 1991) from SNLA (Sandia National Laboratory, Albuquerque), to map out the predicted responses as functions of input parameters, and
- (3) Study of existing scaling laws and comparisons with both experimental data and the results of CTH calculations to determine which (if any) such law fits the data.

This report first addresses the results of each of these approaches separately, then combines the results into sets of conclusions for this study and recommendations for future efforts.

2.0 PHYSICAL LOGIC

2.1 Hypervelocity Impact

Exactly what constitutes a hypervelocity condition is not well defined. For some investigators the condition applies for all impact speeds above 5 km/s, while for others it occurs when $u_0 > c_0$, where u_0 is the impact speed and c_0 is the material (usually the target) stress wave speed (whether this speed should be the Hugoniot shock, the low-pressure bulk, the extensional, the longitudinal [dilatational], or the shear velocity is rarely made clear: most researchers reference the low pressure bulk sound speed). Another definition would be whenever gross plastic flow occurs in a **rotational** flow pattern, and the stress approximates the Bernoulli law for fluids. Note that this definition is obviously material-specific, being easily reached for soft ductile metals but applying only for higher impact speeds for the less ductile, high yield strength, ceramics and glasses. Also note that this definition **never** applies to the well known 1-D plate slap condition, since the true 1-D case does not involve rotational flow. POD is of the opinion that the latter definition is the more logical one, since the impact community refers to hypervelocity conditions associated with impactors of finite lateral dimensions, which invalidate 1-D stress logic (and make the analysis much more difficult).

The reference to the Bernoulli stress state and associated material flow needs to be qualified. As normally used in the impact community (and in this report) it is assumed that the materials are basically **incompressible**. Strictly speaking, this approach is merely an approximation which applies once the stresses decrease to much lower values than the initial impact stresses. Section 3.0, which discusses the CTH calculations, elaborates on this subject.

2.2 Basic Phenomenology

We first describe the fundamental physics of impact cratering in order to establish the overall phenomenology. For convenience we chose our "chunky projectile" to be a cylinder striking the target in the manner of a 1-D plate slap, with the end face of the cylinder parallel to the target surface. The cylinder has length L and diameter d_p , with $L = d_p$, and the impact speed is u_0 and is normal to the target surface.

Immediately upon impact two shock waves are generated, one propagating into the target and one propagating back into the projectile. The initial stress, σ , is given by the 1-D condition

$$\sigma = Z_p Z_t u_0 / (Z_p + Z_t) \quad (1)$$

where Z is the acoustic impedance given by

$$Z = \rho(c_0 + su) \quad (2)$$

where ρ is material density, c_0 is the low-stress bulk sound speed, u is the induced particle motion change in speed, and the term s is material-specific and related to the material Gruneisen

parameter (see Section 2.3.5). Note that for low impact speeds the stress is proportional to this speed, while for high impact speed the stress becomes proportional to the square of the speed. This 1-D stress can be very large. For a symmetric Al/Al impact, with $\rho = 2.7 \text{ g/cm}^3$, $c_0 = 5.1 \text{ km/s}$, $s = 1.4$ and an impact velocity (u_0) of 10 km/s, the stress is 1.63 Mbars (= 63 GPa). This stress is grossly in excess of the plastic yield strength (Y) of aluminum, which is about 2.7 kbars (0.27 GPa) for Al 6061-T6 (Shackelford and Alexander, 1992).

Release waves are generated at the edge of the projectile (free surface relief) and at the edge of the impact region within the target. The projectile release waves cause a drop in the stresses within the projectile, such that after a time $t = r_p/c_p$ (with r_p the projectile radius, and c_p the radial release wave speed) the 1-D shock state reduces to a value closer to the Bernoulli stress. The stress region in the target directly under the impact footprint itself propagates stress laterally, while the corresponding release waves drop the stress under the impactor towards the Bernoulli state, in the time $t = r_p/c_t$, where c_t is the release wave speed in the target. Initially, if the 1-D stress is σ_0 the target lateral stress is $(\sigma_0 - Y)$. The downstream particle motion under the impactor causes a shear wave to propagate laterally into the target. The corresponding maximum propagated shear stress is limited to the yield value. Additionally, the compressive lateral stress itself propagates a stress of value $0.5(\sigma_0 - Y)$, since the boundary under the edge of the impactor is one of like-to-like material. This latter stress itself decreases with distance owing to the radial divergence. This stress propagates as a longitudinal wave laterally and is initially far more important than the shear wave. The radially moving longitudinal wave itself has a lateral stress (that is thus perpendicular to the target free surface outboard of the impactor) of $(\sigma_0/2 - 3Y/2)$. Upon reaching the target free surface this stress causes outer motion (upstream) and generates a release wave traveling back into the target. Clearly, when $\sigma_0 \gg Y$ the material behaves essentially as a fluid with stresses approximately equal in all directions (*i.e.*, we have a *pressure* rather than stresses).

Thus after the release waves cross the impact axis the 1-D stress rapidly vanishes, and the target material is set into a rotational flow, in a similar manner to the flow of a fluid around a moving body. Material on the target surface outboard of the impactor flows in a combined radial-outward/backstream-upward manner. This is the flow associated with the formation of jets of material and the onset of the formation of the lips observed around craters in ductile targets. Once this rotational flow is established the stress state on the impact axis becomes the Bernoulli one, given by

$$\sigma = 0.5 \rho u^2 \quad (3)$$

where u is the local particle speed. For the symmetric Al/Al impact this stress is given by

$$\sigma = \rho_p u_0^2/8 = \rho_t u_0^2/8 \quad (4)$$

which is 337.5 kbars (33.75 GPa) for an impact speed of 10 km/s. Thus the Bernoulli stress is much lower than the initial 1-D shock stress, but still well in excess of the aluminum yield strength. This Bernoulli stress is a transient state, only, for the case of a chunky projectile and

itself rapidly decays unless continued momentum arrives at the projectile/target interface as occurs for a long rod penetrator (LRP).

2.3 Cratering Behavior

It is well known that, when a projectile impacts an infinitely thick target at high velocities, a crater is formed in the target. Cratering behavior for hypervelocity impacts has been studied empirically for over 40 years. However, many issues have remained unresolved, including whether the craters are fundamentally a function of impactor kinetic energy or momentum. Likewise, the appropriate material parameters governing the responses have been uncertain.

2.3.1 Melt Craters

Some investigators assume that craters in targets are associated with the development of impact-induced melting. However, this implies that the cratering phenomenon ceases once the stresses drop below those necessary to promote melting caused by the excess entropy trapping of shock waves. This would cause predictions of craters to be noticeably smaller than those observed, especially for very ductile targets. The true formation of craters must therefore be related to **plastic yield flow**. This makes sense since plastic flow is merely a fluid flow with off-set stresses (*i.e.*, stress deviators exist in the solid material). Melt and vaporization flow is merely plastic flow without stress deviators (we here ignore deviators due to material viscosity, and also ignore surface tension phenomena. **Note:** almost all hydrodynamics codes also ignore these two phenomena. Hydrocodes include **artificial** viscosity, but this is done only to control numerical instabilities that frequently occur when computing strong shocks). If the target cratering involved pure melt (*i.e.*, pure fluid) conditions another problem could also arise, namely the self-healing of the crater due to the internal pressure within the fluid and the effect of surface tension. This latter behavior is typical of impacts into true fluids (*e.g.*, into water), where it is well known that a transient crater is formed that disappears later due to the inflow of the material, leaving no permanent crater.

Clearly, a "melt" crater is the minimum possible crater, and can be expected to dominate the cratering process only for cases where the yield stress of the target is very large and the crater surface is rapidly decelerated once the propagated stresses drop below those that induce melting upon release. Thus the response is also sensitive to the rate of decrease in the yield strength versus temperature (thermal softening). Materials which soften rapidly with increase in temperature (*e.g.*, ductile metals) will effectively extend the apparent "melt" region, whereas materials which soften significantly only as melt is approached (*e.g.*, ceramics) will restrict the apparent melt region.

For reference, it should be noted that for the symmetric aluminum/aluminum impact incipient melting occurs for an impact speed of about 5.6 km/s (1-D stress of 0.65 Mbar) while complete melting occurs at about 6.6 km/s (1-D stress of 0.9 Mbar). Incipient vaporization occurs for an impact speed of about 10.2 km/s (1-D stress of 1.67 Mbar). Thus no melt crater can be formed

for impact speeds of less than 5.6 km/s for this case, yet significant cratering is experimentally observed in aluminum for impact speeds less than this value.

2.3.2 Initial Approach - The "Energy Equation"

One well known approach to cratering is the energy equation, which equates the kinetic energy of the impactor with the energy necessary to excavate a hemispherical crater. Thus we obtain

$$(\pi/12) \rho_p d_p^3 u_0^2 = (\pi/12) \rho_t d_c^3 E_t \quad (5)$$

where ρ is the density of projectile or target, d is the diameter of projectile or crater, u_0 is the impact speed, and E_t is a limiting energy-per-mass to create the crater within the target. Rewriting, we obtain

$$d_c/d_p = (\rho_p/\rho_t)^{1/3} u_0^{2/3} / (E_t)^{1/3} \quad (6)$$

Thus this equation gives the familiar 2/3rd law for velocity, and a 1/3rd law for density. However, there are obvious problems with this approach. Energy absorption (per mass) in the target is presumed to be a constant within the crater, which is clearly wrong since the energy density varies with the stress levels. Further, the logic ignores energy absorption within the impacting projectile, and also ignores the elastic energy stored in the stress wave propagating beyond the crater region. Thus the energy used to excavate the crater is always less than the original impactor kinetic energy, but the fraction varies according to the relative strengths, moduli, thermal properties of the projectile and target, and the relative mass of the crater versus the projectile. The use of a limiting energy density is really the same as defining a limiting stress, since energy-per-mass is equivalent to stress-squared divided by twice a modulus and divided by the density.

$$\text{Thus} \quad E_t = 1/2 \quad \alpha^2 / (\rho_t M) \quad (7)$$

where α is the limiting stress, and M is a modulus of the target. Despite these problems this energy equation does give a reasonable account of cratering provided an empirical multiplier is used. For example, using the incipient melt enthalpy of aluminum of 150 cal/g (6.28×10^9 erg/g) and an impact speed of 10 km/s, Equation 6 predicts $d_c/d_p = 5.42$ which is close to observed values.

2.3.3 More General Approach

Assume that upon impact a pseudo-spherical compressive wave is propagated into the target centered on the impact point. Release waves from the target surface outboard of the projectile will cause the compression to be followed by a tensile wave. Release waves from within the impactor do not cause tensile states by themselves since there is no inter-body strength between the impactor and the target surface. Hence any attempt to propagate a tensile wave would merely lift the impactor away from the target.

For hypervelocity impact the initial stresses and shock-induced heating will cause gross plastic flow in the target. If the heating is sufficient to induce a state above melting (including vaporization) the material will flow as a simple fluid. Once the stresses drop into the solid response region the flow will be standard plastic yielding. There are three cases of such yielding:

- (a) during the passage of the compressive pulse,
- (b) during the passage of the trailing rarefaction pulse, and
- (c) after the main pulse has passed a given point owing to the induced radial divergence motion which leaves the material in a state of hoop strain and thus hoop tension.

If the wave motion were truly 1-D, the radial (*i.e.*, longitudinal) stress would reduce to zero while the lateral stresses would attain a permanent (residual) stress due to plastic hysteresis. For a radial stress greater than $2Y(1-\nu)/(1-2\nu)$ (*i.e.*, twice the Hugoniot Elastic Limit, see Section 2.3.7) this permanent stress is the yield value and is compressive (ν is Poisson's ratio for the target). For a radial stress between the one quoted above and $Y(1-\nu)/(1-2\nu)$ the permanent stress lies between zero and Y . For lower radial stresses the behavior is elastic only and no permanent stress occurs.

However, the response is not 1-D and involves divergence. Thus the true lateral stresses (*i.e.*, the hoop stresses) have the tensile hoop stress superimposed, giving a net tensile stress towards the impact point. Only for radial distances far from the impact point will these stresses become compressive as for the 1-D case, since the hoop tensions will become very small. These effects are seen in the CTH calculations discussed in Section 3.0.

Assume that the latest state (c) defines the final crater surface. The divergent flow-induced hoop strain is given by $\Delta r/r$ where Δr is the induced radial motion at a distance r from the impact point. The corresponding hoop stress then becomes

$$\sigma_{\theta} = \rho_t c_t^2 u_r dt/r = \sigma_r dt c_t/r \quad (8)$$

where σ_{θ} is the tensile hoop stress, σ_r is the radial stress for the pulse, ρ_t is the target density, c_t is the target sound speed, u_r is the induced particle speed and dt is the pulse time-width. Note that the quantity $\sigma_r dt$ represents the outward momentum per unit area at position r .

For a spherical projectile the mean time for a full release wave reverberation across the projectile is given by $dt = 8r_p/3c_p$ where r_p is the projectile radius and c_p is the projectile sound speed, and we assume that this time defines the effective width of the radial pulse.

Assume that the radial stress obeys the momentum rule

$$\sigma_r r^2 = \sigma_0 r_p^2 \quad (9)$$

where σ_0 is the stress generated at the interface between the projectile and the target. Further, assume that this latter stress is given by the Bernoulli law such that

$$\sigma_0 = 0.5 \dot{\rho} u_0^2 = 0.5 \rho_t u_t^2 = 0.5 \rho_p (u_0 - u_t)^2 \quad (10)$$

where u_0 is the impact speed and u_t is the induced target particle speed.

Thus
$$\dot{\rho} = \rho_p \rho_t / (\rho_p^{1/2} + \rho_t^{1/2})^2. \quad (11)$$

Assembling the terms we obtain

$$\sigma_0 = (8/3) \sigma_0 (r_p^3 / r^3)(c_t/c_p) \quad (12)$$

Now set this hoop stress to the yield strength of the target, Y_t , and set the corresponding radial distance from the impact point as the crater radius, r_c , to finally obtain

$$(r_c/r_p)^3 = (4/3)(\rho_p/\rho_t)(\rho_t/Y_t)(c_t/c_p)u_0^2/(1 + (\rho_p/\rho_t)^{1/2})^2 \quad (13)$$

Thus

$$d_c/d_p = r_c/r_p = 1.10064(\rho_p/\rho_t)^{1/3}(\rho_t/Y_t)^{1/3}(c_t/c_p)^{1/3}u_0^{2/3}/(1 + (\rho_p/\rho_t)^{1/2})^{2/3} \quad (14)$$

Several interesting points should be noted about this equation:

- (1) There is no numerical multiplier which did not come from the analysis.
- (2) The equation "looks like" the well known "energy equation", but was based on momentum.
- (3) The velocity index is the familiar 2/3rd value.
- (4) The density index is not a constant value, but depends on the ratio of densities.
- (5) The crater size depends on the ratio of target density to target yield strength. This term in the equation has the same dimensions as an inverse sound speed to the 2/3rd power, but is not a material sound speed. Nevertheless, the term serves the same function as a sound speed, in a similar manner to that invoked by others, who frequently use terms of the form (u_0/c) in their scaling laws. The yield strength is that of the target only, and does not need to be referenced to any other material. Further, note that the yield value used is the low-stress static one. The rationale for this is that the model describes the terminal conditions of crater formation. Factors such as strain-rate hardening and thermal softening are subsumed into the physics of the more highly stressed regions of the crater region,

and are treated as energy absorbing mechanisms within this region. (Note: our logic does not invoke energy as a parameter).

- (6) The equation is sensitive to the ratio of target and projectile sound speeds.
- (7) The equation obeys the rules of dimensional analysis, since the grouping is dimensionless.

The density function can be replaced by a simple ratio if we use the equivalence

$$(\rho_p/\rho_t)^N = (\rho_p/\rho_t)^{1/3} / (1 + (\rho_p/\rho_t)^{1/2})^{2/3} \quad (15)$$

Doing this we immediately find that the index N varies. For a small ratio of projectile density to target density N tends to 1/3. As the density ratio increases so N increases. When the ratio is unity N is indeterminate. For a ratio larger than unity N becomes negative, being large near the unity ratio, decreasing towards zero for very large ratios. This "odd" behavior may be the "excuse" for the varying indexes found in the literature.

Note that most experimental conditions prevent the choice of individual material parameters. To change one property (*e.g.*, density) invariably involves changing other properties (*e.g.*, yield strength, sound speed, etc.). Thus experiments invoke "clusters" of properties. For this reason dependencies on such factors as material sound speeds are difficult to identify.

For the well-known symmetric impact of aluminum into aluminum, with density of 2.7 g/cm³, sound speed of 5.1 km/s, yield strength of 2.7 kbar (*i.e.*, Al 6061 T6) and $u_0 = 10$ km/s, we obtain $d_c/d_p = 6.934$. This is near the observed values. However, this is probably a coincidence! This case is also one that "removes" many dependencies owing to the unity value of the groups involving density and sound speed.

POD believes that Equation 14 contains all the pertinent material parameters for hypervelocity impacts into highly ductile targets. Surface fracture craters are not presently included in this model owing to the assumption that highly ductile materials consume significant energy during the strain-to-fracture. This effect causes a rapid decrease in peak stress and thus prevents fracture (*i.e.*, it results in large fracture toughness; see Section 2.3.10). However, the equation has several pitfalls and the power indexes are not necessarily correct.

2.3.4 Caveats

The caveats include:

- (1) The assumption of a truly hemispherical stress wave is **not** correct. This point is readily demonstrated by considering the impact of a chunky cylinder as described before. The expanding compressive stress front only asymptotes towards a spherical wave at radial distances which are large compared to the impacting projectile radius. Thus for crater

radii which are not large compared to impactor radius the wave front is unlikely to be spherical. Similar arguments apply to the target surface-generated release waves which cause tensile waves to follow the compressive pulse. These waves are centered outside of the impactor, and only coalesce into a single pseudo-spherical wave after travelling several impactor radii.

- (2) Equation 9 describing stress versus distance presupposes a constant pulse-width. This is only true for a non-dispersive condition (e.g., a linear-elastic response). In reality, the dispersion associated with hydrodynamic wave propagation always causes the pulse to widen. This has the effect of modifying the power index for stress versus distance.

Thus we have
$$\sigma_r r^2 dr_r = \sigma_0 r_p^2 dr_p \quad (16)$$

where dr is the pulse-width at either the radius r from the impact point, or dr_p at the impactor. Dispersion gives $dr_r > dr_p$. Thus a more correct description would be

$$\sigma_r r^N = \sigma_0 r_p^N \quad \text{with } N > 2 \quad (17)$$

This will modify Equation 13 to give

$$(r_c/r_p)^{N+1} = (4/3) (\rho_p/\rho_t) (\rho_t/Y_t) (c_t/c_p) u_0^2 / (1 + (\rho_p/\rho_t)^{1/2})^2 \quad (18)$$

then we obtain the following equation

$$(r_c/r_p) = (4/3)^{(1/N+1)} (\rho_p/\rho_t)^{(1/N+1)} (\rho_t/Y_t)^{(1/N+1)} (c_t/c_p)^{(1/N+1)} u_0^{(2N+1)} / (1 + (\rho_p/\rho_t)^{1/2})^{(2N+1)} \quad (19)$$

Thus we finally obtain

$$(d_c/d_p) = (4/3)^{1/N+1} (\rho_p/\rho_t)^{1/N+1} (\rho_t/Y_t)^{1/N+1} (c_t/c_p)^{1/N+1} u_0^{2N+1} / (1 + (\rho_p/\rho_t)^{1/2})^{2N+1} \quad (20)$$

Note that this modifies the various power indexes. The discussion above also defined $N > 2$. As an example, if $N = 2.5$

$$(d_c/d_p) = 1.0857 (\rho_p/\rho_t)^{0.2857} (\rho_t/Y_t)^{0.2857} (c_t/c_p)^{0.2857} u_0^{0.5714} / (1 + (\rho_p/\rho_t)^{1/2})^{0.5714} \quad (21)$$

Thus a proper description that includes the dispersive nature of the propagating wave will give a more complete equation for cratering in ductile targets. Note that $N > 2$ produces a power index for impact velocity which is somewhat smaller than $2/3$. An index of close to 0.58 has been previously suggested by Holsapple (1987). For this reason we choose to "lock" our equation as given in Equation 21.

Substituting values for Al 6061-T6 for both the projectile and the target, and assuming an impact speed of 10 km/s, we obtain $d_c/d_p = 5.26$ which is also close to observations and to the results from the CTH hydrodynamic code calculations (see below).

- (3) The logic presupposed that the active driver-stress ceased after the time $t = 8r_p/3c_p$, which is one complete reverberation through the projectile, both axially and laterally. This does not account for the entire projectile momentum. However, it probably does describe the conditions for the diameter of a crater since the surface of the target is the region most affected by the Bernoulli flow. The late-time remaining momentum does not contribute to the lateral radially propagating stress, rather it contributes to the axially propagating stress. This is because once the full diameter of the projectile has penetrated the target surface, there is no further lateral "push" to the target. This is one reason why craters are not truly hemispherical. The same logic is expected to apply to the crater diameter produced by an LRP. For an LRP the initial stress conditions are identical to those of a chunky projectile. Only after the time $8r_p/3c_p$ does the target "know" that "extra matter" exists in the rod. Thus beyond this time the Bernoulli stress at the head of the rod remains. Use of the Bernoulli law leads to the well known penetration law for LRP (Eichelberger, 1956). Thus rewriting Equation 10 gives

$$u/(u_0-u) = (\rho_p/\rho_t)^{1/2} \quad (22)$$

and if we assume the time of action is

$$t = L/(u_0 - u) \quad (23)$$

where L is the length of the rod being "consumed" with a speed $(u_0 - u)$, then the penetration (P) is given by

$$P = u t = (\rho_p/\rho_t)^{1/2} L \quad (24)$$

which is the equation describing the penetration of either a jet or an LRP into a target (ignoring the initial and final states of penetration, and material strengths).

- (4) The equation includes the two stress wave speeds c_p and c_t . However, these speeds are not simply the low-stress values, but are averages over the entire stress histories. A more accurate integral needs to be performed in order to obtain the appropriate values.

2.3.5 Crater Diameter Versus Penetration Depth

The above logic is thought to apply to the development of crater diameters (d_c). There is no *a priori* reason to expect the rules for penetration depth (P) to be the same. Part of the reason is that, whereas it could be justified to include only part of the projectile momentum for the lateral motion there is no obvious logic to use anything other than the total momentum for describing the penetration depth, particularly if hoop-stress logic is employed. This immediately leads to a different answer.

Again assuming a pseudo-hemispherical crater, with equal local momentum per area over the entire hemispherical surface regardless of angle relative to the impact axis, the axially-directed momentum per area at a distance r (on axis) from the impact site is given by

$$I = (4\pi/3) \rho_p r_p^3 u_0 / \pi r^2 \quad (25)$$

Using the hoop stress logic then leads to

$$P/d_p = (1/2) (4/3)^{1/3} (\rho_p/\rho_t)^{1/3} (\rho_t/Y_t)^{1/3} (c_t u_0)^{1/3} \quad (26)$$

Thus this equation gives a direct 1/3rd law for densities, but also gives a 1/3rd law for impact speed. A modification in this law can be invoked by noting that the sound speed term, c_t , is really stress dependent, and should be $c_t = c_{\alpha} + s u$ where u is the induced local particle speed in the target.

Assuming the Bernoulli state to apply, we have $u = u_0 / (1 + (\rho_t/\rho_p)^{1/2})$. Thus

$$P/d_p = (1/2)(4/3)^{1/3} (\rho_p/\rho_t)^{1/3} (\rho_t/Y_t)^{1/3} \{ (c_{\alpha} + s u_0 / (1 + (\rho_t/\rho_p)^{1/2})) u_0 \}^{1/3} \quad (27)$$

For an Al/Al (6061-T6) impact at 10 km/s this equation predicts $P/d_p = 5.86$ which is too large by a factor of almost two compared to both experimental data and the results from the CTH code calculations (see later). We have not yet found the reason for this factor. To make the equation more in keeping with experimental data we insert a factor of 1/2. However, this factor is made permanent.

Next, we take note of material strengths (see below) by introducing a lower limit velocity term, $u_{t,crit}$ (target, critical speed). Equation 27 then becomes

$$P/d_p = (1/4)(4/3)^{1/3} (\rho_p/\rho_t)^{1/3} (\rho_t/Y_t)^{1/3} \{ (c_{\alpha} + s(u_0 - u_{t,crit}) / (1 + (\rho_t/\rho_p)^{1/2})) (u_0 - u_{t,crit}) \}^{1/3} \quad (28)$$

Note that Equation 28 gradually transforms from a 1/3rd law for velocity into a 2/3rd law at high speeds, becoming

$$P/d_p \Rightarrow (1/4) (4/3)^{1/3} (\rho_p/\rho_t)^{1/3} (\rho_t/Y_t)^{1/3} (u_0)^{2/3} (s / (1 + (\rho_t/\rho_p)^{1/2}))^{1/3} \quad (29)$$

This transition depends on the ratio s/c_{α} with a low ratio causing the response to remain in the 1/3rd law regime even for moderately high impact speeds, while a high ratio transforms into the 2/3rd law at lower speeds. Theoretically, the value for $s = (1 + \Gamma)/2$ where Γ is the Gruneisen parameter. Materials with very low Γ thus have low values of s . Such materials are frequently porous and highly energy absorbing (*i.e.*, dispersive). Most solids have high values of Γ (about 2.0) and absorb energy less (although shock entropy-trapping still causes a degree of absorption). We thus expect very energy-dispersive targets to display the 1/3rd law at moderate impact speeds, while most solids will rapidly display the 2/3rd law. These expectations are in accordance with the conclusions of Holsapple (1987) who states that very energy-absorbing systems tend to obey

the momentum rule for penetration depth, while truly non energy absorbing targets tend to obey the energy rule. The meaning of energy "absorption" is that part of the projectile kinetic energy is irreversibly converted into heat and/or plastic deformation, which always occurs with porous materials and also occurs to a lesser extent with strong shocking in solids. Note that for shocks sufficiently strong to cause complete vaporization the heating is recoverable, since the energy eventually is converted into kinetic energy of gas motion.

Note that if the local momentum is not uniform versus angle from the axis this merely changes the leading numerical multiplier. For example, if momentum obeys the rule $I(\theta) = I(0)\cos\theta$ then the term $4/3$ becomes 2.

As with Equation 21 which described the crater diameter, POD believes that Equation 28 contains all the relevant material parameters for describing crater depth, but that the various power indexes are possibly incorrect.

The u_{crit} term is not included in Equation 21 for crater diameters. The logic for this is that the near-free surface target response involves strong release motion. This means that the distinction between elastic-plastic response and the true Bernoulli response is less apparent, so the transition is more gradual.

2.3.6 Projectile Strength

The previous discussions have referenced only the target strength, but not the projectile strength. During the initial pseudo 1-D impact the stress states in both the projectile and the target are functions of their respective Hugoniot. At low stresses material strength results in an elastic region up to the Hugoniot Elastic Limit (HEL) and an elastic wave only is propagated. For stresses above HEL but below a stress σ^* (defined below) a two-wave structure develops, consisting of an elastic wave precursor followed by a slower plastic wave. In this stress regime the precursor can pre-condition the material for later response to the plastic wave. For stresses above σ^* the plastic wave overtakes the elastic wave, resulting in only one shock wave equal to the plastic wave. The stress σ^* is defined as that point on the Hugoniot given by the condition that the Rayleigh line from the HEL up to the Hugoniot be an extension of the path from zero stress to the HEL. Generally, both the HEL and σ^* are much smaller than the impact stresses for hypervelocity conditions.

Upon passage of the shock wave through the projectile to its rear surface, stress release will occur via a rapid elastic decrease and a slower plastic decrease (unless the liquid or vapor state is induced, for which both yield strength and shear modulus vanish), and these release waves propagate back to the projectile/target interface. However, from this time on the exact state of the projectile has minimal effect on the subsequent cratering process, while the strength of the target continues to influence the cratering process. This is the primary reason why only the target strength is referenced.

2.3.7 Strength Effects at Low Impact Speeds

However, these arguments are only valid provided the impact stresses are much higher than the HEL and $\bar{\sigma}$ values. For low speed impact the material strengths become important, ultimately dominating the response. Clearly, if the impact produces stresses below the HEL of the projectile no permanent deformation of the latter occurs. Likewise, if the stress is below the HEL of the target no cratering occurs (not even simple plastic indentation). The situation is similar to the correction terms used by Tate (1967) for LRP, where the Bernoulli equation is modified by adding a strength term to both the projectile and the target, as in

$$\sigma = 0.5 \rho_p (u_0 - u)^2 + Y_p = 0.5 \rho_t u_t^2 + Y_t \quad (30)$$

Note that this correction is itself wrong since the equation does not allow for a solution at low values of velocity. A more correct version would treat the strength terms in the form $HEL = \rho c u_{crit}$ and $Y = 0.5 \rho u_{crit}^2$, with u_{crit} setting a velocity limit for each material. This form of the equation does allow for solutions as impact speed drops to zero.

Specifically, if the Bernoulli stress limit is not achieved there will be no "fluid flow" induced and the response will become elastic-plastic only. If the HEL is not achieved the response is purely elastic. The critical velocities for Bernoulli yielding are given by

$$\text{for projectile: } u_{p,crit} = (2Y_p/\rho_p)^{1/2}(1+(\rho_p/\rho_t)^{1/2}) = (2Y_p/\rho)^{1/2}(1+(\rho/\rho_p)^{1/2}) \quad (31)$$

$$\text{for target: } u_{t,crit} = (2Y_t/\rho_p)^{1/2}(1+(\rho_p/\rho_t)^{1/2}) = (2Y_t/\rho)^{1/2}(1+(\rho/\rho_p)^{1/2}) \quad (32)$$

For an Al/Al impact of Al 6061-T6, the critical Bernoulli speed is 0.814 km/s. The corresponding speed limit for the HEL is much lower, being 0.039 km/s. Thus between these two impact speeds the response is elastic-plastic, and no Bernoulli flow occurs

For TFE Teflon, Y_t is about 300 bars and ρ_t is 2.17 g/cm³, while for aluminum 6061-T6 the corresponding values are 2.7 kbars and 2.7 g/cm³, respectively. Thus for an aluminum projectile and Teflon target, $u_{t,crit}$ is 0.315 km/s, while $u_{p,crit}$ is 0.946 km/s.

As an example of these effects, consider an impact between an Al 6061-T6 projectile and an alumina target. For alumina the density is 4.0 g/cm³ and the yield strength is about 60 kbars. We find the critical Bernoulli impact speeds are 3.84 km/s for flow in the alumina and 0.815 km/s for flow in the Al. Thus an impact speed of less than 3.84 km/s will not induce Bernoulli flow-style hypervelocity craters in the alumina target, but will cause flow in the Al projectile, causing a crater which is shallow relative to its diameter. The reverse occurs if projectile and target are exchanged (*i.e.*, the projectile does not suffer flow but the target does, giving a crater which is deep relative to its diameter). It is for impact conditions below the Bernoulli limit, where elastic-plastic response dominates, that material hardness values are relevant.

The above example explains why ceramic materials are useful as armor against jets and LRPs. The standard equation (Equation 24) indicates that normally the target material should be of high density to defeat an LRP. Yet most ceramics are of low density. It is the unusually high value of u_{crit} for ceramics that explains their use, which is due to the high ratio of compressive yield strength and low density. Most ordinance is of lower velocity than these critical speeds.

One technique for understanding the responses is to use what are known as P-u (Pressure-particle speed) curves. Such curves are a well-known tool for 1-D impact solutions. The impact stress is given by the intersection of the material Hugoniot. For most solids (except porous bodies) the release paths are very similar to the Hugoniot, resulting in paths which are essentially "mirror images" of the Hugoniot. To understand the responses for "chunky bodies" we introduce the concept of Bernoulli adiabat, by analogy to the Hugoniot being also known as the Shock adiabat. The Bernoulli adiabat applies only to compressive paths, with release following the normal paths.

This approach immediately explains an interesting anomaly: for 1-D impact of a low impedance projectile into a high impedance target the projectile rebounds after the first stress wave reverberation through the projectile, yet for a chunky projectile (same materials and impact speed) the projectile does not rebound. The explanation is as follows.

Immediately upon impact the pseudo 1-D stress is given by the Hugoniot state. When the lateral stress relief reaches the impact axis the stress drops to the Bernoulli stress. If both materials undergo Bernoulli flow this stress is given by the intersection of the two Bernoulli adiabats. If only one material flows then that material jumps to its Bernoulli locus but the other material remains on its Hugoniot. If neither material flows then both materials remain on their Hugoniot.

Figure 1 shows the case of the low impedance projectile impacting the high impedance target. The initial stress rises from (A) along the projectile Hugoniot to the intersection with the target Hugoniot at (B). This stress then rapidly drops to the Bernoulli state (D). The rear surface release wave now originates from the Bernoulli state instead of from the Hugoniot state (path DE instead of BC). Thus the projectile velocity merely decreases instead of reversing. Subsequent recompressions follow the Bernoulli adiabat, while release follows the normal path. Thus a series of reverberations in the projectile occur as the latter comes to rest. Because the projectile is simultaneously thinning as it spreads laterally each subsequent reverberation transit time becomes progressively shorter. Thus the projectile rapidly stops.

The same logic also explains the very deep craters formed when "strong rigid" projectiles (*e.g.*, tungsten carbide) impact "weak soft" targets (*e.g.* aluminum, lead) at relatively low speeds. If the impact speed is above u_{crit} for the target, but below u_{crit} for the projectile, only the target will jump to its Bernoulli locus while the projectile remains on its Hugoniot, as shown in Figure 2. The projectile slows down via a large number of reverberations, and since the projectile does not significantly deform these reverberations have constant transit time. Thus the total time taken to stop is long, and the crater is deep.

This particular logic also applies to the case of trying to capture a particle totally intact (no flow except elastic-plastic deformation). To do so requires the impact speed to be below the u_{crit} of the particle but above the u_{crit} of the target. Since the particle properties are fixed the only option is to choose a target with a very low u_{crit} value. Referring to Equation 31 we see that this implies the need for a target material with very low yield strength and very low density. This description applies to the case of trying to capture micrometeoroids with very low density foams and aerogels.

The result of the strength terms is to produce significant deviations in response at the low impact speeds. Thus none of POD's equations are rigorous for speeds below the 1 km/s range.

2.3.8 General Comments on Scaling (Similarity) Laws

The above approaches reveal that it is rarely self-evident as to whether the analysis should be based on a momentum logic or an energy one. This dilemma has important consequences since momentum conservation logic (as used above) gives an inverse-square law (i.e., $\sigma_r \propto r^{-2}$) for stress amplitude versus propagation distance, whereas energy conservation suggests a simple inverse law ($\sigma_r \propto r^{-1}$), for spherical divergence. Reality suggests that the true response is a mixture, with an index between -1 and -2. Further, the known non-linearities of hydrodynamics suggest that the index is probably variable also, depending on stress levels and propagation distances. Such effects explain why the various power indexes are difficult to derive, and also imply that these indexes may not even be constants.

An obvious question is whether the process of impact cratering should obey a "simple" scaling law. There are reasons to believe the answer is rigorously "no", although a "reasonable approximation" may exist. The basis of this comment rests on work done by such scientists as Zeldovich (1992) who studied the following simple case.

Imagine a semi-infinite half-space of gas of initial finite uniform density but of zero temperature and pressure (this problem is clearly a "thought experiment" since such a gas state is impossible). Allow a piston to impart a transient 1-D push to the free surface of the gas for a short period and then be rapidly withdrawn faster than the release motion of the gas surface, thus transferring a ballistic impulse to the gas.

The result of this impulse is to propagate a shock into the gas and simultaneously cause the free surface of the gas to expand outward. Thus a "turning point" exists within the gas dividing the particle motion into two regions of inward-going and outward-going, and this point itself follows the shock front but at a lower speed.

Zeldovich attempted to find a single similarity rule that described the behavior and, in particular, predicted the rate of decay of the shock pressure versus propagation distance. He immediately met a problem: it was impossible to establish a single rule that simultaneously conserved both momentum and energy. However, Zeldovich was able to find an asymptotic rule that did obey both conservation rules provided a piece of the problem was "ignored". Specifically, if a "slug"

of gas at the leading edge of the free surface expansion was ignored then the remainder of the problem could be described by a scaling law which satisfied the conservation laws. This "slug" contained the gas mass which was initially compressed during the ballistic impulse.

Thus Zeldovich concluded that a scaling law could be asymptotically determined as the "slug" mass became negligible compared to the total mass in the moving gas, which itself continuously increases with time. For the case of a diatomic gas ($\gamma = 7/5$, ratio of specific heats) the result was that the shock pressure decayed with the 4/3rd power of the distance. Note that Zeldovich's problem was simple in the sense that it was 1-D and involved no material strength or phase change effects. Note that the power index was between -1 and -2, even though this is a 1-D condition.

POD is of the opinion that a similar situation applies to cratering. It can be anticipated that the solution is really one which asymptotes when a portion of the problem is ignored. This portion is probably related to the projectile mass and the mass of the target involved in the initial shock wave phase. Thus the solution may have two parts, one describing the initial material response and one describing the later cavitation phase. As the mass of the cavity (*i.e.*, crater) becomes large compared to that of the projectile and initially compressed target material so the response can be expected to approach a condition that can be described by a scaling law that satisfies conservation rules. This logic implies that simple scaling laws are to be expected only for impact conditions which produce large craters (*i.e.*, high speed, low target yield strength, high ratio of projectile to target densities).

2.3.9 Supralinearity

Although supralinearity has been experimentally observed it is not predicted by any known analysis based on hydrodynamics, neither do purely hydrodynamic codes predict it. Suggestions have been made that the effect is related to the fact that the projectile flattens (*i.e.*, "pancakes") as it impacts the target, and that this modifies the apparent diameter of the impactor. This logic has then been coupled with a suggestion that small projectiles are "stronger" than larger ones, and thus deform less.

The hydrodynamic arguments given above involved the term r_p^3 , this being a product of the cross-sectional area of the projectile and the effective "time-width" of the projectile. In reality, the term r_p^3 is a measure of the volume (or mass) of the projectile. Since the latter remains constant during the initial impact the logic suggests that the exact shape of the projectile is not important, at least for small changes. This accords with the common assumption that spheres can be approximated by the equivalent-volume (chunky) cylinders and that cratering is a function of the projectile mass. If this logic is valid, then the "pancaking" process should have no significant effect. Thus supralinearity must be caused by some other mechanism.

A phenomenon that could explain the supralinearity is the "Petch Law" (Petch, 1953) which describes the strength of a ductile material versus its mean grain size. This law states

$$Y_t = Y_\alpha (1 + (\Delta/d)^{1/2}) \quad (33)$$

where Y_α is an intrinsic yield strength, Y_t is the observed strength, d is the mean grain size, and Δ is a material-specific "grain size" parameter. The law predicts an increase in yield strength as the grain size decreases. Experimental data for aluminum (Anderson, 1990) suggests that Δ is about 50 microns. Petch's theory involved consideration of the shearing that occurs between grains. Based on this theory the quantity Δ is given by

$$\Delta = \pi G \gamma / Y_\alpha^2 \quad (34)$$

where G is the material shear modulus and γ is the material surface energy per area for opening cracks.

POD thus suggests that supralinearity is related to target strength properties, and that this effect is related to crater size and projectile size. However, only the former is important because of the arguments given above. Specifically, the important aspect of the problem is the ratio Δ/r_c , the ratio of material-specific size and the crater radius.

To understand the logic, consider that the normal "bulk" yield strength of a material is really an average over a volume large compared with the dimension Δ . If the "active" volume under consideration (e.g., the crater) becomes comparable to this dimension then the normal bulk properties no longer apply. Clearly, if the crater involved only a single material grain the governing yield strength would be that of the grain rather than of the average material. On the other hand, if the impact were on a grain boundary the apparent material strength would be lower. Since the probability of hitting a grain is higher than hitting a boundary for a small impactor the average response will be a higher yield value.

To apply the Petch Law we use Equation 33 to define the effective yield strength in Equations 21 and 28, and replace the term d with r_c . Unfortunately, the solution requires iteration of the resulting equation owing to the form of the r_c terms on either side of the formula. However, the asymptotic solution can be readily obtained for $\Delta \gg r_c$.

$$\text{Let } (r_c/r_p)^N = (A/Y_\alpha) / (1 + (\Delta/r_c)^{1/2}) \Rightarrow (A/Y_\alpha) (r_c/\Delta)^{1/2} \quad (35)$$

with the term A containing all the details of density, impact speed, etc. Then the asymptotic solution becomes

$$(r_c/r_p)^{(N-1/2)} = (A/Y_\alpha)(r_p/\Delta)^{1/2}, \text{ or } (r_c/r_p) = (A/Y_\alpha)^{1/(N-1/2)}(r_p/\Delta)^{1/(2N-1)} \quad (36)$$

Note how we converted a dependence on r_c to one on r_p . Thus if the effective power index is $N = 3.5$ (equivalent to the index used in Equation 21, which employed $N+1$ rather than N), we obtain

$$(r_c/r_p) = (A/Y_\alpha)^{1/3} (r_p/\Delta)^{1/6} \quad (37)$$

giving a supralinear term with a power index of 1/6 (0.1667), which is thus the "small-limit" index. However, the most-quoted supralinear index is that given by Cour-Palais (1985) with a value of 1/18 (0.056). It is interesting to see whether the Petch law can explain the Cour-Palais quote, without invoking "absurd" values for the power index N used in Equations 35 and 36.

The use of the Petch law produces a "downgrading" factor, F , in the crater sizes otherwise predicted, so we multiply Equations 21 and 28 by this factor

$$i.e., \quad F = 1/(1 + (\Delta/r_c)^{1/2})^N \quad (38)$$

Using $\Delta = 50$ microns and $N = 1/3$ we compute F versus the "normal" crater prediction, r_c . We find that for $r_c = 1.0$ micron $F = 0.499$, for $r_c = 10$ microns $F = 0.6761$, for $r_c = 100$ microns $F = 0.8367$, for $r_c = 1$ mm $F = 0.9349$, and for $r_c = 1$ cm $F = 0.9775$. We immediately see that the "effective" supralinear index varies with crater size (hence projectile size). For very small craters (*i.e.*, $\ll 1$ micron) the index approaches 1/6, while for large craters ($\gg 1$ cm) the index approaches zero. Thus the apparent index, n , must be in the range $0 < n < 1/6$. What is relevant is that comparing values over a range of crater sizes can lead to an apparent index in the region of 0.034 to 0.073. Specifically, over the range 10 microns to 1 cm (or 50 microns to 1 mm) the apparent index is 0.0534 (or 0.0546), which is very close to the Cour-Palais value. Thus the Cour-Palais index may merely be an "apparent" index which applies over a restricted range of projectile sizes. Figure 3 plots F versus r_c .

The corresponding value of Δ for Teflon is not well known since no quotes have been found for the γ term. If this term were similar in value to that of aluminum the value of Δ would be a factor of about 1.5 larger than for aluminum taking into account the lower yield strength and lower shear modulus of Teflon. This would have the effect of increasing slightly the corresponding values of crater size (r_c) required to produce a given F value, which in turn means that the size range over which the supralinearity is observed would increase slightly.

If the above logic using the Petch law is correct then a very important corollary results: the supralinearity does not apply over all crater sizes but is in reality a small-size decrease in crater dimensions. In particular, the effect disappears for craters above about 1 cm diameter. It should be noted that most (all?) of the experimental data illustrating the supralinear effect have involved projectiles in the size range of microns to mm, which is consistent with the above logic and expectations.

Two other factors could also produce a supralinear effect, namely thermal conduction and strain-rate effects. If the strongly shock-heated regions were to rapidly cool via thermal conduction to deeper lying regions then the operational yield strength would increase. Normally, thermal conduction is ignored in hydrodynamic calculations owing to the fact that stress waves move much faster than thermal diffusion waves. However, this difference in propagation rates is small for very small scale geometries (below a few microns for metals). Thus very small craters may become thermally "quenched" and grow less than would happen without conduction. This effect

would be strong only for the smallest craters, and should be negligible for craters above 10 microns.

Strain-rate has been proposed as an important mechanism for supralinearity, based on the observation that the yield strength of many materials noticeably increases for very high rate conditions. However, this suggestion has not been well proven in hydrocode analysis. Further, it has not been demonstrated that the cratering is a direct function of the shock front. The increase in yield strength is observed for the shock *front*, but since the effect is related to viscous flow it is also observed that the stress relaxes back toward the normal yield value *behind* the shock front. Thus if cratering is related to the *integral* of the stress pulse versus time the strain-rate effect will only slightly modify the cratering versus the absence of the effect. A more fundamental problem is the fact that strain-rate has the units of time, not length. To obtain a length parameter would require the combination of velocity/strain-rate. Indeed, if strain-rate is responsible for supralinearity then there should be a velocity dependence, such that higher impact speeds give systematic "smaller" craters than would normally be expected. This would reveal itself as an apparent drop in the *velocity* index. Proponents of strain-rate logic never mention this fact.

2.3.10 Brittle Material Response

Because TFE Teflon can behave in a brittle fashion it is appropriate to briefly discuss such responses. The major difference between a brittle material response and that of a ductile one is that the former can produce radial cracks (centered on the impact point) and an outer spall crater surrounding the normal yield crater. Brittle materials fail readily under simple tension by tensile fracture. However, under compression (especially a tri-axial state with simultaneous lateral compressions) such materials display plastic yielding (especially if simultaneously heated). The compressive yield strength is usually significantly higher than the tensile strength. Indeed, for hard ceramics and glasses the yield strength is very high. Ordinary soda-lime glass has a compressive yield value of about 30 kbars (as evidenced by its ability to accept hardness indentations), while alumina has a yield strength of over 60 kbars (as evidenced by it displaying a Hugoniot Elastic Limit under 1-D shock compression).

We can develop an equation describing radial cracks by equating the hoop stress logic given before with the stress necessary to cause crack growth in the mode-1 manner. This latter stress is given by

$$\sigma_{\text{crack}} = \alpha K_{1c} / r^{1/2} \quad (39)$$

where K_{1c} is the fracture toughness (units of $\text{dyne/cm}^{3/2}$) and r is the radius from the impact point, assumed equal to the length of the radial crack. The quantity α relates to the local stress distribution around the crack. The latter is difficult to evaluate from theory since the stress is not the same as that for a static simply loaded sample with a uniform far-field value. Instead, we are dealing with a finite radially moving hoop tensile pulse which effectively applies its stress in a more local manner near the crack tip. Further, the fact that several radial cracks can occur

spaced around the impact point means that the "far-field" distance can be no more than the half-distance between these cracks. Thus α is best determined by empirical experiment.

Equating the hoop tension (Equation 8) with Equation 39 gives

$$r_{\text{crack}}/r_p = (\rho_{\text{eff}}/\alpha K_{1c})^{0.4} u_0^{0.8} r_p^{0.2} \quad (40)$$

where
$$\rho_{\text{eff}} = \rho_p \rho_t / (\rho_p^{1/2} + \rho_t^{1/2})^2 \quad (41)$$

The following should be noted:

- (1) The equation predicts supralinearity with an index of 0.2. Cour-Palais (1985) quotes this **same** index as being the one for brittle material response for the spall craters, versus the index of 0.056 for ductile materials.
- (2) The velocity index is 0.8 rather than the roughly 2/3 value for ductile craters.
- (3) Because of these differences in the two indexes it follows that "cross-over" points exist. Keeping all other factors constant, if the variable is either velocity or projectile size there will be a critical velocity or critical projectile size where $r_{\text{crack}} = r_{\text{crater}}$. Projectiles which are both large and at high speed will tend to produce radial cracks which extend out further than the corresponding ductile craters. Materials with low yield strength and high values of fracture toughness (e.g., most metals) will tend to have $r_{\text{crack}} < r_{\text{crater}}$. For this case the cracks are "lost" within the ductile crater. For materials with low fracture toughness and high yield strength (e.g., most ceramics and glasses) the reverse occurs. The ductile craters are limited in size while extensive radial cracking will be observed extending beyond the crater.

Experimental impact data from Hörz (1992) on TFE Teflon indicate spall cratering surrounding a yield crater. However, when the samples are sectioned (see Figure 4) a series of radial cracks are observed. These cracks are roughly equi-spaced around the hemisphere centered on the impact point. The hemispherical surface which circumscribes these cracks is observed to intersect the original target surface at the radius of the spall crater. Thus the spall crater radius is intimately linked to the radial cracks, and the latter define the spall crater radius. The evidence implies that the spall crater depth is determined by "peel-back" and fracture of the outer portions of the material between the original surface and the first radial crack from the surface. Thus Equation 40 gives the spall crater dimension. However, at present there is no simple manner for predicting how many radial cracks will be produced, and thus how deep the spall crater may be.

2.3.11 Phase Changes and Momentum Enhancement

Thus far the phenomena of melting and/or vaporization have been discussed only in terms of the induced fluid state which has negligible yield strength, shear modulus or tensile strength. However, as vaporization starts to occur another factor must be included, namely the

enhancement of the impact momentum caused by the backstreaming of the vapor. Although there is always some backstreaming material during cratering (e.g., the jetted material and parts of the crater lips which break off) the momentum associated with this is usually small if the material states do not include vaporization.

The major effect associated with vaporization is a dramatic change in the behavior of the release adiabat (isentropes). For solids and liquids the release adiabats are steep and have very little curvature in the pressure-volume (P-V) plane. Thus the release wave speeds are high and there is only a limited spread in the wave speeds (wave speeds are given by $c^2 = -V^2 dP/dV$, where V is specific volume). Furthermore, the expansion required to reach zero pressure is also small. Consequently, the stress relief is "rapid". The released energy (i.e., PdV) converted into motion is also small (i.e., the shocked material remains hot even at zero stress).

For the vapor state, however, the release adiabats have significant curvature in the P-V plane and significant expansion is required to reach zero pressure. Hence the average wave speed is lower and there is a significant spread in release wave speeds giving the well-known "Taylor Fan". The time to reduce the stress is much longer than for the solid/liquid states. Thus the extra momentum is a consequence of the larger release pressure-time integral for vapors. The released energy for a vapor is large and ultimately becomes converted totally into kinetic energy of motion and thus the temperature adiabatically decreases as expansion occurs, for a full-vapor state (i.e., one whose adiabat passes above the material Critical Point).

For release states which cross the two-phase liquid-vapor condition there is a gradual change from the liquid behavior to the pure vapor behavior as the initial shock loading increases.

If cratering is dependent on net momentum then the vaporization will cause deeper craters, but will have little effect on crater diameter since the latter is mostly determined during the initial reverberation within the projectile during which the "long release tail" has not developed. For total vaporization of the projectile the net momentum increases by considerably less than a factor of two, partly because the vapor state of the projectile occurs upon generation of the first release wave from the back of the impactor, and at this time the projectile is moving forward with about half the initial impact speed, but also because the vapor cloud expands hemispherically upstream.

Since half the projectile momentum (for a like-on-like impact) is transferred to the target during the first shock wave motion from the projectile/target interface back to the target free surface, only the second half of the momentum can "bounce". Thus at worst we expect the total momentum to be 1.5 the initial projectile value. This is an upper limit since it assumes the rebounding material remains as a solid particle with no lateral spreading.

An approximate evaluation of the additional momentum for total vaporization can be obtained by using the logic developed by Gurney (1943). The essence of Gurney's theories is that the expanding vapor cloud rapidly asymptotes to a condition where there is a leading edge velocity, u_∞ , which becomes a constant, and the gas between the source of the gas expansion and the leading edge, at r_∞ , has a linear distance relationship of the form $u(r) = ru_\infty/r_\infty$. The second

assumption is that, at any time, the density in the vapor cloud is a constant determined solely by the volume swept out by the advancing edge r_o versus the source. Using these rules, and assuming hemispherical expansion from a fixed source we integrate the energy within the hemisphere and set it to one-half of the impactor energy (since one-half is transferred during the same wave motion) to get

$$u_o = (5/6)^{1/2} u_0 \quad (42)$$

We now integrate over the hemisphere to obtain the net directed momentum (*i.e.*, along the impact axis) to get

$$I = (3/16) (5/6)^{1/2} I_0 \quad (43)$$

where I_0 is the initial projectile momentum. Thus the total momentum becomes

$$I_{total} = 1.171 I_0 \quad (44)$$

A further refinement occurs when we assume that the vapor expansion occurs from a moving source. For a like-on-like impact this speed is $-u_0/2$, where we define a positive speed as the backstreaming motion, and the initial impact speed as negative. Hence the velocity distribution becomes

$$u_r = -u_0/2 + r/r_o (u_o + u_0/2) \quad (45)$$

Note that this implies there is a "turning point" within the vapor, which divides the flow into two regions, one following the projectile/target interface and the other flowing back upstream. Next, for a like-on-like impact one-half of the kinetic energy is transferred to the target during the first shock wave transit through the projectile, before the vapor expansion starts. We therefore equate the remaining half-energy with the energy in the hemispherical cloud by integrating

$$0.5 KE_p = \pi r_p^3 \rho_p u_0^2/3 = \int_0^{r_o} 2\pi r^2 \dot{\rho}_p (u_r^2/2) dr \quad (46)$$

$$\text{where } \dot{\rho}_p = 2\rho_p (r_p/r_o)^3 \quad (47)$$

$$\text{Solving, we obtain: } u_o = +u_0/4 \quad (48)$$

Thus the vapor backstreams with a leading edge speed of one quarter of the initial impactor speed. Integrating over the hemisphere for the momentum we find

$$\text{Momentum} = I_0/32 \quad (49)$$

Thus the total momentum becomes

$$I_{total} = I_0 + I_0/32 = 1.03 I_0 \quad (50)$$

Thus the effect of strong vaporization of the projectile is to produce an increase in the total momentum by a factor in the range of 3% to 17%, with the true value closer to the smaller quote since the vaporization generates much of its motion before the projectile stops. For this reason the effect is not readily identified in terms of crater sizes, and the cratering response will appear to be "smooth" with no "jumps" as vaporization occurs. This implies that ultra-hypervelocity impact responses will appear to be continuations of the lower speed impact responses.

Because a portion of the target crater can also be vaporized the momentum can increase even more. However, since the peak stresses drop rapidly with propagation distance the target material subject to vaporization is usually only a small fraction of the crater, except for very high impact speeds. However, it is necessary to be aware of a "chicken and egg" problem. Lawrence (1989) has predicted a significant momentum enhancement for very high speed impacts. The source of this enhancement is the large mass ejected from the crater which is assumed to be in the vapor state and to contain a significant fraction of the projectile kinetic energy. However, is the mass ejected greater because the momentum was higher, or is the momentum higher because the mass ejected is greater? POD believes the latter is the correct interpretation. If so, the momentum enhancement provides a larger net push to the target but may have little effect on the cratering dynamics. This is because a large fraction of this momentum consists of a long-lived low pressure state, and this low pressure will tend not to cause much further cratering. Thus if the pressure decreases below that necessary to ensure the Bernoulli state in the target, the cratering efficiency rapidly drops. Overall, the effect of strong vaporization of the target is probably to deepen the crater somewhat, but not necessarily by a significant amount. This matter deserves further study.

2.3.12 Dimensional Analysis

Many investigators (Holsapple, 1987; Herrmann, 1986, and others) have used the techniques of "Dimensional Analysis" to derive cratering scaling laws. Such techniques employ Buckingham "pi" groups of parameters, as described in Bluman (1981). Thus because the quotients (d/d_p) and (P/d_p) are both dimensionless, the "pi" groups must likewise be dimensionless. However, this logic is really a mathematics-based one rather than a physics-based one. Consequently, it is necessary to correctly identify the material parameters which make up the "pi" groups, else erroneous answers can ensue.

For example, for densities it is common for the ratio (ρ_p/ρ_t) to be used. A corresponding group used by POD, however, is $((\rho_p/\rho_t)/(1+(\rho_p/\rho_t)^{1/2}))^2$ which is within POD's equations for diameter. Whereas the former ratio is "intuitive", the grouping used by POD is not.

Similarly, it is common to find the groups $(\rho c^2/Y)$ and (u/c) in many scaling laws. POD, however, puts these two groups together to obtain $((\rho/Y)u^2)$ which is still dimensionless but does not include material sound speed, which is handled independently.

The primary reason for these differing groups in POD's analyses is that, unlike the Dimensional Analysis approach, POD's analyses are based on a consideration of the physics involved. Thus

POD's equations obey the rules of dimensionality as a by-product of the analyses, rather than as the starting point for the analyses. POD believes that deriving results on the basis of physical logic is a much more appropriate approach than the use of Dimensional Analysis.

2.4 Perforation Behavior

The above discussion applies to infinitely thick targets. As the target is progressively thinned, however, the following sequence of events occurs, assuming all other factors remain constant.

First, below a certain thickness the target rear surface will display a permanent outward bulge. This is due to a region of target beyond the crater depth being subjected to a permanent residual compressive plastic stress which attempts to relieve its stress by outward motion. This bulge progressively increases as the target is thinned. For slightly thinner targets an internal spall occurs (a void) allowing the back surface bulge to protrude even more. However, the bulge does not break off, and the void can only be observed by sectioning the target.

Second, with further target thinning, the bulge splits and lips are formed around a spall crater on the target rear surface. This occurs because the reflected compressive stress returns into the target as a tensile rarefaction. Beyond a certain distance away from the rear surface, the algebraic sum of this tension and the remnant of the still-forward moving compression add up to a tensile value which exceeds the local target material strength. This explains the void described above. The spalled region detaches itself due to the stored momentum which allows the resultant edge stresses to exceed the tensile strength.

Third, with further target thinning, the final spall surface (there can be multiple sequential spalls) approaches the original front-surface crater depth. The resulting relief of stress at the deepest regions of the crater also allows continued increases in the crater depth. Thus at a critical target thickness the rear surface spall meets the crater depth, and a hole is created through the target. This condition is generally referred to as the "ballistic limit".

Fourth, for even thinner targets, the central hole rapidly increases in diameter. Simultaneously, relief waves from the target back surface arrive at the front surface and begin to modify the crater mouth, ultimately reducing its diameter. Until this happens, the crater mouth is essentially "ignorant" of the target rear surface behavior, and the perforation response resembles a case of a "truncated" crater, where only the deepest sections of the crater are affected.

Fifth, even thinner targets cause the central perforation hole to pass through a maximum in diameter, and to then decrease. Simultaneously, the crater mouth diameter progressively decreases, as does the rear surface spall hole. These two latter diameters are always larger than the central hole.

Sixth, for very thin targets, all three diameters decrease in a systematic manner, becoming closer in value to each other and also to the projectile diameter. Ultimately, a hole is formed which asymptotes to the same size (and even cross-sectional shape) as the projectile. Thus for very thin

targets (*i.e.*, $T < d_p/100$) the projectile essentially punches its own cross-sectional image through the target. This effect is of major use for identifying projectile dimensions, since the target gives a direct measurement of the latter, while the damage done to the projectile is minimal. This minimal projectile damage is a consequence of the very short-lived shock pulse which enters the projectile. Such thin pulses undergo very rapid hydrodynamic attenuation. Thus the stress levels rapidly drop and any damage in the projectile is limited to a thin skin on the impact surface.

All these events have been well characterized by laboratory impact experiments. However, such experiments have been done over a limited range of impact speeds, or with only very small projectiles (*e.g.*, micron sized) and with a limited range of impacting projectile and target materials. It therefore remains an issue of establishing the physics of the processes in order to anticipate the responses for generic conditions.

2.4.1 Stress Wave Logic: The Ballistic Limit

We shall attempt here to describe the processes leading to the Ballistic Limit condition. Note that the latter term has more than one definition. For some researchers it represents the condition of just producing a through-hole; for others it represents the case where the projectile just passes through the target (*i.e.*, $d_h = d_p$). However, the change in target thickness (all other factors remaining constant) between these two conditions is quite small. Since POD is attempting to establish physical models for development of scaling laws we believe that such "nuances" are beyond the capabilities of simplified analysis. Consequently, we shall describe a generic Ballistic Limit condition that does not attempt to distinguish these subtleties.

The logic invoked to explain front surface cratering implies that a spherically diverging compressive stress wave moves through the target as if centered on the impact point. At distances beyond the crater depth the momentum law is expected to apply. This gives

$$\alpha_r = \alpha_0 (r_p/r)^N \quad (51)$$

where α_0 is a source stress originating at the projectile/target interface, r_p is the projectile radius, r is the local distance from the impact point, and the index $N=2$ for a non-dispersive system. We assume that the source stress is the Bernoulli one, given by

$$\alpha_0 = 0.5 \rho_p u_0^2 / (1 + (\rho_p/\rho_t)^{1/2})^2 \quad (52)$$

and we also assume that when this stress wave reflects from the target rear surface it continues to spherically diverge as if centered on an image point at twice the target thickness on the impact axis. Thus the stress amplitude inverts into tension, but otherwise acts as if the wave continued to move into matter beyond the back of the target. The algebraic sum of this tensile wave and the remains of the forward-going compressive wave gives the net stress. The forward-going compressive wave drops its radial stress to zero at the crater surface. Thus the reflected wave generates the maximum tension as it approaches the crater surface.

Assume that if this tension exceeds the local target spall (fracture) strength, σ_s , the material fractures. If this fracture occurs close to the crater bottom, then the total propagation distance for the pulse was

$$r = T + (T-P) = 2T-P \quad (53)$$

where T is the target thickness and P is the crater depth. Thus we rewrite

$$((2T-P)/r_p)^N = \alpha_v/\sigma_s, \text{ or } (2T-P)/r_p = (\alpha_v/\sigma_s)^{1/N} \quad (54)$$

But $(2T-P)/r_p = ((2T-P)/P)(P/r_p)$ (55)

Hence $2T/P = 1 + (r_p/P)(\alpha_v/\sigma_s)^{1/N}$ (56)

and $T/P = (1/2) (1 + (d_p/2P)(\alpha_v/\sigma_s)^{1/N})$ (57)

Alternatively, since $T/P = (T/d_p)(d_p/P)$ we may rewrite to obtain

$$T/d_p = 0.5(P/d_p) + 0.25(\alpha_v/\sigma_s)^{1/N} \quad (58)$$

This equation thus states that there are two components to the condition causing the spall plane to coincide with the crater bottom.

Substituting Equations 28 and 52 we obtain

$$\begin{aligned} T/d_p = & (1/8)(4/3)^{1/3}(\rho_p/\rho_t)^{1/3}(\rho_t/Y)^{1/3}\{(c_{st}+s(u_0-u_{t,cr}))/(1+(\rho_t/\rho_p)^{1/2})(u_0-u_{t,cr})\}^{1/3} \\ & + (1/4)\{\rho_p u_0^2/(2\alpha_s(1+(\rho_p/\rho_t)^{1/2}))\}^{1/N} \end{aligned} \quad (59)$$

If N=2 the second term becomes

$$(1/4) (\rho_p/2\alpha_s)^{1/2} u_0 / (1+(\rho_p/\rho_t)^{1/2}) \quad (60)$$

Several relevant points can be made:

(1) The equation contains two independent parts.

(2) The equation employs both yield strength (with a 1/3 index) and tensile strength (with a 1/2 index, if N=2). We believe this explains the confusion over which strength term to use for perforations.

(3) The two parts of the equation have different velocity indexes. The first term has an effective index that starts below 2/3rd but asymptotes to 2/3rd at high speed. The second term has an index of about 1.0 (if N=2). Thus the combination of terms will appear to

have a velocity index (M) in the range $2/3 < M < 1.0$. Further, this apparent index will itself not be constant, but will slowly change with impact speed, increasing if $N < 2$, and decreasing if $N > 2$. All previous existing equations (see Section 4.0) for the Ballistic Limit have a velocity index of $2/3 < M < 1.0$.

Figure 5 shows the effects of variations in N on Equation 59 for aluminum on aluminum impacts. As will be discussed in Section 3, the previous CTH calculations done for aluminum cratering in infinite targets demonstrated that, for distances greater than the crater depth, the stress decayed in magnitude with approximately an inverse distance squared law. Thus $N=2$ is a good approximation for aluminum.

It should be noted that, as the Ballistic Limit condition is approached, the reflected stress wave actually passes the crater bottom before the latter has finished full development. If the crater were fully formed before the generation of a spall surface just beyond the crater bottom, the result would be to leave a thin wall of material at the crater bottom. There would not be a through-hole. However, because the crater has not completely stopped when the spall occurs, the continued hoop stretching causes this thin wall to open up into the hole.

The CTH data indicated that the deceleration of the crater bottom was at a pseudo-constant rate. Hence, the mean speed was almost one-half of the initial speed generated at impact.

$$\text{Thus } u_w = 0.5 u_0 / (1 + (\rho_t / \rho_p)^{1/2}) \quad (61)$$

and the time to form the crater depth is

$$\tau = P / u_w \quad (62)$$

During this time the stress waves moves at speed c_t and propagates a distance

$$x = c_t P / u_w \quad (63)$$

$$\text{Thus } x/P = 2 c_t (1 + (\rho_t / \rho_p)^{1/2}) / u_0 \quad (64)$$

For an Al/Al impact, this ratio becomes $4c_t/u_0$. For a sound speed of 5.1 km/s and impact speed of 10 km/s the ratio is about 2. Thus $2T - P = 2P$, or $T = 1.5 P$ is the maximum value to allow the stress to reach the crater before the latter has fully developed.

In the same manner as was done for the sound speed term in the rule for cratering depths (Equation 28), we introduce a mean correction for high stress (high speeds) to obtain

$$x/P = 2 \{c_{\alpha} + s u_0 / (1 + (\rho_t / \rho_p)^{1/2})\} (1 + (\rho_t / \rho_p)^{1/2}) / u_0 \quad (65)$$

which for high speed impact reduces to

$$x/P = 2 s \quad (66)$$

For aluminum $s=1.4$, therefore $x = 2.8 P$. But the required propagation distance for the stress wave to reflect and reach the crater bottom is $x = 2T - P$. Thus, $T = 1.9 P$ is the **maximum** limiting target thickness (for aluminum) at high impact speed that allows the reflected wave to pass the crater bottom before the latter has finished its full "normal" (*i.e.*, infinite target) development. The above quote should be compared to the quote of $T = 1.8P$ to just prevent perforation, as given by Christiansen (1992b).

For TFE Teflon $s = 0.795$, therefore $x = 1.59 P$. But the required propagation distance for the stress wave to reflect and reach the crater bottom is $x = 2T - P$. Thus, $T = 1.295 P$ is the **maximum** limiting target thickness (for TFE Teflon) at high impact speed that allows the reflected wave to pass the crater bottom before the latter has finished its full "normal" (*i.e.*, infinite target) development.

2.4.2 Ultra-Thin Targets (Foil)

For perforations of ultra-thin targets ($T < d_p/100$), we assume a similar logic to that used to describe crater diameters. Again, we assume that the radially propagating pulse contains momentum which induces hoop strains and stresses, and that the cratering process stops when the latter drop to the local yield strength of the target. Thus

$$Y_t = \alpha_t dt c_t/r_c \quad (67)$$

However, there are two major modifications for ultra-thin targets. First, the effect of rapidly arriving release waves from both the front and rear target free surfaces causes the stress to decrease with propagation distance very rapidly, such that

$$\alpha_t = \alpha_0 (r_p/r)^N \quad (68)$$

with $N \gg 2$. Second, the effective time-width of the pulse is no longer related to the reverberation time within the projectile, but instead is given by the reverberation time across the target, since beyond this time the projectile has effectively punched through the target and there is no further lateral push. Thus

$$dt = 2T/c_t \quad (69)$$

Thus from Equations 52, 67, 68 and 69 we obtain

$$Y_t = (\rho_p/2)(1/(1+(\rho_p/\rho_t)^{1/2})^2) u_0^2 (2T/c_t) (c_t/r_c) (r_p/r_c)^N \quad (70)$$

which gives

$$(r_c/r_p)^N = \{ \rho_p u_0^2 / (1+(\rho_p/\rho_t)^{1/2})^2 \} (T/r_c)/Y_t \quad (71)$$

or

$$(d_c/d_p) = (r_c/r_p) = (\rho_p/\rho_t)^{1/(N+1)} (\rho_t/Y_t)^{1/(N+1)} u_0^{2/(N+1)} (2T/d_p)^{1/(N+1)} / (1 + (\rho_p/\rho_t)^{1/2})^{2/(N+1)} \quad (72)$$

Clearly, if $N \gg 2$ this equation collapses toward $(r_c/r_p) \Rightarrow 1.0$, regardless of the values of densities, yield strength, target thickness or impact speed. This latter is an important point, since it accords with experimental observations. Thus the crater diameter in the target asymptotes to the same size as the projectile. For this case there is no significant difference between the crater "mouth" diameter and the central hole diameter.

The logic for $N \gg 2$ is that, although local momentum must be conserved, much of it becomes entrapped in the surface jets and front and back lips and, therefore, the "effective drive" on the target wall is strongly reduced. Also, very narrow pulses undergo rapid attenuation due to the release waves which overtake the shock front.

2.4.3 The Intermediate Case

Most investigators have concentrated on either the Ballistic Limit case or the thin foil case. However, Hörz (1992) has studied the details of perforation for the intermediate case, by tracking the hole size versus target thickness for otherwise constant conditions. We here make an initial attempt to predict the overall behavior as a function of target thickness.

Starting with Equation 72, and based on the above arguments for rapidity of stress relief, we assume that the index N is itself a function of T/d_p . A simple possibility is the function

$$N = 2 (1 + m d_p/T) \quad (73)$$

where m is a multiplier whose value is chosen so as to make Equation 72 identical to POD's cratering equation, Equation 21, when $T = 2/3 d_p$. This latter logic is based on the fact that the crater diameter is almost identical to the infinite-target case for this condition. Thus N asymptotes to 2 when $T \gg d_p$ (the infinite target case), and to $2md_p/T$ for $T \ll d_p$ for ultra-thin foils. Further, dividing Equation 72 by Equation 21 we obtain

$$(d_c/d_p)^{N-2.5} = 3T/2d_p \quad (74)$$

which can equate if $N = 2.5$ when $T = 2/3 d_p$.

Thus we chose $m = 1/6 = 0.16667$. Hence

$$N = 2 (1 + 0.1667 d_p/T) \quad (75)$$

Hence for $T = 2/3 d_p$ we obtain $1/(N+1) = 0.2857$ for Equation 72, which is the same index used in Equation 21. Thus for $T \geq 2/3 d_p$ we use Equation 21, while for $T \leq 2/3 d_p$ we use Equation 72.

Figure 6 plots Equation 72, using the index in Equation 75, for (d_c/d_p) versus (d_p/T) . Also shown on this plot are the experimental data from Hörz for (d_h/d_p) . We see that the trends are very similar. POD does not claim that the final equation has been derived; rather we believe that the form of the behavior has been identified.

Applying the logic of Equation 75 within Equation 72 also leads to the following behavior as $T/d_p \Rightarrow 0.0$

$$(d_c - d_p)/d_p = (3.0 T/d_p) (\ln(A) - \ln(T/d_p)) \quad (76)$$

where
$$A = 2 (\rho_p/\rho_J) (\rho_r/Y_J) u_0^2 / (1 + (\rho_p/\rho_J)^{1/2})^2 \quad (77)$$

This suggests that the hole closes down to the projectile size in a roughly linear fashion as target thickness is reduced for very thin targets. However, the logarithmic term for (T/d_p) produces a net "effective" index which is somewhat less than unity, especially as T/d_p increases. For example, for $0.005 < T/d_p < 0.01$ the apparent index is about 0.894, while for $1.0 < T/d_p < 2.0$ the apparent index is about 0.776. These index quotes should be compared to values of about 2/3 given by Sawle (1969), Maiden (1963) and Brown (1970), and the quote of 0.895 given by Schonberg (1988). The logarithmic behavior for the term A demonstrates a very weak dependence on material properties and impact speed, in accordance with observations.

Figure 7 shows the effects of variations in N on Equation 59 for aluminum on TFE Teflon impacts. The CTH calculations done for TFE Teflon cratering in infinite targets demonstrated that, for distances greater than the crater depth, the stress decay roughly obeys a $1/r$ law near the impact point but steadily asymptotes towards a $1/r^{2.4}$ law with increasing distance. Thus $N=2.4$ is a good approximation for TFE Teflon.

Starting with Equation 72, we assume that the index N is itself a function of T/d_p . As for aluminum a simple possibility is the function

$$N = 2.4 (1 + m d_p/T) \quad (78)$$

which asymptotes to 2.4 when $T \gg d_p$ (the infinite target case), and to $2.4md_p/T$ for $T \ll d_p$ for ultra-thin foils. The value of m is chosen so as to make Equation 72 identical to Equation 21 when $T = 2/3 d_p$. Thus we chose $m = 1/36 = 0.0278$. Hence

$$N = 2.4 (1 + 0.0278 d_p/T) \quad (79)$$

Applying the logic of Equation 78 within Equation 72 also leads to the following behavior as $T/d_p \Rightarrow 0.0$

$$(d_c - d_p)/d_p = (15.0 T/d_p) (\ln(A) - \ln(T/d_p)) \quad (80)$$

where
$$A = 2 (\rho_p/\rho_J) (\rho_r/Y_J) u_0^2 / (1 + (\rho_p/\rho_J)^{1/2})^2 \quad (81)$$

2.4.4 Perforation Supralinearity

Experimentally observed supralinearity for aluminum targets was explained by invoking the "Petch Law" (Petch, 1953) which describes the strength of a ductile material versus its mean grain size. POD anticipates the size effect to also apply to perforations, and to cause the critical target thickness for ballistic perforation to scale with projectile diameter in a similar manner as does the crater diameter. Thus the above equations describing the Ballistic Limit, etc., should be "downgraded" for very small projectiles, by a factor F , as described in Section 2.3.9.

2.5 Oblique Impacts: Summary of Typical Behavior

All of the above discussions referred to impacts normal to the target surface. The following is a brief description of typical responses for oblique impacts.

Defining the angle θ as that between the projectile motion and the normal to the target surface, it has been observed in experiments that for $\theta < 60$ degrees the major effect is for the craters to develop as if the impact speed were given by $u_0 \cos\theta$. Therefore, all of the existing scaling laws are adjusted for oblique impacts by adding in a $\cos\theta$ correction. Thus as the component of the impact speed normal to the surface decreases so the crater also decreases in both diameter and depth. Further, the crater aspect ratio changes very little, and the craters are essentially still axially symmetric.

However, it has also been observed that for $\theta > 60$ degrees, the craters start to become more asymmetric. The "downstream" portion tends to become elongated. At this stage portions of the projectile also start to ricochet and material is ejected downstream at a small angle to the target surface (typically within about 15 degrees). Other phenomena include observations of the projectile itself shearing, such that the upper portion (away from the impact surface) can detach itself and impact the target downstream as a separate impactor(s).

2.5.1 Idealized Theory

The general response for oblique impacts can be understood if we start with an "idealized" condition; namely, the assumption that the interface between the projectile and the target has a zero coefficient of friction. We also ignore the fact that the projectile penetrates (*i.e.*, "digs" itself) into the target. Under these circumstances, an oblique impact will transmit to the target only the component of momentum and energy that is along the target surface normal. The remaining momentum and energy reside within the projectile as components parallel to the target surface (we call these latter components the orthogonal ones). Since hypervelocity impacts produce an effective coefficient of restitution of zero (*i.e.*, there is negligible bounce) there are also no components remaining along the target surface normal. Thus the projectile ricochets by skimming along the target surface in the downstream direction.

The above logic implies that the target response will always be that for the normal component of the impact speed only, and also implies that the projectile always ricochets across the target surface.

Reality, of course, is a little different. Because the projectile impact immediately causes jetting and the onset of lip formation outboard of the projectile diameter, the ability of the projectile to simply "skim" across the target surface is suppressed. Consequently, the orthogonal components of momentum and energy parallel to the target surface become dissipated by providing a degree of asymmetry in the crater diameter. This asymmetry is quite small until the obliquity increases to about 60 degrees. The influence of the orthogonal momentum and energy on the crater depth is essentially zero.

Following this logic, POD's cratering Equations 21 and 28 become, respectively,

$$(d_c/d_p) = 1.0857(\rho_p/\rho_t)^{0.2857}(\rho_t/Y_t)^{0.2857}(c_t/c_p)^{0.2857}(u_0 \cos \theta)^{0.5714}/(1 + (\rho_p/\rho_t)^{1/2})^{0.5714} \quad (82)$$

$$P/d_p = (1/4)(4/3)^{1/3}(\rho_p/\rho_t)^{1/3}(\rho_t/Y_t)^{1/3}\{(c_{0t} + s(u_0 \cos \theta - u_{t,crtr})/(1 + (\rho_p/\rho_t)^{1/2}))(u_0 \cos \theta - u_{t,crtr})\}^{1/3} \quad (83)$$

whereas POD's perforation Equations 59, 72 and 77 become, respectively,

$$T/d_p = (1/8)(4/3)^{1/3}(\rho_p/\rho_t)^{1/3}(\rho_t/Y_t)^{1/3}\{(c_{0t} + s(u_0 \cos \theta - u_{t,crtr})/(1 + (\rho_p/\rho_t)^{1/2}))(u_0 \cos \theta - u_{t,crtr})\}^{1/3} + (1/4)\{\rho_p(u_0 \cos \theta)^2/(2\sigma_t(1 + (\rho_p/\rho_t)^{1/2})^2)\}^{1/N} \quad (84)$$

$$(d_c/d_p) = (r_c/r_p) = (\rho_p/\rho_t)^{1/(N+1)}(\rho_t/Y_t)^{1/(N+1)}(u_0 \cos \theta)^{2/(N+1)}(2T/d_p)^{1/(N+1)}/(1 + (\rho_p/\rho_t)^{1/2})^{2/(N+1)} \quad (85)$$

$$A = 2(\rho_p/\rho_t)(\rho_t/Y_t)(u_0 \cos \theta)^2 / (1 + (\rho_p/\rho_t)^{1/2})^2 \quad (86)$$

Figure 8 shows a normalized plot of how Equations 82, 83, and 84 vary with the angle of incidence (θ). The equations are normalized by Equations 21, 28, and 59, respectively. Note that the angle of incidence must exceed 30 degrees to get more than a 10% change in T/d_p , and must exceed 35 degrees to get more than a 10% change in d_c/d_p or P/d_p . In fact, to get more than a 20% change (the limit of many experimental measurements), the angle of incidence must exceed 40 degrees and 48 degrees, respectively. Also, note that, due to the two components of Equation 59, for angles above 80 degrees, T/d_p varies linearly.

2.5.2 The Ricochet Case

We define ricochet as being the case where the projectile, in whole or in part, escapes from the impact crater before the crater lips are formed. For a hypervelocity impact, where both projectile and target behave as fluids, a simple condition for guaranteeing that the whole of the projectile can ricochet across the target surface is that the orthogonal component of the projectile velocity be greater than the speed of the corresponding target surface disturbance. The latter is the sound speed in the target, adjusted for the high pressure impact state. Thus we require

$$u_0 \sin \theta \geq c_{\alpha} + s u_0 \cos \theta / (1 + (\rho_t / \rho_p)^{1/2}) \quad (87)$$

where s is the Hugoniot term relating shock speed to particle speed, and c_{α} is the target low stress bulk sound speed. Rewriting

$$\sin \theta \geq c_{\alpha} / u_0 + s \cos \theta / (1 + (\rho_t / \rho_p)^{1/2}) \quad (88)$$

This equation predicts that the critical angle, θ , which ensures total ricochet monotonically decreases from 90° at $u_0 \leq c_{\alpha}$, toward 35° for very high impact speed, for aluminum into aluminum. In the impact speed range of 6 to 10 km/s the angle changes from about 79° to 60° .

A second condition to consider is the limiting condition which ensures that the top of the projectile just escapes the crater lip formation. This is the limiting case for partial projectile ricochet. This case is defined purely by the geometry of the impact such that

$$\tan \theta = r_c / d_p = 1/2 (d_c / d_p) \quad (89)$$

Figure 9 plots $2 \tan \theta$ versus d_c / d_p at various velocities. The points where the $2 \tan \theta$ line crosses any given d_c / d_p line is the limiting angle for partial projectile ricochet for that velocity. The corresponding condition for the mid-point of the projectile to clear the crater is given by plotting $\tan \theta$ versus d_c / d_p instead.

A final condition to consider is that which ensures the materials behave as fluids. Thus we require

$$u_0 \cos \theta \geq u_{\text{crit}} \quad (90)$$

where u_{crit} (defined before) is the minimum speed necessary to ensure Bernoulli flow behavior. For impact speeds below this value the response becomes elastic-plastic.

These three conditions thus bound the ricochet phenomenon for the case of Bernoulli flow. For impacts which are within the Bernoulli flow condition but outside of both the ricochet boundaries, ejection of crater and projectile material can still occur, but this is not a ricochet condition.

Figure 10 shows a composite of Equations 88, 89 and 90. This figure also shows the two loci for top and mid-point of the projectile using Equation 89, using d_c / d_p as a function of θ . We see that for impact speeds in the range 2 to 6 km/s there is a broad peak in angle of incidence necessary to guarantee projectile ricocheting with Bernoulli flow logic. It's interesting to note that the limiting angle for partial ricochet is in the range of 65 to 60 degrees (respectively, for the Equation 89 criteria used) as is normally seen in experiments.

Also plotted is the incipient vapor locus for Al/Al (*i.e.*, $u_0 \cos \theta = 10.2$ km/s). We see that only for very high impact speeds above about 30 km/s does this locus catch the ricochet loci. Above these speeds the ricochet is of an expanding vapor cloud.

Christiansen (1992c) has also studied ricocheting effects for Al/Al. For thick targets he derived a locus of critical angle versus impact speed. The logic used was that if the stress wave in the projectile travelled from the impact point to the projectile rear surface and then back to the mid-point before the mid-point itself reached the target surface, then the upper portion of the projectile can suffer breakup and cause downstream multiple cratering. Thus defining the mean projectile wave speed as c_p (shock out, rarefaction back), the projectile radius as r_p and the normal component of impact speed as $u_0 \cos \theta$ (with θ the obliquity) we have

$$3r_p/c_p \leq r_p/u_0 \cos \theta \quad \text{or} \quad \cos \theta \leq c_p/3u_0 \quad (91)$$

This locus is also shown in Figure 10. We see that it is close to the loci given by POD.

3.0 CTH HYDRODYNAMIC CALCULATIONS

3.1 Cratering in Aluminum

The CTH code from Sandia National Laboratory, Albuquerque (SNLA), has been used to investigate the cratering responses of an aluminum target. Parameters varied have included impact velocity, projectile density, and target and projectile yield strengths. In all cases the target was sufficiently thick to behave as an infinite body. For all cases the projectile was a sphere of diameter 100 microns. The resulting data have been mapped and compared to equations of the form

$$P/d_p = \text{constant} (\rho_p/\rho_t)^A (\rho_t/Y_t)^B u_0^C \quad (92)$$

$$\text{and } d_c/d_p = \text{constant} \left\{ (\rho_p/\rho_t) / (1 + (\rho_p/\rho_t)^{1/2}) \right\}^A (\rho_t/Y_t)^B u_0^C (c_t/c_p)^D \quad (93)$$

Figures 11 to 20 show the data in log-log form. It is immediately clear that the indexes are not constants and that they vary with the impact speed. This effect is strongest at the lowest speed of 1 km/s (which normally would not be considered as hypervelocity) and slowly asymptotes to steadier values at the higher impact speeds.

To date, the best overall fits are given by:

$$\text{for } P/d_p: \quad \text{constant} = 0.0725, A = 0.60, B = 0.263, C = 0.664$$

(Note that these indexes are similar to those in Equation 28, except for the density index, and the leading constant).

$$\text{for } d_c/d_p: \quad \text{constant} = 0.468, A = 0.33, B = 0.258, C = 0.575, D = \text{indeterminate (not tested)}$$

These fits are primarily for data above 5 km/s impact speeds, since the low speed impacts clearly are near the limit of applicability of Bernoulli logic and expectations. It is gratifying to see that the responses are similar to the expectations.

Of particular interest are the plots of (P/d_p) and (d_c/d_p) versus projectile density and speed (Figures 15 and 16). Note how for the crater diameters the plots "curve over" as projectile density increases. This is the form predicted by Equations 14 and 21. For the penetration depths the plots follow a more direct power law, which is as predicted by Equation 28. Figures 19 and 20 show the ratios P/d_c . From Equations 21 and 28 we obtain a ratio which is complex and contains low power indexes for density, yield strength and impact speed. For very high impact speed, this asymptotic ratio gives the following equation

$$P/d_c \Rightarrow 0.253 (\rho_p/\rho_t)^{0.0476} (\rho_t/Y_t)^{0.0476} (c_p/c_t)^{0.2857} s^{1/3} u_0^{0.095} (1 + (\rho_p/\rho_t)^{1/2})^{0.5714} / (1 + (\rho_t/\rho_p)^{1/2})^{1.14} \quad (94)$$

Specifically, the ratio P/d_c then becomes a positive function of (ρ_p/ρ_t) and an inverse function of Y_t . The plots show a similar behavior. We thus conclude that much of the basics of the scaling laws for either crater diameter or crater depth are indeed contained in Equations 21 and 28, although we cannot yet vouch for the exact values of the power indexes.

Figures 21 to 26 show some of the geometries of the crater for the 10 km/s impact velocity case. The dark spots on the impact axis are Lagrangian points, as described below. These figures are split, with the right side showing geometry only and the left side giving stress contours as per the bar legend to the right of each figure.

Scrutiny of the CTH runs reveals many interesting facts. It is observed that the maximum depth of the crater occurs (in Figure 24) before the maximum crater diameter has formed (in Figure 26), and that the ratio depth/diameter is not 0.5 in general (*i.e.*, the crater is generally not hemispherical). Various tracer points (Lagrangian points) were placed along the impact axis. For these points the time histories of pressure, velocity and position were obtained. Figures 27 to 32 show such data for the case of a 100 micron Al ball hitting an Al target at 10 km/s. Both materials were Al 6061-T6 with a yield strength of 2.7 kbars. The Lagrangian points were L1 through L6 at initial depths of 0.0 (surface), 120 microns, 240 microns, 360 microns, 480 microns and 600 microns, respectively. Of these, the points L1 to L3 were within the finally formed crater which developed a maximum depth of 300 microns, giving $P/d_p = 3.0$. The final crater diameter was 500 microns. Thus $d_c/d_p = 5.0$, and $P/d_c = 0.6$. In all cases the definitions of depth and diameter are relative to the initial target surface.

The fact that these three L points remain on the axis and form part of the crater itself demonstrates that the material on the impact axis does not flow out of the crater but merely moves into the target. Only target material off the axis takes part in the circumferential rotational flow, with that nearest the free surface affected the most.

Immediately upon impact the peak stress is about 900 kbars. This is lower than the expected 1-D stress of 1.63 Mbars (perhaps owing to the artificial viscosity in the code?) but is considerably higher than the corresponding Bernoulli stress of 337.5 kbars. This peak stress rapidly drops through the Bernoulli value to a very low stress of the order of the plastic yield value, whereupon the stress drops much more slowly. Some residual stress reverberation ringing can be seen on the plots. The initial shock wave speed is 12 km/s at the 1-D stress, while the release wave speeds are even faster. Thus the 1-D stress lasts for less than 10 ns and immediately collapses toward the Bernoulli stress. The peak stress then propagates at a wave speed of near 6 km/s, which is close to the dilatational speed for aluminum, and decays in value with distance. This decay roughly obeys a $1/r$ law near the impact point but steadily asymptotes towards a $1/r^2$ law with increasing distance. Thus at early time the stress is obeying the "energy" logic, while at later time it obeys the "momentum" logic. The previous suggestion of mixed non-steady power indexes indeed applies.

The induced compressive strain during the 1-D condition is given by (u/W) , where u is the induced particle speed change and W is the shock wave speed. Thus for a speed u of 5 km/s and

a W of 12 km/s the strain is 0.417 and the density has increased by the ratio $W/(W-u)$ which is 1.7! Thus the concept of treating the materials as "incompressible" is clearly not correct for this state. Thus the conventional Bernoulli logic applies only after the shock moves away from the impact site.

After the stress peak passes a given point a stress gradient exists between this pulse and the crater surface. This gradient decelerates the surface and eventually brings it to rest. This deceleration is given by

$$du/dt = - (1/\rho) dP/dx \quad (95)$$

where dP/dx is the stress gradient. If this gradient stayed constant the crater surface motion would become a simple quadratic function versus time. However, the gradient varies with time and position giving a more complex solution.

The plots indicate a very small elastic recovery. The stress gradient appears to be attached to the rear of the shock pulse at a value of about the target yield strength.

The CTH calculations demonstrate that the yield strength of the target is indeed a major player in the crater formation. Further, a large region (extending to beyond twice the crater depth) of the target is put into permanent plastic strain. This effect is most clearly seen for the deepest Lagrangian points (Figures 31 and 32) where it is seen that the material is ultimately left with a permanent compression of about the yield stress. This is the response expected for a material which has been subjected to a pseudo 1-D stress wave which exceeds the Hugoniot Elastic Limit (HEL). Note that $HEL = Y(1-\nu)/(1-2\nu)$ where ν is the Poisson ratio. For aluminum $\nu = 0.33$, thus $HEL = 1.97Y$ (i.e., 5.32 kbars for Al 6061-T6). Upon shocking the material returns to a state of zero stress in the direction of the stress wave but has lateral compressive stresses equal to the yield stress. Thus the pressure becomes $2Y/3$. At these large radii the hoop stress is very small and provides only a small correction.

A considerable amount of strain energy is stored within this plastic region beyond the crater, and energy also exists in the propagating elastic wave beyond the plastic region. This highlights the problem of trying to equate the impactor kinetic energy with the energy necessary to excavate the crater, as mentioned before.

3.2 Cratering in TFE Teflon

As was described above for cratering in aluminum, the CTH code has been used to investigate the cratering responses of a Teflon (TFE) target. Parameters varied have included impact velocity, projectile density, and target yield strength. In all cases the target was sufficiently thick to behave as an infinite body. For all cases the projectile was an aluminum sphere of diameter 100 microns. As with the aluminum runs, calculations were done at 1, 5, 10 and 15 km/s, with yield values of $0.1Y_p$, Y_p , and $10Y_t$ (where Y_t is the normal value for the Teflon target), and for densities of $\rho_p/3$, ρ_p , and $3\rho_p$ (where ρ_p is the normal value of the aluminum projectile).

The properties used for Teflon were:

density = 2.17 g/cm³, bulk sound speed = 1.29 km/s, yield strength = 300 bars, $\nu = 0.795$, Poisson ratio = 0.433, and spall strength = 200 bars. The melt temperature is 327°C and melt energy is 82 cal/g. These are POD's "best guesses" for the material parameters, since the literature (Harper, 1992; Moses, 1978; Dean, 1992; Rice, 1980) reveals some inconsistencies (some references even fail to distinguish between TFE and FEP Teflon, which have somewhat different properties).

As with aluminum, the resulting data have been mapped and compared to equations of the form

$$P/d_p = \text{constant} (\rho_p/\rho)^A (\rho_p/Y)^B u_p^C \quad (96)$$

$$\text{and } d_c/d_p = \text{constant} \left\{ (\rho_p/\rho)/(1 + (\rho_p/\rho)^{1/2})^2 \right\}^A (\rho_p/Y)^B u_p^C (c/c_p)^D \quad (97)$$

Figures 33 to 42 show the data in log-log form. It is immediately clear that the indexes are not constants and that they vary with the impact speed, as occurred for aluminum. This effect is strongest at the lowest speed of 1 km/s (which normally would not be considered as hypervelocity) and slowly asymptotes to steadier values at the higher impact speeds.

To date, the best overall fits for Teflon TFE are given by:

$$\text{for } P/d_p: \quad \text{constant} = 0.68, A = 0.49, B = 0.23, C = 0.475$$

(Note that these indexes are similar to those in Equation 28, except for the density index, and the leading constant).

$$\text{for } d_c/d_p: \quad \text{constant} = 0.18, A = 0.333, B = 0.20, C = 0.58, D = 0.333$$

These fits are primarily for data above 5 km/s impact speeds.

Of particular interest are the plots of (P/d_p) and (d_c/d_p) versus projectile density and speed (Figures 37 and 38). Note how for the crater diameters the plots "curve over" as projectile density increases. This is the form predicted by Equation 21. For the penetration depths the plots follow a more direct power law, which is as predicted by Equation 28. Figures 41 and 42 show the ratios P/d_c .

Figures 43 to 51 show some of the geometries of the crater for the 10 km/s impact velocity case. The dark spots on the impact axis are Lagrangian points, as described below. Note the dynamic variations in the shape of the crater and the repeated sequence of lip spallation. The final crater shape has a surface spall region surrounding the crater proper. This is very similar to the features observed experimentally, as shown in Figure 4.

A problem was met when trying to determine the crater diameters from the CTH calculations. For some of the larger craters the geometry was not smooth, with the crater outer region displaying re-entrant shapes due to lip spallation and surface fractures. Consequently, more than one possible value could be identified for the diameter measured in the initial target surface plane. This effect is indicated on Figure 52 as an error bar in the values of (d_c/d_p) . This problem of measurement also occurred with the experimental data, as discussed in Section 5.2 below.

Scrutiny of the CTH runs reveals many interesting facts. It is observed that, as for the aluminum case, the maximum depth of the crater occurs (in Figure 49) before the maximum crater diameter has formed (in Figure 51), and that the ratio depth/diameter is not 0.5 in general (i.e., the crater is generally not hemispherical, and the CTH runs sometimes indicated a "central 'pip'" at the bottom of the craters with the deepest part of the crater slightly off the impact axis). Various tracer points (Lagrangian points) were placed along the impact axis. For these points the time histories of pressure, velocity and position were obtained. Figures 53 to 59 show such data for the case of a 100 micron Al ball hitting a Teflon target at 10 km/s. The aluminum was 6061-T6 with density 2.7 g/cm^3 and yield strength of 2.7 kbars, while the Teflon had the normal values quoted above. The Lagrangian points were L1 through L7 at initial depths of 0.0 (impact surface of the projectile), 0.0 (surface of the target), 110 microns, 220 microns, 340 microns, 460 microns and 570 microns, respectively. Of these, the points L1 to L6 were within the finally formed crater which developed a maximum depth of 500 microns, giving $P/d_p = 5.0$. The final crater diameter was 720 microns. Thus $d_c/d_p = 7.2$, and $P/d_c = 0.694$. In all cases the definitions of depth and diameter are relative to the initial target surface.

Immediately upon impact the peak stress is about 550 kbars. This is lower than the expected 1-D stress of 900 kbars (perhaps owing to the artificial viscosity in the code?) but is considerably higher than the corresponding Bernoulli stress of 302 kbars. This peak stress rapidly drops through the Bernoulli value to a very low stress of the order of the plastic yield value, whereupon the stress drops much more slowly. Some residual stress reverberation ringing can be seen on the plots. The initial shock wave speeds are about 7.5 km/s in the Teflon and about 10 km/s in the aluminum at the 1-D stress, while the release wave speeds are even faster. Thus the 1-D stress lasts for less than 13 ns and immediately collapses toward the Bernoulli stress. The peak stress then propagates at a wave speed of from 3.7 km/s at 200 microns depth to 1.47 km/s at a depth of 600 microns, which is asymptoting to the dilatational speed for Teflon, and decays in value with distance. This decay roughly obeys a $1/r$ law near the impact point but steadily asymptotes towards a $1/r^{2.4}$ law with increasing distance.

The CTH plots reveal that a pulse is propagated away from the impact site. This is clearly seen as a "loop" of constant stress in Figures 44 through 46. The existence of such a pulse was the fundamental concept in POD's derivation of its scaling laws.

The induced compressive strain during the 1-D condition is given by (u/W) , where u is the induced particle speed change and W is the shock wave speed. Thus for a speed u of about 6.4 km/s and a W of 7.5 km/s the strain is 0.853 and the density has increased by the ratio $W/(W-u)$

which is 6.8. The plots indicate a very small elastic recovery. A stress gradient is attached to the rear of the shock pulse at a value of about the target yield strength.

As with the aluminum runs the CTH calculations demonstrate that the yield strength of the target is indeed a major player in the crater formation. Further, a large region (extending to beyond twice the crater depth) of the target is put into permanent plastic strain. This effect is most clearly seen for the deepest Lagrangian points (Figures 58 and 59) where it is seen that the material is ultimately left with a permanent compression of about the yield stress. This is the response expected for a material which has been subjected to a pseudo 1-D stress wave which exceeds the Hugoniot Elastic Limit (HEL). Note that $HEL = Y(1-\nu)/(1-2\nu)$ where ν is the Poisson ratio. For Teflon $\nu = 0.433$, thus $HEL = 4.23Y$ (i.e., 1.27 kbars for Teflon TFE). Upon shocking, the material returns to a state of zero stress in the direction of the stress wave but has lateral compressive stresses equal to the yield stress. Thus the pressure becomes $2Y/3$. At these large radii the hoop stress is very small and provides only a small correction.

A considerable amount of strain energy is stored within this plastic region beyond the crater, and energy also exists in the propagating elastic wave beyond the plastic region. As stated above, this highlights the problem of trying to equate the impactor kinetic energy with the energy necessary to excavate the crater.

3.3 Perforations in Aluminum

CTH has been used to investigate the perforation responses of an aluminum 6061-T6 target. Parameters varied have included impact velocity and the target thickness. For all cases the projectile was a sphere of diameter 100 microns. As with the aluminum cratering runs, calculations were done at 1, 5, 10 and 15 km/s, with the normal yield value of Y_p and normal densities of ρ_p and ρ_t .

The properties used for Al 6061-T6 were:

density = 2.7 g/cm³, bulk sound speed = 5.1 km/s, yield strength = 2.7 kbars, $s = 1.4$, Poisson ratio = 0.33, spall strength = 3.1 kbars.

The resulting data have been mapped and compared to equations of the form

$$T/d_p = \text{const} (\rho_p/\rho_t)^A (\rho_t/Y)^B u_0^C \quad (98)$$

and to POD's Equation 59.

Figures 60 and 61 show the data in both linear and log-log form. It is immediately clear that the velocity index is not constant and slowly varies with the impact speed. This variation is strongest at the highest speeds above 10 km/s.

To date, the best overall fits to Equation 98 for aluminum are given by:

constant = 0.133, A = 1/3, B = 1/3, C = 0.75

The direct application of Equation 59 is shown in Figures 60 and 61. The responses are similar to the expectations. However, locating the Ballistic Limit threshold requires many calculations (e.g., at least two for a given impact speed, one above and one below the threshold). For this reason POD has yet to fully investigate the influence of density, yield strength and spall strength. However, we anticipate responses similar to those observed for cratering.

Figures 62 to 67 show some of the geometries of the crater for the 10 km/s impact velocity case, for a case of "not quite" causing perforation. The dark spots on the impact axis are Lagrangian points, as described below. These figures are split, with the right side showing geometry only and the left side giving stress contours as per the bar legend to the right of each figure. Note the dynamic variations in the shape of the crater and the repeated sequence of rear surface spallation.

The CTH runs reveal many interesting facts. For the non-perforation case (500 micron thick target) it is observed that the maximum depth of the crater occurs (in Figure 65) before the maximum crater diameter has formed, and that the ratio depth/diameter is not 0.5 in general (i.e., the crater is generally not hemispherical). Various tracer points (Lagrangian points) were placed along the impact axis. For these points the time histories of pressure, velocity and position were obtained. Figures 68 to 74 show such data for the case of a 100 micron Al ball hitting a 500 micron thick Al target at 10 km/s. The Lagrangian points were L1 through L7 at initial depths of 0.0 (impact surface of the projectile), 0.0 (surface of the target), 110 microns, 220 microns, 340 microns, 460 microns and 570 microns, respectively. Of these, the points L1 to L5 were within the finally formed crater which developed a maximum depth of 350 microns, giving $P/d_p = 3.5$. Note that this depth is larger than the corresponding thick target case, where the depth was 300 microns. Also note the thin wall remaining at the bottom of the crater. The final crater diameter was 500 microns, which is identical to the thick target case. Thus $d_f/d_p = 5.0$, and $P/d_p = 0.70$. In all cases the definitions of depth and diameter are relative to the initial target surface.

Immediately upon impact the peak stress is about 900 kbars. This is lower than the expected 1-D stress of 1.63 Mbars (perhaps owing to the artificial viscosity in the code?) but is considerably higher than the corresponding Bernoulli stress of 337.5 kbars. This peak stress rapidly drops through the Bernoulli value to a very low stress of the order of the plastic yield value, whereupon the stress drops much more slowly. Some residual stress reverberation ringing can be seen on the plots. The initial shock wave speed is about 12 km/s in the aluminum at the 1-D stress, while the release wave speeds are even faster. Thus the 1-D stress lasts for less than 10 ns and immediately collapses toward the Bernoulli stress. The peak stress then propagates at a wave speed of 6 km/s which is asymptoting to the dilatational speed for aluminum, and decays in value with distance. This decay roughly obeys a $1/r$ law near the impact point but steadily asymptotes towards a $1/r^2$ law with increasing distance.

The induced compressive strain during the 1-D condition is given by (u/W) , where u is the induced particle speed change and W is the shock wave speed. Thus for a speed u of about 5 km/s and a W of 12 km/s, the strain is 0.417 and the density has increased by the ratio $W/(W-u)$,

which is 1.7. Thus the concept of treating the materials as "incompressible" is clearly not correct for this state. Thus the conventional Bernoulli logic applies only after the shock moves away from the impact site.

The perforation case (400 micron thick target) is shown in Figures 75 to 80 (geometry versus time), and in Figures 81 to 89 (Lagrangian tracer points). The figures clearly show that the crater mouth forms identically to that for the case of no perforation. The major difference is the deeper spall leading to crater break through. Note how the bottom of the crater has a conical shape. These effects have been observed experimentally for impacts which just cause perforations.

3.4 Perforations in TFE Teflon

CTH has also been used to investigate the perforation responses of a TFE Teflon target. Parameters varied have included impact velocity and the target thickness. For all cases the projectile was a sphere of diameter 100 microns. As with the Teflon cratering runs, calculations were done at 1, 5, 10 and 15 km/s, with the normal yield value of Y_1 and normal density of ρ_p and ρ_t . The properties used for Al 6061-T6 and TFE Teflon were the same as for the other calculations.

The resulting data have been mapped and compared to equations of the form

$$T/d_p = \text{const} (\rho_t/\rho_p)^A (\rho_t/Y_1)^B u_0^C \quad (99)$$

and to POD's Equation 59.

The direct applications of Equation 59, together with the CTH data in both linear and log-log form are shown in Figures 90, 91 and 92. It is immediately clear that the velocity index is not constant and slowly varies with the impact speed. This variation is strongest at the highest speeds above 10 km/s.

To date, the best overall fits to Equation 99 for TFE Teflon are given by:

$$\text{constant} = 0.25, A = 1/3, B = 1/3, C = 0.71$$

Figure 90 shows a comparison of the CTH results against POD's Equation 59 for $N = 2$. As expected and explained above, the equation overpredicts the CTH data for this case. The explanation above stated that $N = 2.4$ should be the correct case for TFE Teflon and Figures 91 and 92 confirm this. Locating the Ballistic Limit threshold requires many calculations (e.g., at least two for a given impact speed, one above and one below the threshold), consequently POD has yet to fully investigate the influence of density, yield strength and spall strength. However, we anticipate responses similar to those observed for cratering.

For the non-perforation case it is again observed that the maximum depth of the crater occurs before the maximum crater diameter has formed, that the ratio depth/diameter is not 0.5 in

general, and that in general the crater depth is larger than the corresponding thick target case. In addition, we observed dynamic variations in the shape of the crater and repeated sequences of lip spallation, and the CTH runs sometimes indicated a "central 'pip'" at the bottom of the craters with the deepest part of the crater slightly off the impact axis. The final crater shape has a surface spall region surrounding the crater proper. This is very similar to the features observed experimentally, as shown in Figure 4. In all cases the definitions of depth and diameter are relative to the initial target surface.

Figures 93 to 101 show some of the geometries for the 10 km/s impact velocity case for the perforation case (700 micron thick target). The dark spots on the impact axis are Lagrangian points. Note the dynamic variations in the shape of the crater and the repeated sequence of rear surface spallation. Also note the odd crater shape with local radial cracks, very similar to those observed by Hörz (1992) and shown in Figure 4.

The crater mouth forms identically to that for the case of no perforation. The major difference is the deeper spall leading to crater break through. Note how the bottom of the crater has a conical shape. These effects have been observed experimentally for impacts which just cause perforations.

Various tracer points (Lagrangian points) were placed along the impact axis. For these points the time histories of pressure, velocity and position were obtained. The Lagrangian points were L1 through L9 at initial depths of 0.0 (impact surface of the projectile), 0.0 (surface of the target), 110 microns, 220 microns, 340 microns, 460 microns, 570 microns, 680 microns and 800 microns, respectively. Figures 102 to 108 show the data for Lagrangian points L1 through L7 for the case of a 100 micron Al ball hitting a 700 micron thick TFE Teflon target at 10 km/s. Note from these Lagrangian points how slowly the perforation occurs with a very long-lived gradual downstream motion of the crater bottom.

3.5 Oblique Impacts into Aluminum

The CTH code has been used to investigate the oblique impact responses of an aluminum 6061-T6 target. Because such calculations are 3-D (and hence require much computer memory and run time) the only parameter varied was the angle of incidence, which was set at 70° and 50° . The projectile was a sphere of diameter 0.5 cm, and the calculation was done at 5 km/s, with the normal properties used for Al 6061-T6.

Figures 109 to 115 show the 70° impact as an isometric view. The projectile approaches the target from the top left, proceeds to cause a crater, and then ricochets off to the right. Figures 116 to 122 show the same impact but in cross-section in the plane of the impactor (*i.e.*, a view "sideways" at the collision), while Figure 123 shows the orthogonal cross-section (*i.e.*, a view from "behind" the projectile).

The figures clearly show how the crater develops a significant asymmetry, especially on the downstream side. The projectile is seen to "ride up" the extended crater wall and to slowly

stretch and fragment. For this impact, POD's Equations 87 and 88 predict that the upper portion of the projectile will suffer a partial ricochet. The figures clearly show that, as predicted, the top of the projectile never actually enters the crater, but instead passes over the crater lips to impact the target further downstream. Note also how this portion of the projectile essentially moves parallel to the target surface.

From the CTH data, the maximum crater depth is 0.42 cm. Thus $P/d_p = 0.8$. The crater diameter measured in the orthogonal cross-section is $d_c = 1.0$ cm. Thus $d_c/d_p = 2.0$. For an impact speed of 5 km/s at 70° angle of incidence the component normal to the surface is 1.71 km/s. For this speed POD's Equations 21 and 28 give $d_c/d_p = 2.0$ and $P/d_p = 1.0$, respectively. (Note that although POD's prediction for P is about 20% too high, no direct CTH calculations were done for an impact speed of 1.71 km/s normal to the surface. Thus the "exact" value expected is slightly uncertain).

For the 50° impact the prediction given before (Figure 10) suggests that the projectile should be on the limit of ricocheting. The CTH results confirm this. Figures 124 through 128 show a "side" view of the impact, and Figure 129 shows the "rear" view. It is seen that the top of the projectile initially just escapes its own crater at early time. However, the crater is still growing and succeeds in just catching the projectile fragments at later time, whereafter the projectile never subsequently escapes its own crater, although there is a lot of lip formation and ejecta. The final lateral crater diameter is 1.44 cm ($d_c/d_p = 2.88$) while the depth is 0.634 cm ($P/d_p = 1.27$). These values should be compared to 2.9 and 1.5, respectively, which are the expectations for this case (normal impact speed component of 3.21 km/s). Thus the CTH calculations confirm that oblique cratering does obey the "cosine law" for depth of penetration and orthogonal crater diameter.

An important point to note is that these particular CTH calculations were done for a much larger projectile (0.5 cm) than were all the previous calculations (100 microns) for normal impacts. Yet the scaling rules still apply! This demonstrates that (as POD previously stated) the "supralinearity" effect is not associated with hydrodynamics per se. However, this fact also suggests that the effect is not associated with changes in strain rates either. POD therefore believes that the Petch Law is still the most probable explanation for supralinearity.

An issue raised in Section 1.4 concerned the possibility that the cosine law breaks down for very high speed impacts, since the latter might be dominated by energy rather than momentum. However, none of POD's analyses invoke energy as a criterion for cratering. Based on this fact, POD presently believes that the cosine law continues to apply even for the highest impact speeds.

4.0 COMPARISONS WITH OTHER SCALING LAWS

4.1 Cratering in Aluminum

A large number of existing scaling laws describing either penetration depth and/or crater diameter have been identified and compared. Christiansen (1992a,b) has given quotes for the Cour-Palais equations. Schonberg (1989) has also listed many of these laws. For convenience we include the equations from his report, together with his list of references, in Appendix B (Note that Schonberg's data accidentally *misquotes* the Cour-Palais equations, giving a velocity index of 4/3 instead of 2/3. For this reason POD uses the Christiansen quotes only). Figure 130 compares the results of POD's Equations 21 and 28 with CTH calculations. We see that for a projectile and target both of Al 6061-T6 the equations give good fits to the CTH predictions. Figures 131 to 141 show comparisons between POD's equations and these other scaling laws for the same impact conditions.

Of all the existing equations the one by Sedgwick et al. (1978) seems to be the closest to the CTH data for both penetration depth and crater diameter. The good agreement with Sedgwick's equations is not entirely unexpected, since his equation is itself based on fits to calculations done with the HELP hydrodynamic code. If anything, this merely proves that CTH and HELP give similar answers (both correct or both incorrect?).

We see that the scaling laws of Cour-Palais (1985) (for $d_p = 1$ cm) and Bruce (1962) are very close to POD's equations. Cour-Palais' equation utilizes a supralinearity term $c_p^{0.056}$, and is

$$P/d_p = 5.24 d_p^{0.056} (\rho_p/\rho_t)^{0.5} (1/H)^{0.25} (u_0 \cos\theta/c_w)^{2/3} \quad (100)$$

where H is the Brinell hardness number.

It is of interest to note the good agreement of his equation for unit diameter. As stated in Section 2.3.9, POD believes the supralinear index effectively goes to zero for a 1 cm diameter projectile.

Unfortunately, the later data of Bruce (1979) gives a much poorer fit. Other reasonable fits are those by Dunn, Goodman-Liles, Sawle, and (for crater diameter only) Summers. The scaling laws of Christman, Herrmann-Jones, Sorenson, and Summers-Charters give much poorer fits. Disconcertingly, the law of Summers-Charters (P/d_p) shows the wrong power index versus impact speed, indicating an index greater than unity. This is contrary to all other laws, experimental observations and physical logic, except at very low impact speeds. It is possible that this is another misquote by Schonberg. POD has not yet checked this possibility.

With regard to experimental data there are some ambiguities since not all researchers have used consistent definitions of crater diameter and depth. This would help explain why differing "fits" to similar experiments are often seen to be "off-set" from one another on the plots. The most respected definitions (Cour-Palais) are those that reference the original target surface, and POD's analysis and measurements from the CTH calculations have used these definitions.

4.2 Cratering in TFE Teflon

The results of POD's Equations 21 and 28 were shown in Figure 52. We see that for a projectile of Al 6061-T6 these equations give good fits to the CTH predictions, being about 18% low across the entire velocity range. A large number of existing scaling laws describing either penetration depth and/or crater diameter have been identified and compared. Schonberg (1989) has listed many of these laws. For convenience, we list the appropriate laws, and Schonberg's references in Appendix B. However, these laws are mostly based on observation for aluminum targets. Therefore, those equations which do not explicitly contain material yield strengths cannot be used to describe Teflon targets. Consequently, only those laws which do contain the yield parameter have been used. Figures 142 through 146 show the predictions from these other scaling laws for the case of an AL 6061-T6 projectile into Teflon.

If these other scaling laws were truly "generic" they should fit the Teflon data just as well as they did the aluminum data, when the appropriate material properties are used. It is clear, however, that this does not happen. POD's equations, however, do give good fits to both Teflon and aluminum data.

Only the equations of Sedgwick, Bruce (his 1979 version), Dunn and Sorenson can be used for these comparisons, since none of the others contain the yield parameter (although some contain hardness numbers).

The Cour-Palais equation makes use of Brinell Hardness of the target, rather than the yield strength. This is unfortunate, since the Cour-Palais equation is frequently used by NASA for cratering predictions. The problem with hardness numbers is that they do not directly relate to other material properties, such as yield, and are difficult to compare if different scales are used for different materials. Thus while aluminum has a well quoted Brinell hardness number (BHN 95 for 6061-T6), TFE Teflon has a Shore hardness of D52. An approximate equivalent is a Brinell value of about BHN5 (or Rockwell R60) (Harper, 1992). Using the Cour-Palais equation with this hardness value, with a Teflon density of 2.17 g/cm^3 , and a sound speed of 1.29 km/s , the predictions are too large for penetration depths or diameters, as seen in Figure 143.

The equation by Sedgwick et al. (1978) is reasonably close to the CTH data for penetration depth, but it significantly overpredicts the crater diameter. Sedgwick's equations give good fits for aluminum, but not for Teflon. Since his equation is itself based on fits to calculations done with the HELP hydrodynamic code for aluminum, this demonstrates that the latter fit is somewhat fortuitous. POD believes this is an example of wrongly choosing the "pi" groups for the equation, as discussed earlier.

We see that the scaling laws of Bruce (1979) give very poor fits (grossly overpredicting), for either depth or diameter. The equations of Bruce (1979) give very poor fits to aluminum data, also. Dunn's equations also give gross overpredictions for both depth and diameter for Teflon, but give reasonable fits for aluminum. Lastly, Sorenson's (1962) equations give a good fit for

Teflon depth data, but overpredict the diameter data. Sorenson's equations give gross underpredictions for both depths and diameters for aluminum.

With regard to experimental data there are some ambiguities since not all investigators have used consistent definitions of crater diameter and depth. This would help explain why differing "fits" to similar experiments are often seen to be "off-set" from one another on the plots. The most respected definitions are those that reference the original target surface, and POD's analysis and measurements from the CTH calculations have used these definitions.

POD concludes that, unlike the POD equations presented here, practically none of the previous existing scaling laws can be considered generic.

4.3 Perforations in Aluminum

Several existing scaling laws describing perforation, specifically the Ballistic Limit, have been identified and compared. McDonnell and Sullivan (1992) have listed many of these laws. For convenience, we list the appropriate laws, and McDonnell's references in Appendix B. Figures 147 and 148 show the predictions from the laws for the case of an Al 6061-T6 projectile into Al 6061-T6. Also shown are the results of POD's Equation 59. We have previously shown in Figures 60 and 61 that, for a projectile of Al 6061-T6, this equation gives a good fit to the CTH predictions.

In Figure 147, it is seen that of the various equations by McDonnell (1992), his Equations 6, 7, and 10 all closely fit the CTH data for Al 6061-T6 projectile and target, provided the value of 800 bars is used for σ_{Al} (as done by McDonnell), σ_t is set to 2.7 kbars, and $d_p = 1.0$ cm (to "remove" the supralinear term, as suggested by POD in Section 2.3.9 for such large projectiles). However, his Equation 11 (McDonnell, 1979) is a poor fit, tending to rise too fast as the impact speed increases. McDonnell assumes that the tensile strength should be used, whereas POD concluded that both yield and tensile strengths are needed, as per Equation 59. All three of these McDonnell's equations are close fits to the CTH data. However, since McDonnell recommends (in his report) the use of his Equation 10, and since it fit POD's Equation 59 the best, we have used this equation in Figure 148 to compare with the predictions of scaling laws from other investigators.

The equation by Naumann (1966) over-predicts the CTH data by a factor of about three, and is clearly not good for aluminum into aluminum.

The equation by Cour-Palais (1979) is reasonable for an Al/Al impact, but is consistently a factor of about 1.2 too high. Perhaps this is because the equation was based on a softer material than Al 6061-T6.

Both the equations of Fish and Summers (1965) and of Pailer and Grün (1980) involve a term, ϵ , describing ductility. Since this quantity is not well defined it is difficult to determine exactly

how well either of these equations fit the CTH data. However, both equations have the highest of all the various velocity indexes, suggesting over-predictions at higher speeds.

For predictions of the perforation hole sizes, equations have been given by Maiden et al. (1964), McHugh (1962), Sawle (1969), and Brown (1970). All of these equations have the property of predicting significantly ever larger holes as the impact velocity increases. Further, only that by Sawle includes material densities, most only use linear dimensions!

Herrmann and Wilbeck (1986) point out that such equations rarely fit a wide range of data. The equations by Sawle, Maiden and Brown imply that the hole size increases with almost a $(T/d_p)^{2/3}$ rule, but the data is not well confirmed. Brown observed "odd non-linearities" as the target thickness decreased to zero, but no rational explanation was given.

POD's Equations 75 and 76 indicated a roughly simple linear rule for hole size versus (T/d_p) when the latter was very small, but a reducing index as T/d_p increased.

4.4 Perforations in Teflon

As described above for aluminum, several existing scaling laws describing perforation, specifically the Ballistic Limit, have been identified and compared. McDonnell and Sullivan (1992) have listed many of these laws. For convenience, we list the appropriate laws, and McDonnell's references in Appendix B. Figures 149 and 150 show the predictions from the laws for the case of an Al 6061-T6 projectile into TFE Teflon. Also shown are the results of POD's Equation 59. We have previously shown in Figures 91 and 92 that, for a projectile of Al 6061-T6, this equation gives a good fit to the CTH predictions.

In Figure 149, it is seen that of the various equations by McDonnell (1992), his Equations 6, 7, and 10 all fit the CTH data (slightly low) for Al 6061-T6 projectile and TFE Teflon target, provided the value of 800 bars is used for σ_{Al} (as done by McDonnell), α is set to 0.2 kbars (as with the CTH data), and $d_p = 1.0$ cm (to "remove" the supralinear term, as suggested by POD in Section 2.3.9 for such large projectiles). However, his Equation 11 (McDonnell, 1979) is a poor fit, tending to give very low predictions. McDonnell assumes that the tensile strength should be used, whereas POD concludes that both yield and tensile strengths are needed, as per Equation 59. All three of these McDonnell's equations are close fits to the CTH data. However, since McDonnell recommends (in his report) the use of his Equation 10, and since it fit POD's Equation 59 the best, we have used this equation in Figure 150 to compare with the predictions of scaling laws from other investigators.

The equation by Naumann (1966) overpredicts the CTH data by a factor of about two, and is clearly not good for aluminum into TFE Teflon. In Section 4.3 it was shown that Naumann was also high by a factor of about three for aluminum into aluminum.

The equation by Cour-Palais (1979) is too low by a factor of about 0.6 for an Al/Teflon impact.

Both the equations of Fish and Summers (1965) and of Pailer and Grün (1980) involve a term, ϵ , describing ductility. Since this quantity is not well defined it is difficult to determine how well either of these equations fit the CTH data. For TFE Teflon, we took this quantity as an average of the values quoted by Shackelford and Alexander (1992). Thus we used $\epsilon = 275\%$. However, for the Al/Teflon impact, Fish and Summers predict low (similar to Co-Palais), while Pailer and Grün are very close to POD's Equation 59.

If these other scaling laws were truly "generic" they should fit the Teflon data just as well as they did the aluminum data, when the appropriate material properties are used. It is clear, however, that this does not happen. POD's equation, however, does give good fits to both Teflon and aluminum data.

5.0 COMPARISONS WITH EXPERIMENTAL DATA

5.1 Cratering in Aluminum

Some recent well characterized experimental impact data have been provided by Hörz (1992). These experiments have made use of a gas gun at NASA Johnson Space Center to accelerate projectiles of soda-lime glass at aluminum targets of Al 1100 and Al 6061-T6. The impact speeds were all about 5.8-5.9 km/s and were normal to the target surfaces. The projectiles were of 50, 150, 1000 and 3175 microns diameter. Hörz carefully measured the crater diameters for each experiment, using the initial target surface as the reference plane. The primary purpose of these experiments was to study perforations, consequently only a small fraction of the data were for craters in thick targets.

For the thick Al 1100 targets the values of (d_c/d_p) versus projectile diameter were found to be 4.33 (3175 microns), 5.01 (1000 microns), 4.92 (150 microns) and 3.2 (50 microns). For the Al 6061-T6 the ratio was 3.35 (3175 microns). This latter value is about 15% lower than the POD CTH calculation for an Al/Al impact. Soda-lime glass has a density of about 2.2 g/cm³ and a slightly lower sound speed than aluminum. Accordingly, Equation 21 predicts only a very small difference (*i.e.*, a few percent) versus the Al/Al impact.

Although the data base is small and therefore subject to some error, a distinct drop in crater diameter is seen for the smallest projectiles versus the larger ones. The larger projectiles tend to give a systematic trend in crater diameter, except for the largest ones. Comparing the 50 micron projectile data with the 3175 micron data there is an apparent supralinear index of about 0.073, while comparing the 50 micron data with the 1000 micron data gives an index of 0.149. These apparent indexes are both larger than the Cour-Palais quote of 0.056 and may be a consequence of the small data base.

Comparing the results for Al 1100 versus those for Al 6061-T6 we see that the crater diameters were in the ratio of 4.33 to 3.35, *i.e.*, 1.293. The only significant difference in these two aluminums are the yield strengths. Equation 21 gives an index of -0.2857 for crater diameter versus yield strength, while the fit to the CTH data gave an index of -0.258. Thus to explain the experimental data, assuming the yield strength of Al 6061-T6 is 2.7 kbars, requires the Al 1100 to have a yield strength of either 1.098 or 0.997 kbars. Engineering data (Shackelford, 1992) identifies this aluminum to be of temper H12 (*i.e.*, Al 1100 H12), which is one of the softer aluminums.

Recent cratering data have also been provided by Christiansen (1992c) for aluminum projectiles into Al 6061-T6. This work was done at the NASA JSC HIT-F gas gun facility, as part of a careful study of oblique impact responses. For a normal impact with an impact speed of 6.83 km/s the experiments give $P/d_p = 2.1$ and $d_c/d_p = 4.55$. These values are close to both the CTH predictions and POD's predictions using Equations 28 and 21, respectively. CTH gives $P/d_p = 2.2$ and $d_c/d_p = 4.0$, while POD's equations give $P/d_p = 2.2$ and $d_c/d_p = 4.1$.

5.2 Cratering in Teflon

There is only a limited data base for impacts into Teflon TFE. Some recent well characterized experimental impact data have been provided by Hörz (1992) for projectiles of soda-lime glass and Teflon TFE targets. The impact speeds were all about 5.8-6.3 km/s and were normal to the target surfaces. The projectiles were of 50, 150, 1000 and 3175 microns diameter, but only the largest ones were used for cratering in thick targets. Hörz carefully measured the crater diameters for each experiment, using the initial target surface as the reference plane. The primary purpose of these experiments was to study perforations, consequently only a small fraction of the data were for craters in thick targets. Hörz also sent photographs to POD of cross-sections through the Teflon samples, shown in Figure 4. It is evident from these pictures that the craters in Teflon are not smooth-surfaced as with a ductile metal target. Instead, the craters suffer from rough surfaces and show signs of surface fracture, some radial cracking, and also have a "hairy" morphology indicating "strings" of partially melted/resolidified material (with the exception of the "strings" these morphological features are similar to the CTH example given above). Because of these features the "exact" value of crater diameter is difficult to define. For example, for the case of $D_p/T_r = 0.125$ in Figure 4, Hörz quotes a crater diameter of 1.18 cm, for a 3175 micron soda-lime projectile into a one inch thick Teflon target (*i.e.*, $(d_c/d_p) = 3.72$). POD's independent estimate of this diameter is 1.3 to 1.5 cm (*i.e.*, $(d_c/d_p) = 4.09$ to 4.72), based solely on the photograph. Thus a possible 27% error in the quote exists. This is consistent with Hörz's (1992) findings that the "standard" crater in Teflon was difficult to measure.

Thus for the thick Teflon targets the values of (d_c/d_p) were found to be in the range 3.72 to 4.72 (3175 micron projectile). The CTH value is about 5.7 for an impact speed of 6.3 km/s and a Teflon yield strength of 300 bars. This CTH value, for an Al/Teflon impact, is higher than the experimental value(s), for soda-lime glass/Teflon impacts, by a factor of between 1.21 to 1.53. Soda-lime glass has a density of about 2.2 g/cm^3 and a slightly lower sound speed than aluminum, so Equation 21 predicts a very small difference (*i.e.*, a few percent) versus the Al/Teflon impact. To make the CTH calculations agree with the experiments it would be necessary to either increase the assumed yield strength, or decrease the assumed bulk sound speed of the Teflon.

With the exception of Sedgwick's 1978 law (which is close to the CTH penetration depth predictions for Teflon TFE) and Sorenson's 1962 law (which is close to the Equation 28 penetration depth predictions for Teflon TFE), the other scaling laws (presented in Section 4.0) substantially overpredict the CTH values and, thus, the experimental data. However, as previously stated, the Equation 21 and 28 predictions of crater diameter and penetration depth are consistently 18% below the CTH values. Thus these equations predict values between the CTH values and Hörz's experimental data. As shown in Figure 52, for the experimental velocity regime over which Hörz found the Teflon (d_c/d_p) values to be in the range of 3.72 to 4.72, Equation 21 predicts (d_c/d_p) values in the range of 4.6 to 4.95. Picking the highest value (at 6.3 km/s), Equation 21 is higher than the experimental value(s) by a factor of between 1.05 and 1.33, for an Al/Teflon impact. Since the soda-lime glass used in Hörz's experiments has a lower

density and sound speed than aluminum, Equation 21 predicts a very small difference (*i.e.*, a few percent) versus the Al/Teflon impact.

Since only one projectile size was used there is no data concerning supralinearity.

5.3 Perforations in Aluminum

Some recent experimental impact data have been provided by Hörz (1992) for projectiles of soda-lime glass and thin aluminum targets. The impact speeds were all about 5.8-6.3 km/s and were normal to the target surfaces. The projectiles were of 50, 150, 1000 and 3175 microns diameter. However, only the largest projectiles were used to obtain data on Al 6061-T6 (modelled in this report). All projectile sizes were used for Al 1100 targets, however. Hörz carefully measured the crater diameters for each experiment, using the initial target surface as the reference plane. The primary purpose of these experiments was to study perforations. Hörz also sent photographs to POD of front and rear views of the aluminum samples, shown in Figures 151 and 152.

Although Hörz used soda-lime glass instead of aluminum for the projectiles, POD's equations indicate that the difference in perforation responses is only a few percent. For Al 6061-T6 the experiments indicate that the Ballistic Limit occurs for T/d_p of about 3.0. As shown in Figures 60 and 61, this number is very close to the CTH predictions of 2.8 (perforation) to 3.3 (no perforation) for an impact speed of 6 km/s. Likewise, POD's Equation 59 gives a similar, but slightly lower, value of 2.6.

For Al 1100 the major material properties which differ from Al 6061-T6 are the yield and tensile strengths. Based on the cratering data we deduced that the temper of the metal was H12. Standard handbook quotes (Shackelford and Alexander, 1992) give the yield strength of Al 1100 H12 as 1.0 kbar and the tensile strength as 1.1 kbars, versus 2.7 kbars and 3.1 kbars, respectively, for 6061-T6. Equation 59 suggests that this will increase the limiting value of T/d_p to about 3.5 at 6 km/s. This value is consistent with the experimental data.

Comparing Hörz's data as a function of projectile diameter reveals that a supralinear behavior exists. Comparing the 50 micron results versus the 3175 micron results, the data indicates an index of about 0.07, which is a little higher than the Cour-Palais quote of 0.056, and both values are consistent with the supralinearity indexes expected from POD's approach in Section 2.3.9.

5.4 Perforations in Teflon

Recent experimental impact data have also been provided by Hörz (1992) for projectiles of soda-lime glass and thin TFE Teflon targets. The impact speeds were all about 5.8-6.3 km/s and were normal to the target surfaces. The projectiles were of 150, 1000 and 3175 microns diameter. Hörz carefully measured the crater diameters for each experiment, using the initial target surface as the reference plane. The primary purpose of these experiments was to study perforations. Hörz also sent a photograph to POD of cross-sectional views of the Teflon samples, shown in Figure 4.

Although Hörz used soda-lime glass instead of aluminum for the projectiles, POD's equations indicate that the difference in perforation responses is only a few percent. For TFE Teflon the experiments indicate that the Ballistic Limit occurs for T/d_p of about 5.8 ± 0.25 . As shown in Figures 91 and 92, this number is very close to the CTH predictions of 5.5 (perforation) to 6.4 (no perforation) for an impact speed of 6 km/s. Likewise, POD's Equation 59 gives a similar, but slightly lower, value of 5.1. All of the other investigators' (e.g., McDonnell, Cour-Palais) predict much lower values (the closest being Pailer and Grün with a value of about 4.7), with the exception of Naumann (who substantially overpredicts a value of about 7.9).

Hörz's data as a function of projectile diameter is presently insufficient to allow determination of supralinear behavior.

5.5 Oblique Impacts in Thick Aluminum

Some recent careful studies of oblique impacts of aluminum into thick Al 5061-T5 targets have been done by Christiansen (1992c) at the NASA JSC HIT-F gas gun facility. Christiansen studied the responses over an obliquity range of from 0° incidence to 88° incidence, using small incremental angular changes at the high obliquities. The experiments were all done with an impact speed of about 6.75 ± 0.2 km/s. The data show that the value of P/d_p roughly obeys a $(\cos\theta)^{2/3}$ law, as expected, but tends to drop somewhat faster at very large angles of incidence above 70° . This behavior is similar to POD's prediction of Equation 83 which is shown in Figure 8. The data also show that the value of d_e/d_p roughly obeys a $(\cos\theta)^{2/3}$ law, and is an even better fit to a $(\cos\theta)^{0.5714}$ law as given by POD's Equation 82 and shown in Figure 8.

Of great interest is the data for d_{long}/d_{short} , where d_{long} is the extended diameter for oblique impact and d_{short} is the perpendicular diameter. For angles of incidence below about 60° this ratio is essentially 1.0 indicating that the craters are basically axisymmetric. However, for larger angles the ratio rapidly increases. To a first approximation the ratio fits the rule $0.55\tan\theta$ over the angular range 60° to 88° . This behavior should be compared with the "tan θ " logic of POD's Equation 89 which describes the ability of the top of the projectile to just escape its own crater. An interpretation is that by just failing to escape its own crater the projectile is causing the downstream stretching of the crater.

5.6 Oblique Impacts in Thin Aluminum

Unfortunately, there is little data concerning the definition of the Ballistic Limit for thin target perforations as functions of obliquity. Instead, most experimenters have used fixed-thickness thin targets to study the effects of obliquity on ricochet of the projectile and perforation debris ejecta. Christiansen (1992c) and Schonberg (1988, 1989) have done such studies. As with cratering it is observed that ricocheting occurs above about 60° angle of incidence.

6.0 OTHER MATERIAL COMPARISONS

6.1 Copper Cratering

POD has recently received details of work done by Wingate et al. (1992) at Los Alamos National Laboratory (LANL), presented at the 1992 HyperVelocity Impact Symposium (HVIS). The work involves copper on copper impacts, and compares four code predictions. The codes are: EPIC, MESA, SPH and CALE, and experimental data is also compared. The following table lists the codes' results and the POD predictions.

The calculations are for an impact at 6 km/s. The projectile diameter was $d_p = 0.4747$ cm (0.5g). Properties for copper were: $\rho_p = \rho_t = 8.93$ g/cm³, $c_{\alpha} = 3.94$ km/s, $s = 1.49$, $Y_t = 2.4$ kbars. To compute our values POD used Equations 28 for P and 21 for d_c .

RESULTS

QUANTITY	EXPERIMENT	EPIC	MESA	SPH	CALE	POD
P (CM)	1.4	1.8	1.59	1.73	1.51	1.55
D_c (CM)	2.54	2.4	2.8	2.6	2.44	2.71
P/D_c	0.55	0.75	0.57	0.67	0.62	0.572

We observe that POD's predictions are close to the experimental data. Also note that the variations in the code answers are themselves about 19% (for P), 17% (for d_c) and 32% (for P/d_c). The ratios for the POD values versus experiment are:

1.107 (for P), 1.07 (for d_c) and 1.04 (for P/d_c).

Part of Wingate's work was to explain supralinearity for small (micron size) projectiles. To do so he invoked strain-rate hardening and proposed that the effective yield strength of copper acted as if 5 times larger than normal, and thus was set at 12 kbars. This increased yield value reduced the code predictions for crater *volume* by a factor of 4.1 (EPIC), 4.4 (MESA) and 3.3 (SPH). The POD prediction is 3.973 (Equation [21]³) for the same higher yield. Note that LANL did *not* actually use a strain-rate model, they merely increased the yield value in the elastic-plastic model.

6.2 Lead Cratering

As part of his recent studies of cratering and perforation, Hörz also used lead targets with soda-lime glass projectiles. Hörz also sent photographs to POD of cross-sectional, front and rear views of the lead samples, shown in Figures 153, 154 and 155. Using Equation 21 for crater diameter we can find the ratio of lead crater diameter versus aluminum 6061-T6 crater diameter for

constant projectile size and impact speed. Assuming a lead density of 11.35 g/cm^3 , sound speed of 2 km/s , and yield strength of 0.13 kbars , we predict that lead craters are approximately 1.54 times larger than aluminum craters. Hörz's data gives a ratio of about 1.48 . Thus Equation 21 appears to give a good prediction.

7.0 CONCLUSIONS

7.1 Cratering

Based on the present work POD believes it has a strong insight into cratering laws. Clearly the concept of hemispherical craters is rarely correct, and it appears that diameter is governed by different rules from those giving depth, although the craters do asymptote towards hemispheres for the higher impact speeds. The work demonstrates that target strength is a strong driver for crater size. While increasing the ratio of projectile density to target density always increases crater size the responses are not simple power laws. Likewise the power index for impact speed is not the simple 2/3rd value. Overall, the data suggest that several of the indexes are "coupled" (e.g., the index for density is itself dependent on the velocity, etc.).

POD believes it has identified the source of the supralinearity observed in cratering, and has shown the effect to be related to material strength behavior, in particular that of the target. The resulting analysis suggests that the supralinear effect is really a small-size downgrading and that the effect essentially vanishes for craters larger than about 1 cm diameter. Although insufficient material property data exists for Teflon TFE, POD believes the size effect to be roughly the same as for aluminum. Accordingly, projectiles of size 3175 micron (1/8 inch) are close to the limit where supralinearity asymptotes. Unfortunately, there were no quotes by Hörz for crater diameters for smaller projectiles.

POD has considered the possible effects of momentum enhancement for grossly vaporizing projectiles (e.g., for very high impact speeds), and has concluded that this enhancement is generally only a few percent. Accordingly, the effect is minor and no obvious "step jumps" in cratering responses are expected as materials vaporize. The CTH aluminum and Teflon calculations do not indicate any "vapor" effects on either crater diameter or penetration depth up to 15 km/s impact speeds, even though partial vaporization of both the aluminum projectile and some of the aluminum and Teflon targets occurs at the higher speeds. (Note that both the Mie-Grüneisen and ANEOS equations of state were tried in the CTH runs with little difference in results).

From the above efforts, POD believes that, for aluminum, the physics-based scaling laws presented in Equations 21 and 28 should be used for making predictions of, or interpreting data from, crater diameters and depths, respectively. An alternative would be to use Sedgwick's 1978 scaling law for penetration depth. However, if Sedgwick's law is used, it must be borne in mind that Sedgwick does not account for the difference between crater diameter and penetration depth. A further alternative would be to use the two CTH fits which do differentiate between diameter and depth. However, both of these alternatives are based purely on a hydrodynamic approach. For these reasons, POD presently recommends that its Equations 21 and 28 be used.

Based on the present work, these scaling laws apply to both aluminum and Teflon, and also seem to work well for copper and lead. Equations 21 and 28 are dimensionless; however, these equations were derived from physics and thus suffer none of the irregularities (caused by

improper selection of "pi" terms) which hamper the other existing scaling laws. In comparisons to CTH hydrodynamic code calculations, Equations 21 and 28 closely matched the predictions for aluminum and was within 18% of the predictions for Teflon. In addition, these equations predict trends in crater diameters and penetration depths, with varying target and projectile material properties and impact velocities, which match the trends predicted by CTH. In comparison with experimental data (Hörz, 1992), Equations 21 and 28 closely matched the data for aluminum impacts and was within a factor of 1.05 to 1.33 for Teflon impacts.

This work has also shown that the maximum depth of the craters usually occurs before the maximum crater diameter has formed.

While alternative scaling laws exist, none of the previous existing scaling laws can be considered generic since they fit impact data either for aluminum or for Teflon, but not for both materials. In addition, these other scaling laws are only applicable over limited velocity and material property regimes (*i.e.*, they do not correctly predict trends in crater diameter or penetration depth). For the above reasons, POD strongly recommends that, for both aluminum and Teflon TFE, the physics-based scaling laws presented in Equations 21 and 28 should be used for making predictions of, or interpreting data from, crater diameters and depths, respectively.

7.2 Perforations

Based on the present work, POD believes it has an insight into perforation laws, and has developed a generically applicable scaling law (Equation 59) for predicting the Ballistic Limit perforation conditions for both aluminum and Teflon. We conclude that the equation describing the Ballistic Limit has two parts, one relating to the crater depth, and one relating to the reflection of the shock pulse from the target rear surface. The former term depends on yield strength and has roughly a 2/3 index for impact speed, while the latter term depends on tensile strength and has roughly a unit index for impact speed. Thus the work demonstrates that both target yield strength and tensile strength are strong drivers for determining perforations. Since most other researchers use only a single equation term, it is not surprising that ambiguities arise with regard to which material strength term to use, and with regard to the correct speed index.

POD believes the supralinearity effect also applies to perforation.

From the above efforts, POD believes that, for aluminum and Teflon, the physics-based perforation law presented in Equation 59 should be used for making predictions of the Ballistic Limit. An alternative would be to use any of the three referenced McDonnell and Sullivan 1992 scaling laws (Equations 6, 7 and 10) for perforations in aluminum. There is no clearly obvious "best case" among these three McDonnell equations. McDonnell's Equation 10 gives the closest fit to POD's Equation 59, and all three of these McDonnell equations give close fits to the CTH data. A further alternative would be to use the CTH fit. However, these McDonnell and CTH fit equations are not based on the physics approach (as taken by POD) and may not be directly applicable to other materials.

Equation 59 is dimensionless; however, this equation was derived from physics and thus suffers none of the irregularities (caused by improper selection of "pi" terms) which hamper the other existing scaling laws. In comparisons to CTH hydrodynamic code calculations for perforations, Equation 59 closely matched the predictions for aluminum and was within 10% of the predictions for Teflon. In comparison with experimental data (Hörz, 1992), Equation 59 closely matched the data for aluminum impacts and was within a factor of 1.09 to 1.19 for Teflon impacts.

This work has shown that, for the Ballistic Limit case, the crater diameter is essentially the same as for the semi-infinite target case. However, this work has also developed physics-based equations (Equations 72, 76 and 77) which predict both this effect, and the effect observed experimentally in ultra-thin targets (foils) where the crater diameter asymptotes to the projectile diameter.

While alternative scaling laws exist, none of the previous existing scaling laws can be considered generic since they fit impact data either for aluminum or for Teflon, but not for both materials. POD's equation, however, does give good fits for both Teflon and aluminum data. In addition, these other scaling laws are only applicable over limited velocity and material property regimes (*i.e.*, they do not correctly predict trends in crater diameter or penetration depth). For the above reasons, POD strongly recommends that, for both aluminum and TFE Teflon, the physics-based perforation scaling law presented in Equation 59 should be used for making predictions of the Ballistic Limit.

7.3 Oblique Impacts

POD believes it has confirmed that for oblique impact the component of impact velocity normal to the target correctly describes the target responses. POD has implemented a $\cos\theta$ correction in its Equations 21, 28 and 59 to account for this phenomenon, giving final corrected Equations 82, 83 and 84. POD recommends that these equations be used for impacts at any angle of incidence into both aluminum and TFE Teflon targets.

POD has also indicated the important factors which determine the process of ricocheting of the projectile and has developed and validated criteria (Equations 87 and 88) for predicting partial and complete projectile ricochets.

Finally, it should be noted that all of POD's equations were derived from physics using the logic of the conservation of **momentum** versus conservation of **energy**.

7.4 Implications for LDEF

The primary implication for LDEF (and for other returned spacecraft materials) is that the Cour-Palais equations should be used with care for data interpretations, since while these equations give good fits for thick aluminum targets, they give much poorer fits for Teflon and for perforations. For the Ballistic Limit for thin foils, the McDonnell equations (McDonnell and Sullivan, 1992) are the best existing scaling laws and can be used (although we recommend using

POD's equations in the future). However, the McDonnell equations should not be used for cases where the target thickness is large compared to the particle diameter. It should be noted that this latter is largely the case for LDEF's TFE Teflon blankets. For these reasons, we recommend that the LDEF data be interpreted using the POD equations presented in this series of reports. In addition, the Solar Maximum Mission data should be reinterpreted for determining the meteoroid and debris particle impactor sizes for use in developing the environment models

8.0 RECOMMENDATIONS FOR FUTURE WORK

For future work POD recommends that cratering studies be done for other ductile and brittle target materials, including plastics (*e.g.*, Kevlar, Mylar, Kapton). Also there remains a need to study the effects of projectile shape, and the progression of responses as the shape changes from plate-like through spherical to rod-like.

POD believes that most of the uncertainties in the appropriate indexes could be resolved by more detailed studies of the "inner responses" of the CTH code calculations (*e.g.*, using many tracer points to track out the behavior of stress, velocity and motion). This should better determine the "N+1" index in Equation 21. Likewise, such detailed studies done for the lower impact speeds would allow a better understanding of the regime of small craters, where the assumption of hemispherical shock waves is far from valid. This is the region where the responses change from the Bernoulli flow state into the elastic-plastic, and can occur at speeds of greater than 3 km/s for the case of strong ceramics.

A parameter that needs tracking is the strain-rate effect on cratering. POD's present analyses used only the standard elastic-plastic models for CTH. By testing for sensitivity to variations in strain-rate it will be possible to determine whether high strain rates change the final crater dimensions (*i.e.*, contribute to supralinearity as *suggested but never proven* by many investigators), or merely alter the dynamic shape and rate of development (as suspected by POD).

The issue of high impact speed vapor momentum enhancement needs to be studied more accurately. POD's present analysis suggests only a relatively minor enhancement for a vaporizing projectile. Analysis by others (Lawrence, 1989) suggest a much larger effect at very high impact speeds where substantial portions of the target also vaporize. The issue is whether the larger momentum translates into noticeably larger craters (or a different shape) for a given impact speed.

For additional work in the future, POD recommends that the analytic approach for transition between pure cratering (in semi-infinite targets) and marginal perforation be more fully developed. Additionally, an approach needs to be developed to determine the back surface spallation and the perforation hole sizes. Also, perforation studies need to be done for other materials.

CTH calculations could be done to track out the data observed by Hörz of varying hole size versus target thickness. This would allow a firmer understanding of this behavior. Hörz's work is important because it indicates one of the very few techniques for deciphering perforation data for projectiles which are **not** much larger than the target thickness.

Based on the ricochet and oblique impact laws reported here, studies should be done to extend the laws and correlate oblique impact crater asymmetries versus diameter and depth to allow direct interpretations of impact angles.

Studies should also be done for layered targets, such as the thermal blankets on LDEF, and the thermal paints on aluminum.

Additionally, those individuals working on alternative scaling laws (e.g., McDonnell, Cour-Palais) should use the "pi" terms identified in this series of reports in order to provide better physics-based fits to the data.

REFERENCES

- Anderson, J.C. et al., *Materials Science*, Fourth Edition, Chapman and Hall, 1990, p 197.
- Bell, R.L. et al., The CTH code (Version 1.024), Structural and Solid Mechanics Department, Sandia National Laboratory, Albuquerque, NM, October 1991.
- Bluman, G.W., "Dimensional Analysis, Symmetry and Modelling", *Appl. Math. Notes*, 6, 122-135, 1981.
- Brown, M.L., Hypervelocity Impact in Thin Nickel Targets, Lockheed Electronics Company, 644D-40-64, August, 1970.
- Christiansen, E.L., Design and Performance Equations for Advanced Meteoroid/Debris Shields, 1992 HyperVelocity Impact Symposium, Austin, TX, November 1992a.
- Christiansen, E.L., Design and Performance Equations for Advanced Meteoroid and Debris Shields, *International Journal of Impact Engineering*, Nov. 1992b.
- Christiansen, E.L., Cykowski E. and Ortega J., Highly Oblique Impacts into Thick and Thin Targets, *International Journal of Impact Engineering*, Nov. 1992c.
- Cour-Palais, B.G. et al. (1969) NASA SP-8013.
- Cour-Palais, B.G., Hypervelocity Impact Investigations and Meteoroid Shielding Experience Related to Apollo and Skylab, NASA CP-2360, pps. 247-275, 1985.
- Dean, J.A., *Lange's Handbook of Chemistry*, Fourteenth Edition, McGraw-Hill, 1992.
- Eichelberger, R.J. et al., *Experimental Test of the Theory of Penetration by Metallic Jets*, *J. of Appl. Phys.*, Vol.27, pp 63-68, 1956.
- Gurney, R.W., "The Initial Velocities of Fragments from Bombs, Shells, and Grenades", BRL Report 405, Ballistics Research Laboratory, Norton Air Force Base, CA, September 1943.
- Harper, C.A., *Handbook of Plastics, Elastomers, and Composites*, Second Edition, McGraw-Hill, Inc., 1992.
- Herrmann, W. and Wilbeck, J., Review of Hypervelocity Penetration Theories, SANDIA REPORT, SAND-86-1884C, 1986.
- Holsapple, K.A., The Scaling of Impact Phenomena, *Int. J. Impact Engng* Vol. 5, pp 343-355, 1987.
- Hörz, F. et al., Dimensionally Scaled Penetration Experiments to Extract Projectile Sizes from Space Exposed Surfaces, 1992 HyperVelocity Impact Symposium, Austin, TX, November 1992.
- Kessler, D.J., et al. (1987) NASA TM-100471, and updates (1990).
- Lawrence, R.J., Momentum Enhancement From Hypervelocity Particle Impacts, SANDIA REPORT, SAND89-0713, July 1989.
- Maiden, C.J. et al., Investigation of Fundamental Mechanism of Damage to Thin Targets by Hypervelocity Projectiles, Final Report to U.S. Naval Research Laboratory, GM Research Laboratories, September, 1963.
- McDonnell, J.A.M. and Sullivan, K., Proceedings of the Workshop on Hypervelocity Impacts in Space, University of Kent at Canterbury, 1992, pp. 39-47.
- McHugh, A.H., Evaluation of Hypervelocity Impact Damage to a Thin Sheet by Multiple Regression Analysis, NAA/SDI Report STR-152, June 1966.
- Moses, A.J., *The Practicing Scientist's Handbook*, Van Nostrand Reinhold, 1978.

- Petch, N.J., The Cleavage Strength of Polycrystals, J. of Iron and Steel Institute, Vol. 174, pp 25-26, 1953.
- Rice, M.H., *Puff74 EOS Compilation*, Systems, Science and Software, La Jolla, CA 92038, 1980
- Sawle, D.R., Hypervelocity Impact in Thin Sheets and Semi-Infinite Targets at 15 km/s, AIAA Hyp. Vel. Imp. Conf., April/May 1969, Paper No. 69-378.
- Sedgwick, R.T., et al, High Velocity Long Rod Impact: Theory and Experiment, Tenth International Symposium on Ballistics, San Diego, CA, October 1987
- Shackelford, J.F. and Alexander, W., The CRC Materials Science and Engineering Handbook 1992.
- Schonberg, W.P., Taylor R.A. and Horn J.R., An Analysis of Penetration and Ricochet Phenomena in Oblique Hypervelocity Impact, NASA TM-100319, 1988.
- Schonberg, W.P. and Taylor, R.A., Oblique Hypervelocity Impact Response of Dual-Sheet Structures, NASA TM-100358, January 1989.
- Tate, A., *A Theory for the Deceleration of Long Rods After Impact*, J. of Mech. and Phys. of Solids, Vol. 17, pp387-399, 1967.
- Wingate, C.A., Stellingwerf R.F., Davidson R.F. and Burkett M.W., Models of High Velocity Impact Phenomena, 1992 Hypervelocity Impact Symposium, Austin, TX., Nov. 1992.
- Zeldovich, Ya.B., "Selected Works of Ya. B. Zeldovich", Vol. 1, Princeton University Press, pp 106-120, 1992.
- Zook, H.A., "Flux Versus Direction of Impacts on LDEF by Meteoroids and Orbital Debris", Lunar and Planetary Science XXI, 1990.

APPENDIX A - FIGURES

Figure 1-P:u Logic 1-D Verses Bernoulli Flow

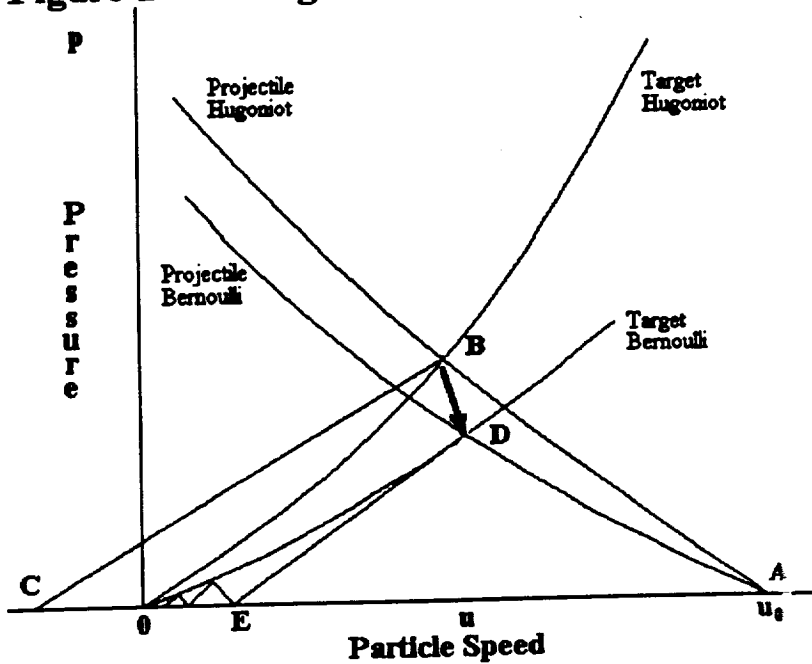


Figure 2-P:u Logic Rigid Projectile Into Soft Target

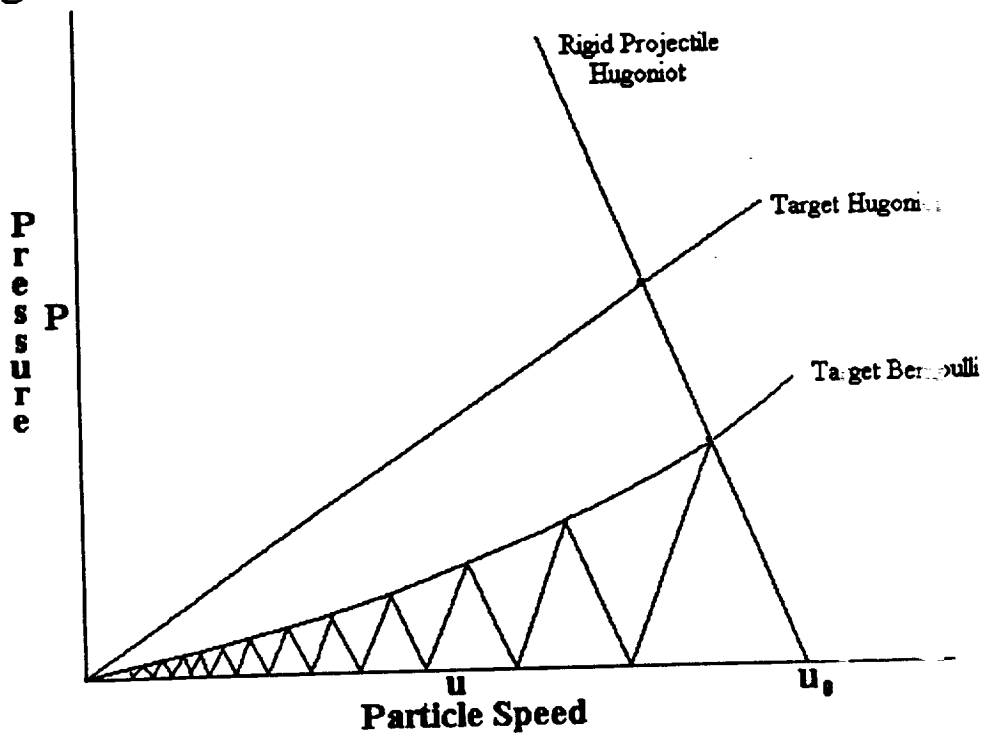
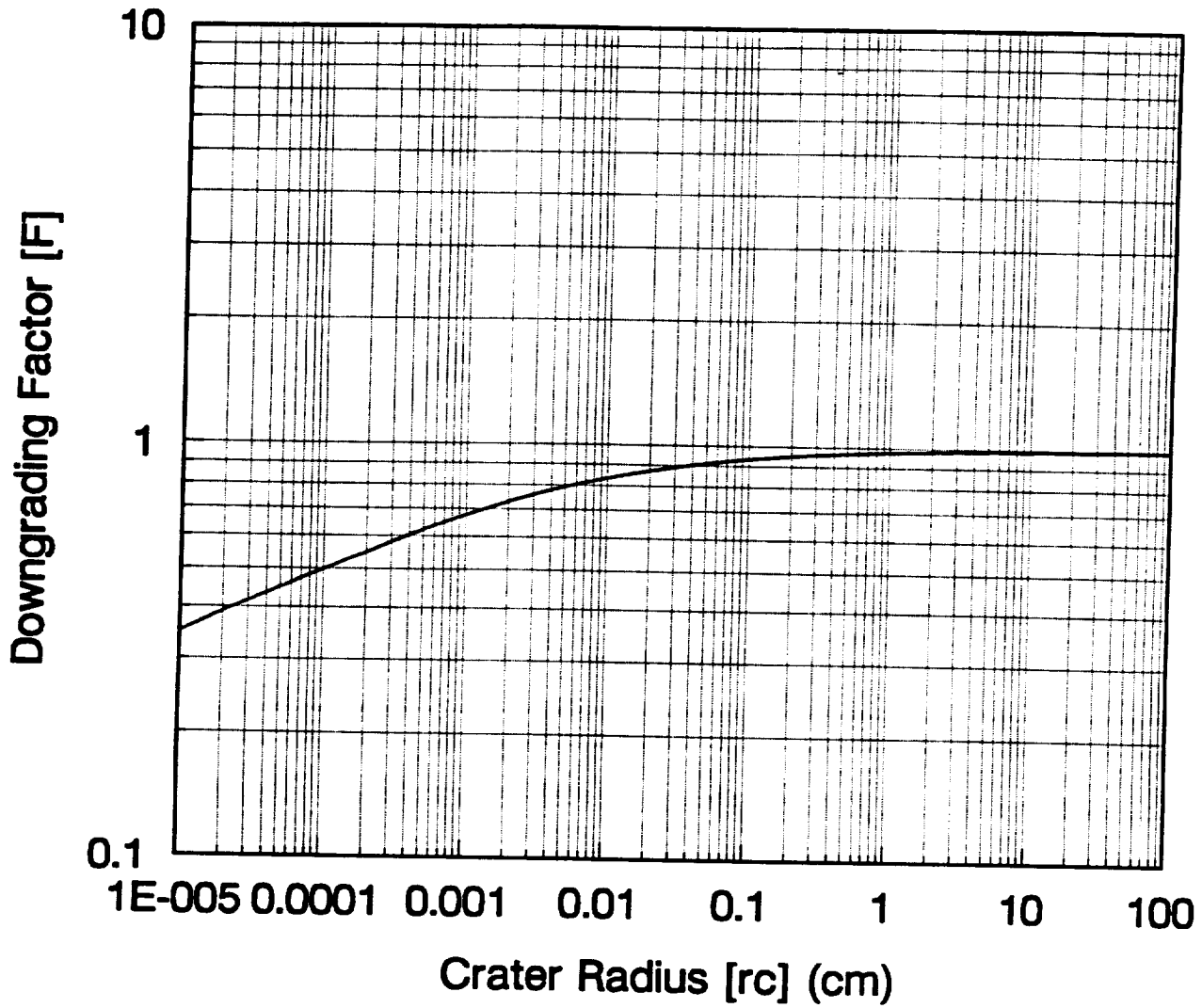


Figure 3. Plot of the Petch Law's Supralinearity Downgrading Factor vs. Crater Radius (for Aluminum)



Soda Lime Glass Into Teflon

at 6.3 km/s ($D_p = 1/8"$)

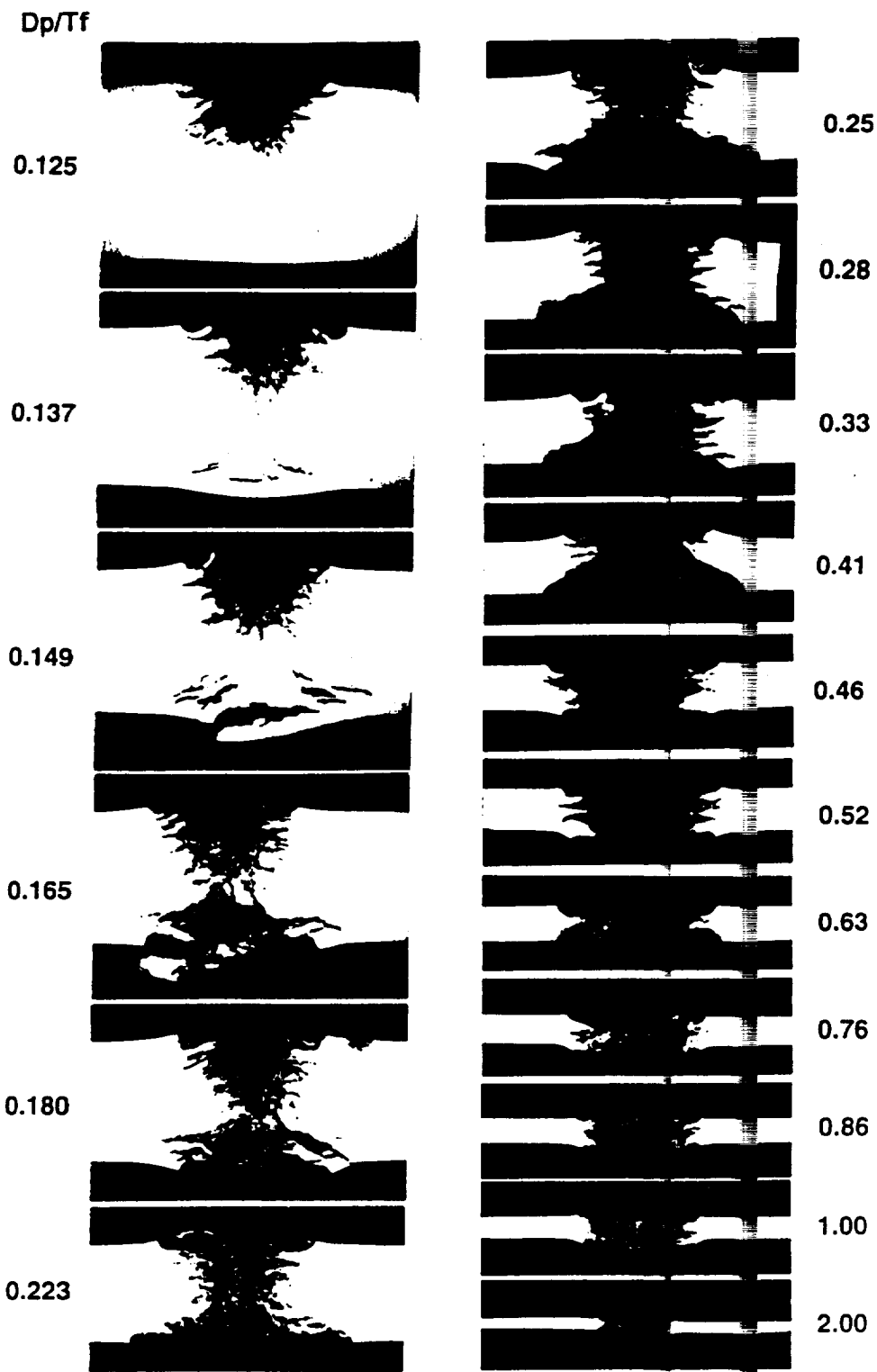


Figure 4.

Figure 5. Plot Showing How Watts' Eq. 59 Varies With N (Al into Al Impact)

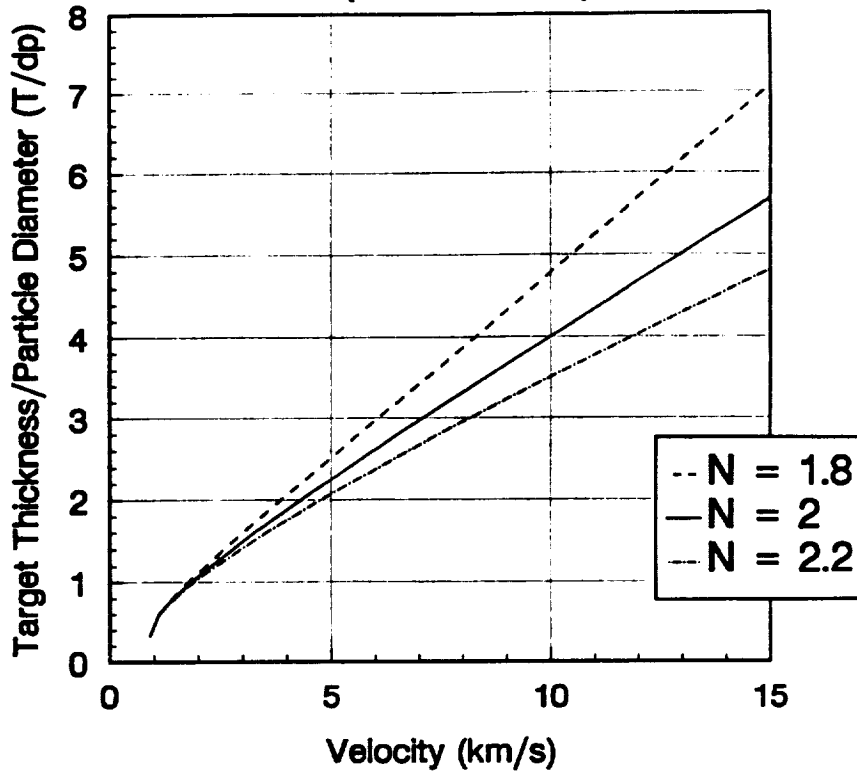


Figure 6. Comparison of Watts' Equations with Horz Data for Aluminum 6061-T6 Impacts at 6 km/s

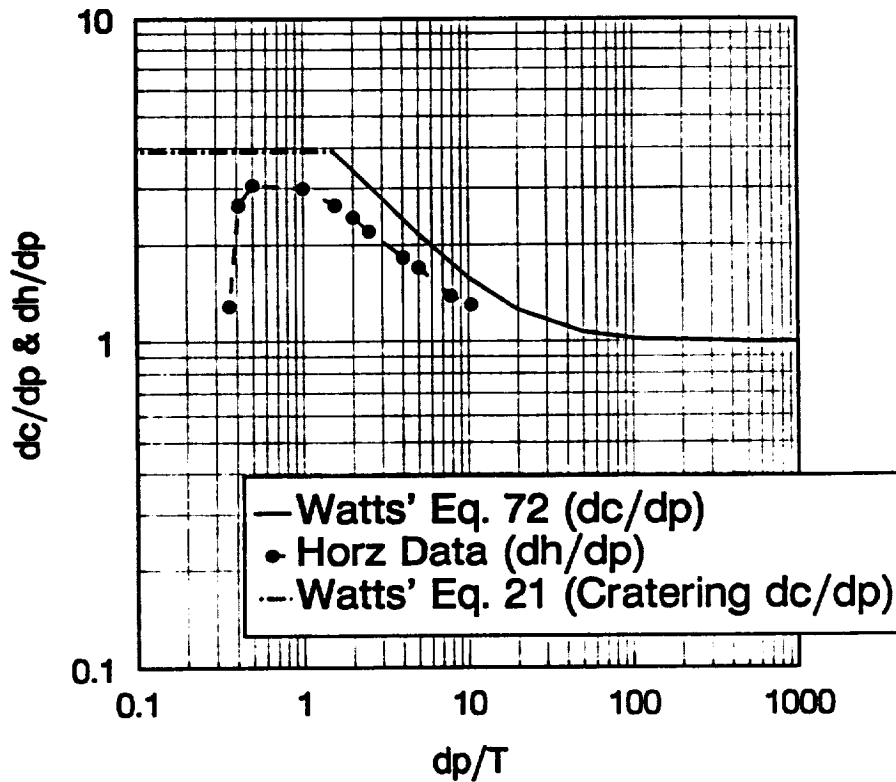


Figure 7. Plot Showing How Watts' Eq. 59 Varies With N (Al into TFE Teflon Impacts)

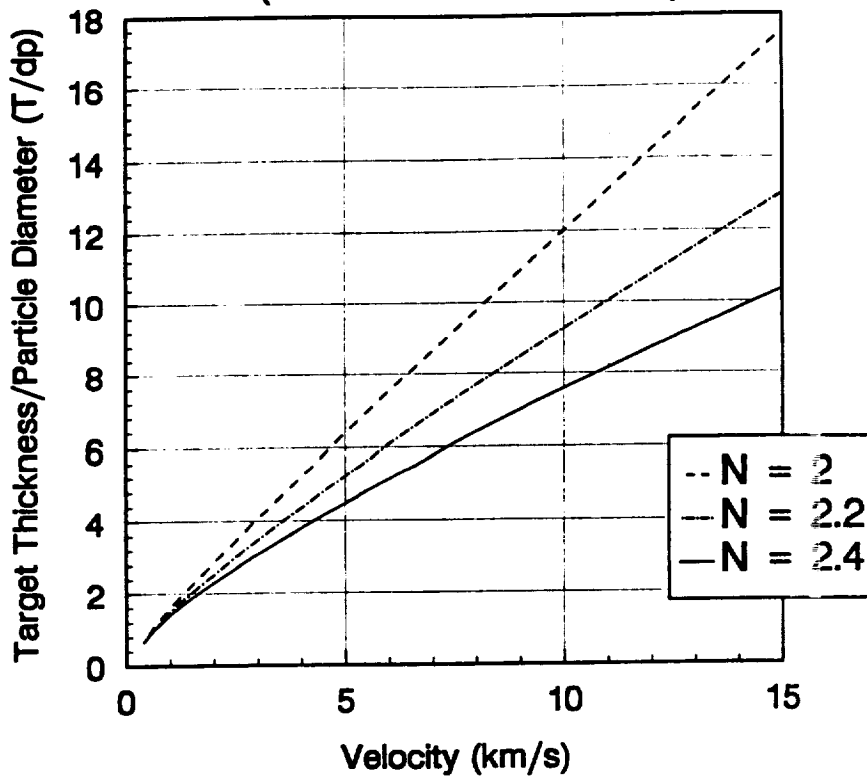


Figure 8. Variations in Equations (82), (83) and (84) with Angle of Incidence - Theta

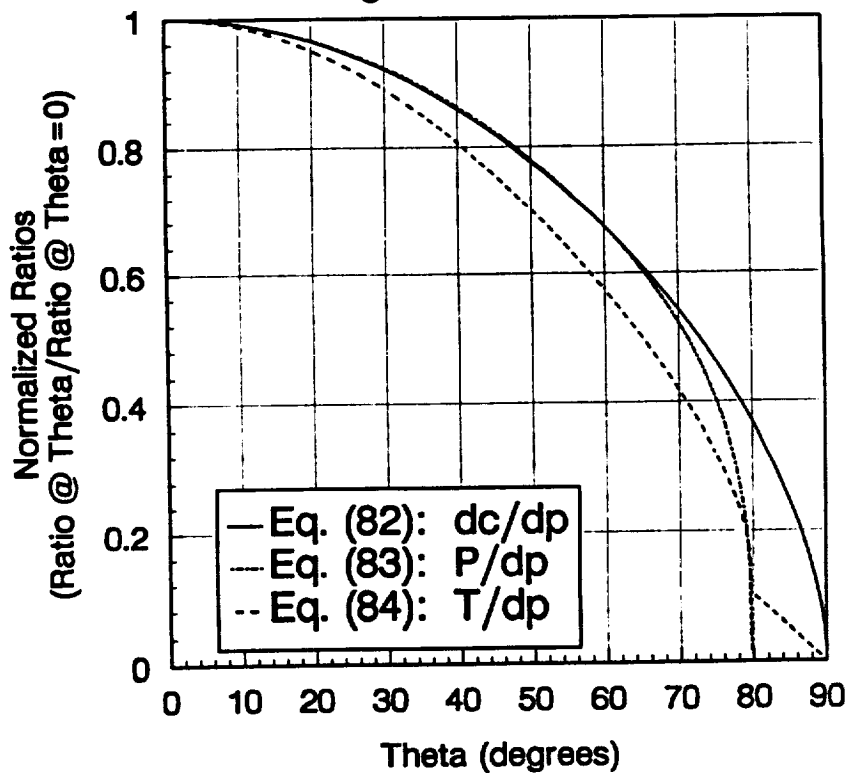


Figure 9. Variations in dc/dp with Angle of Incidence

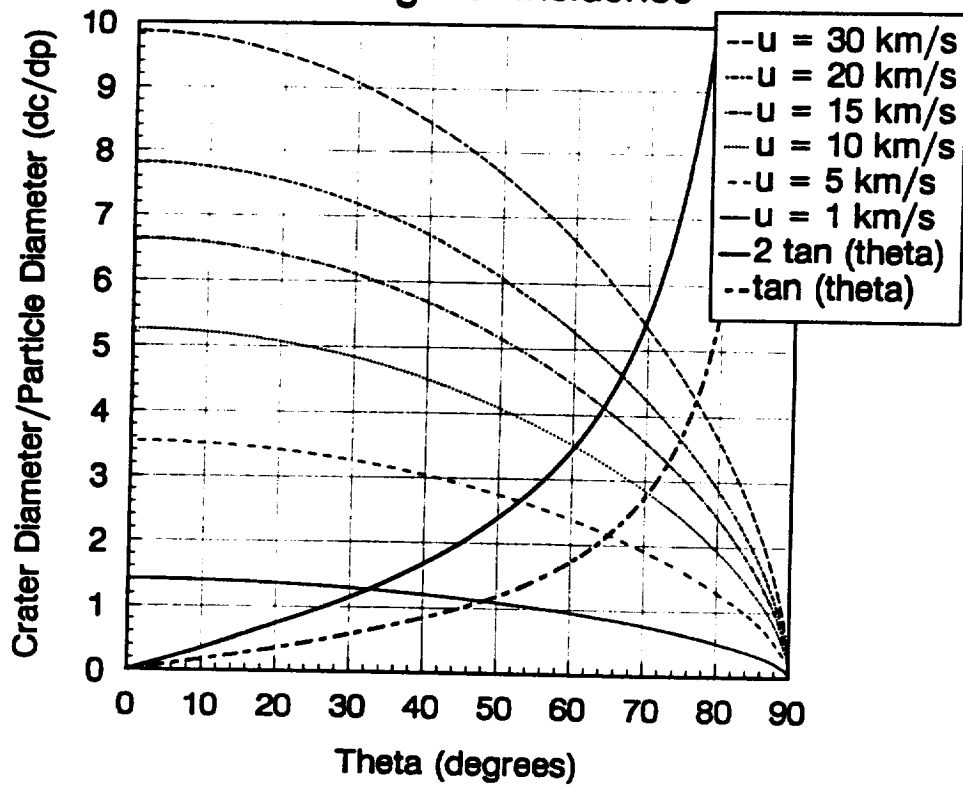


Figure 10. Ricochet Angles for Al into Al

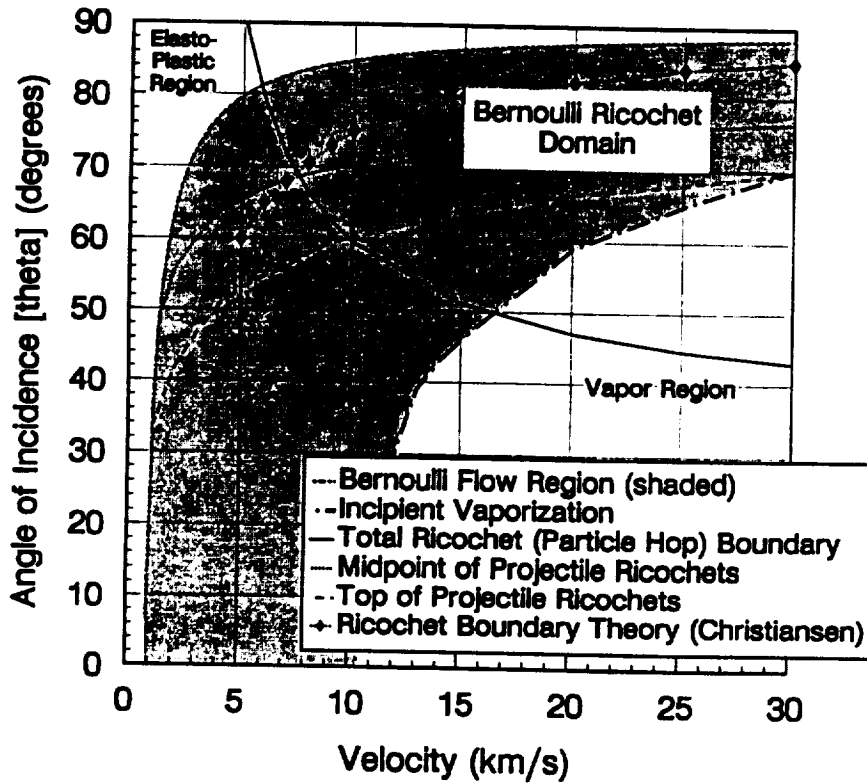


Figure 11. Plot of CTH Results Showing How F/dp Varies With Velocity and Projectile Density for Al into Al

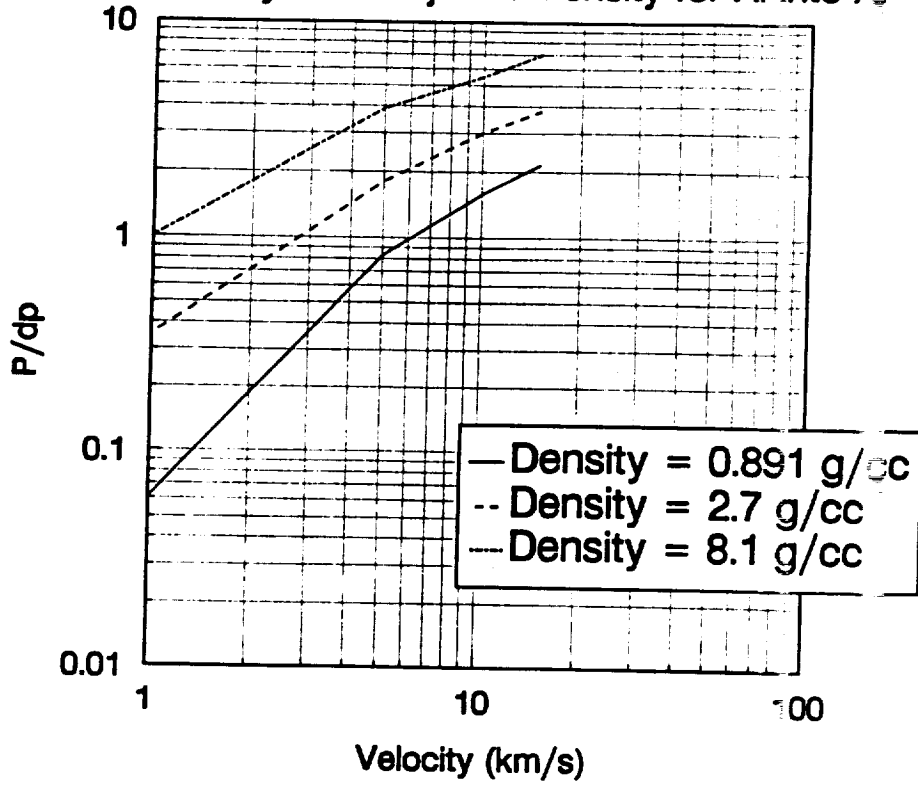


Figure 12. Plot of CTH Results Showing How dc/dp Varies With Velocity and Projectile Density for Al into Al

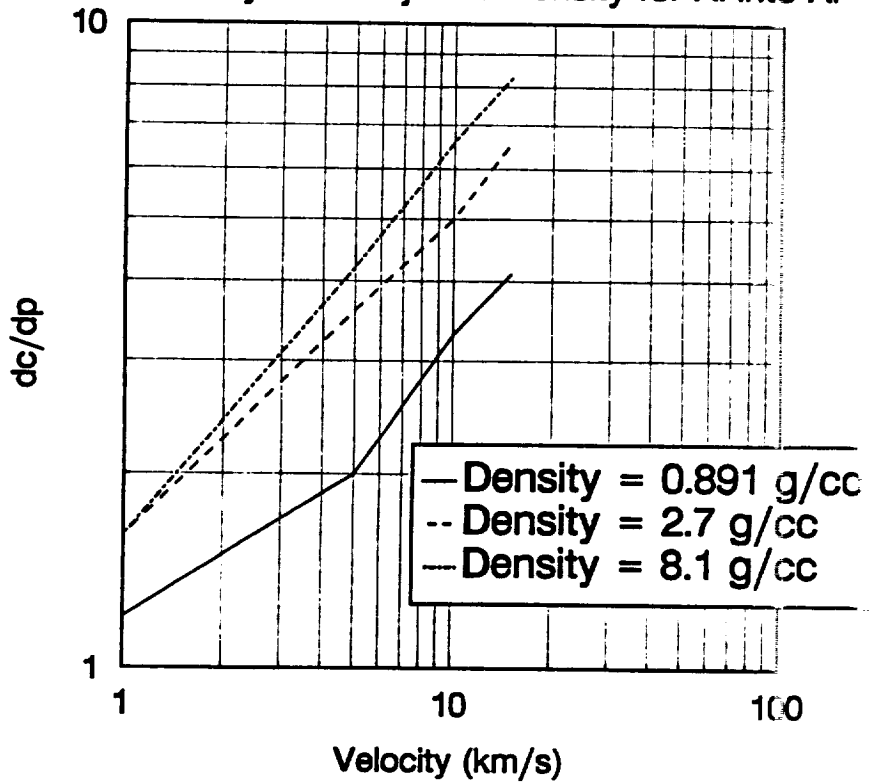


Figure 13. Plot of CTH Results Showing How P/dp Varies With Velocity and Target Yield Strength for Al into Al

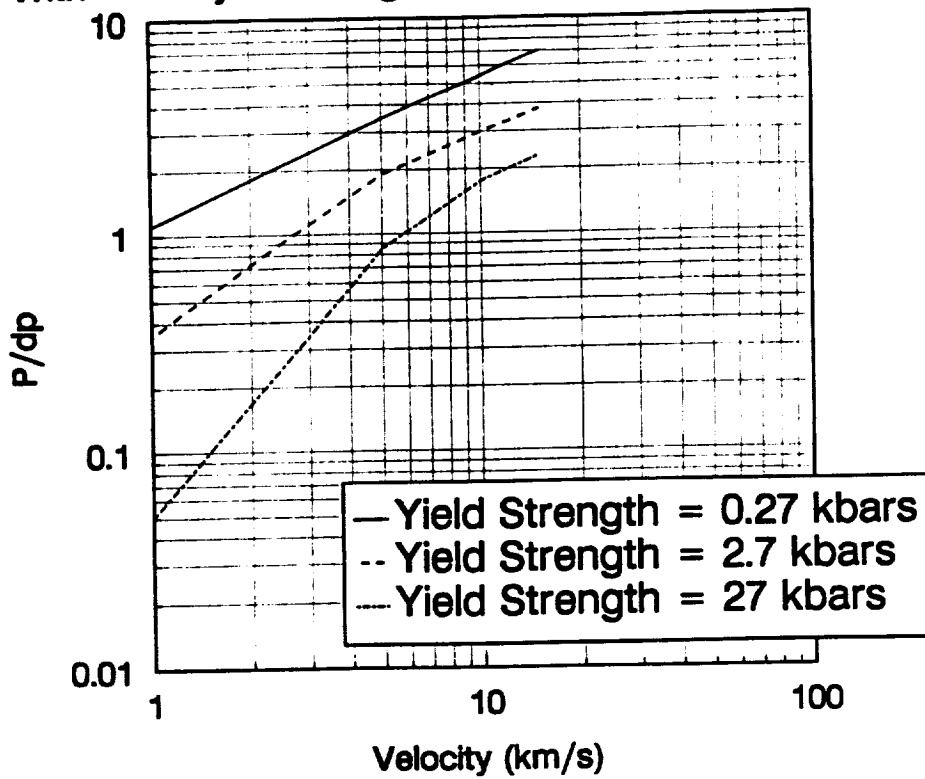


Figure 14. Plot of CTH Results Showing How dc/dp Varies With Velocity and Target Yield Strength for Al into Al

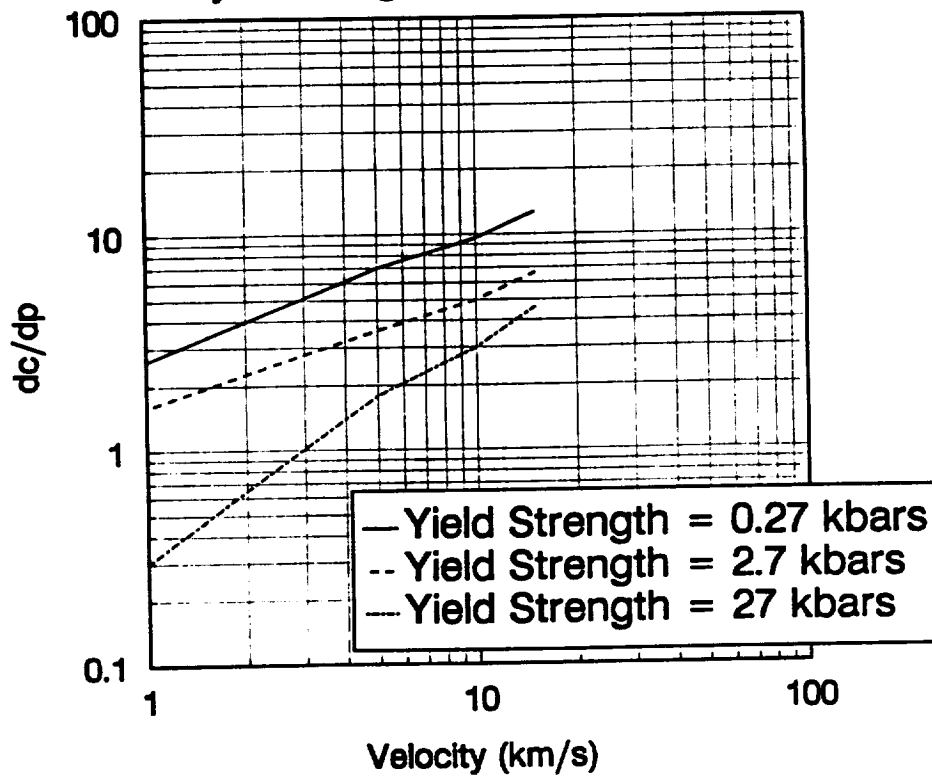


Figure 15. Plot of CTH Results Showing How P/dp Varies With Projectile Density and Velocity for Al into Al

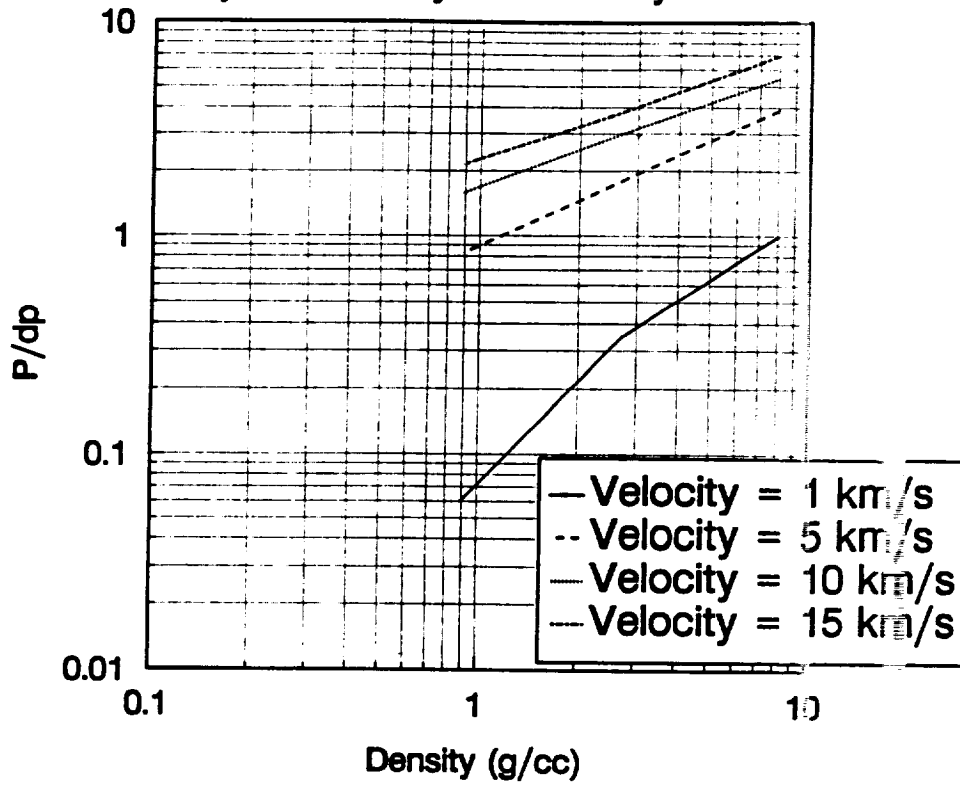


Figure 16. Plot of CTH Results Showing How dc/dp Varies With Projectile Density and Velocity for Al into Al

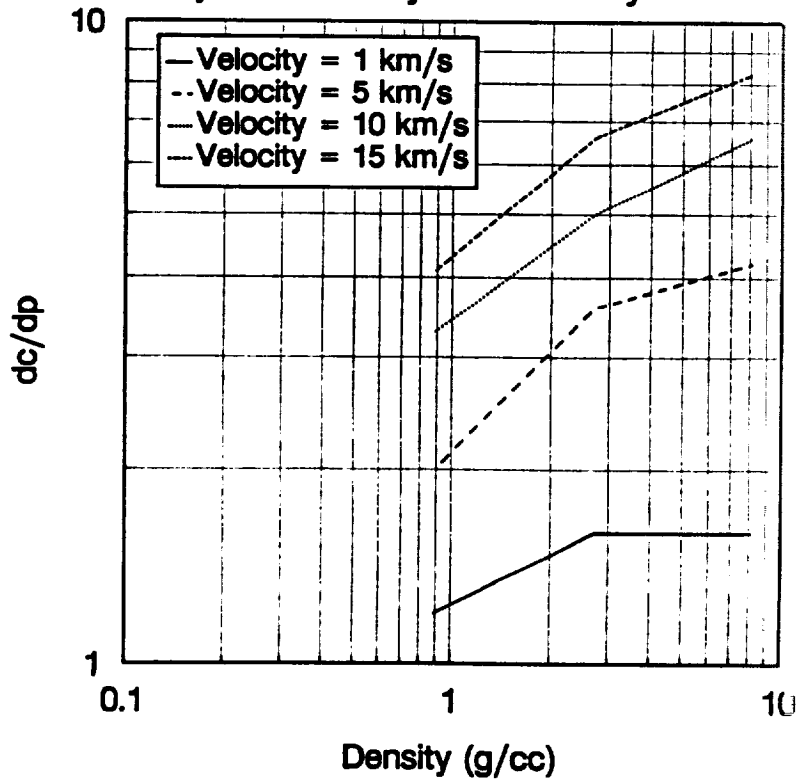


Figure 17. Plot of CTH Results Showing How P/dp Varies With Target Yield Strength and Projectile Velocity For Al into Al

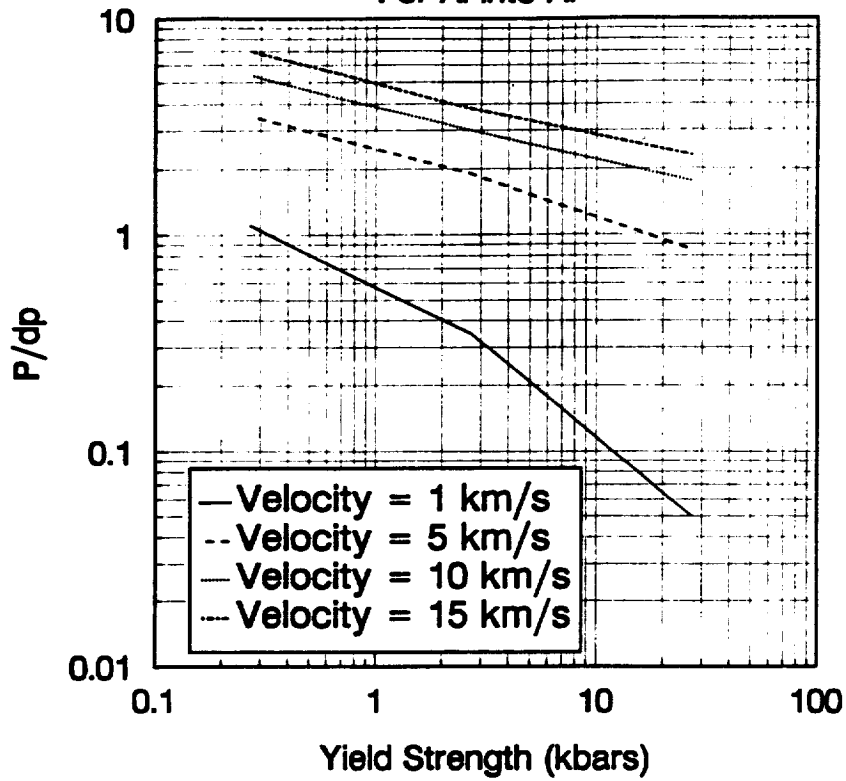


Figure 18. Plot of CTH Results Showing How dc/dp Varies With Target Yield Strength and Projectile Velocity For Al into Al

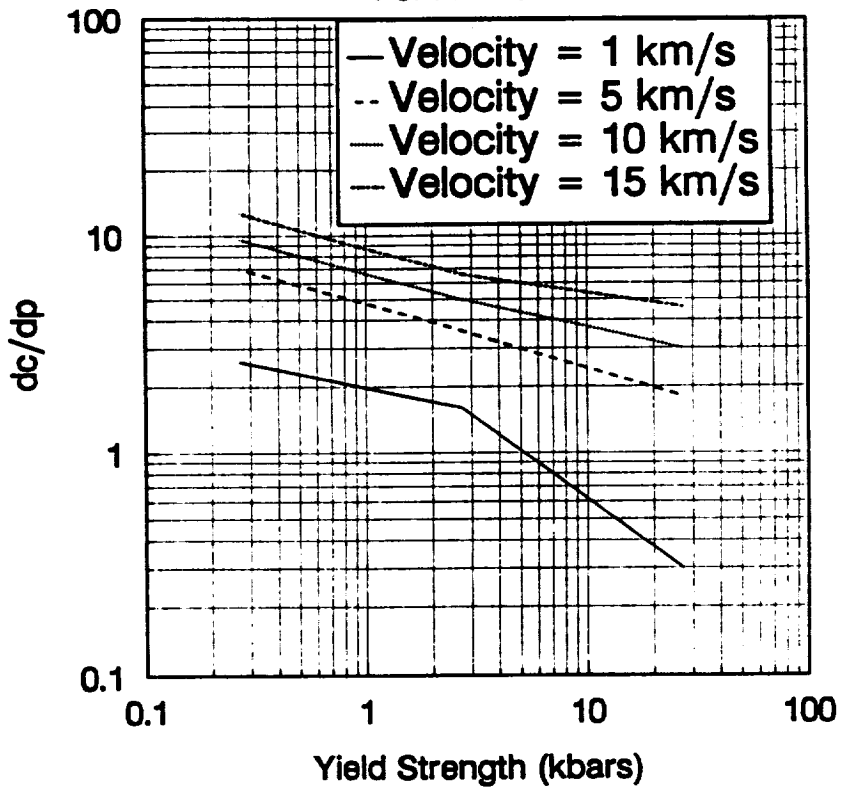


Figure 19. Plot of CTH Results Showing How P/dc Varies With Velocity and Projectile Density for Al into Al

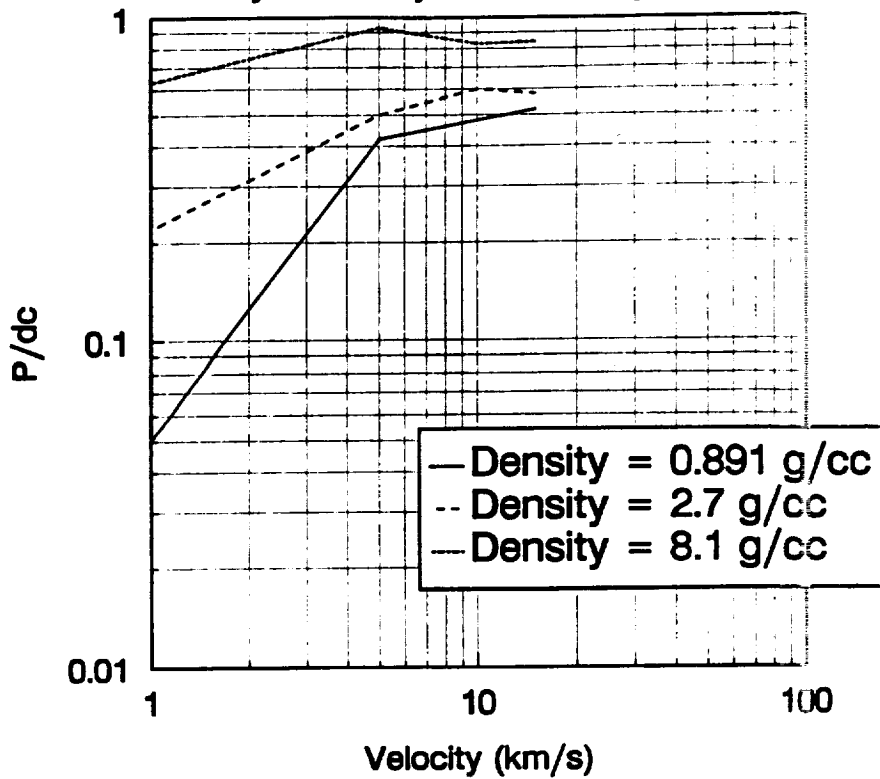


Figure 20. Plot of CTH Results Showing How P/dc Varies With Velocity and Target Yield Strength for Al into Al

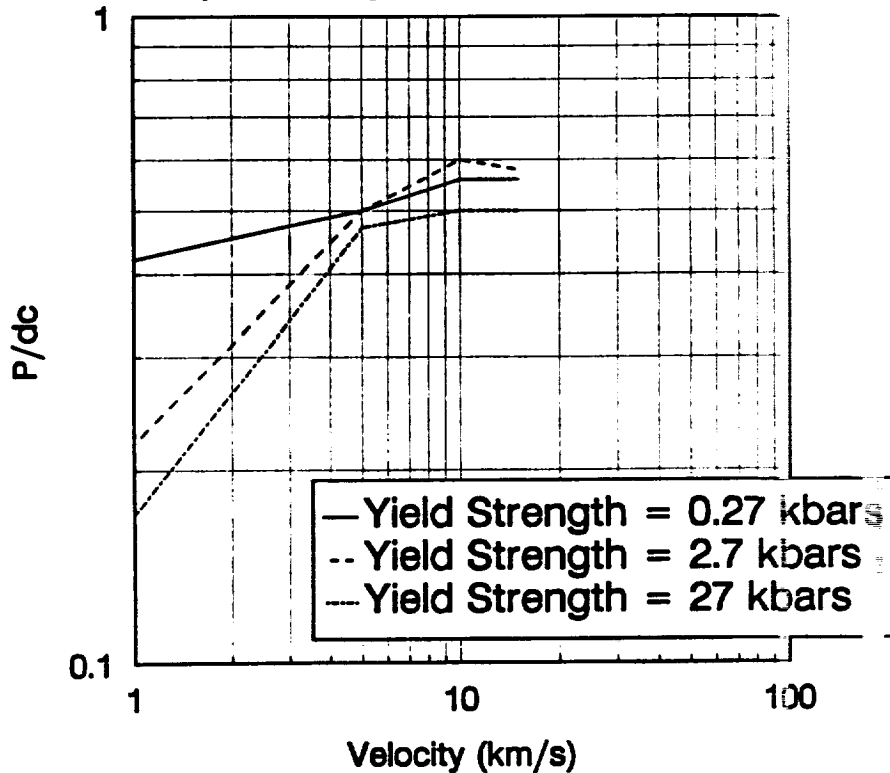


Figure 21.

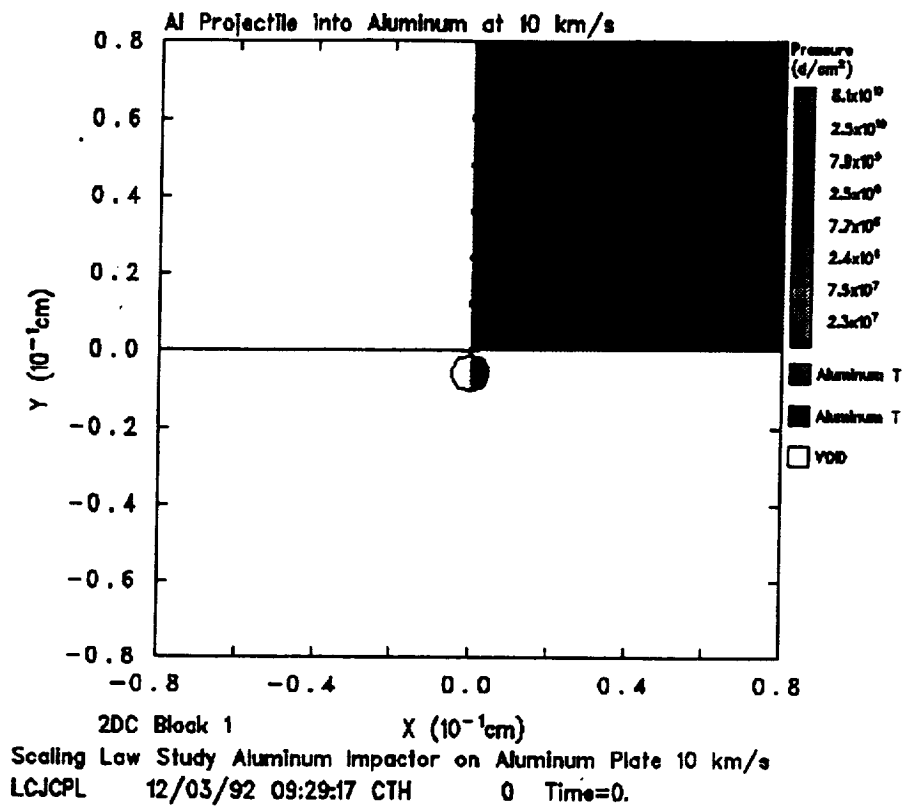


Figure 22.

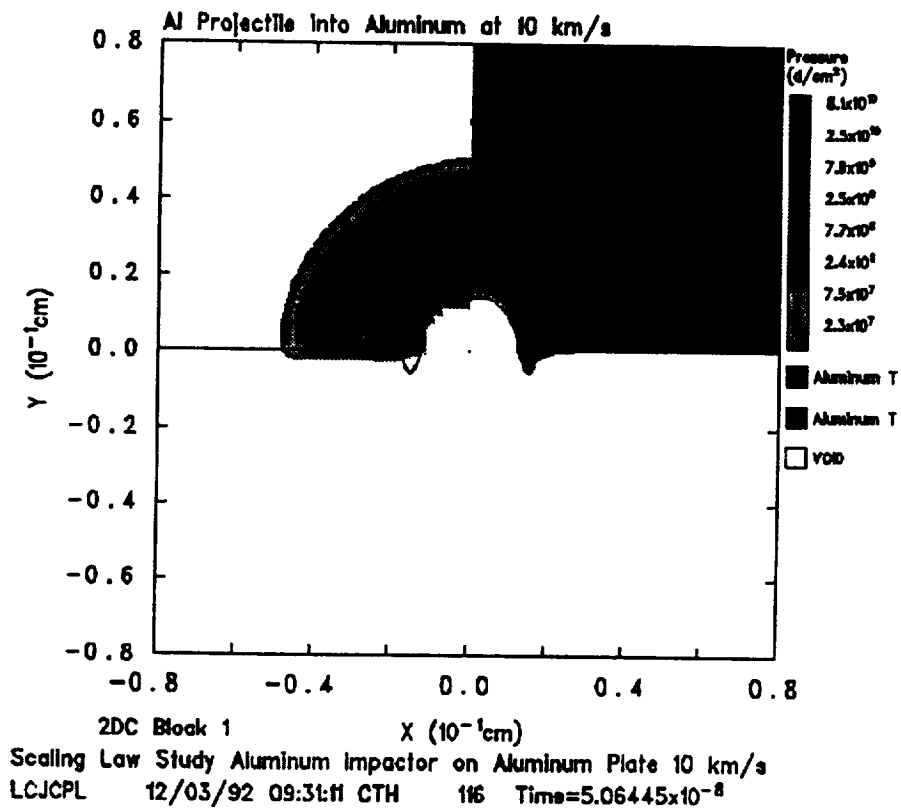
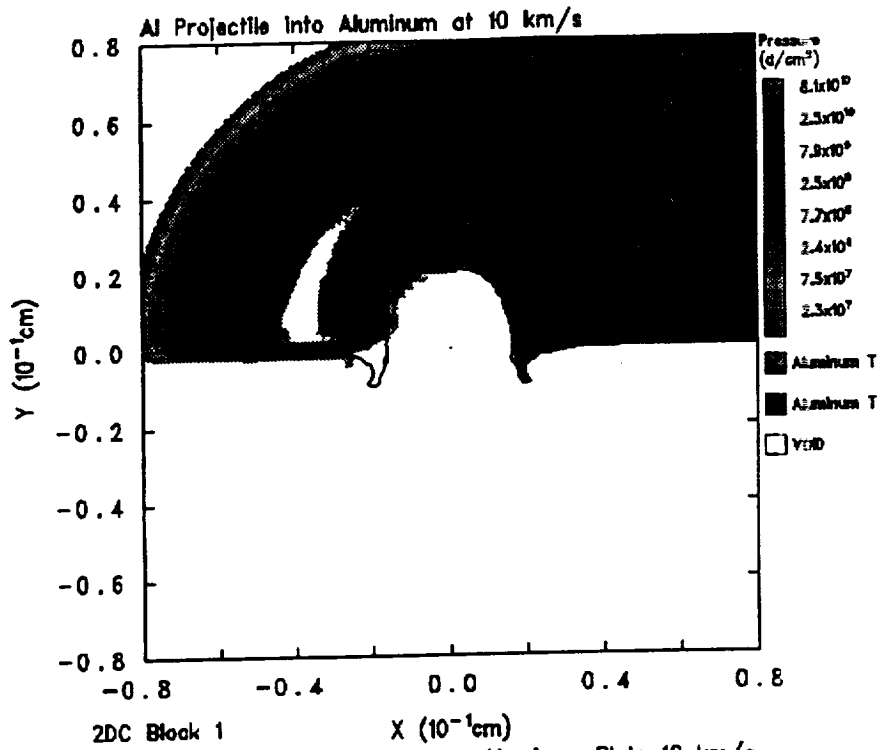
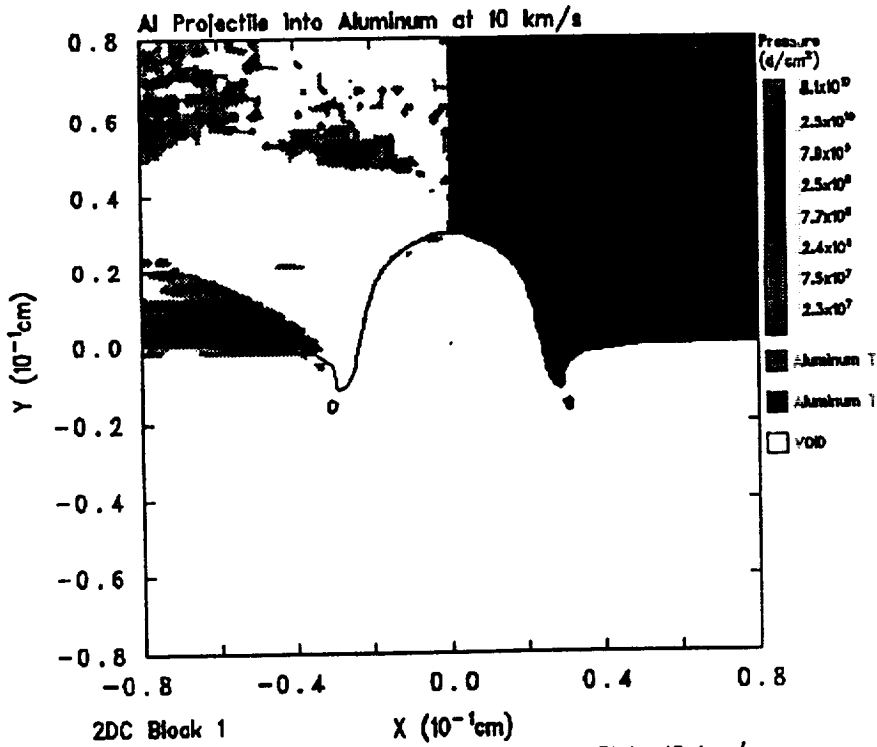


Figure 23.



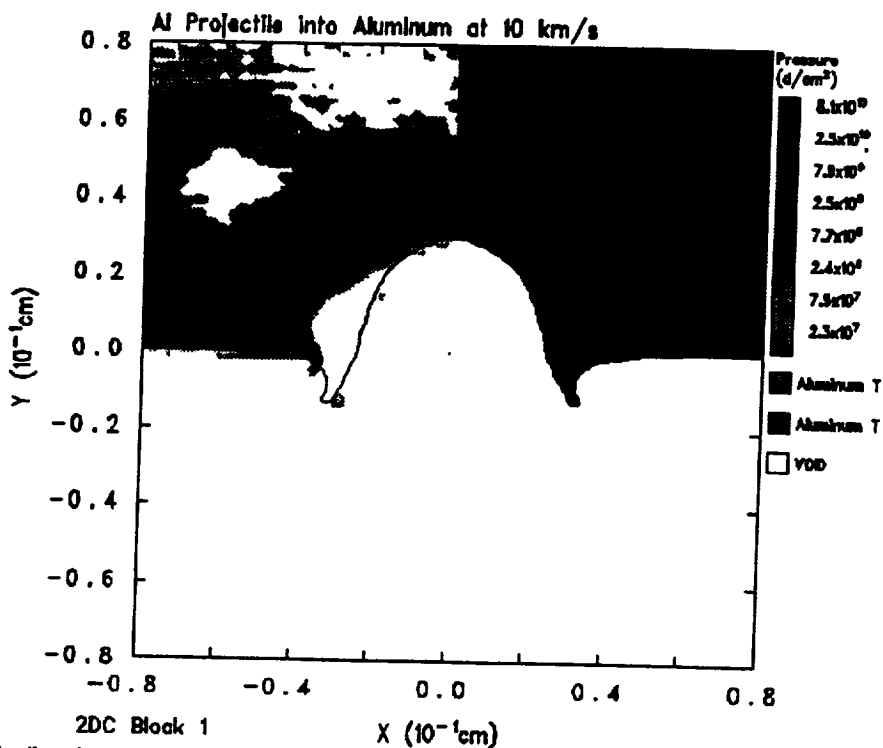
Scaling Law Study Aluminum Impactor on Aluminum Plate 10 km/s
 LCJCPL 12/03/92 09:32:46 CTH 151 Time=1.00076x10⁻⁷

Figure 24.



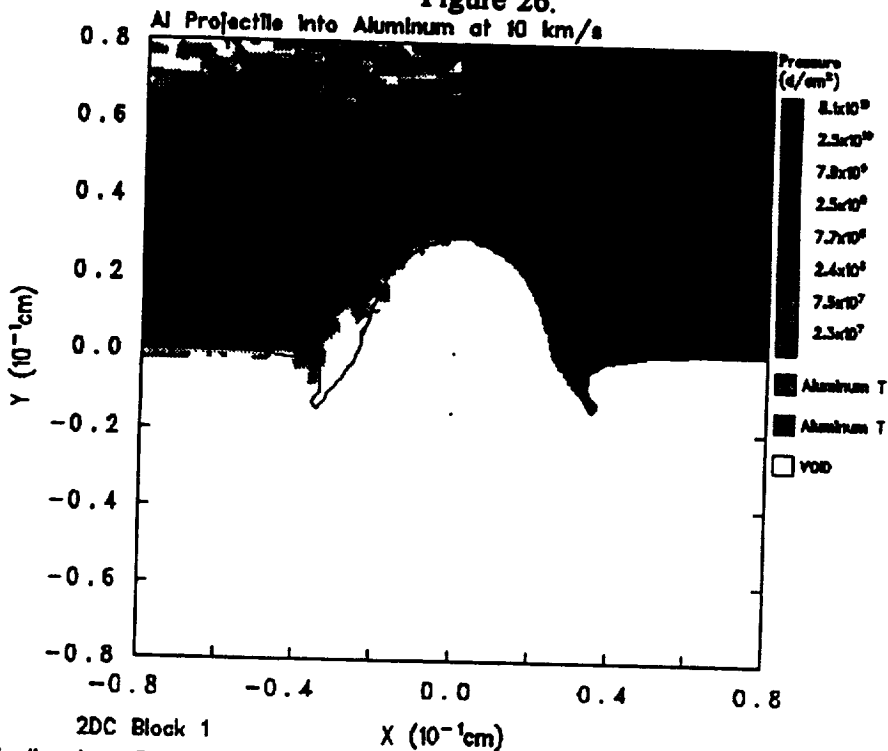
Scaling Law Study Aluminum Impactor on Aluminum Plate 10 km/s
 LCJCPL 12/03/92 09:44:15 CTH 278 Time=3.01457x10⁻⁷

Figure 25.



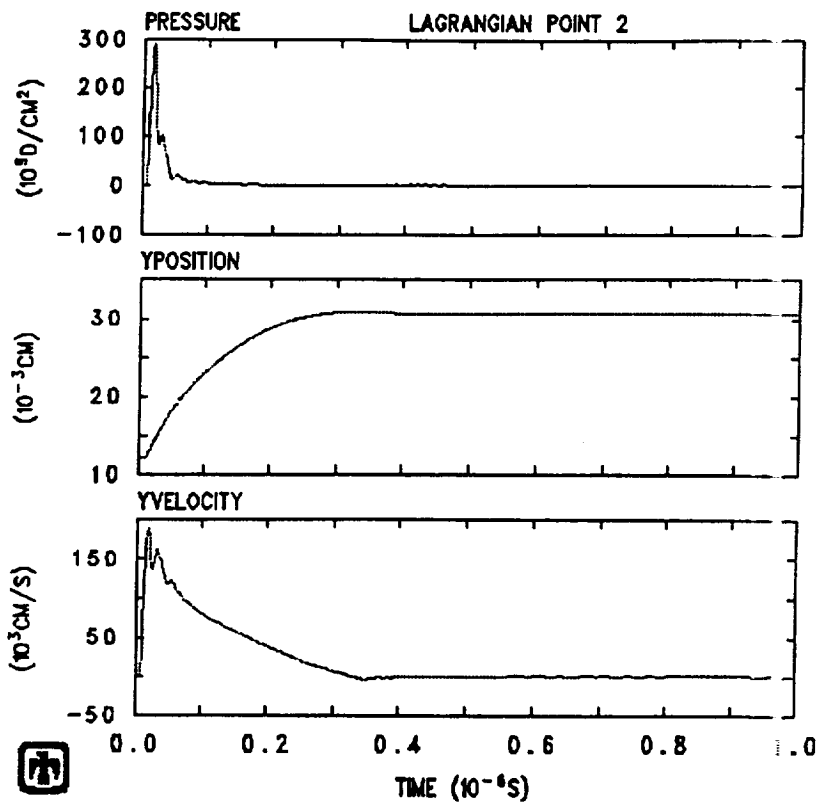
2DC Block 1 X (10⁻¹cm)
Scaling Law Study Aluminum Impactor on Aluminum Plate 10 km/s
LCJCP 12/03/92 09:45:16 CTH 339 Time=4.00664x10⁻⁷

Figure 26.



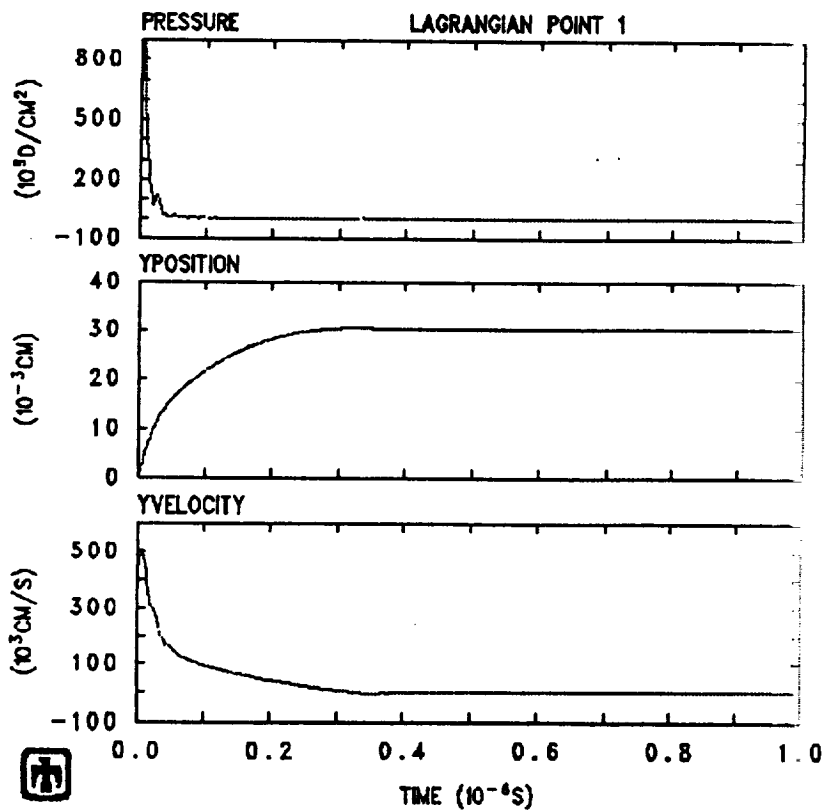
2DC Block 1 X (10⁻¹cm)
Scaling Law Study Aluminum Impactor on Aluminum Plate 10 km/s
LCJCP 12/03/92 09:49:18 CTH 401 Time=5.01594x10⁻⁷

Figure 27.



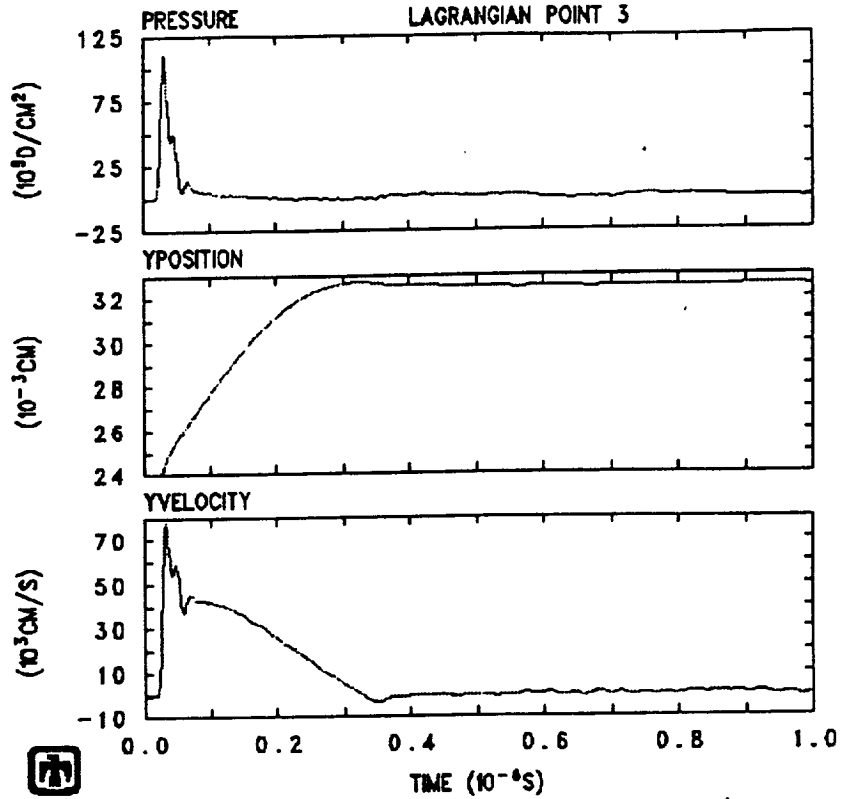
Scaling Low Study Aluminum Impactor on Aluminum Plate 10 km/s
LCJCP 12/03/92 10:08:51 CTH

Figure 28.



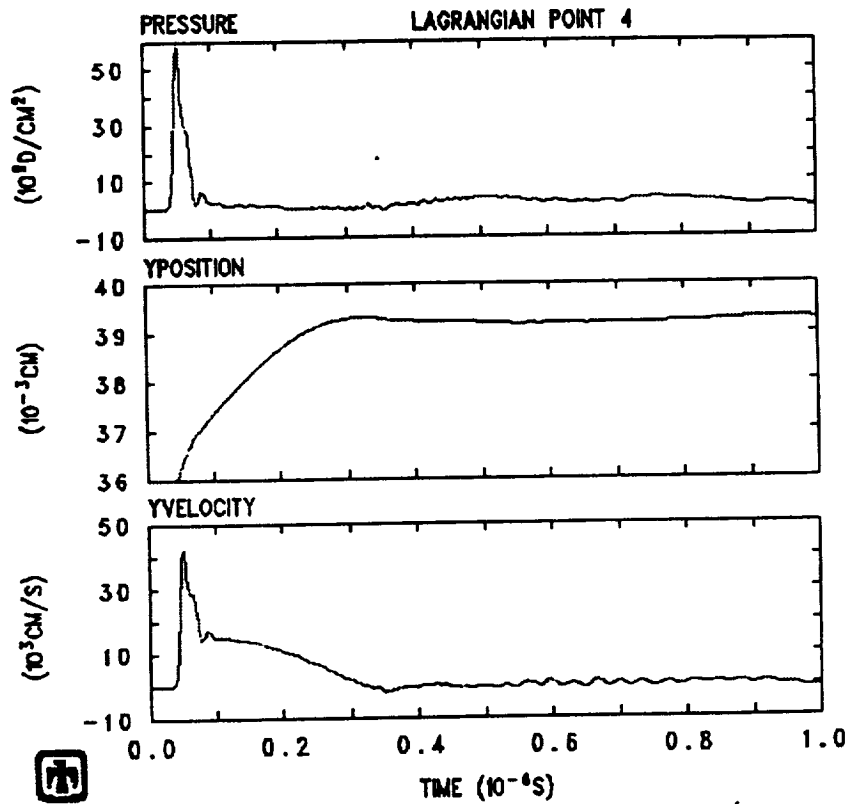
Scaling Low Study Aluminum Impactor on Aluminum Plate 10 km/s
LCJCP 12/03/92 10:08:51 CTH

Figure 29.



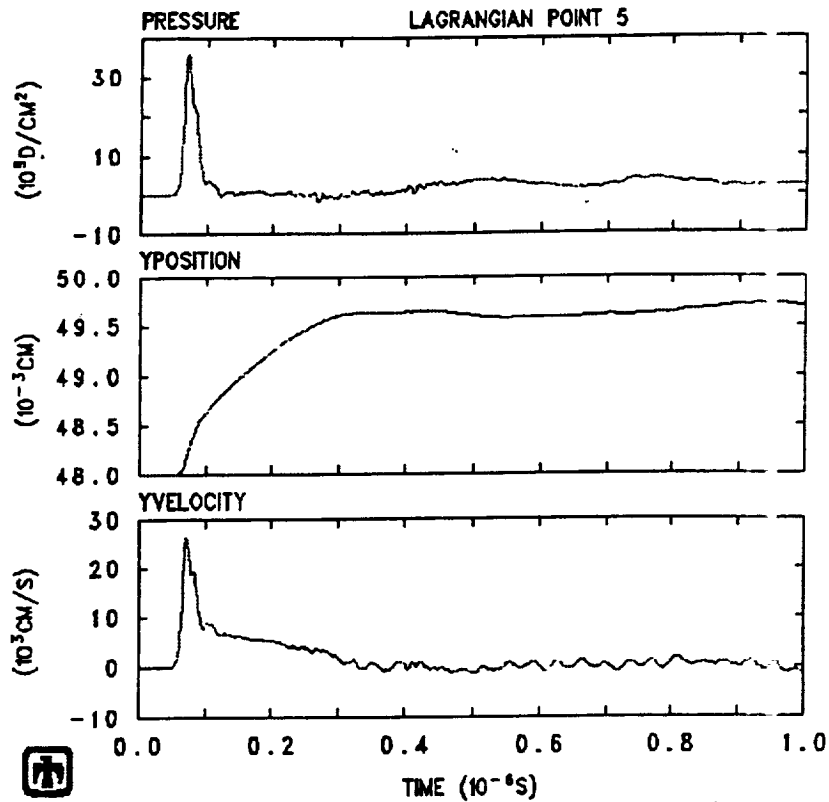
Scaling Low Study Aluminum Impactor on Aluminum Plate 10 km/s
LCJCPL 12/03/92 10:08:51 CTH

Figure 30.



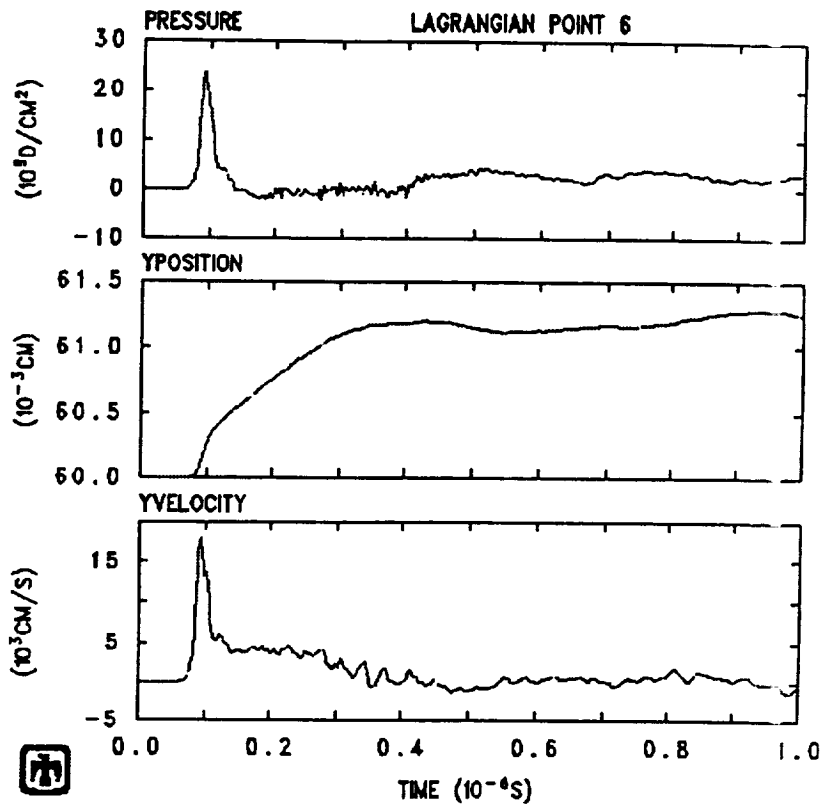
Scaling Low Study Aluminum Impactor on Aluminum Plate 10 km/s
LCJCPL 12/03/92 10:08:51 CTH

Figure 31.



Scaling Law Study Aluminum Impactor on Aluminum Plate 10 km/s
LCJCPL 12/03/92 10:08:51 CTH

Figure 32.



Scaling Law Study Aluminum Impactor on Aluminum Plate 10 km/s
LCJCPL 12/03/92 10:08:51 CTH

Figure 33. CTH Data Showing How P/dp Varies With Projectile Density and Velocity for Al into TFE Teflon

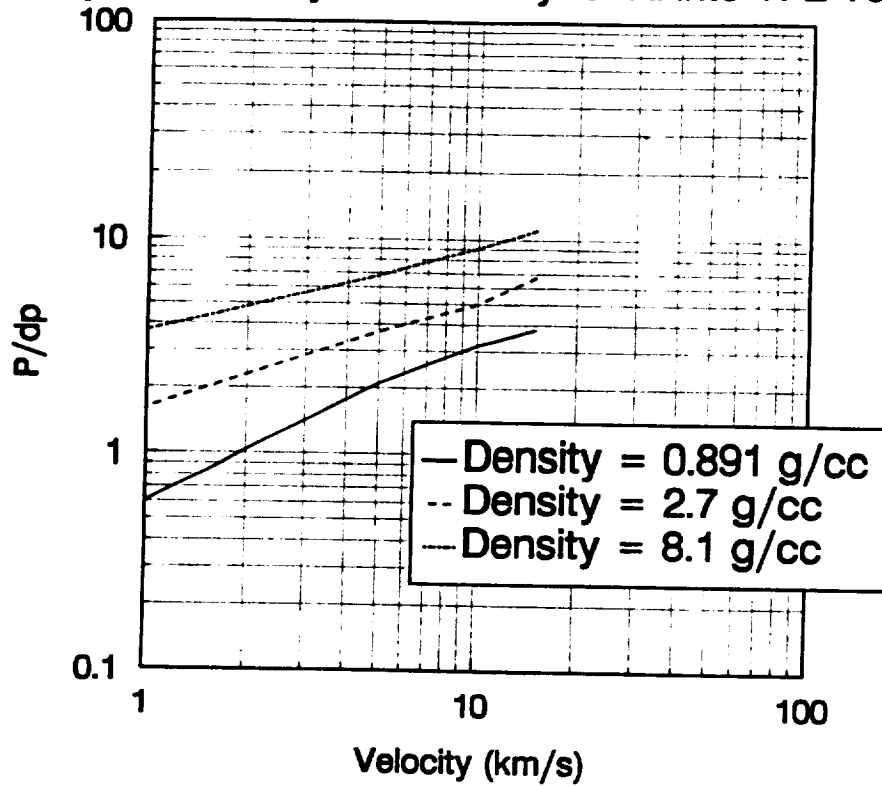


Figure 34. CTH Data Showing How dc/dp Varies With Projectile Density and Velocity for Al into TFE Teflon

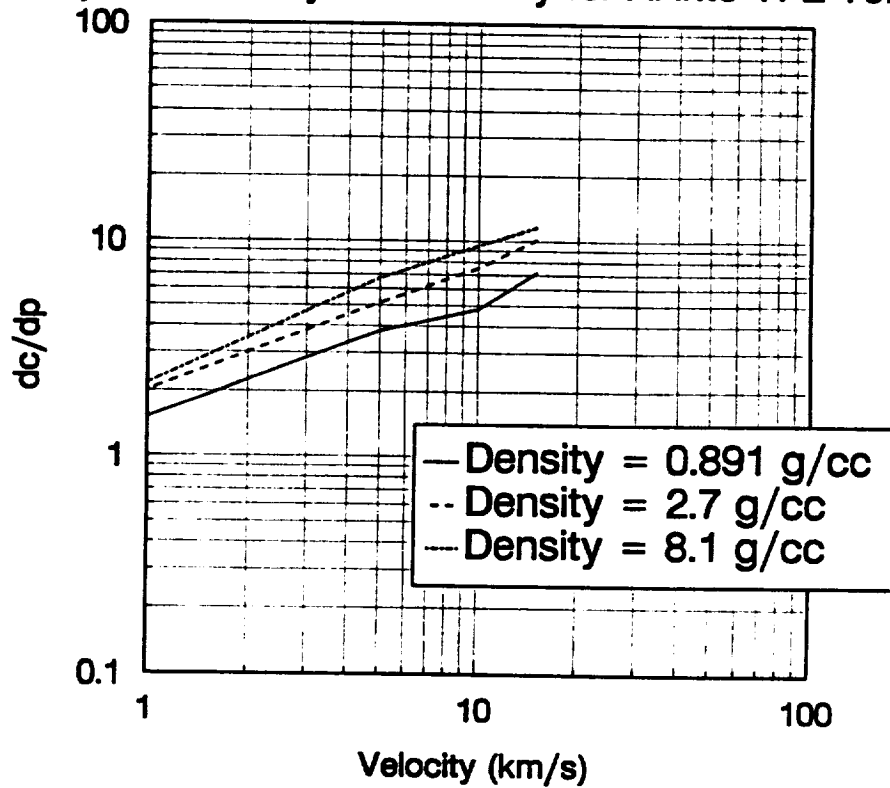


Figure 35. CTH Data Showing How P/dp Varies With Target Yield Strength and Projectile Velocity For Al into TFE Teflon

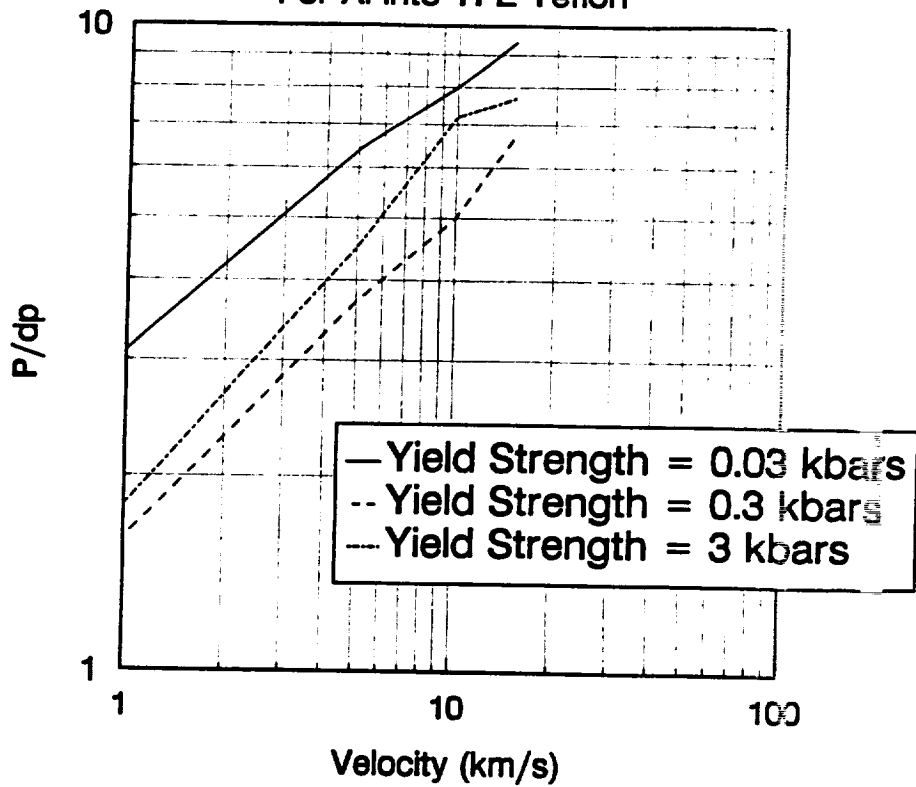


Figure 36. CTH Data Showing How dc/dp Varies With Target Yield Strength and Projectile Velocity For Al into TFE Teflon

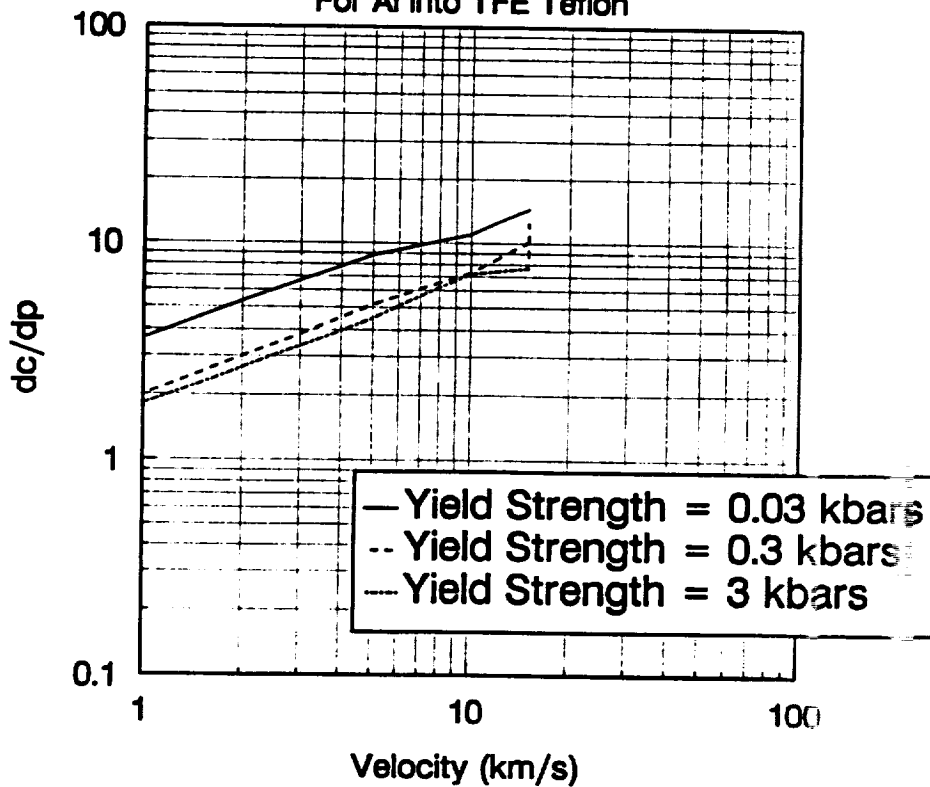


Figure 37. CTH Data Showing How P/dp Varies With Projectile Density and Velocity for Al into TFE Teflon

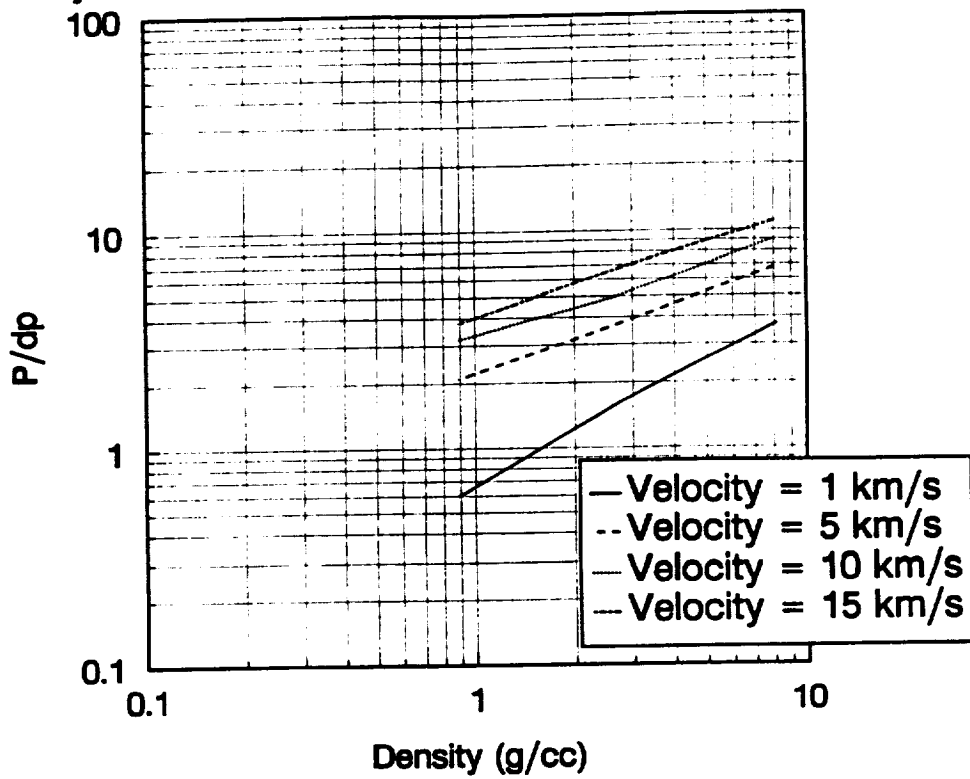


Figure 38. CTH Data Showing How dc/dp Varies With Projectile Density and Velocity for Al into TFE Teflon

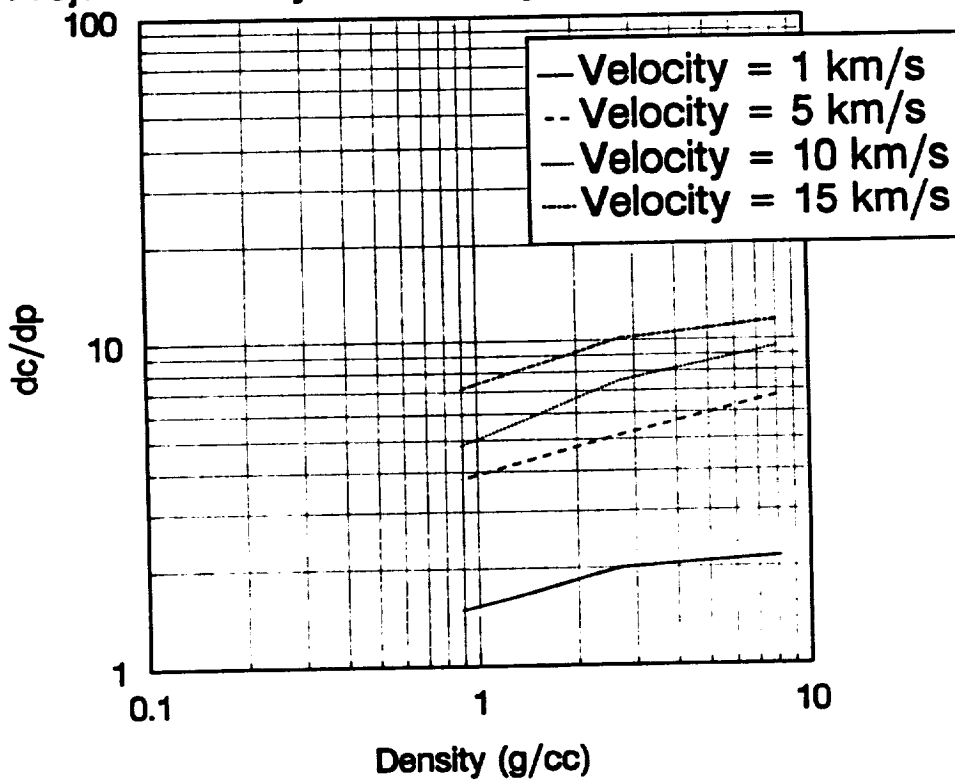


Figure 39. Plot of CTH Results Showing How P/dp Varies With Target Yield Strength and Projectile Velocity For Al into TFE Teflon

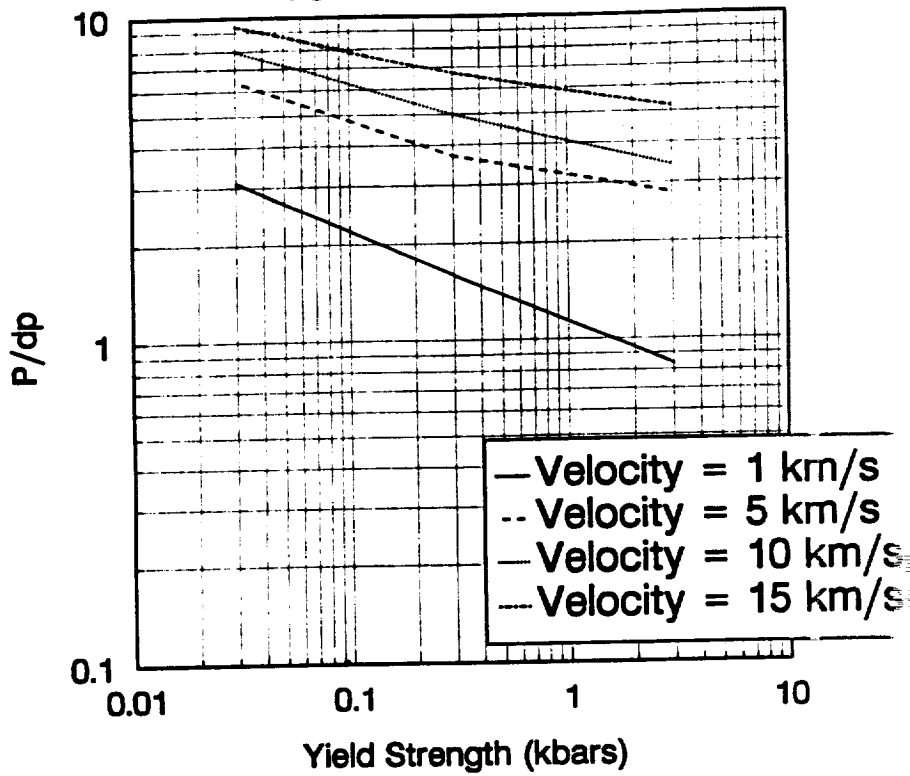


Figure 40. CTH Data Showing How dc/dp Varies With Target Yield Strength and Projectile Velocity For Al into TFE Teflon

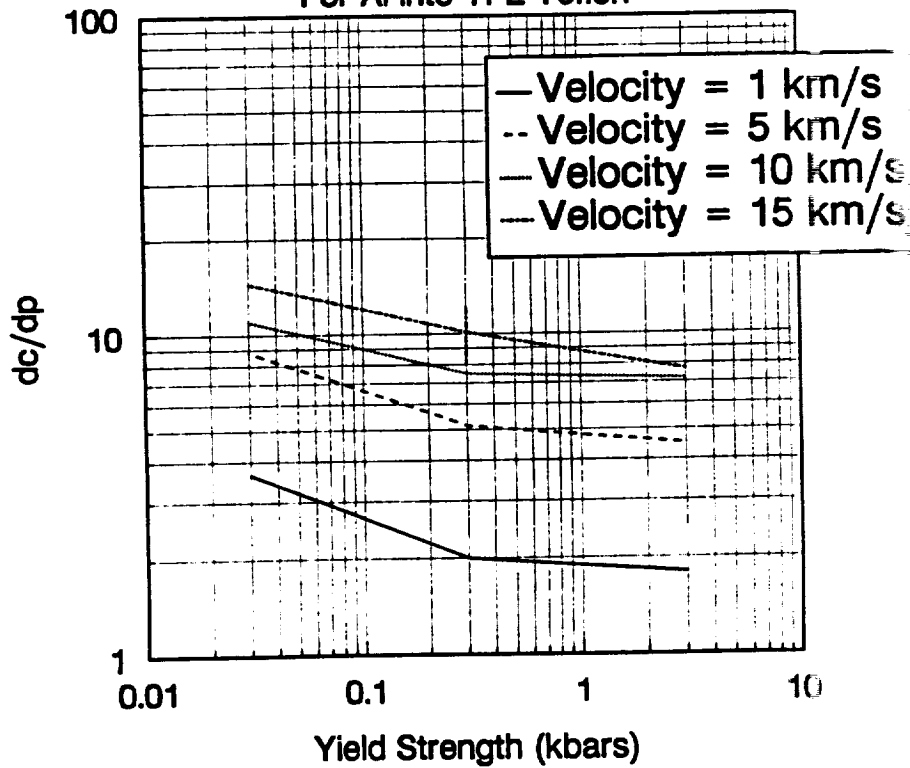


Figure 41. CTH Data Showing How P/dc Varies With Projectile Density and Velocity for Al into TFE Teflon

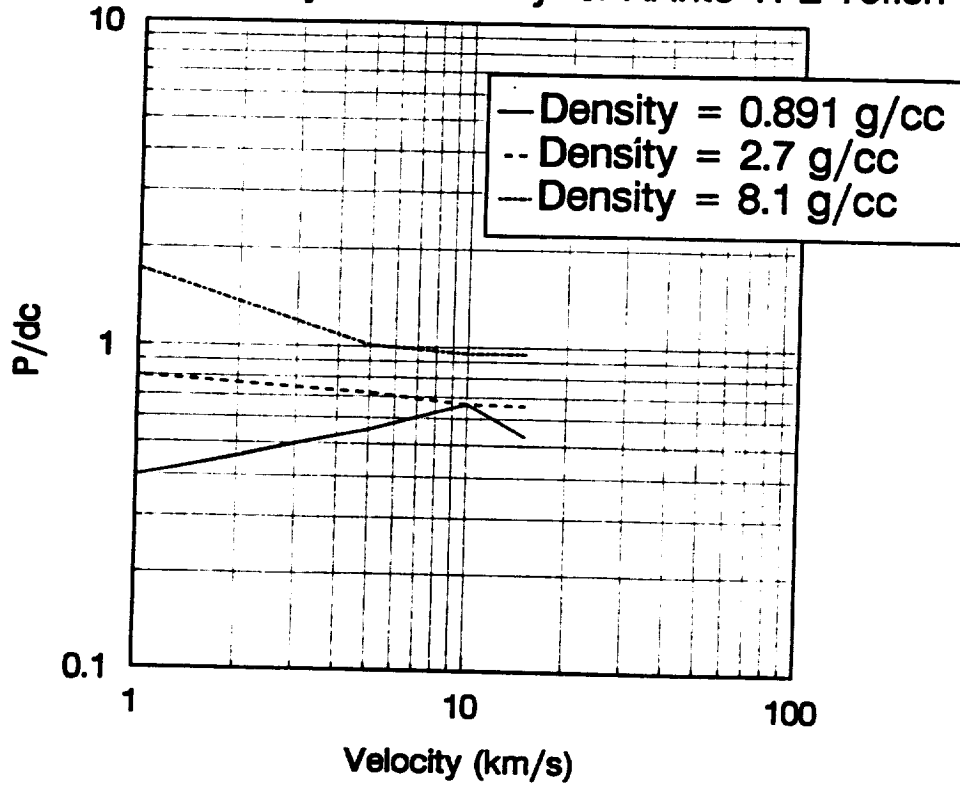


Figure 42. CTH Data Showing How P/dc Varies With Target Yield Strength and Projectile Velocity For Al into TFE Teflon

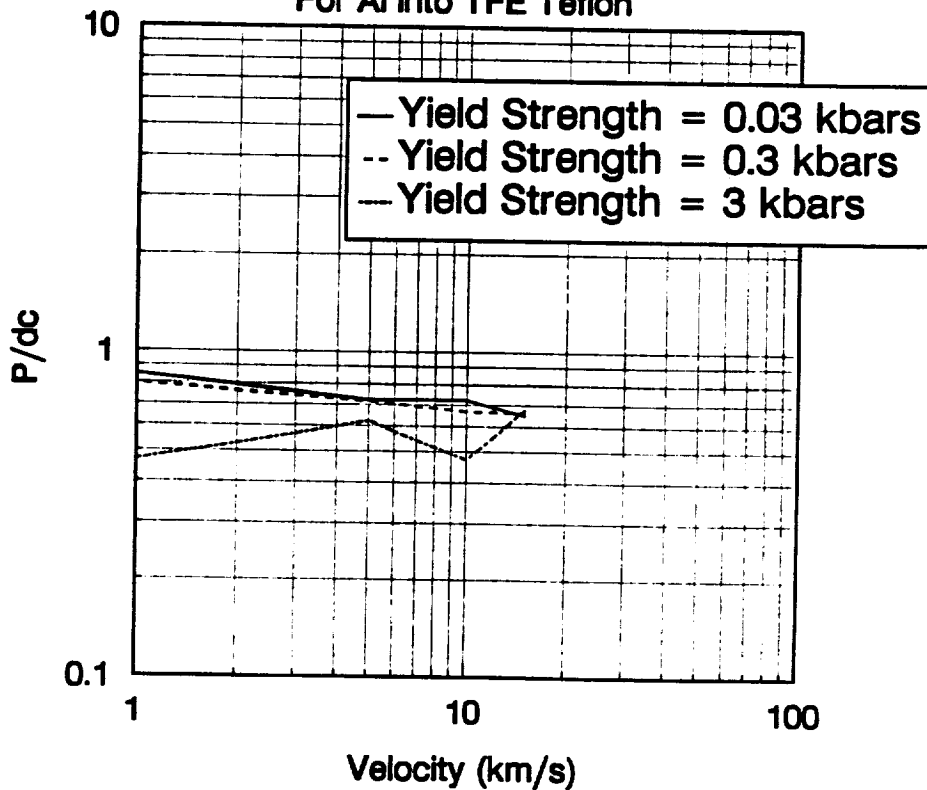


Figure 43.

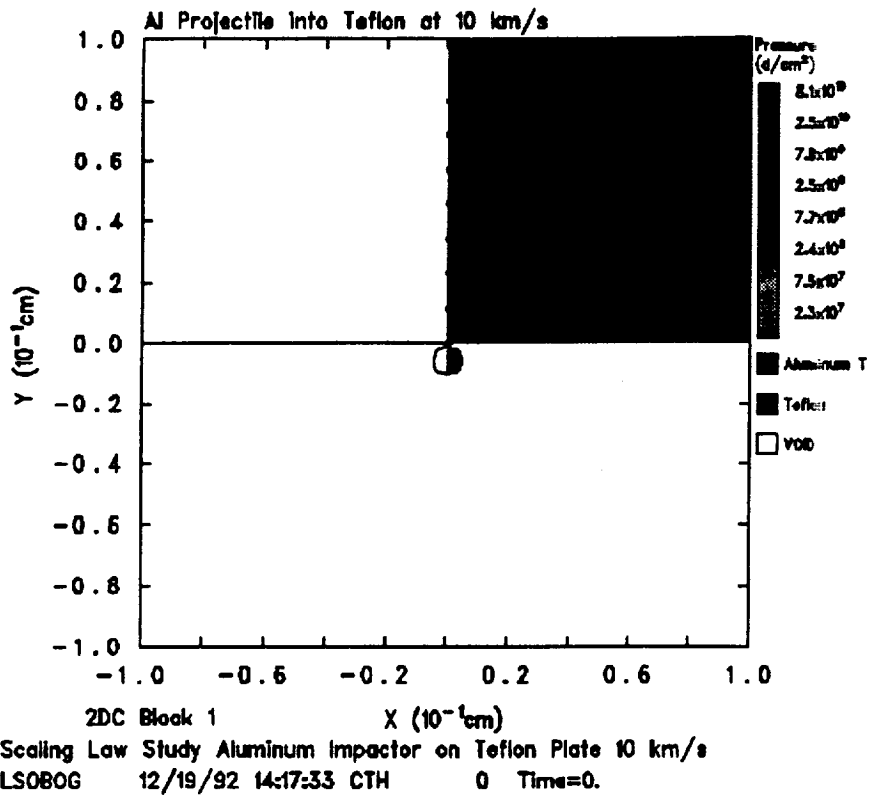


Figure 44.

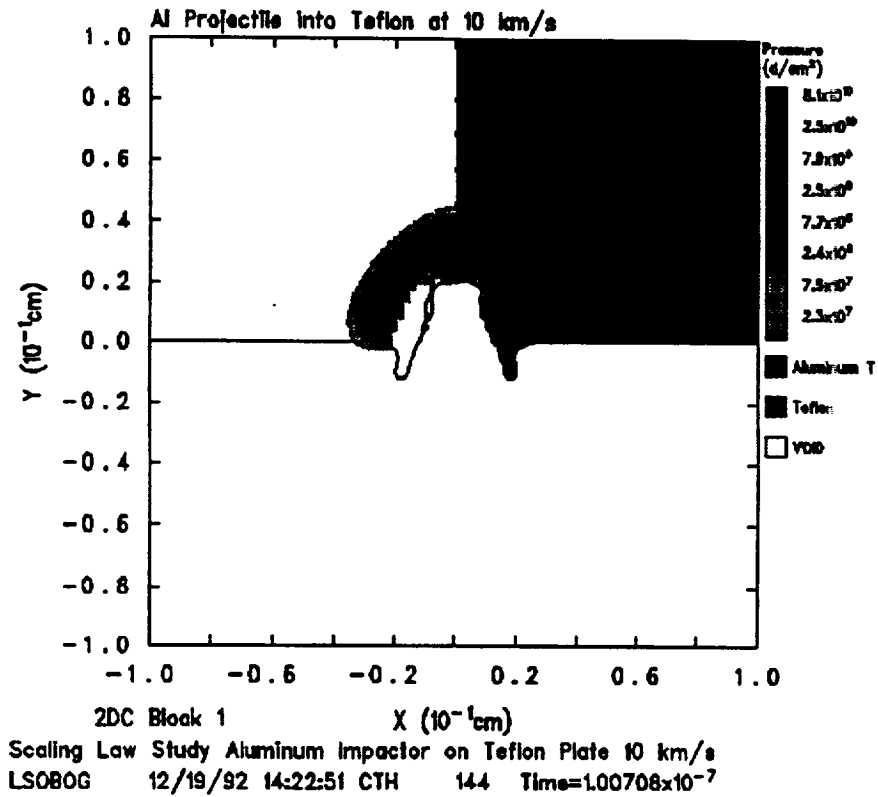
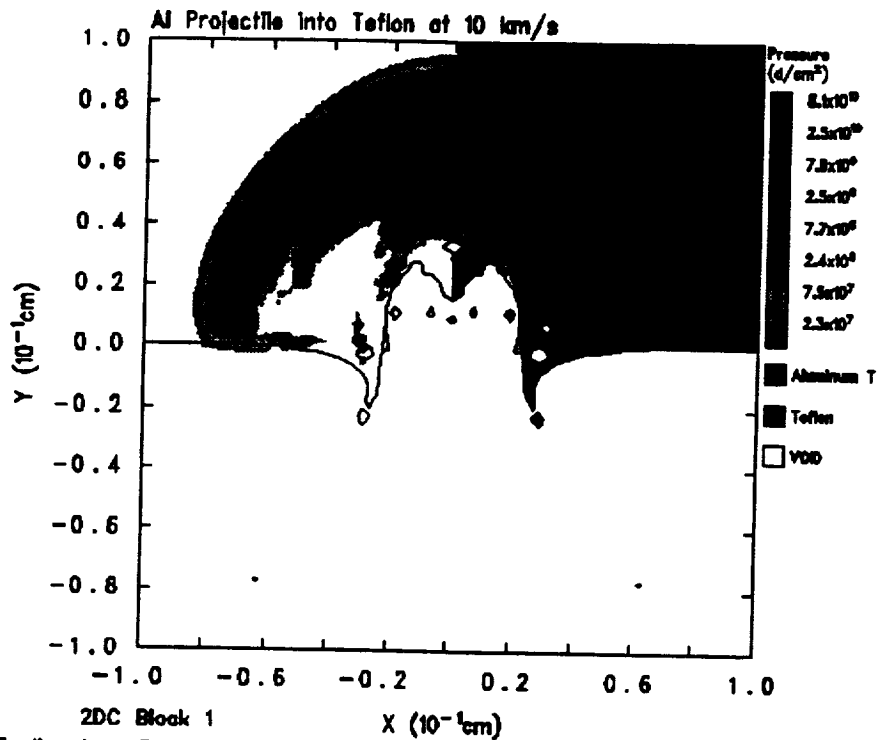
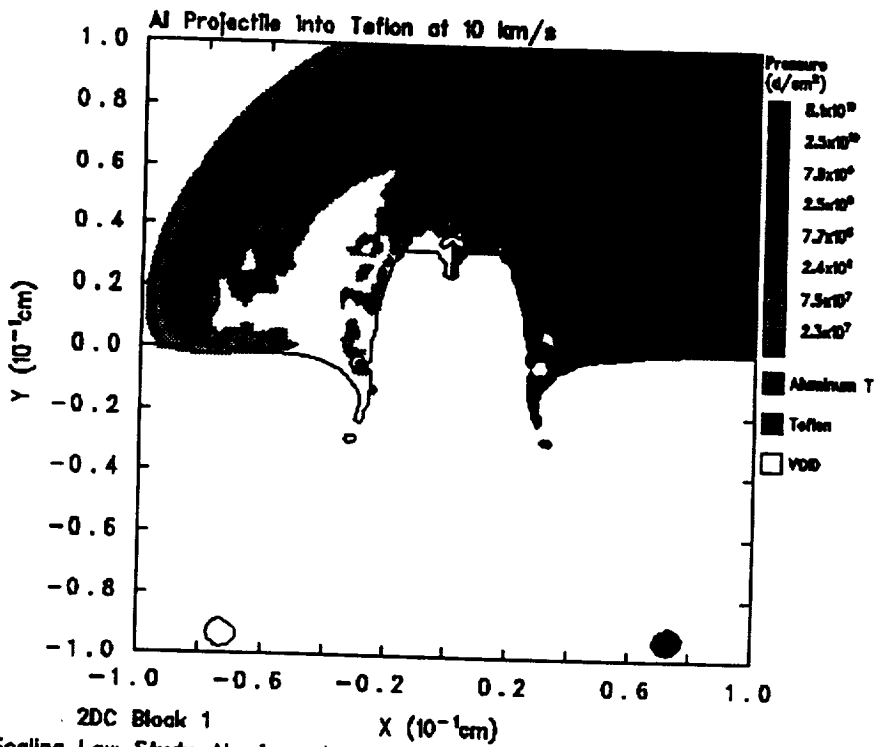


Figure 45.



2DC Block 1
Scaling Law Study Aluminum Impactor on Teflon Plate 10 km/s
LSOBOG 12/19/92 14:37:11 CTH 267 Time=4.0268x10⁻⁷

Figure 46.



2DC Block 1
Scaling Law Study Aluminum Impactor on Teflon Plate 10 km/s
LSOBOG 12/19/92 14:42:35 CTH 293 Time=5.00139x10⁻⁷

Figure 47.

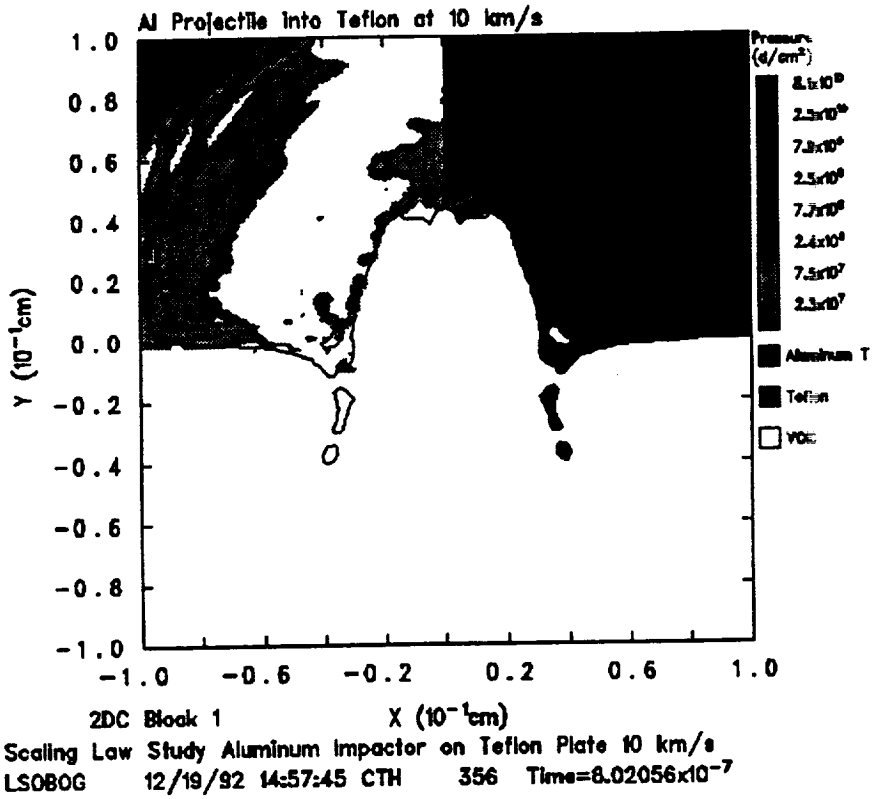


Figure 48.

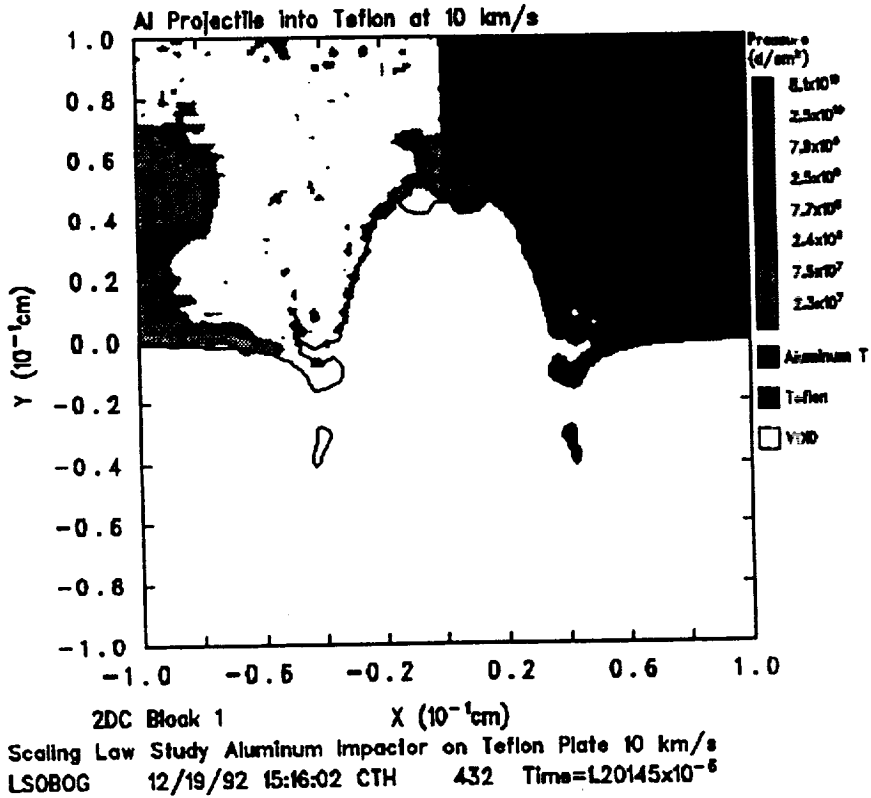


Figure 49.

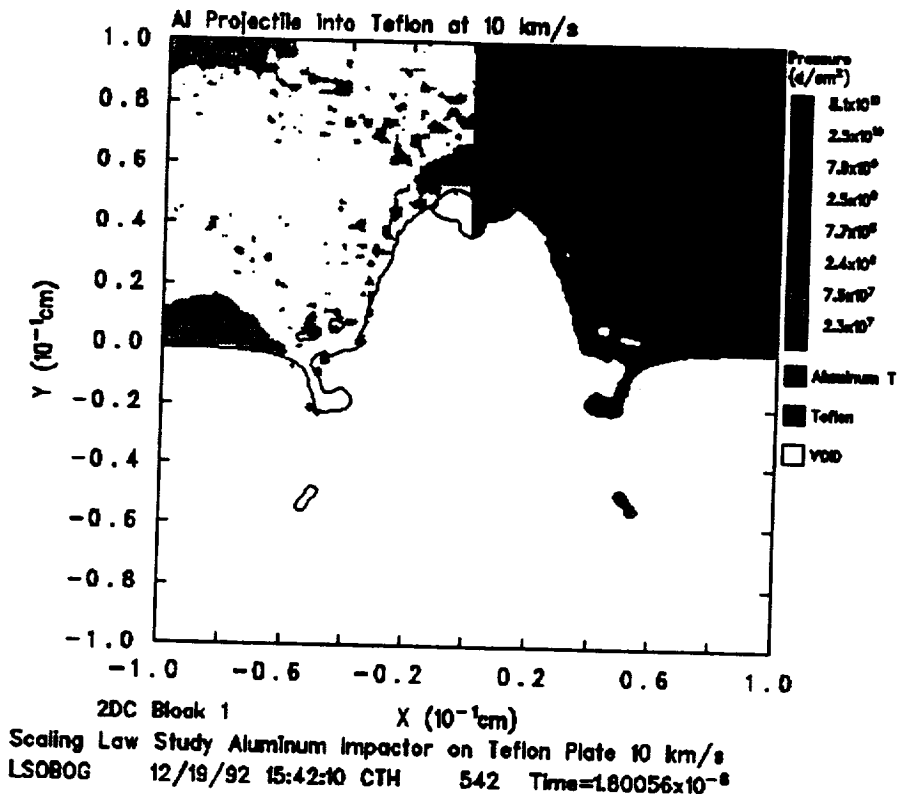


Figure 50.

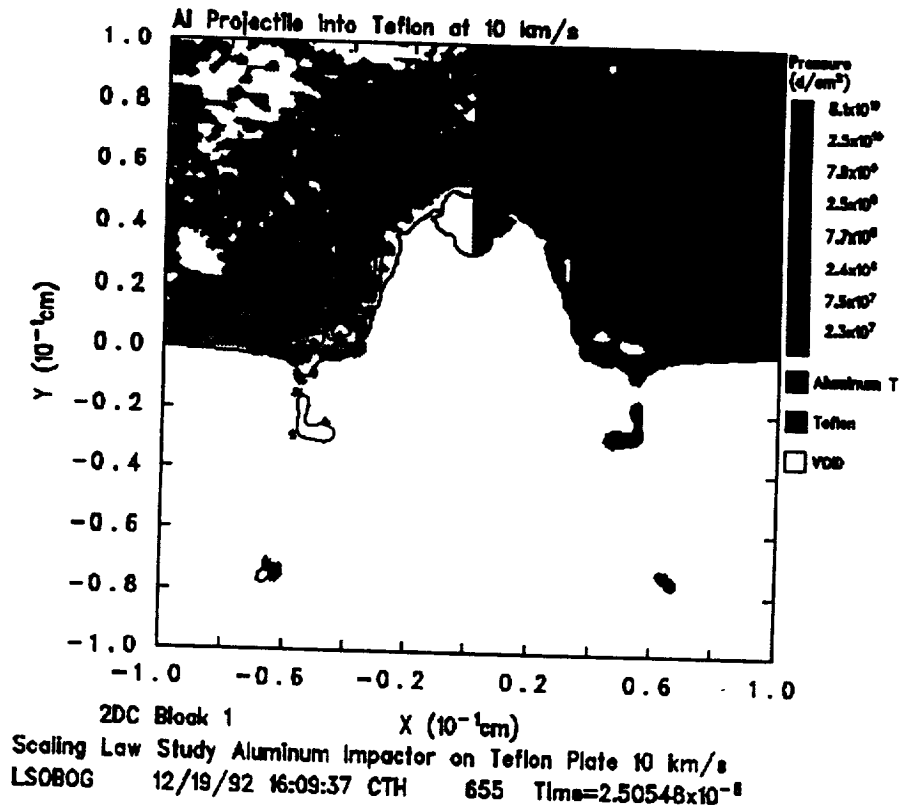


Figure 51.

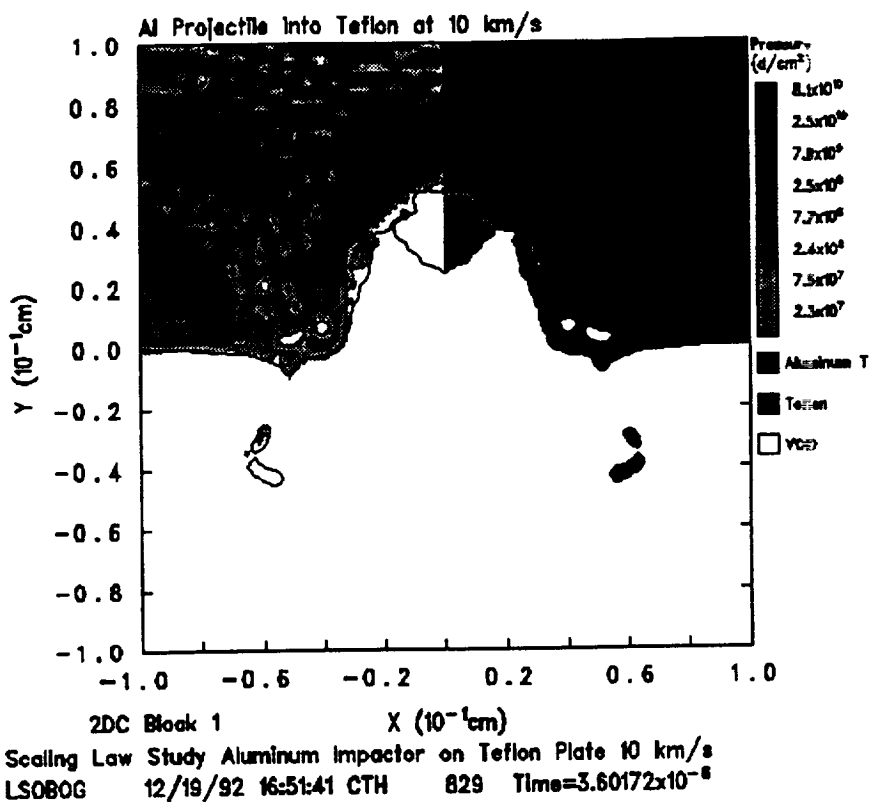


Figure 52. Comparison of Watts' Equations with CTH Predictions for Aluminum on TFE Teflon

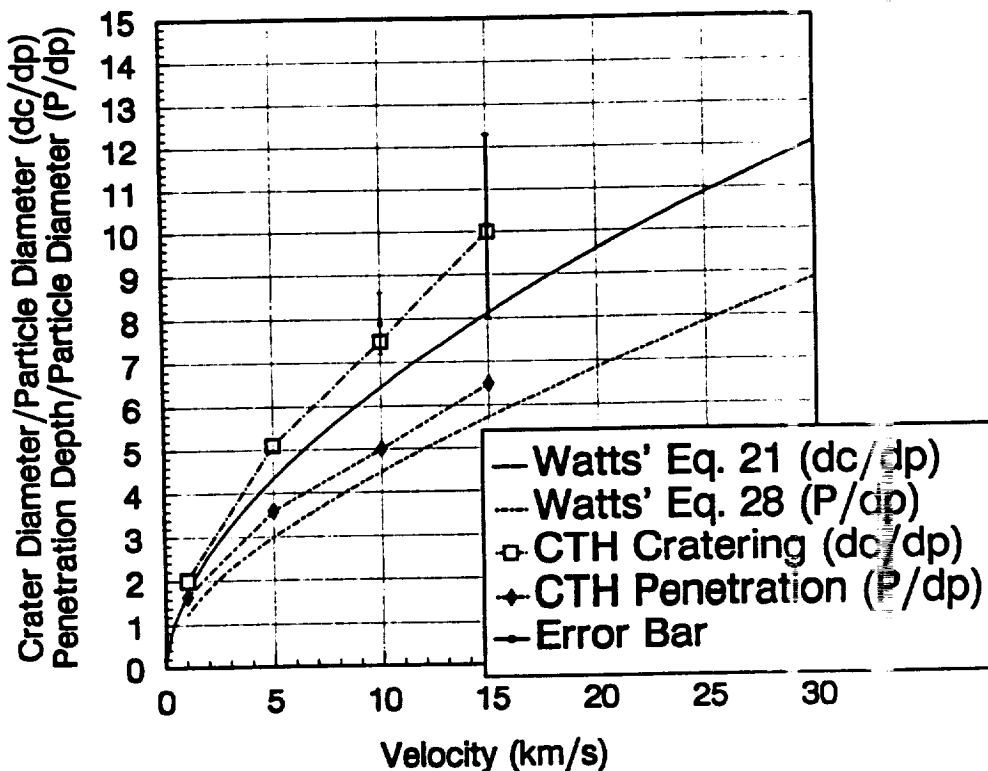
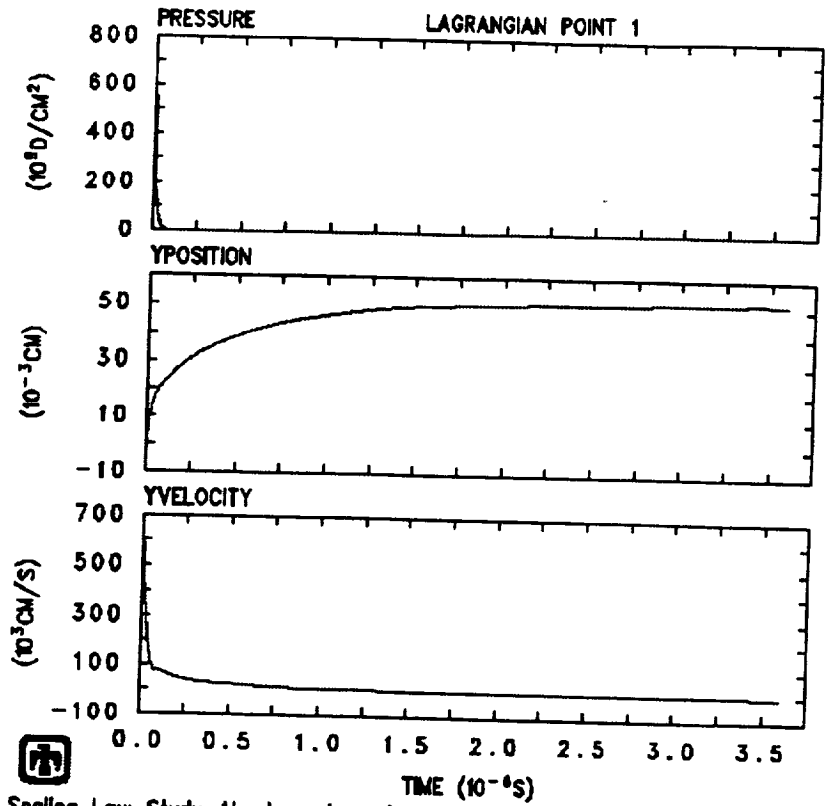
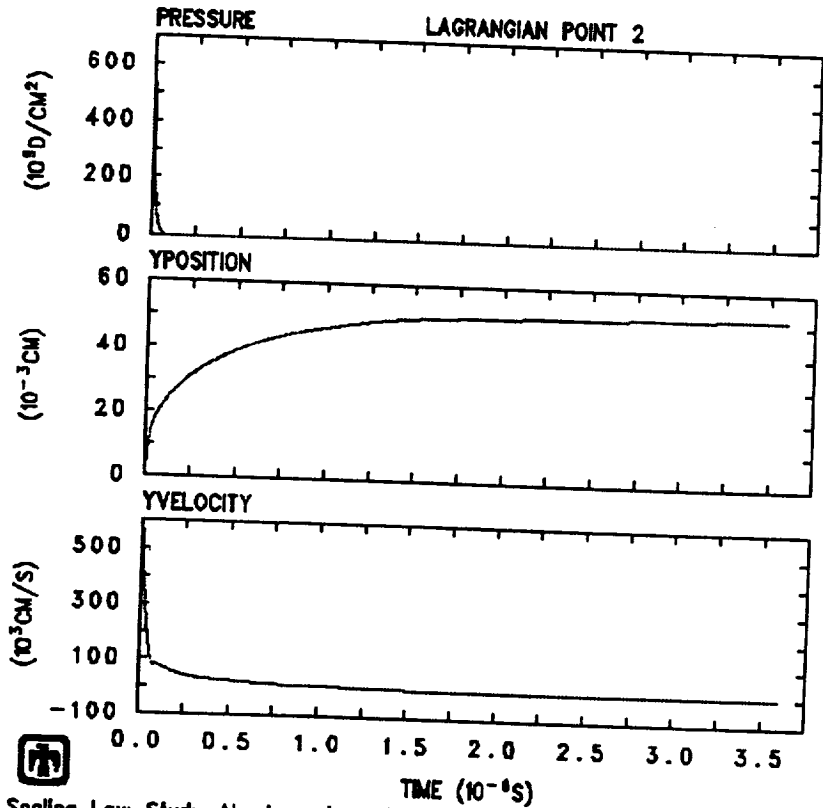


Figure 53.



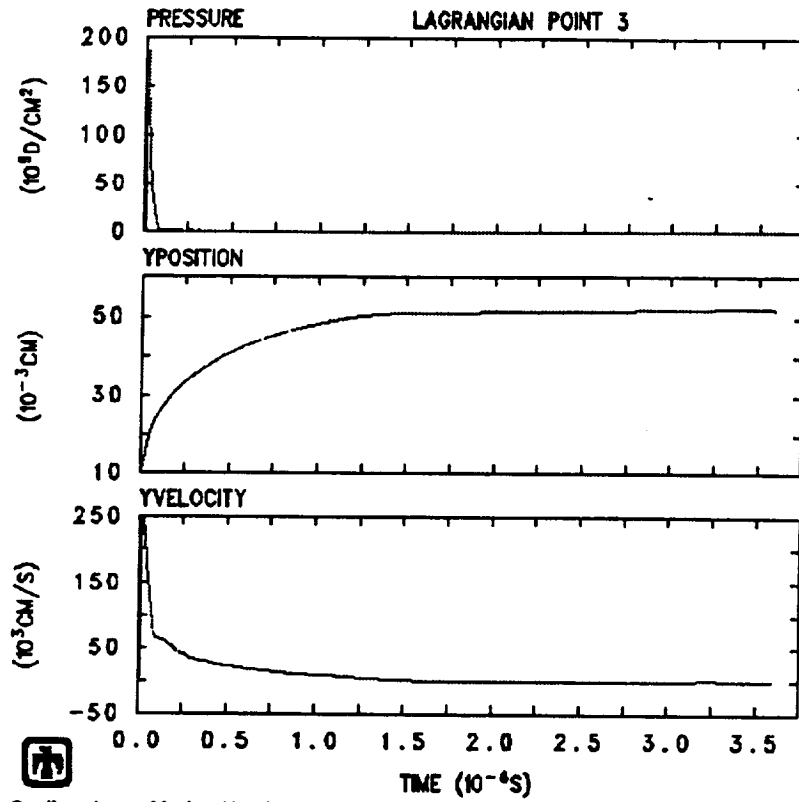
Scaling Law Study Aluminum Impactor on Teflon Plate 10 km/s
LSOBOG 12/19/92 16:51:42 CTH

Figure 54.



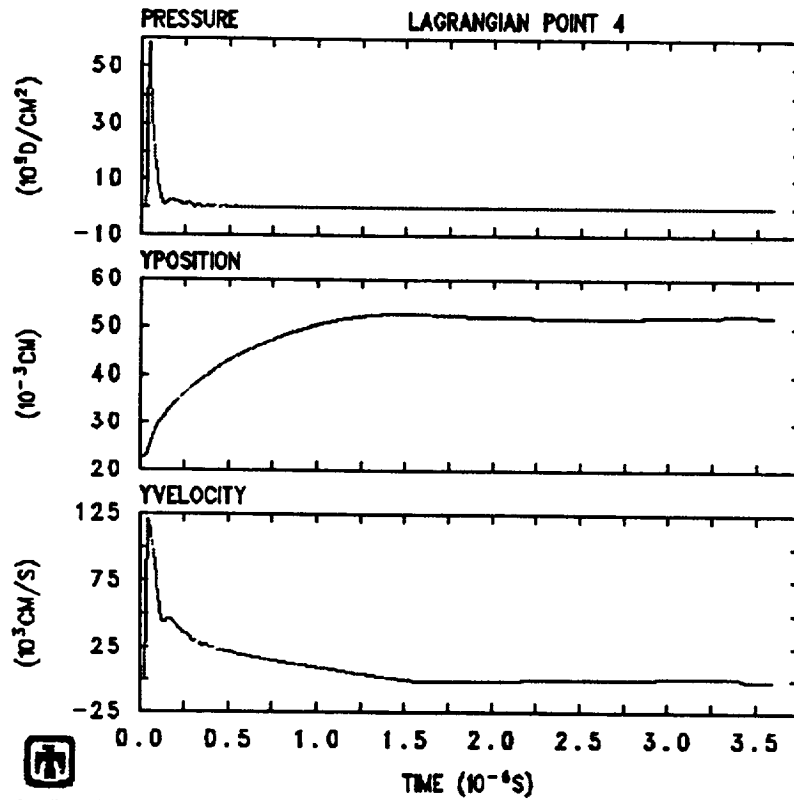
Scaling Law Study Aluminum Impactor on Teflon Plate 10 km/s
LSOBOG 12/19/92 16:51:42 CTH

Figure 55.



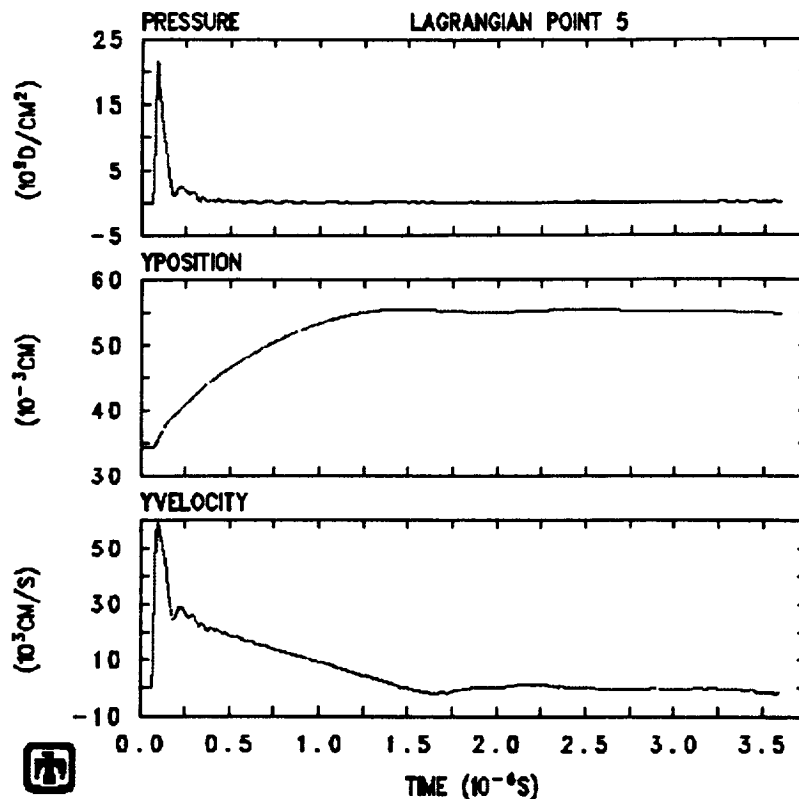
Scaling Law Study Aluminum Impactor on Teflon Plate 10 km/s
LSOBG 12/19/92 16:51:42 CTH

Figure 56.



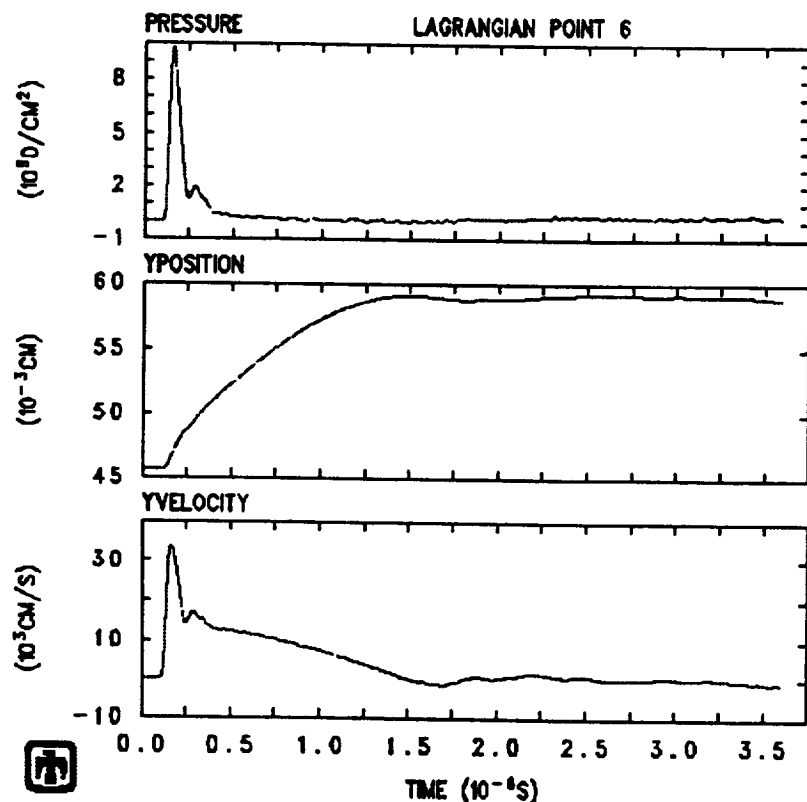
Scaling Law Study Aluminum Impactor on Teflon Plate 10 km/s
LSOBG 12/19/92 16:51:42 CTH

Figure 57.



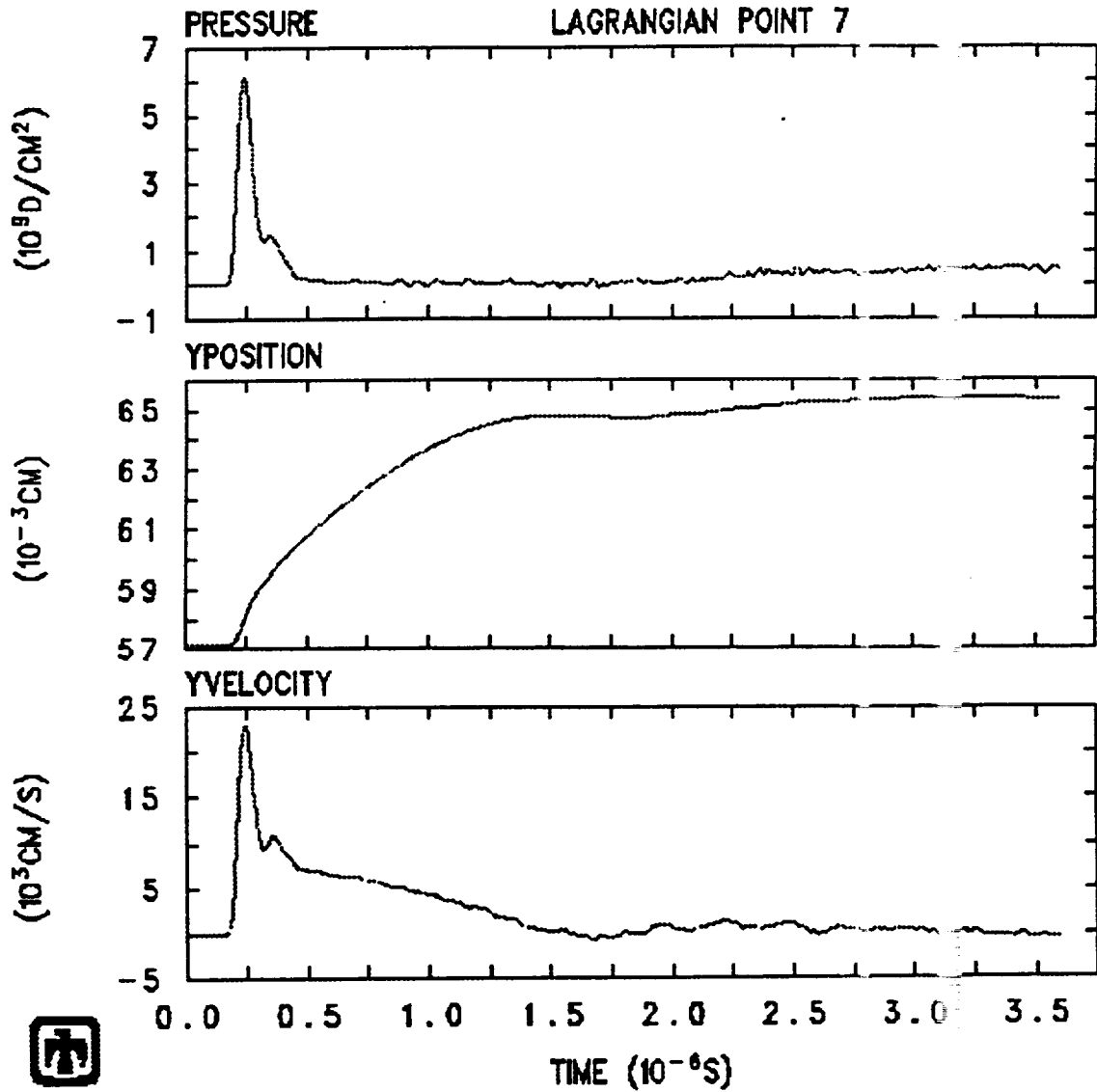
Scaling Law Study Aluminum Impactor on Teflon Plate 10 km/s
LSOBOG 12/19/92 16:51:42 CTH

Figure 58.



Scaling Law Study Aluminum Impactor on Teflon Plate 10 km/s
LSOBOG 12/19/92 16:51:42 CTH

Figure 59.



Scaling Law Study Aluminum Impactor on Teflon Plate 10 km/s
LSOBOG 12/19/92 16:51:42 CTH

Figure 60. Comparison of CTH Results versus Watts' Eq. 59 for Al into Al (6061-T6)

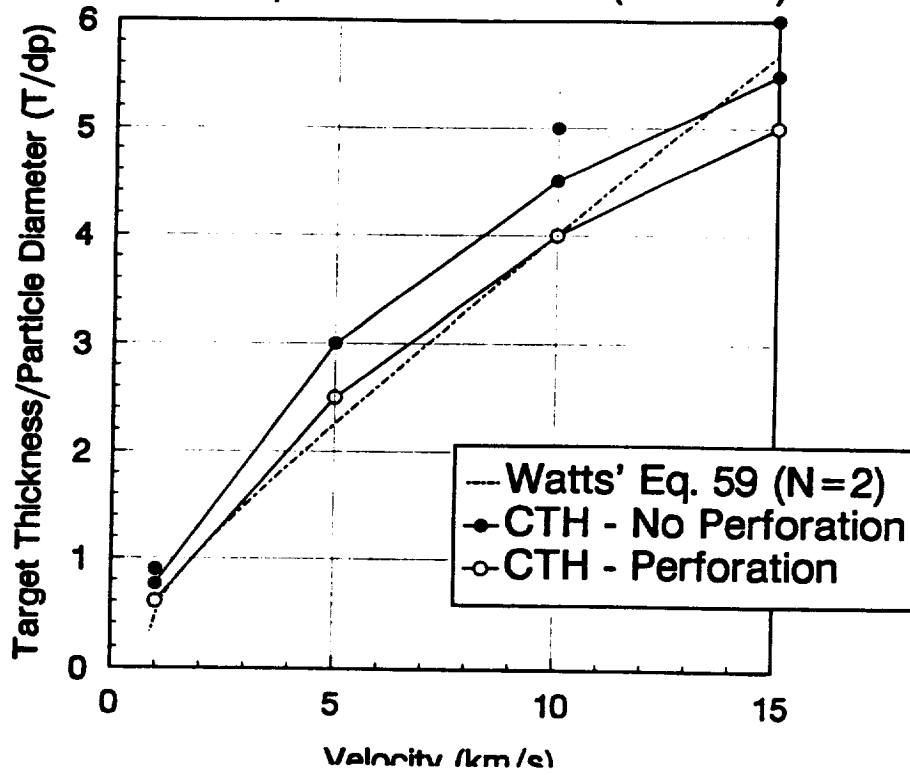


Figure 61. Comparison of CTH Results versus Watts' Eq. 59 for Al into Al (6061-T6)

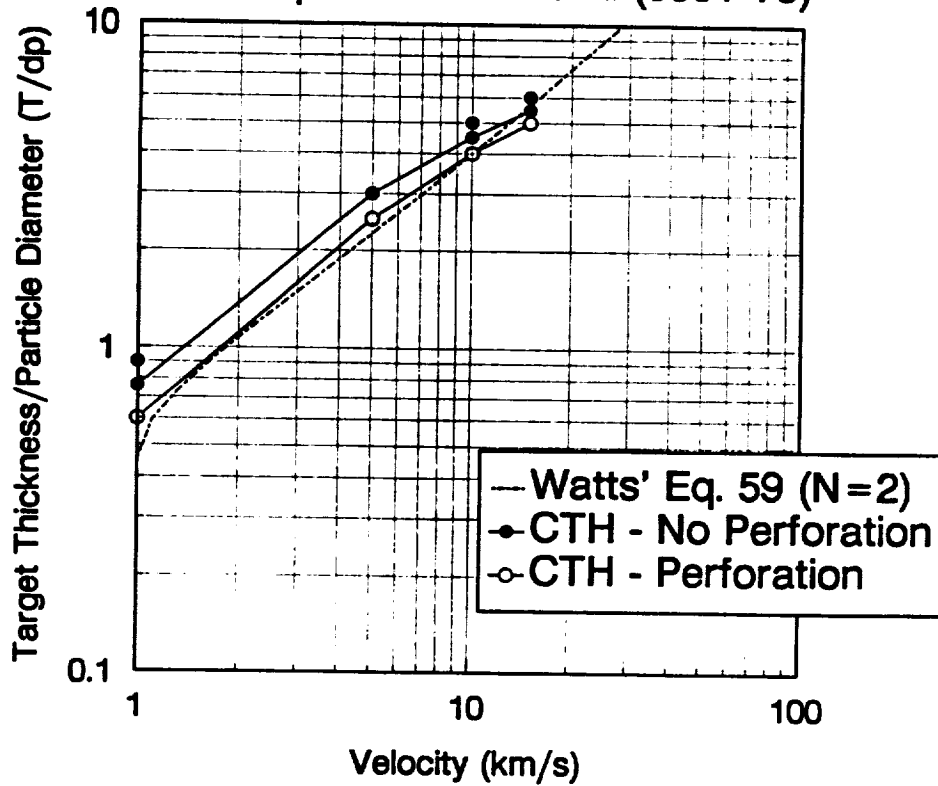


Figure 62.

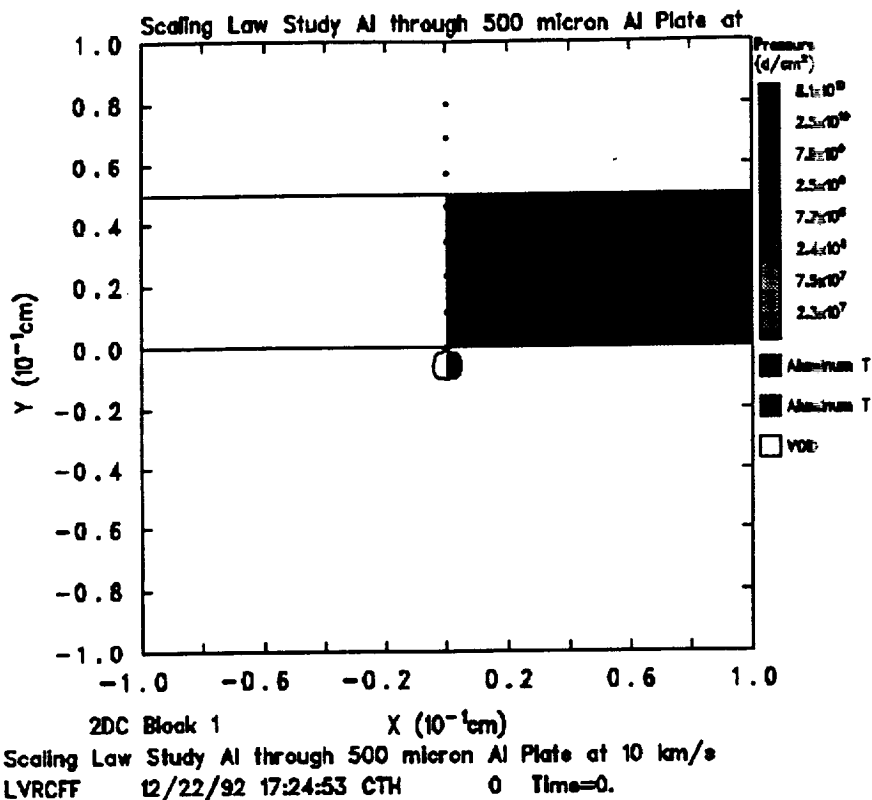


Figure 63.

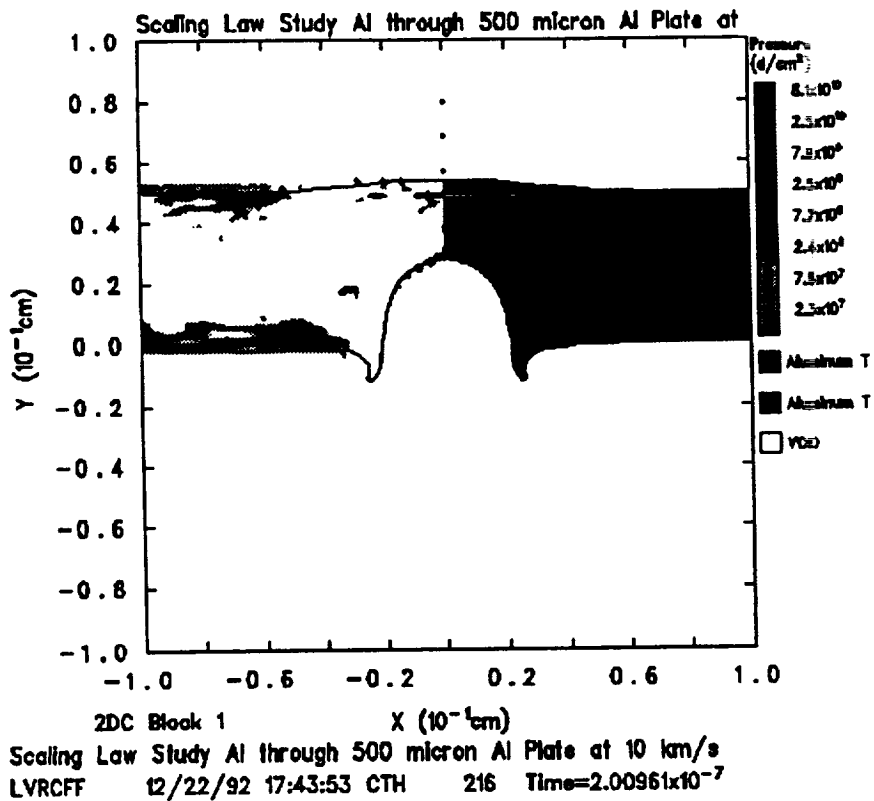


Figure 64.

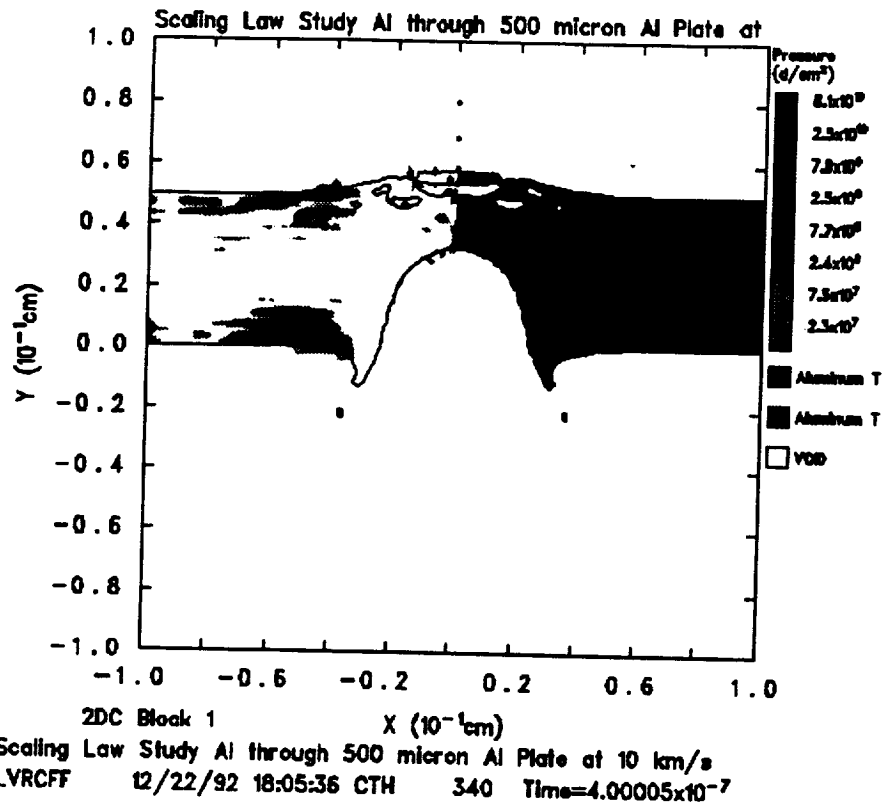


Figure 65.

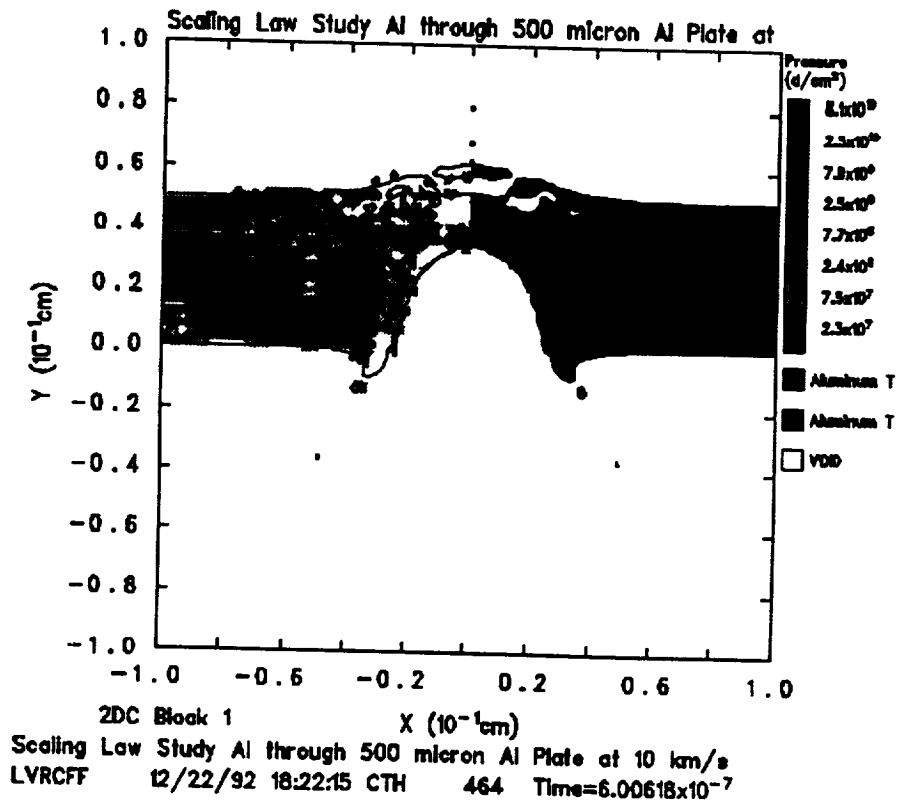


Figure 66.

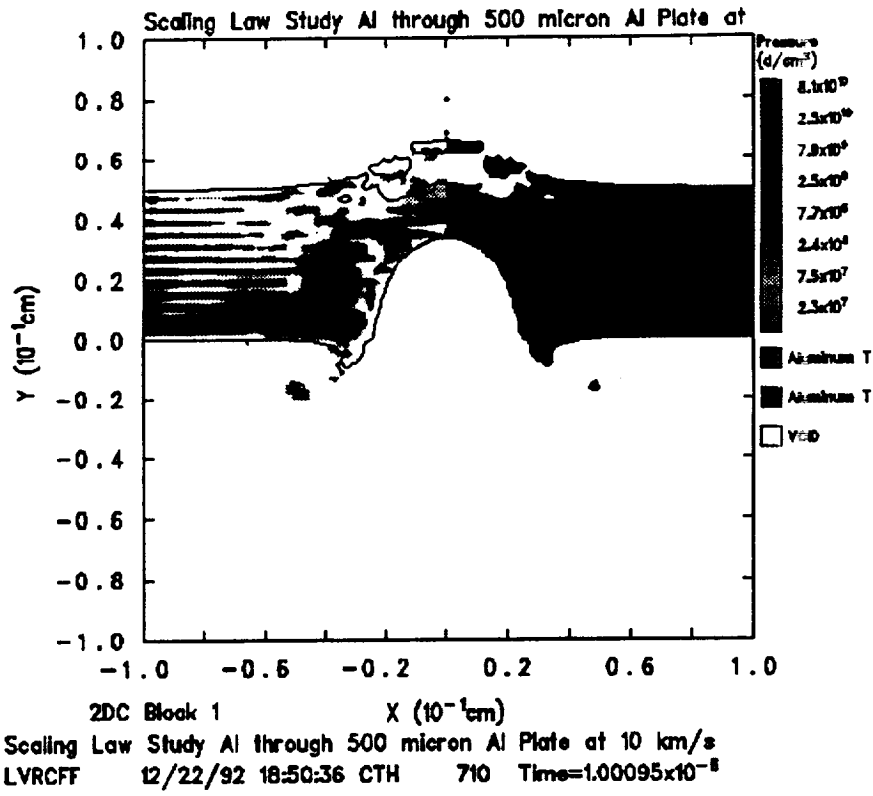


Figure 67.

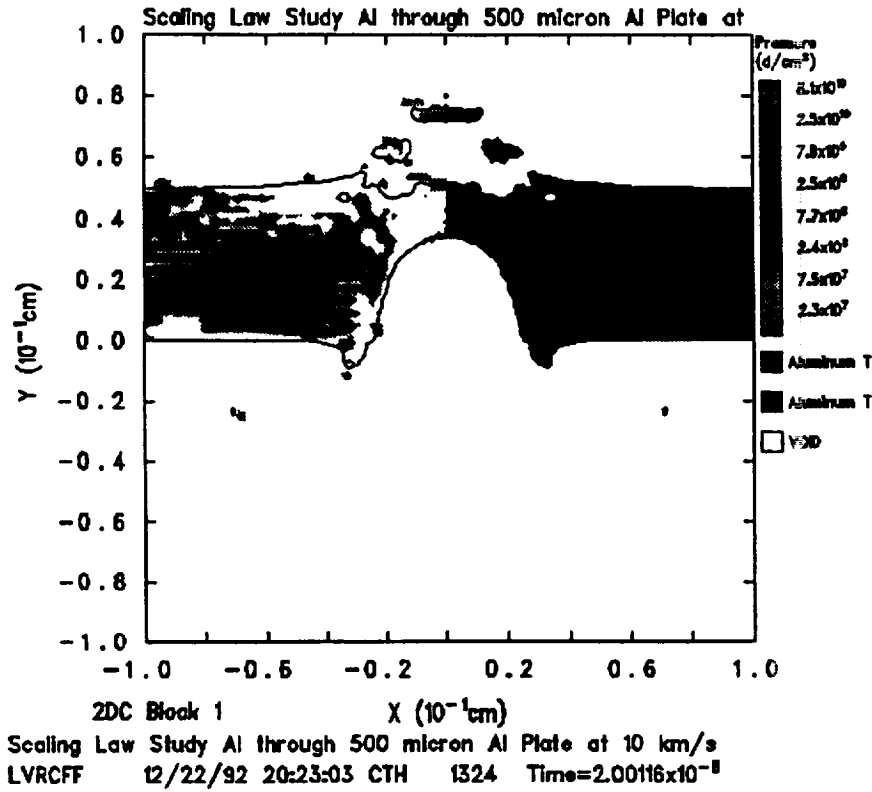
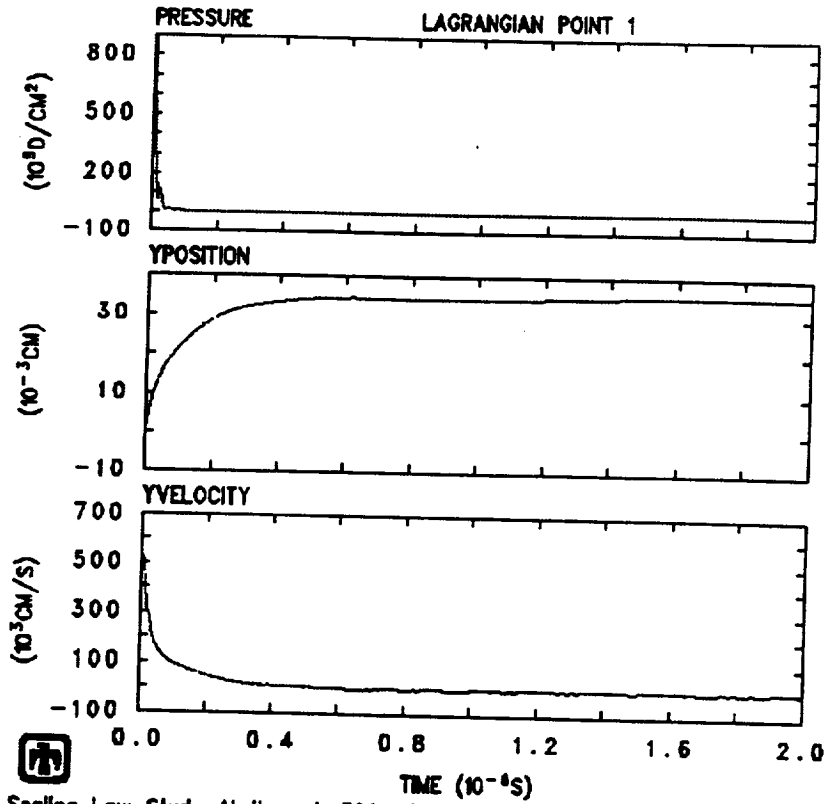
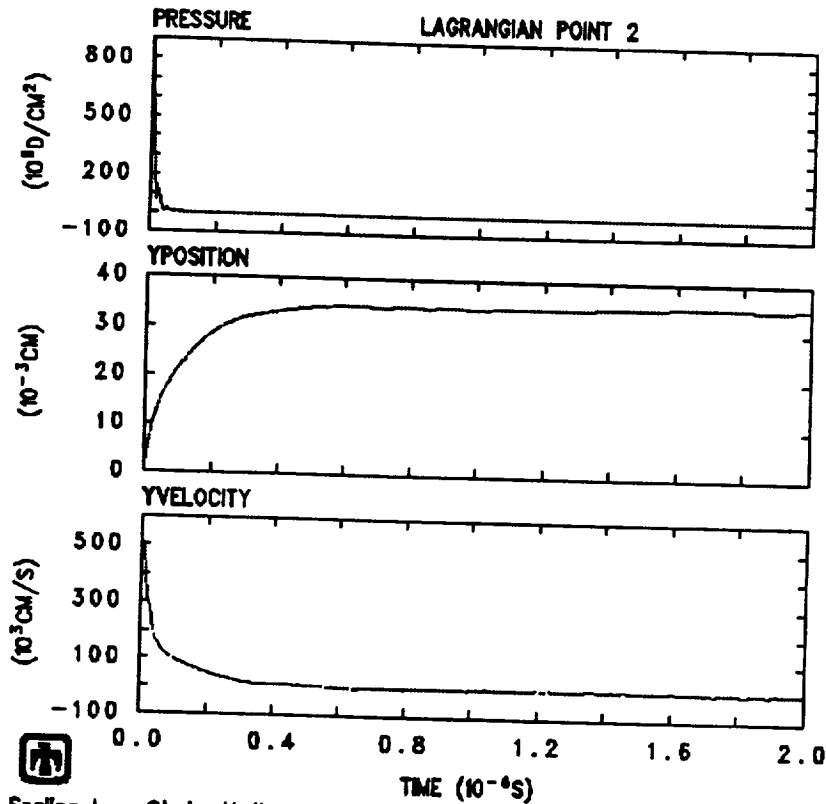


Figure 68.



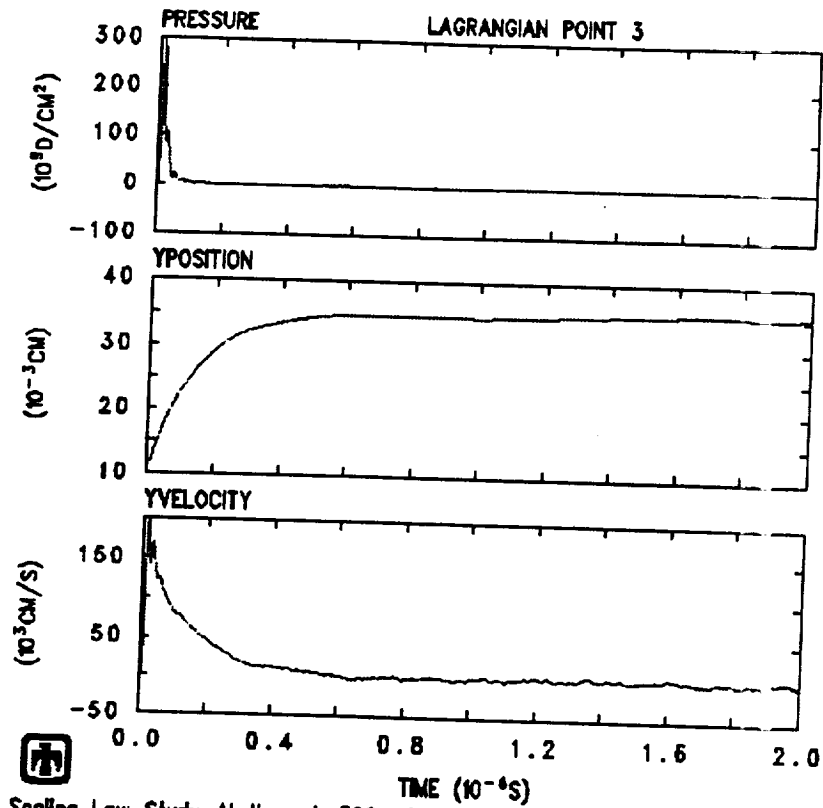
 Scalling Low Study Al through 500 micron Al Plate at 10 km/s
LVRCFF 12/22/92 20:23:04 CTH

Figure 69.



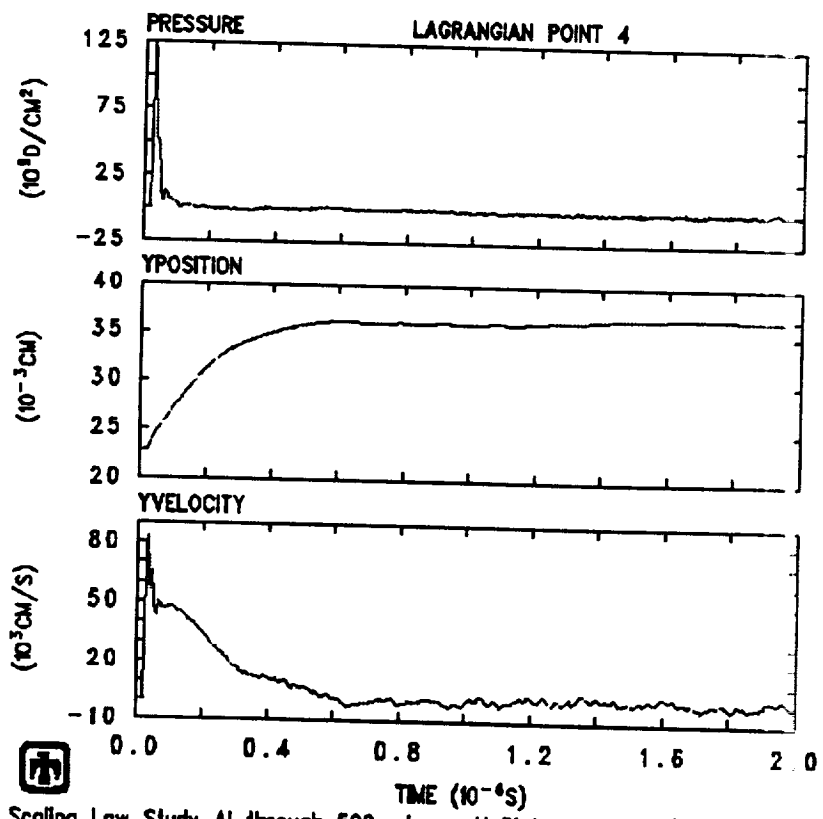
 Scalling Low Study Al through 500 micron Al Plate at 10 km/s
LVRCFF 12/22/92 20:23:04 CTH

Figure 70.



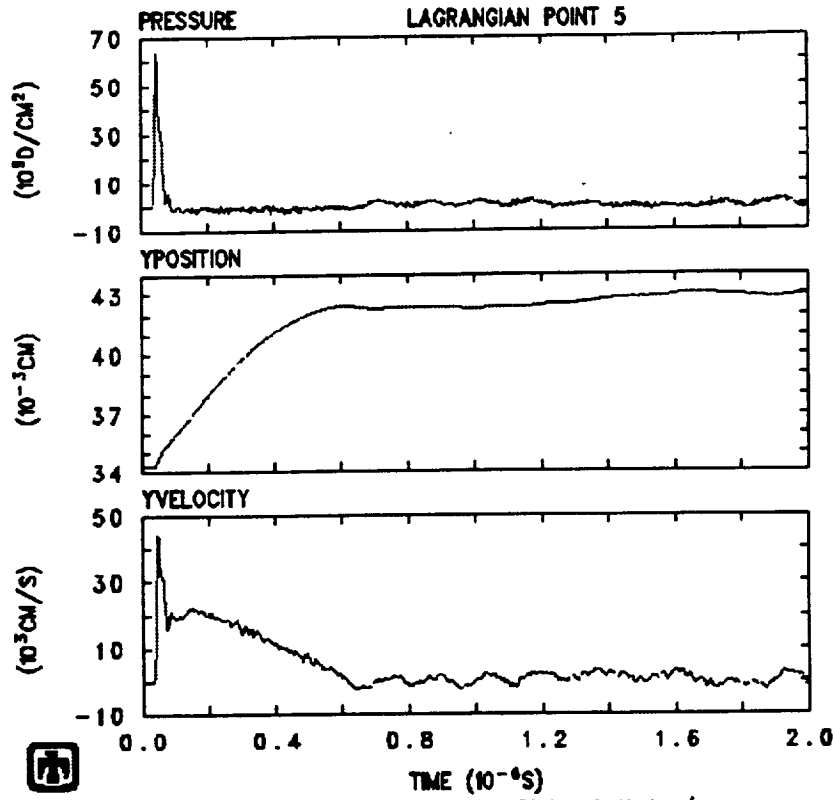
Scaling Law Study Al through 500 micron Al Plate at 10 km/s
LVRCCF 12/22/92 20:23:04 CTH

Figure 71.



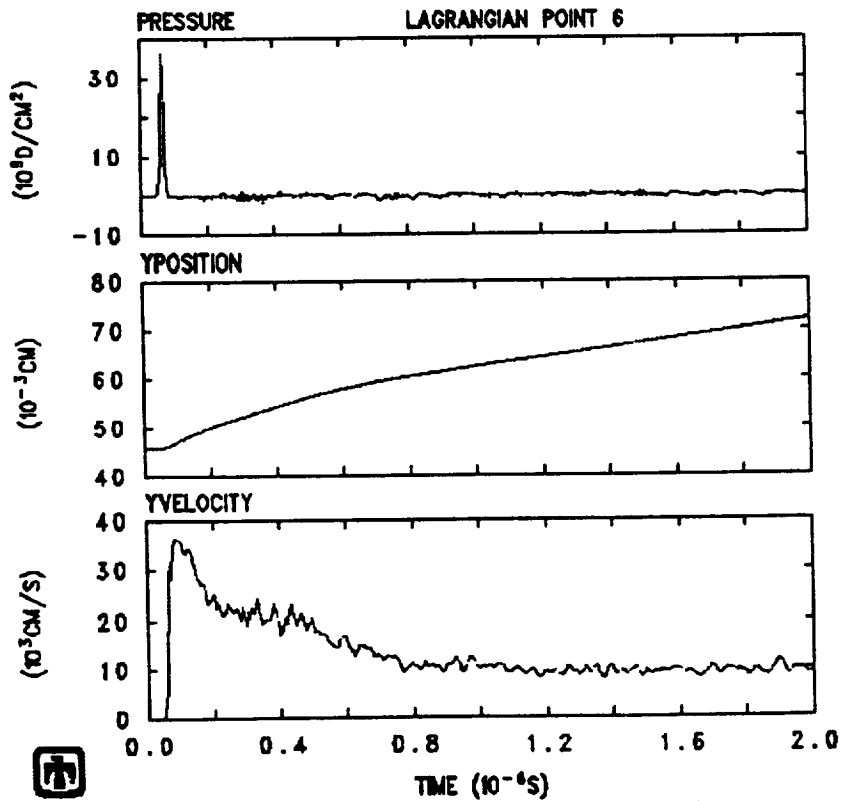
Scaling Law Study Al through 500 micron Al Plate at 10 km/s
LVRCCF 12/22/92 20:23:04 CTH

Figure 72.



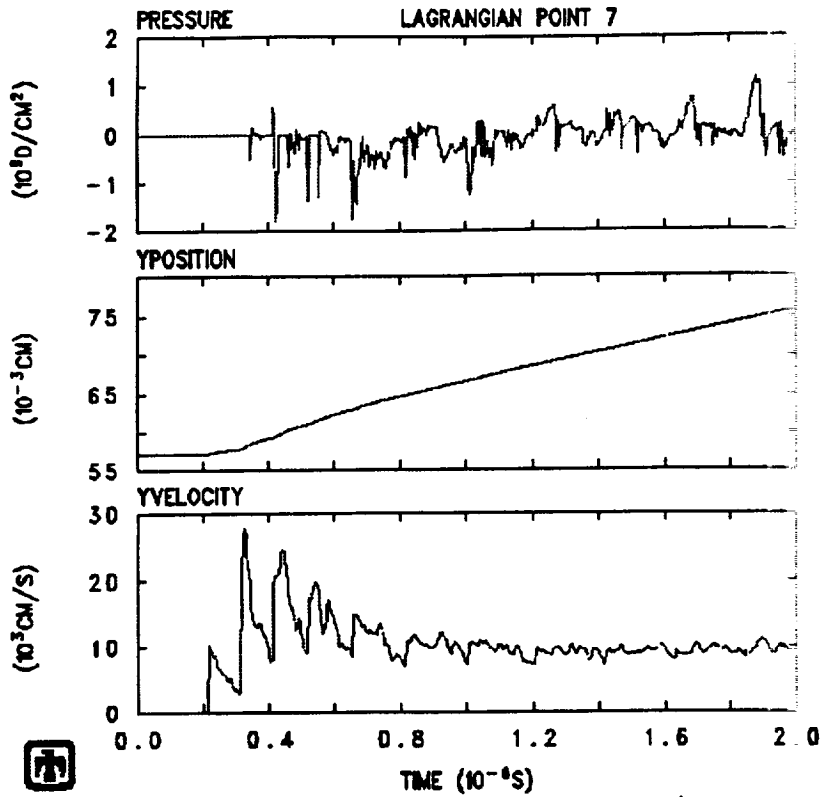
Scaling Low Study Al through 500 micron Al Plate at 10 km/s
LVRCPF 12/22/92 20:23:04 CTH

Figure 73.



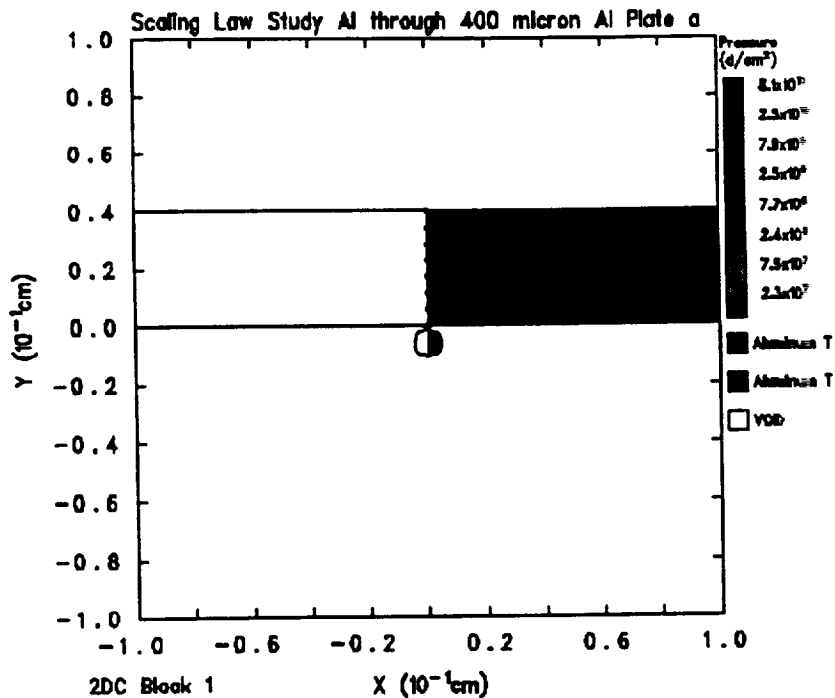
Scaling Low Study Al through 500 micron Al Plate at 10 km/s
LVRCPF 12/22/92 20:23:04 CTH

Figure 74.



Scaling Law Study Al through 500 micron Al Plate at 10 km/s
 LVRCCF 12/22/92 20:23:04 CTH

Figure 75.



2DC Block 1
 Scaling Law Study Al through 400 micron Al Plate at 10 km/s
 LVUCEE 12/22/92 20:24:26 CTH 0 Time=0.

Figure 76.

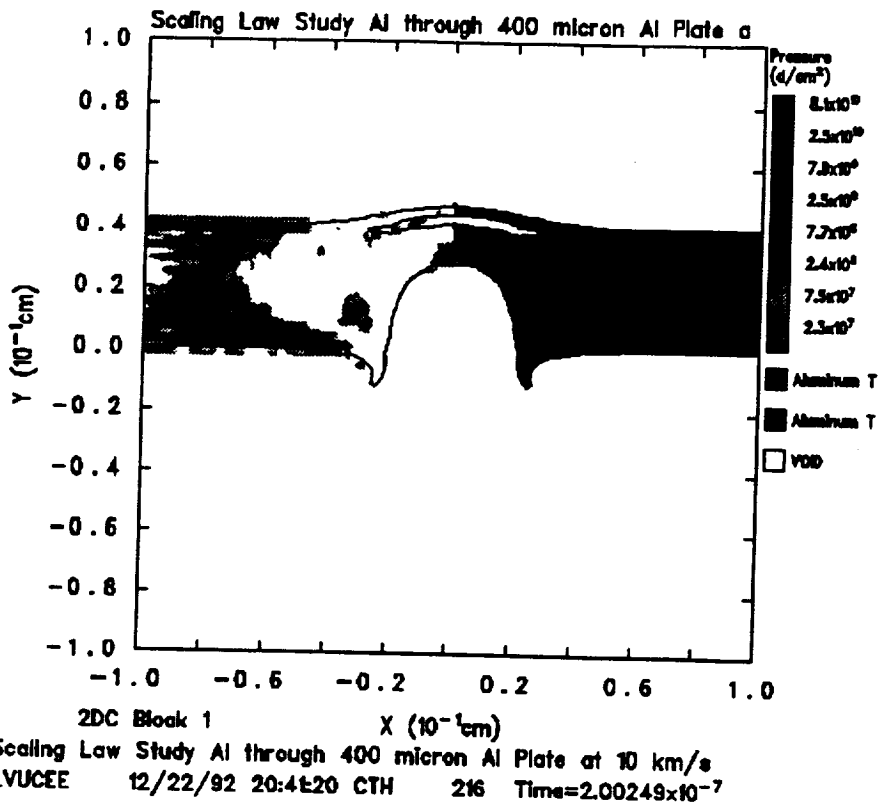


Figure 77.

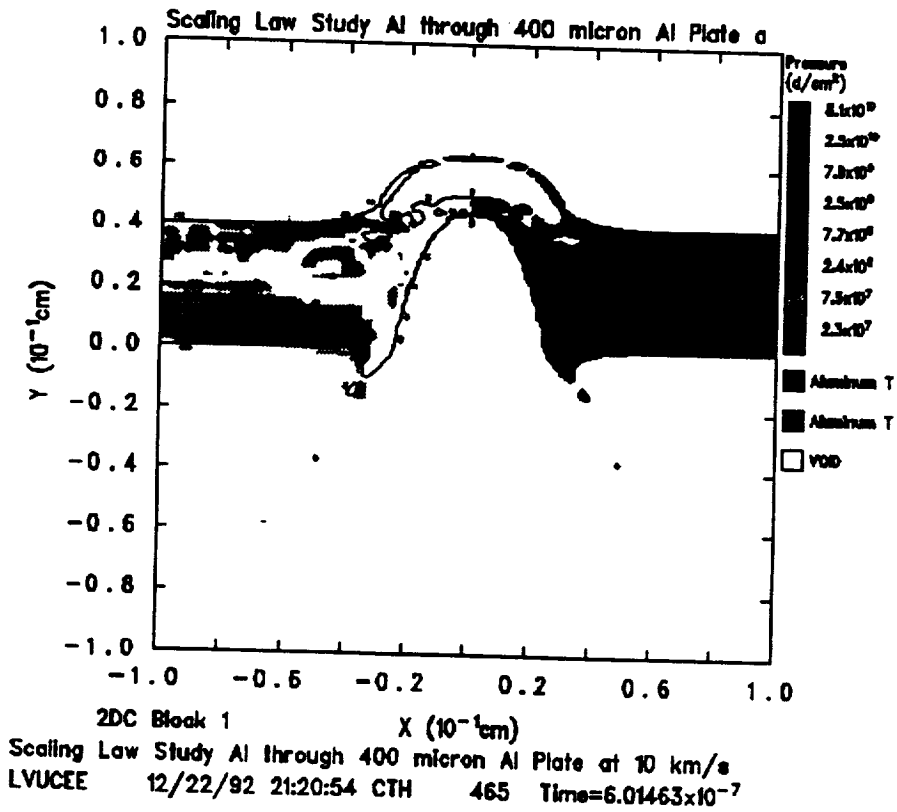


Figure 78.

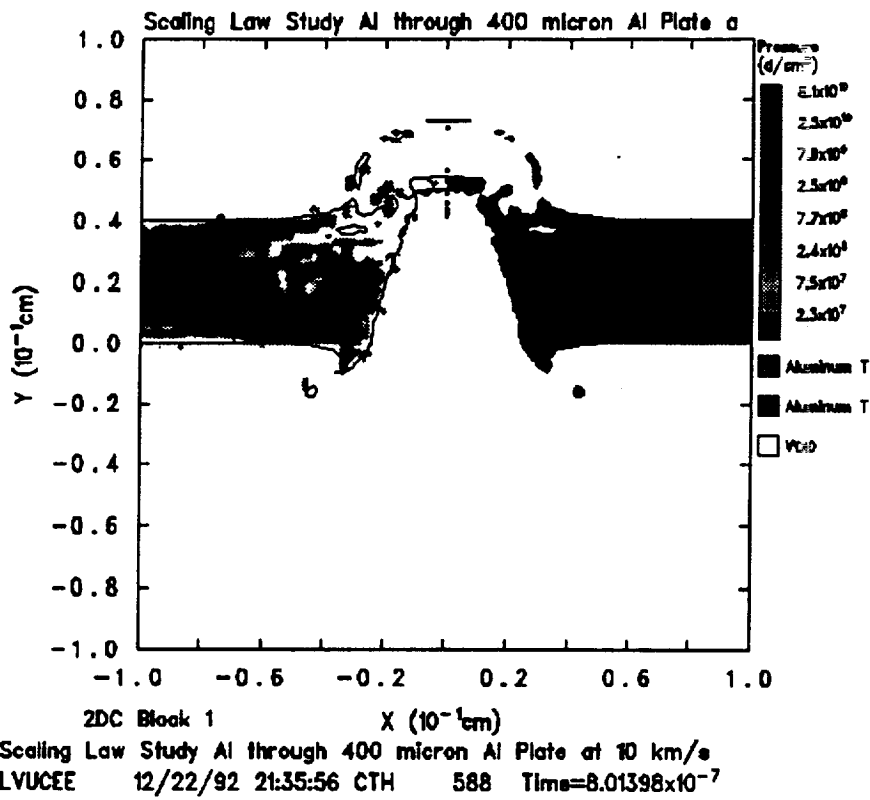


Figure 79.

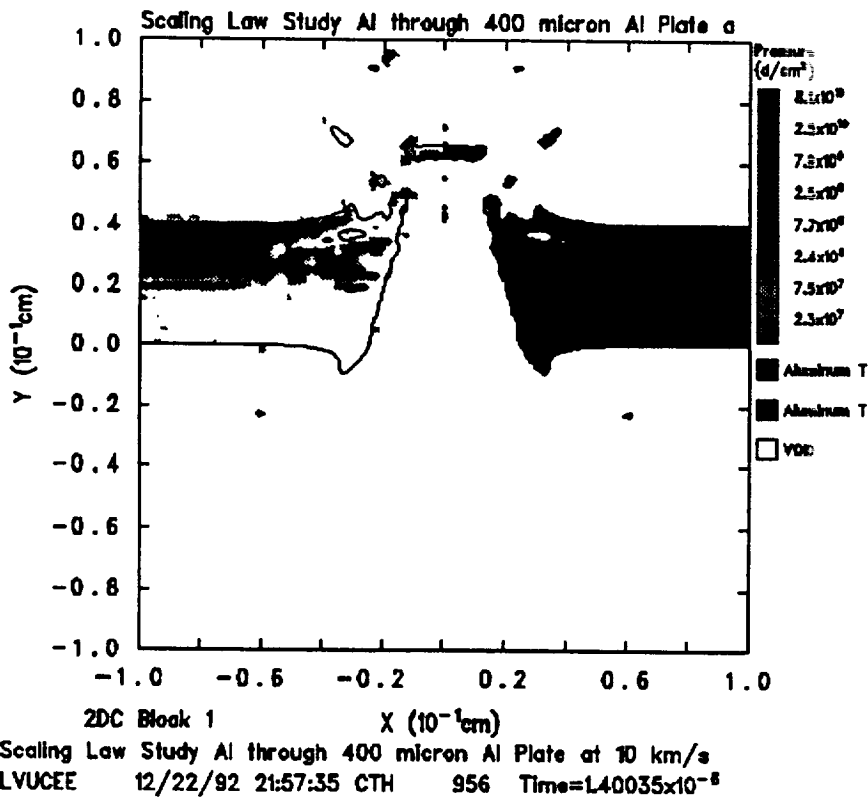


Figure 80.

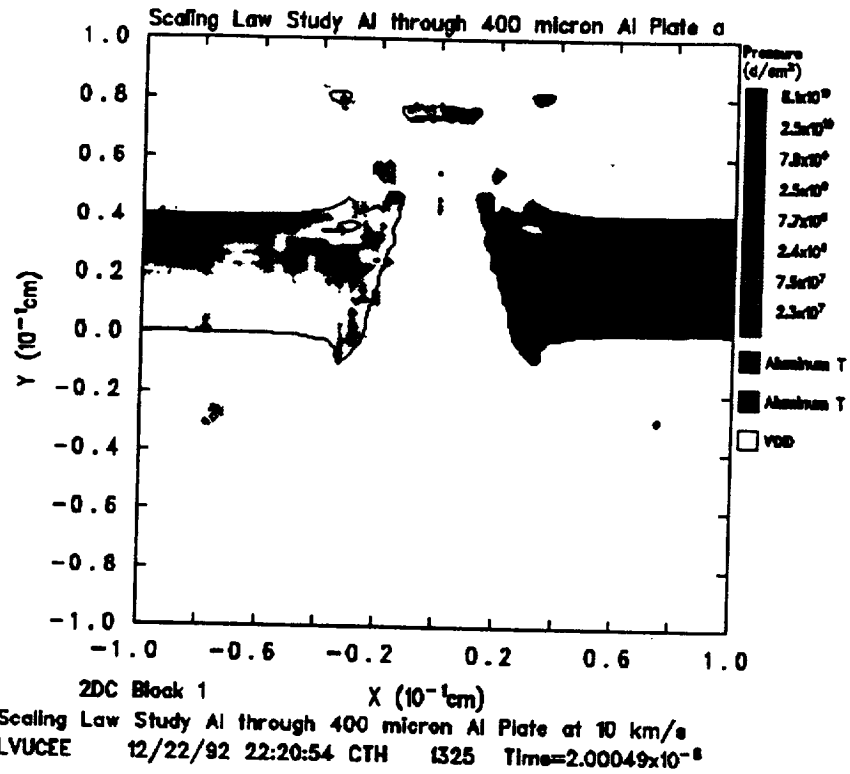


Figure 81.

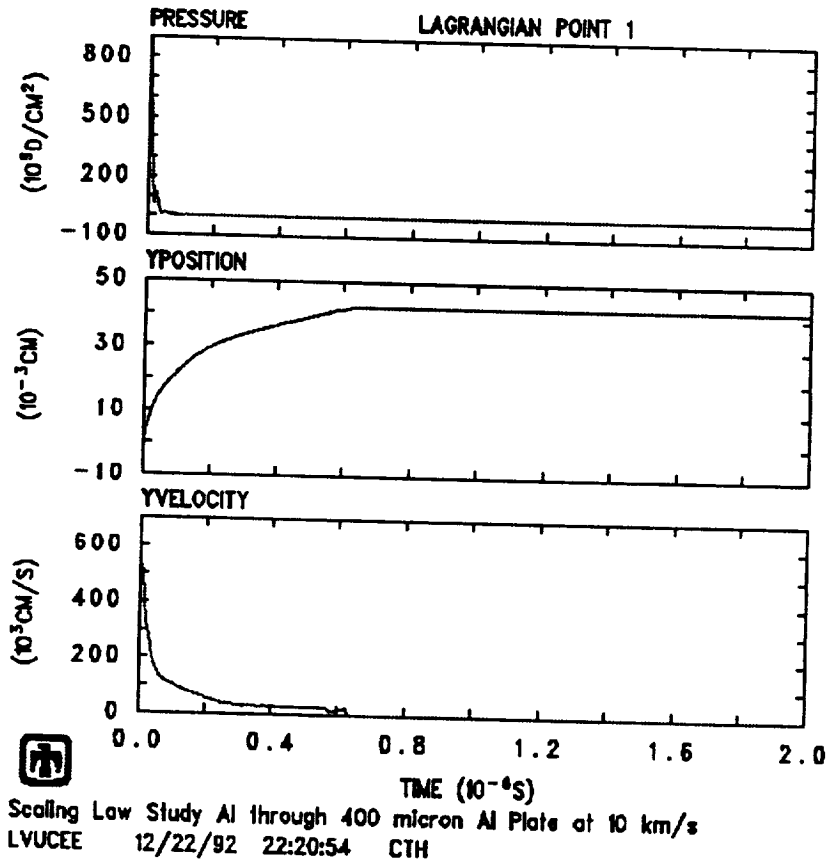
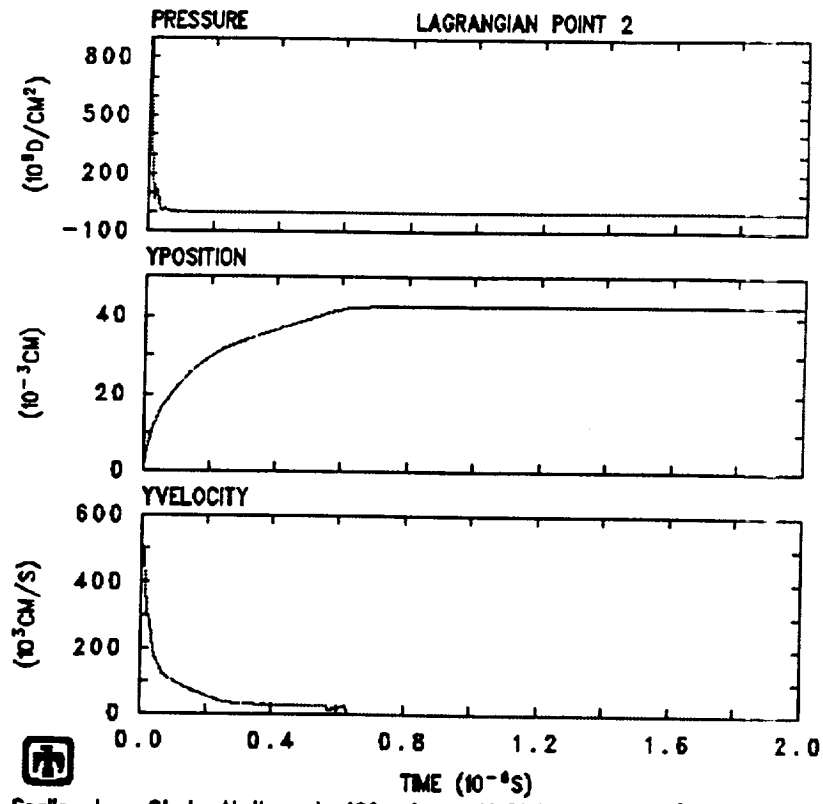
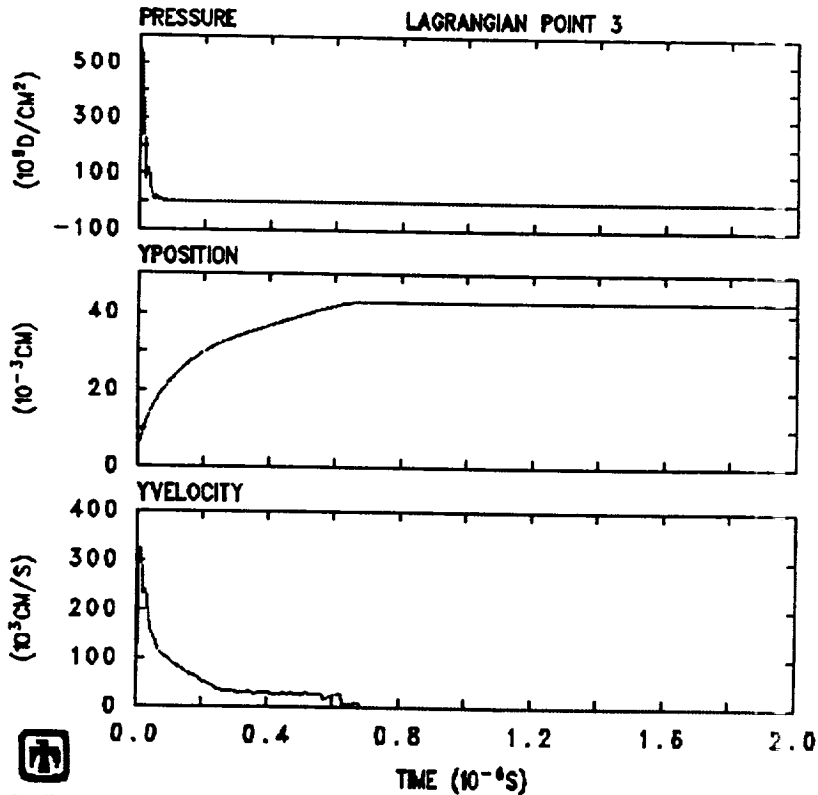


Figure 82.



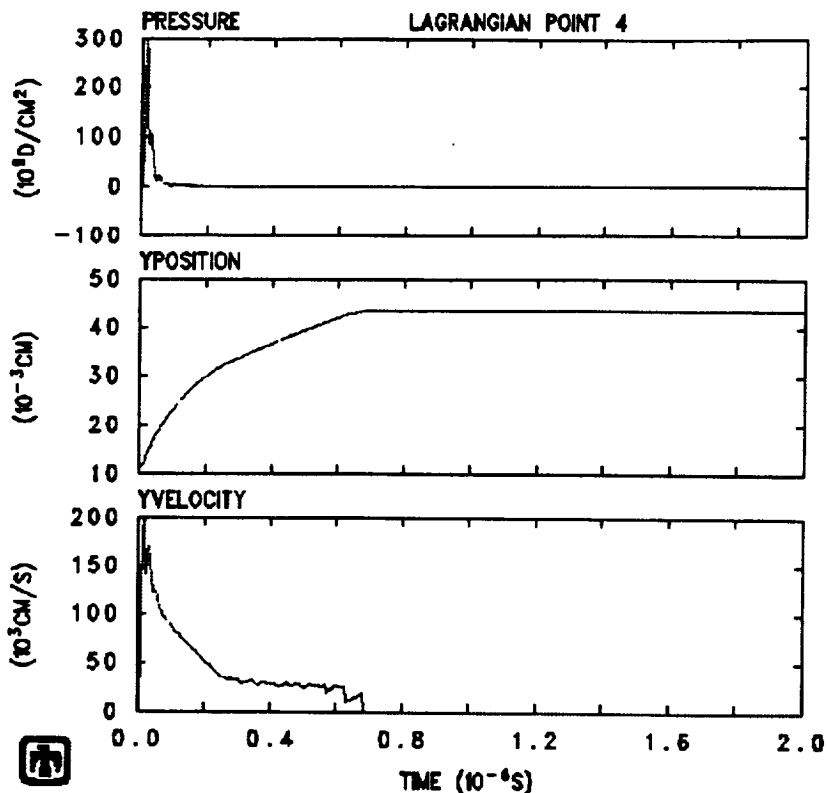
 Scaling Law Study Al through 400 micron Al Plate at 10 km/s
LVUCEE 12/22/92 22:20:54 CTH

Figure 83.



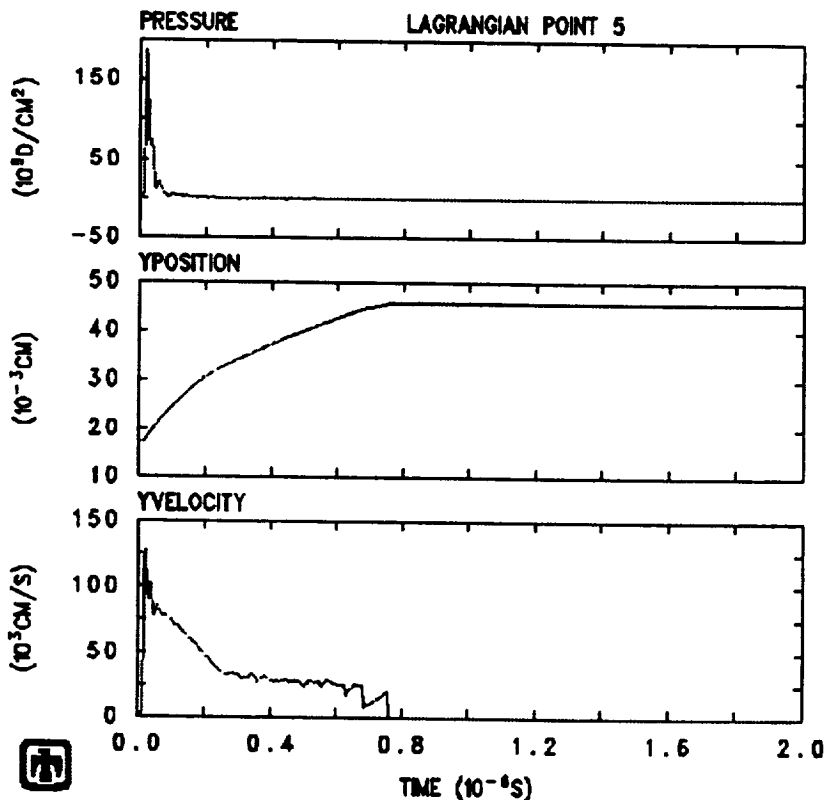
 Scaling Law Study Al through 400 micron Al Plate at 10 km/s
LVUCEE 12/22/92 22:20:54 CTH

Figure 84.



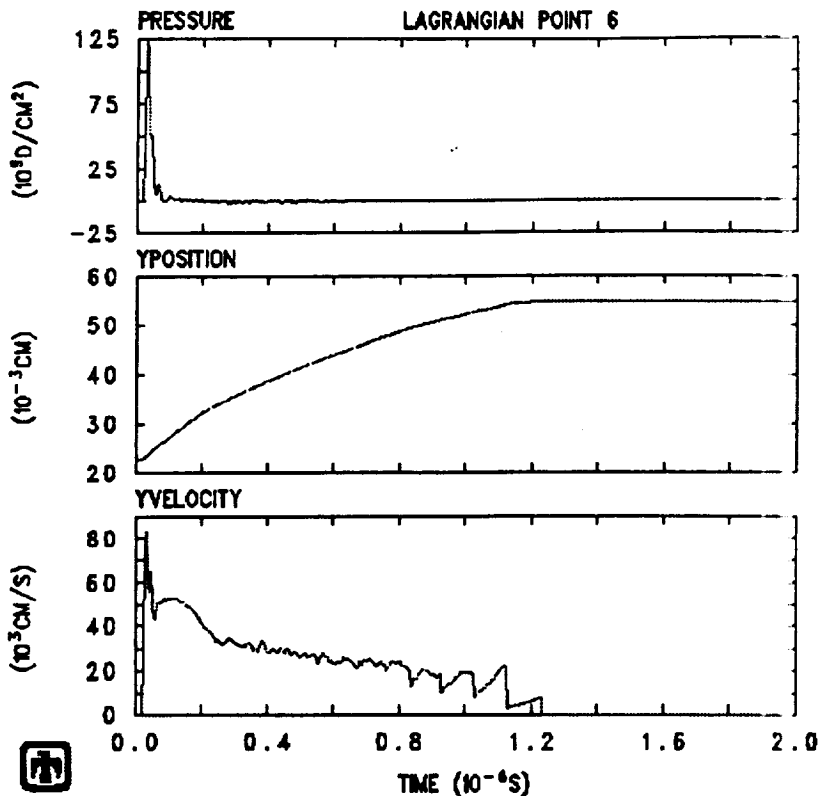
Scaling Law Study Al through 400 micron Al Plate at 10 km/s
LVUCEE 12/22/92 22:20:54 CTH

Figure 85.



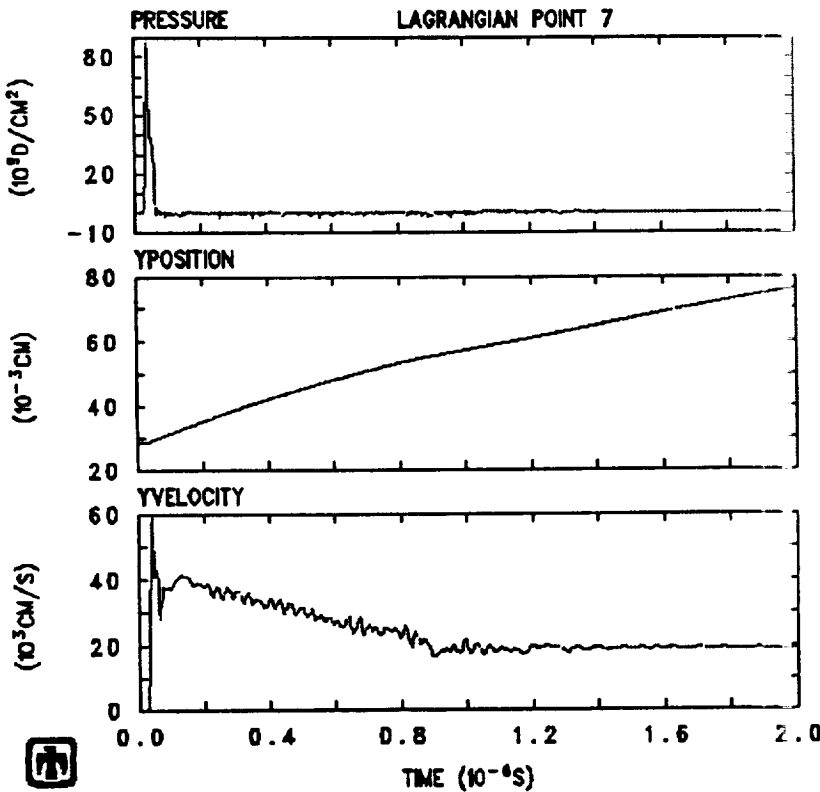
Scaling Law Study Al through 400 micron Al Plate at 10 km/s
LVUCEE 12/22/92 22:20:54 CTH

Figure 86.



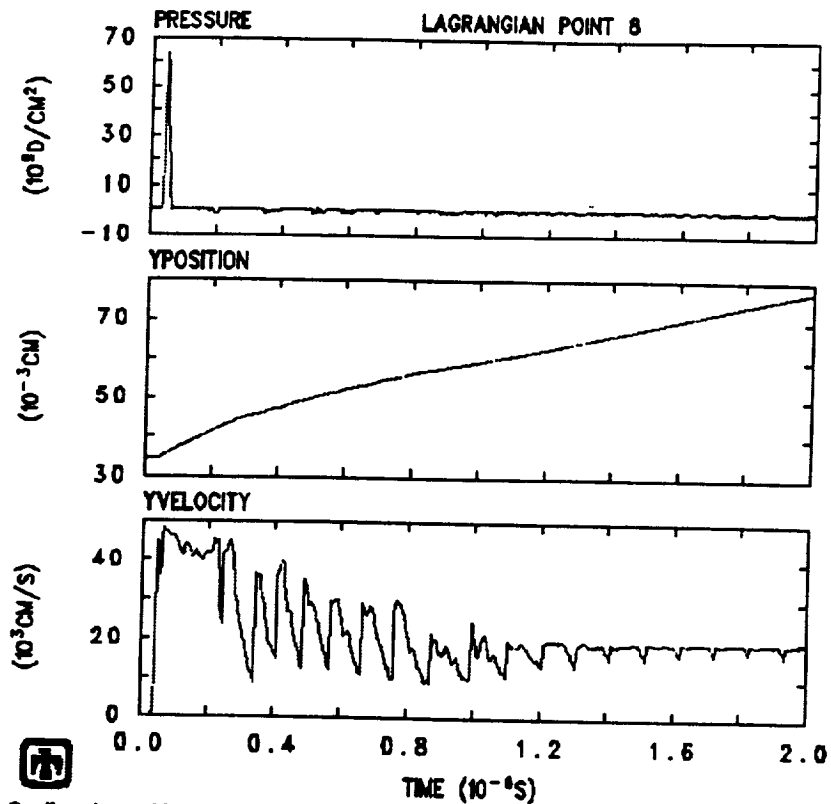
Scaling Law Study Al through 400 micron Al Plate at 10 km/s
LVUCEE 12/22/92 22:20:54 CTH

Figure 87.



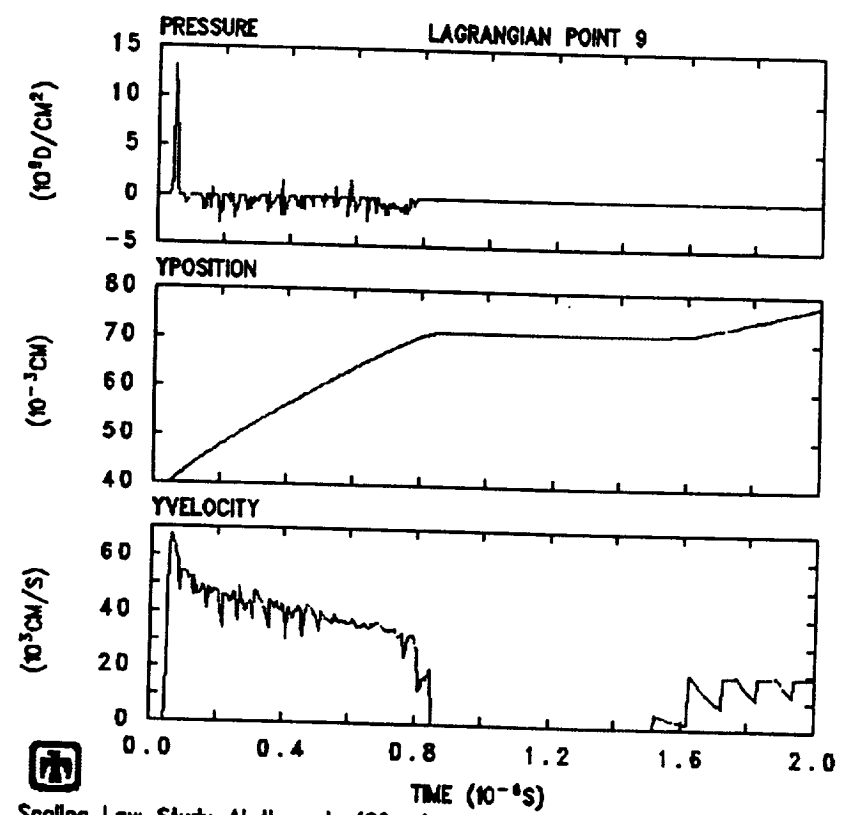
Scaling Law Study Al through 400 micron Al Plate at 10 km/s
LVUCEE 12/22/92 22:20:54 CTH

Figure 88.



 Scalling Law Study Al through 400 micron Al Plate at 10 km/s
LVUCEE 12/22/92 22:20:54 CTH

Figure 89.



 Scalling Law Study Al through 400 micron Al Plate at 10 km/s
LVUCEE 12/22/92 22:20:54 CTH

Figure 90. Comparison of CTH Results versus Watts' Eq. 59 for Al into TFE Teflon

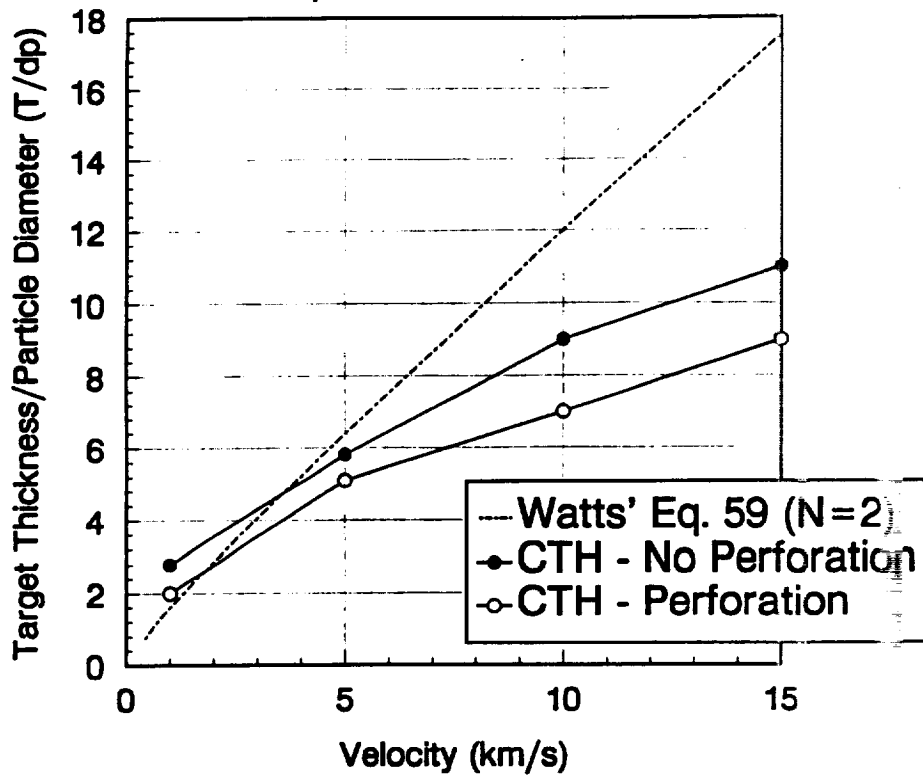


Figure 91. Comparison of CTH Results versus Watts' Eq. 59 for Al into TFE Teflon

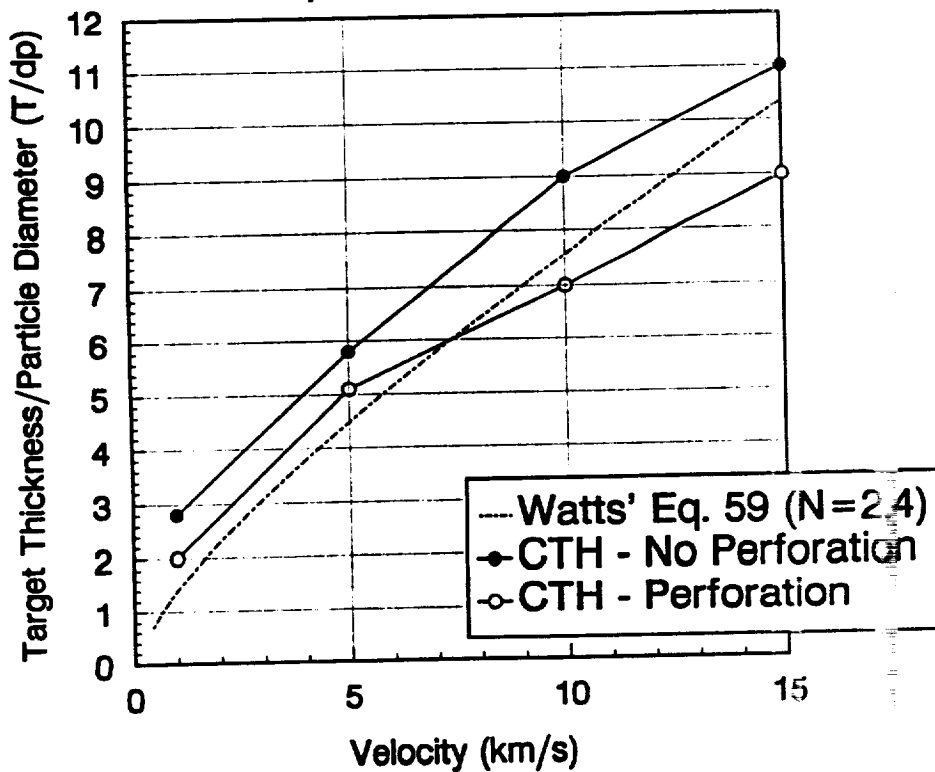


Figure 92. Comparison of CTH Results versus Watts' Eq. 59 for Al into TFE Teflon

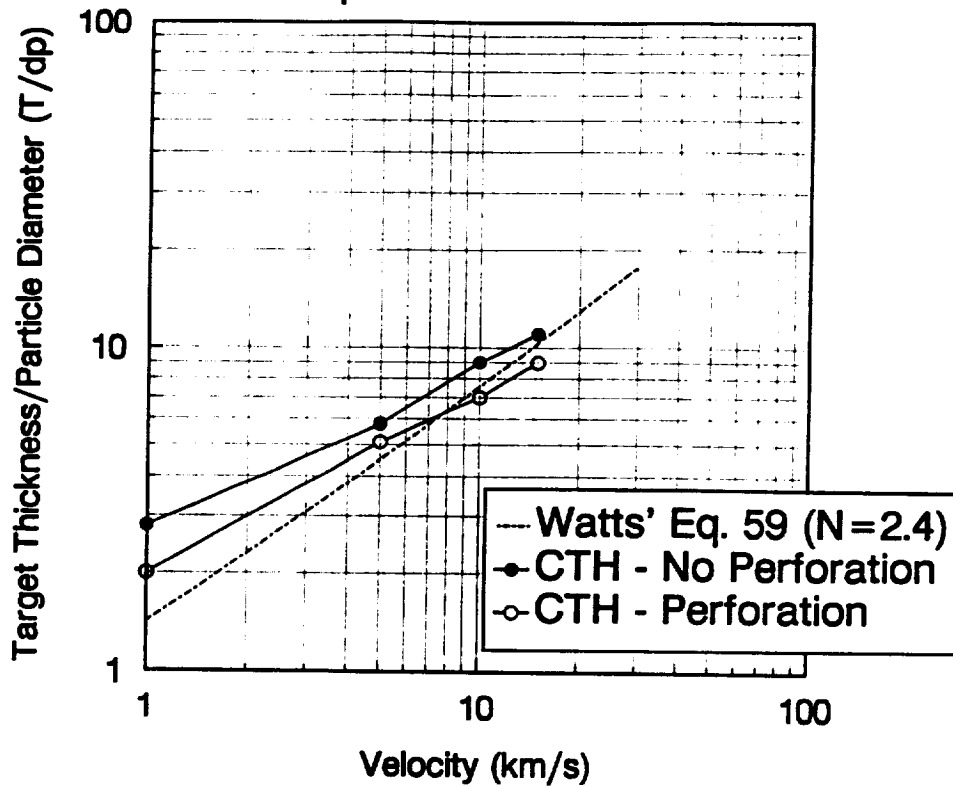
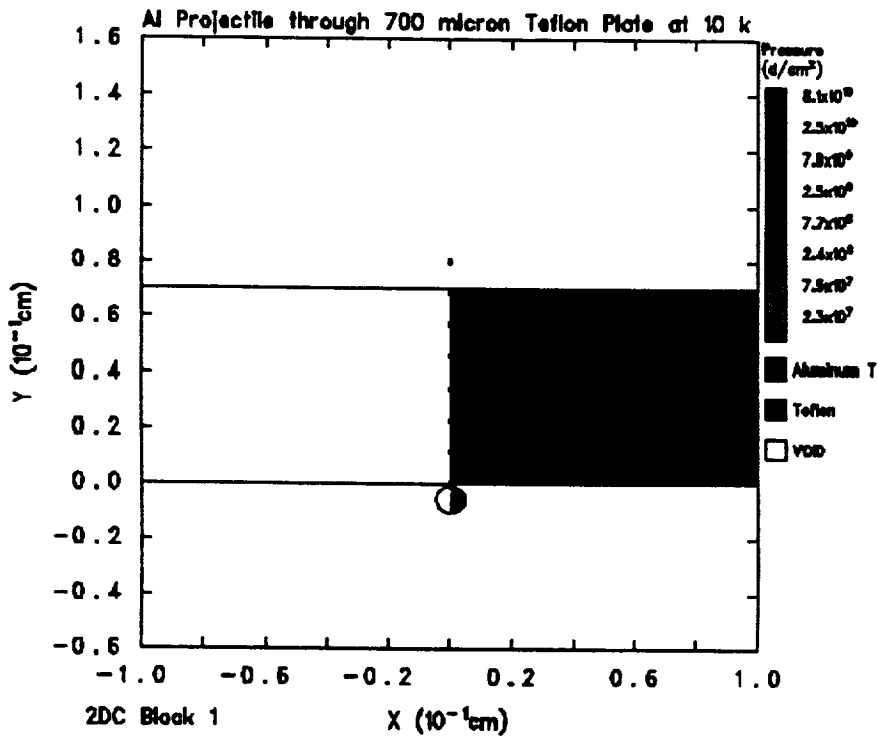


Figure 93.



ZDC Block 1 X (10⁻¹cm)
 Al Impactor Into 700 micron Teflon Plate at 10 km/s
 L2NCNK 12/29/92 13:28:25 CTH 0 Time=0.

Figure 94.

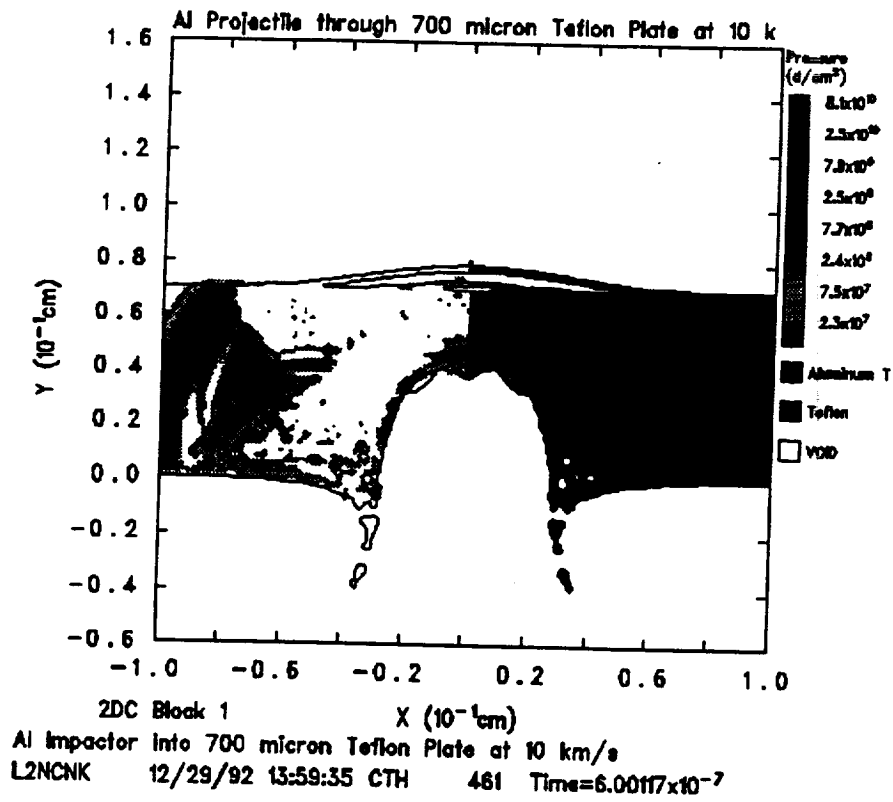


Figure 95.

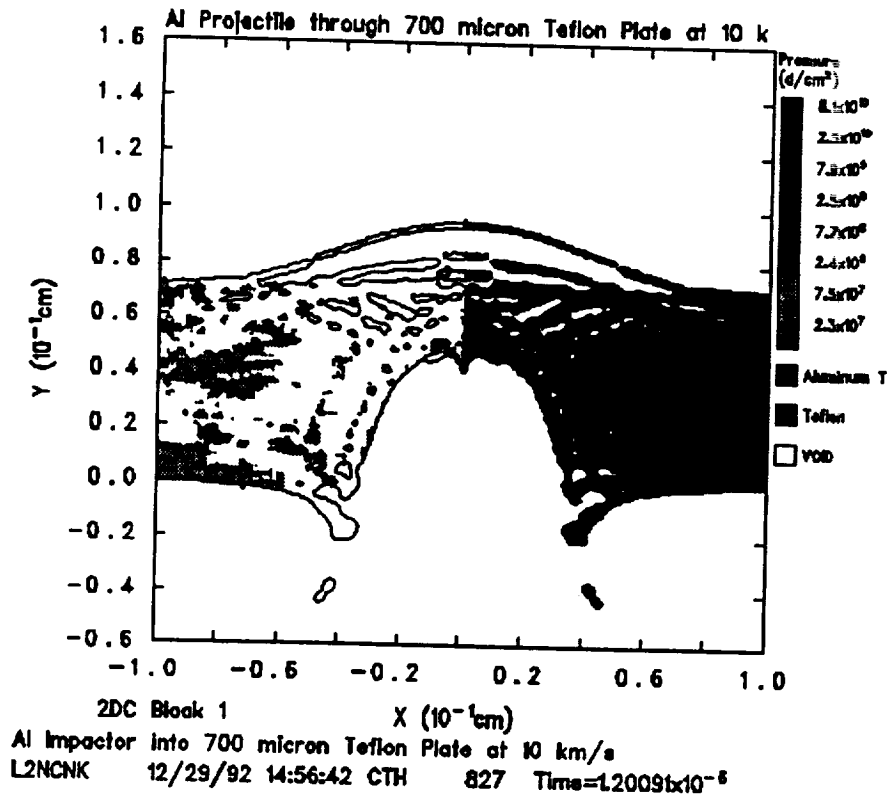


Figure 96.

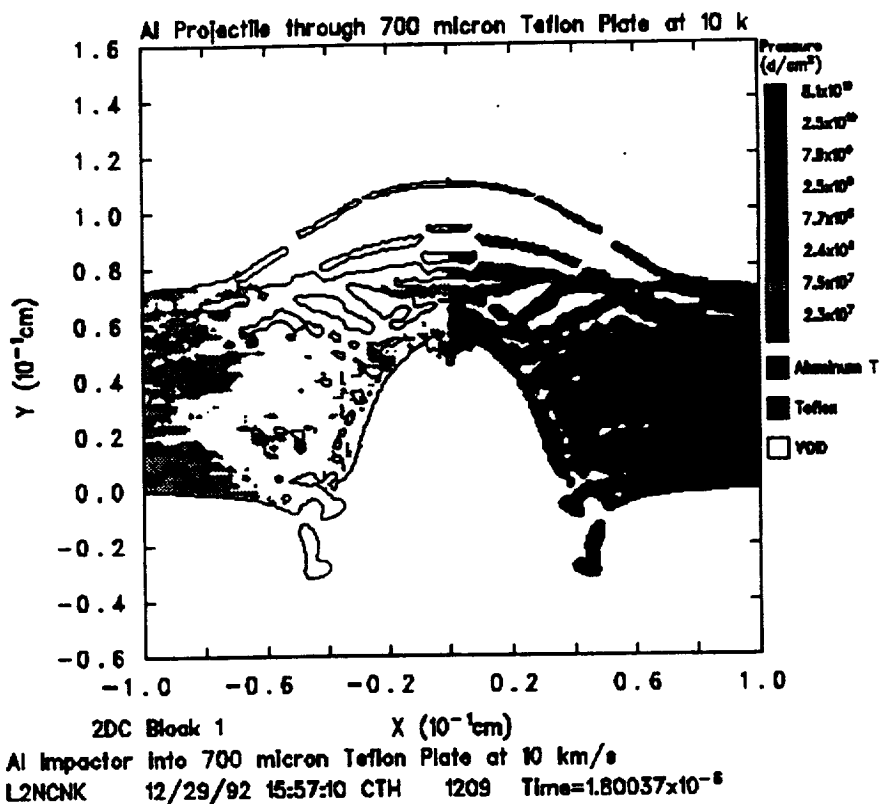


Figure 97.

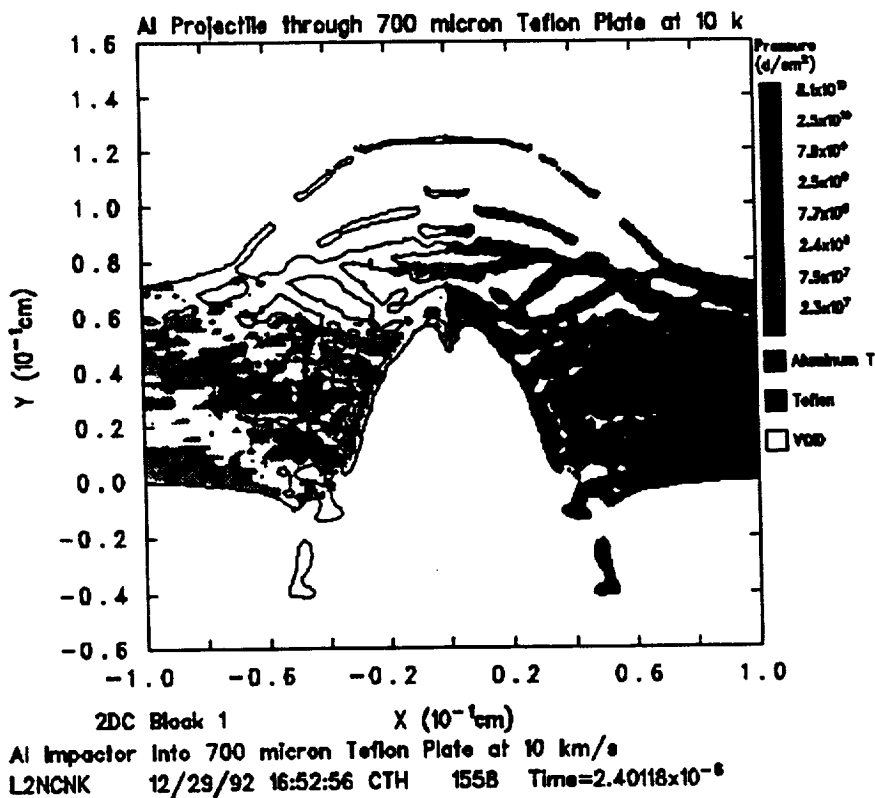
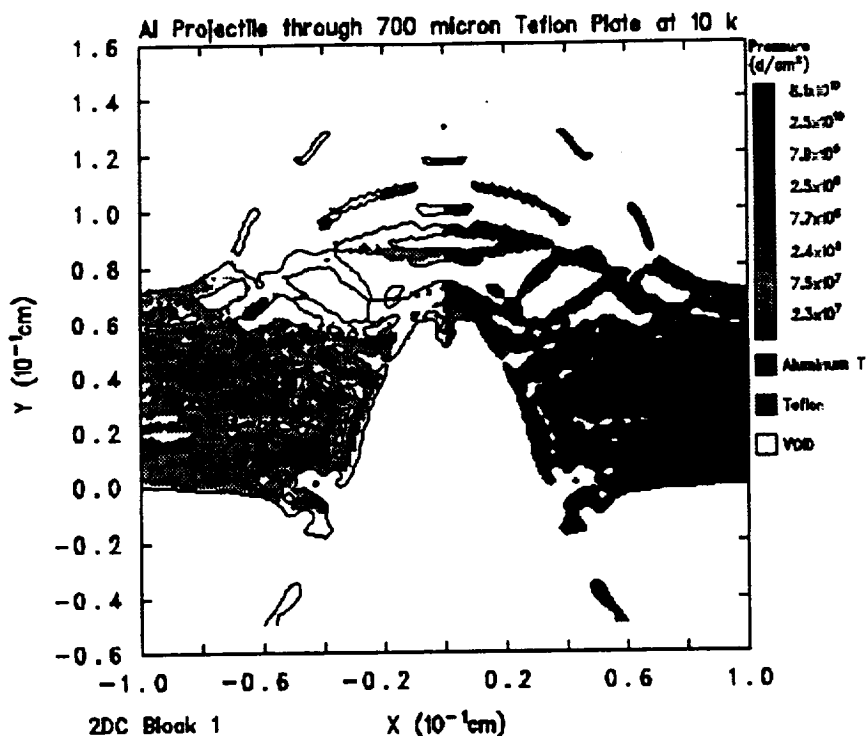
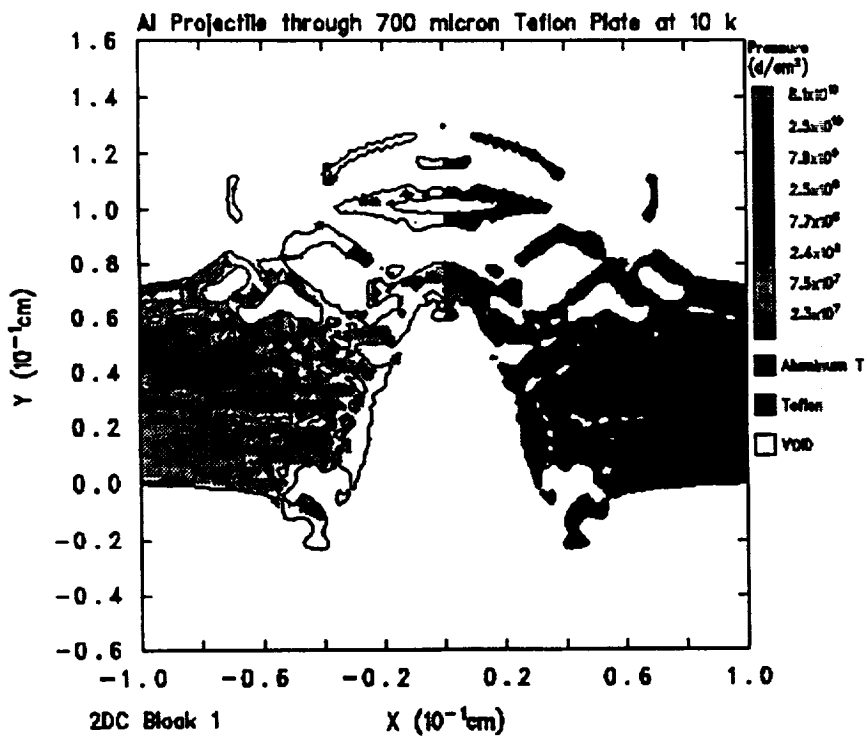


Figure 98.



Al Impactor into 700 micron Teflon Plate at 10 km/s
L2CNCK 12/29/92 18:59:38 CTH 2042 Time=3.20061x10⁻⁶

Figure 99.



Al Impactor into 700 micron Teflon Plate at 10 km/s
L2TEIF 12/29/92 22:05:24 CTH 2515 Time=4.60045x10⁻⁶

Figure 100.

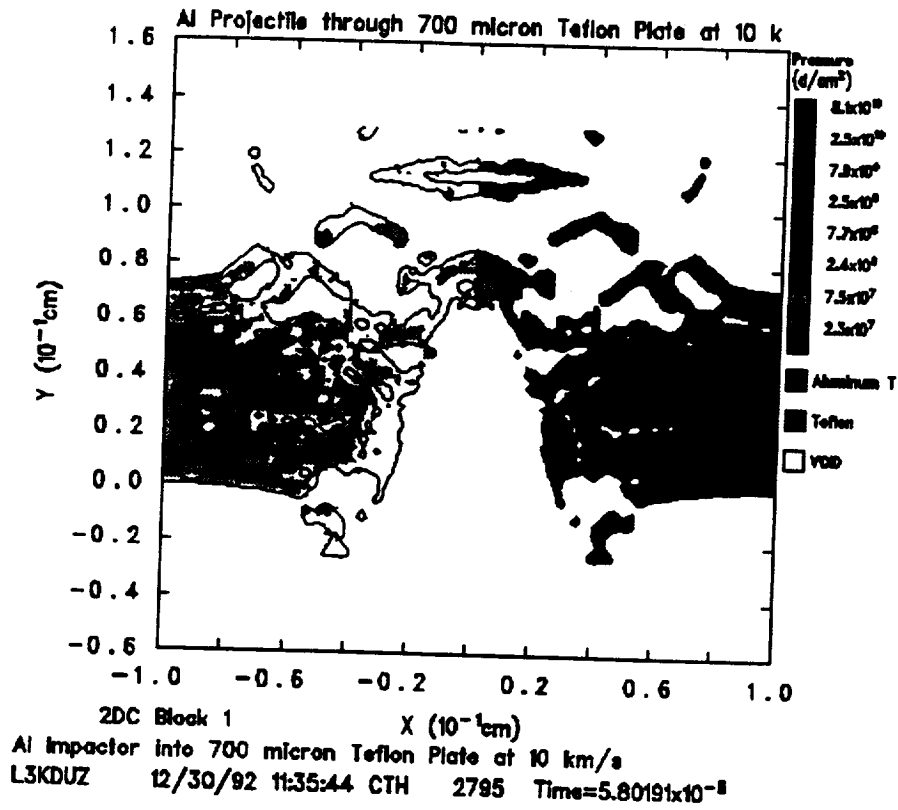


Figure 101.

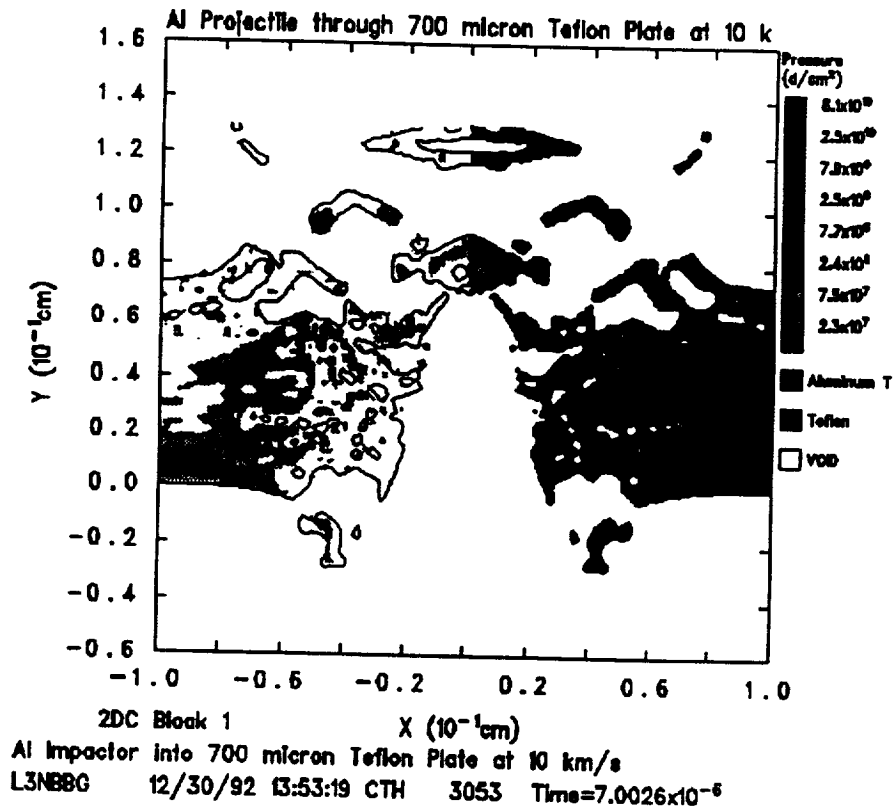
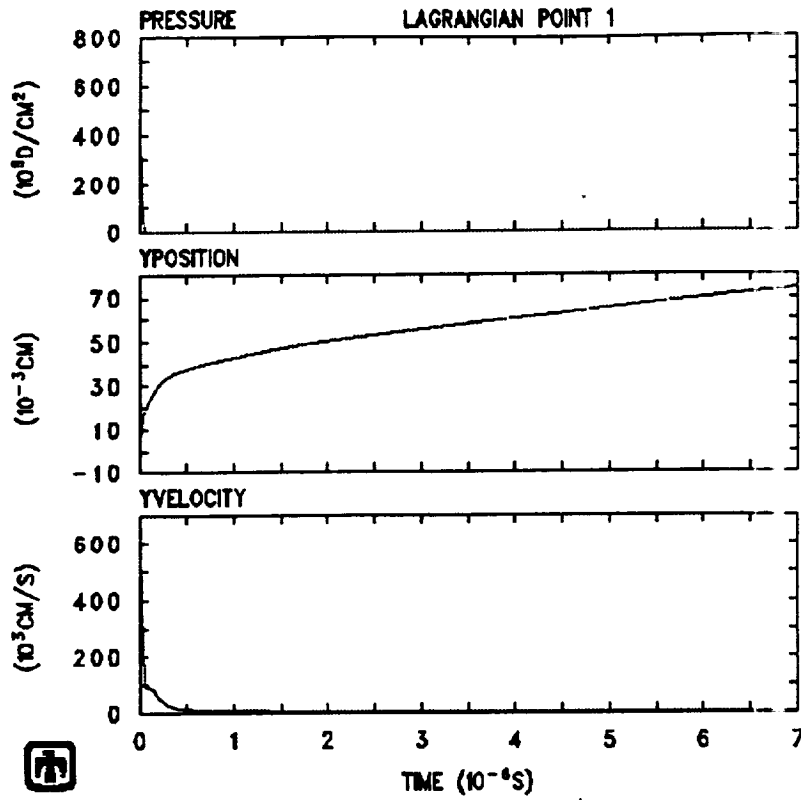
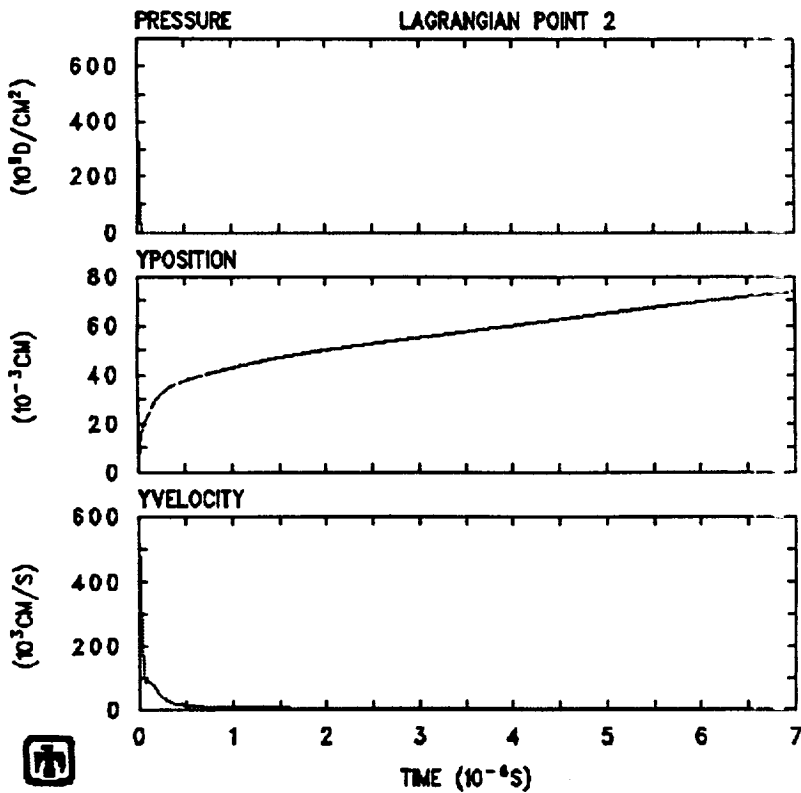


Figure 102.



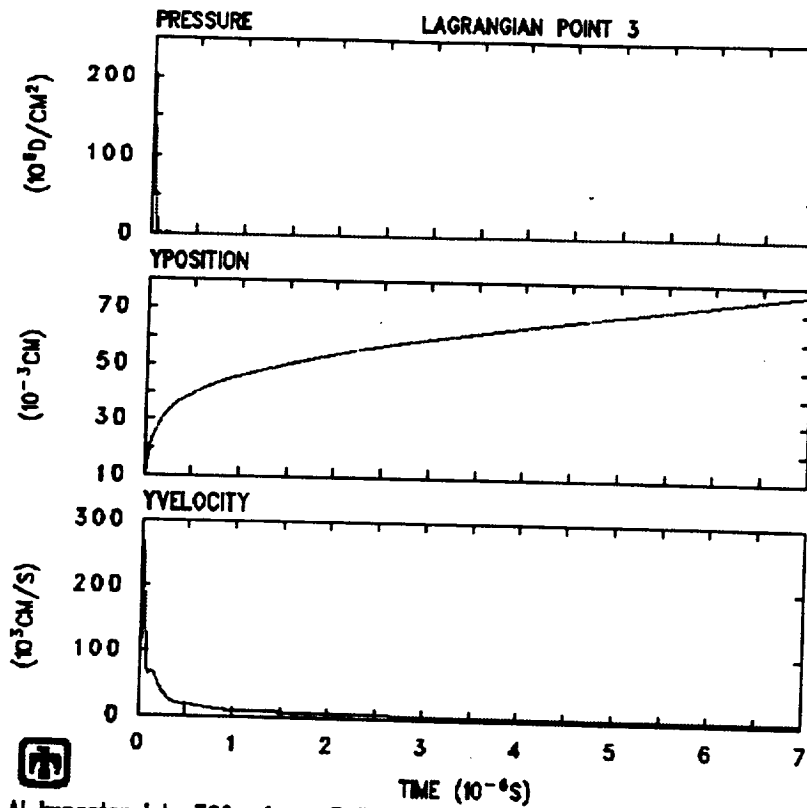
Al Impactor Into 700 micron Teflon Plate at 10 km/s
 L3NBBG 12/30/92 13:53:20 CTH

Figure 103.



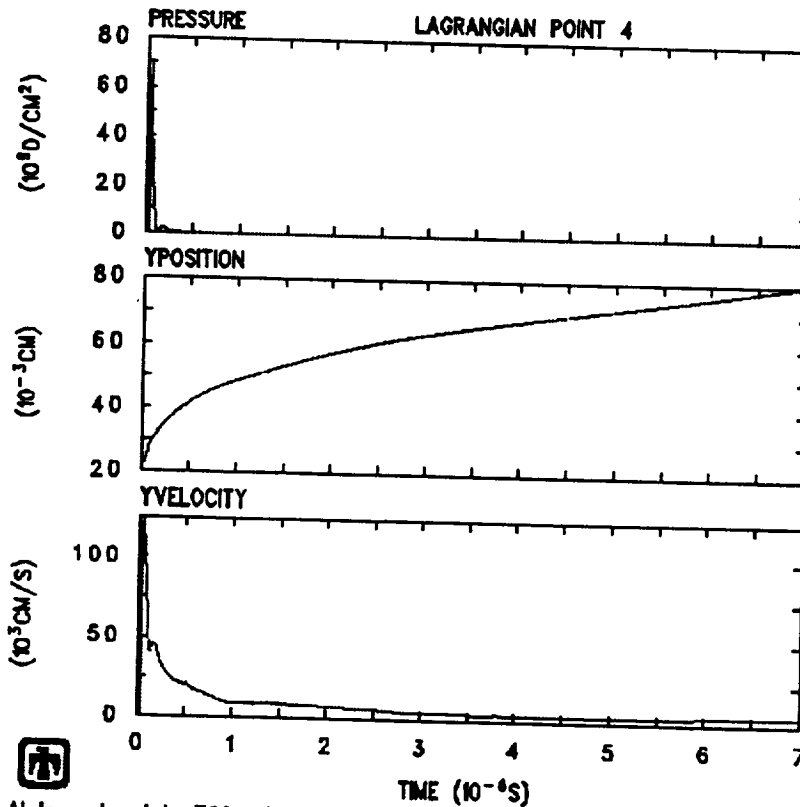
Al Impactor Into 700 micron Teflon Plate at 10 km/s
 L3NBBG 12/30/92 13:53:20 CTH

Figure 104.



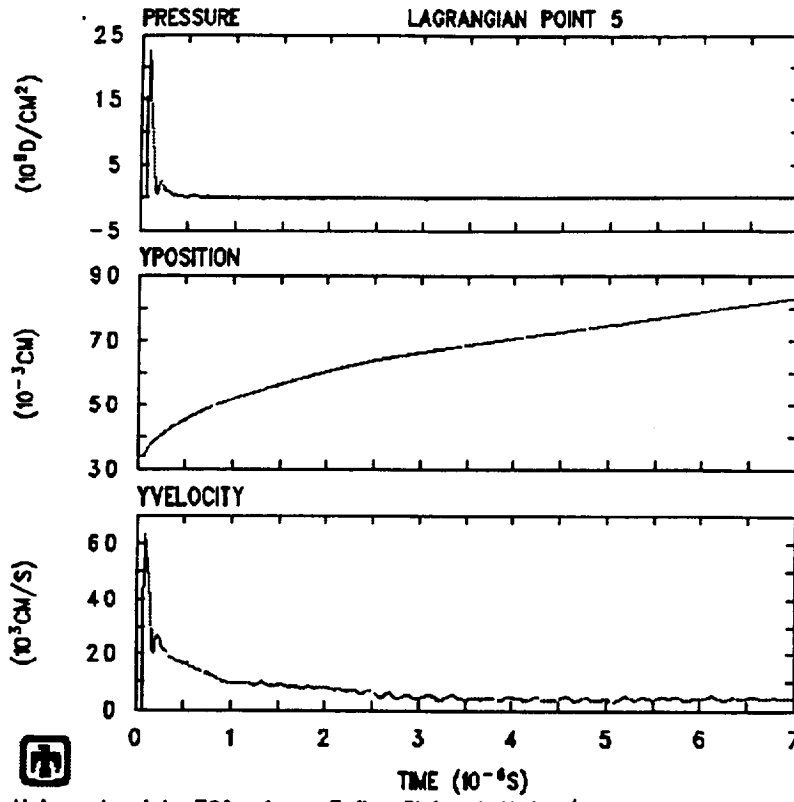
Al Impactor Into 700 micron Teflon Plate at 10 km/s
L3NBGG 12/30/92 13:53:20 CTH

Figure 105.



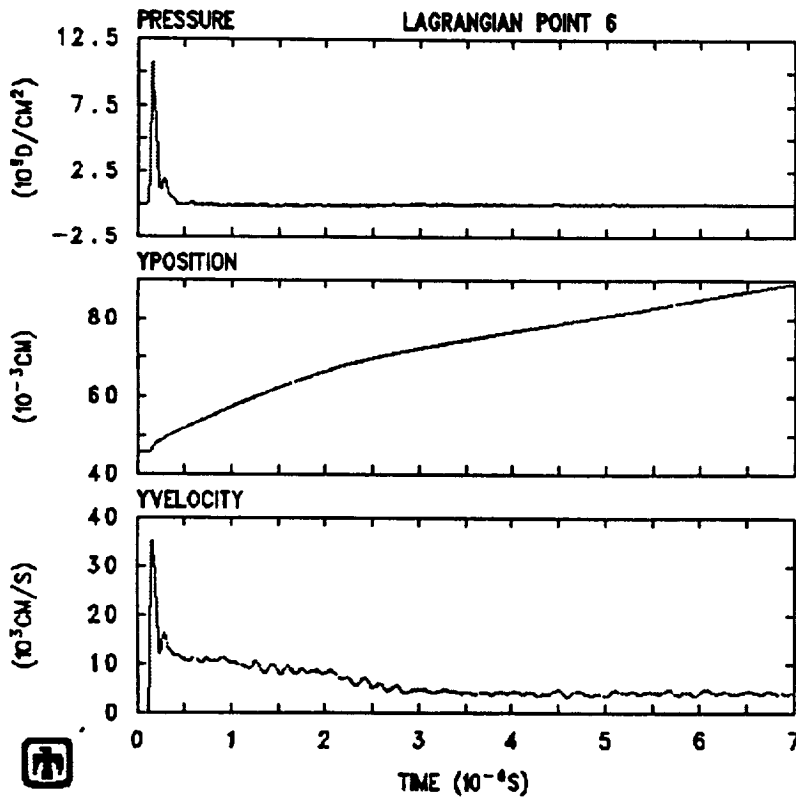
Al Impactor Into 700 micron Teflon Plate at 10 km/s
L3NBGG 12/30/92 13:53:20 CTH

Figure 106.



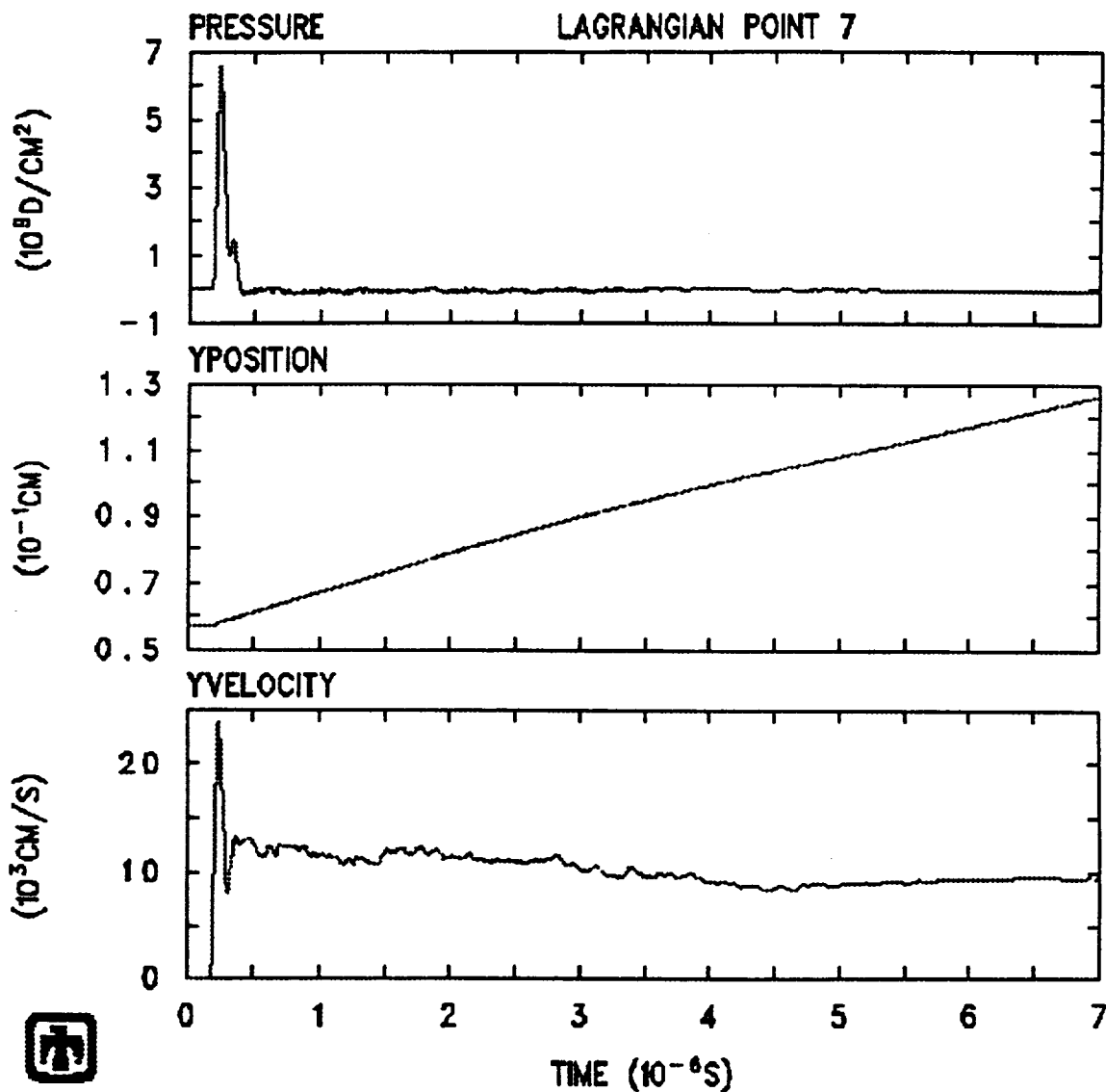
Al Impactor Into 700 micron Teflon Plate at 10 km/s
L3NBGG 12/30/92 13:53:20 CTH

Figure 107.



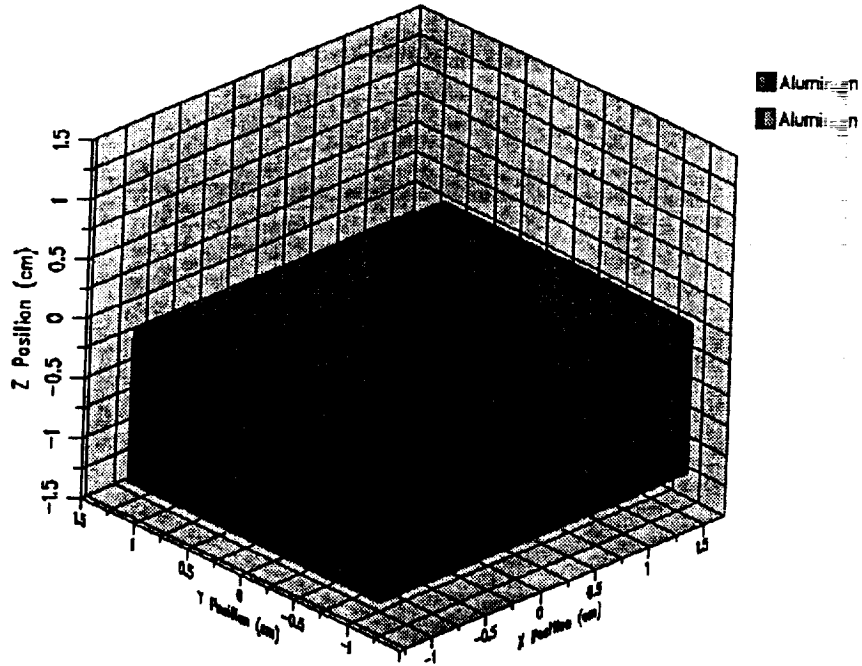
Al Impactor Into 700 micron Teflon Plate at 10 km/s
L3NBGG 12/30/92 13:53:20 CTH

Figure 108.



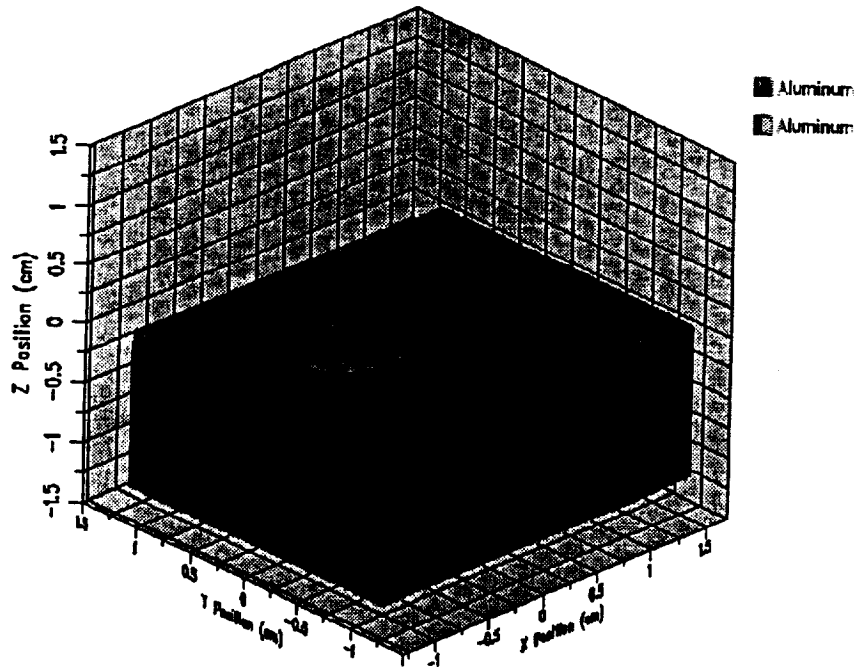
Al Impactor Into 700 micron Teflon Plate at 10 km/s
L3NBBG 12/30/92 13:53:20 CTH

Figure 109.



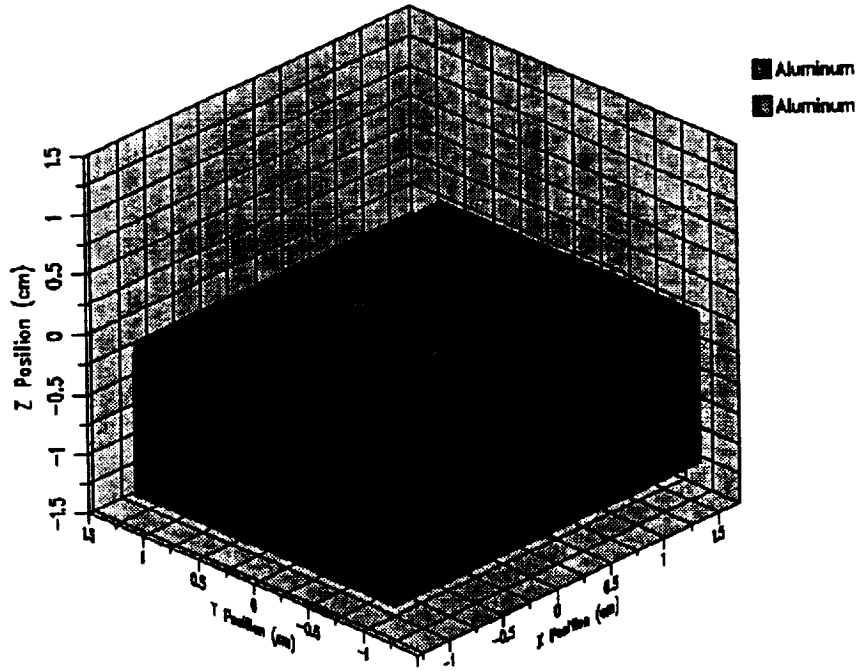
3-D Al into Al Plate, 70 degrees, 5.0 km/s, .08 cm zones
L3UAVF 12/30/92 20:09:36 CTH 0 Time 0. s

Figure 110.



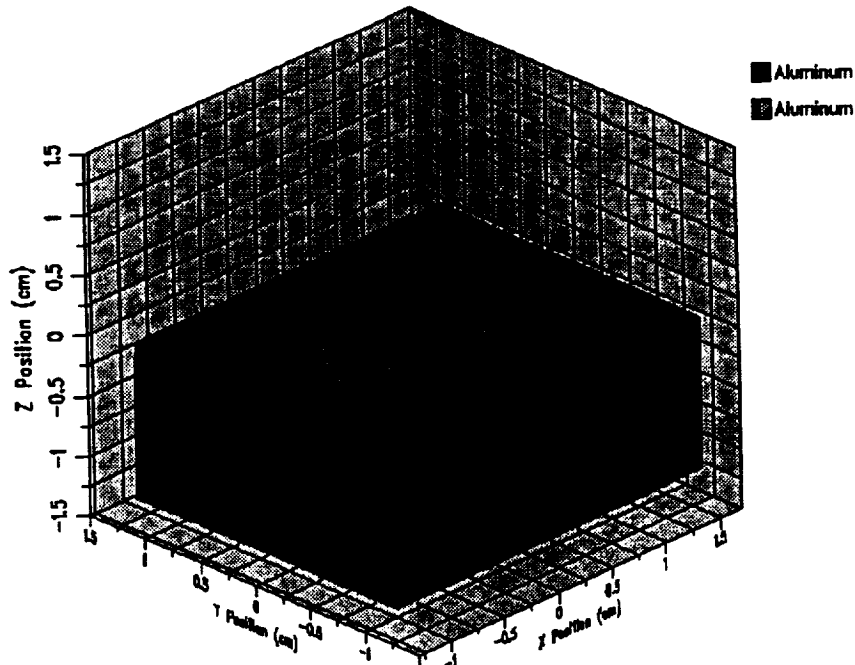
3-D Al into Al Plate, 70 degrees, 5.0 km/s, .08 cm zones
L3UAVF 12/30/92 20:25:23 CTH 93 Time 1.2099x10⁻⁸ s

Figure 111.



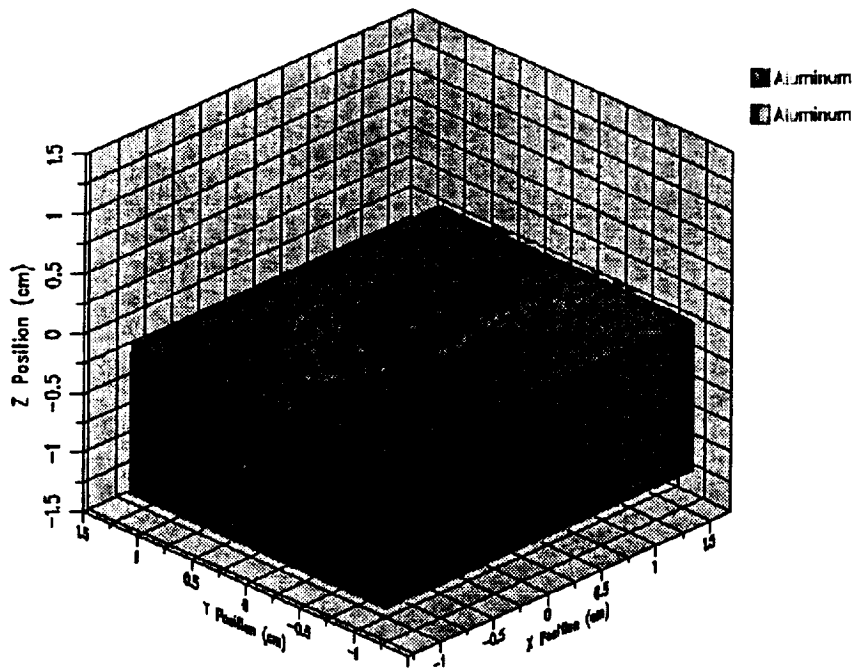
3-D Al into Al Plate, 70 degrees, 5.0 km/s, .08 cm zones
L3UAVF 12/30/92 20:45:53 CTH 125 Time 2.1309x10⁻⁶ s

Figure 112.



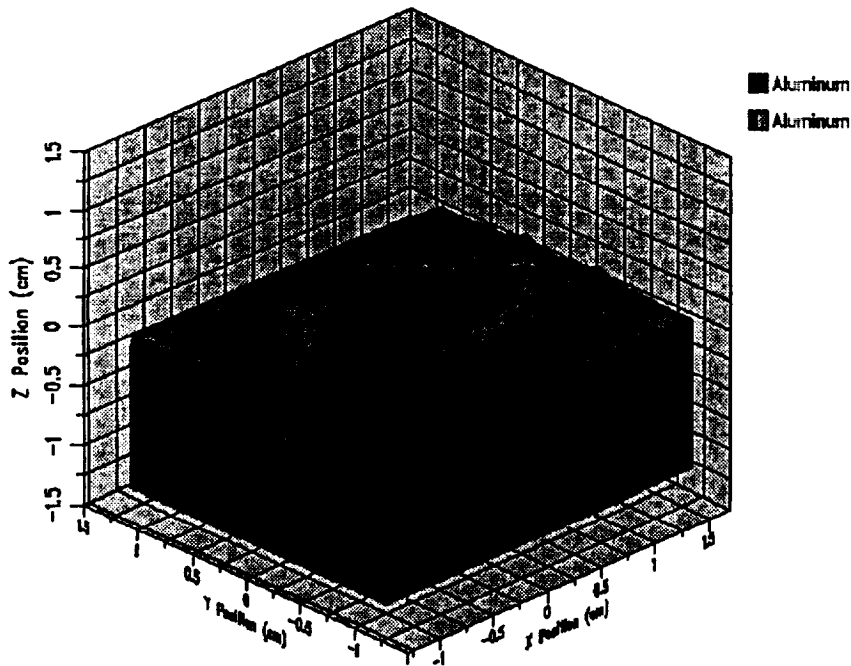
3-D Al into Al Plate, 70 degrees, 5.0 km/s, .08 cm zones
L3UAVF 12/30/92 21:1t45 CTH 153 Time 3.0228x10⁻⁶ s

Figure 113.



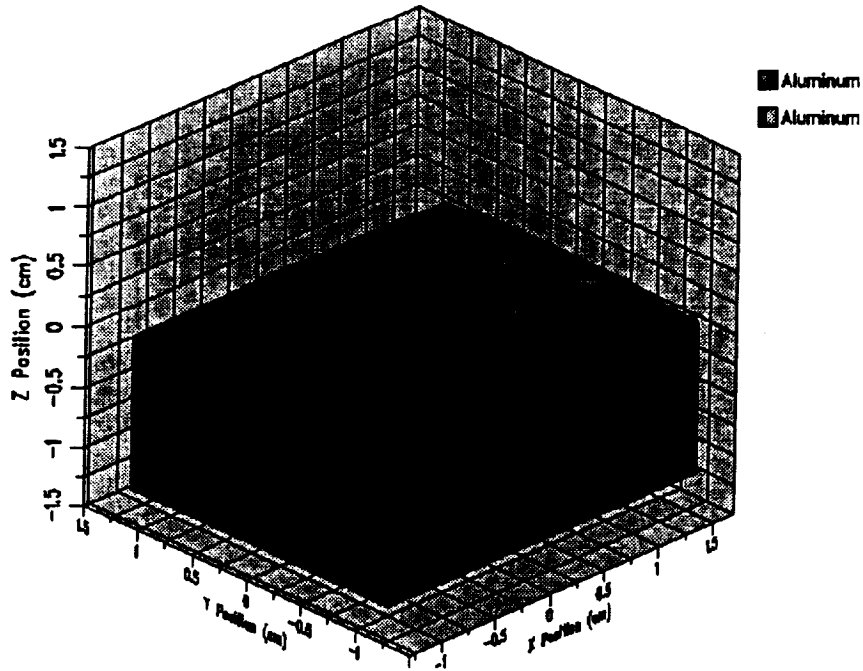
3-D Al into Al Plate, 70 degrees, 5.0 km/s, .08 cm zones
L3UAVF 12/30/92 21:41:22 CTH 181 Time 3.929x10⁻⁶ s

Figure 114.



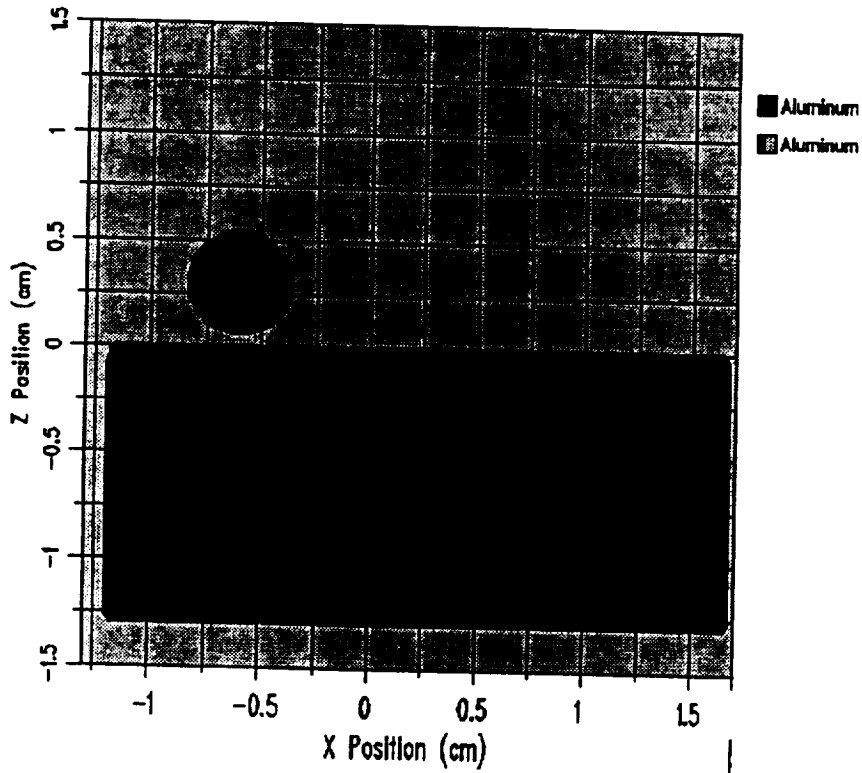
3-D Al into Al Plate, 70 degrees, 5.0 km/s, .08 cm zones
L3UAVF 12/30/92 22:59:54 CTH 251 Time 5.1108x10⁻⁶ s

Figure 115.



3-D Al into Al Plate, 70 degrees, 5.0 km/s, .08 cm zones
L3UAVF 12/31/92 00:02:47 CTH 302 Time 6.0029x10⁻⁶ s

Figure 116.



3-D Al into Al Plate, 70 degrees, 5.0 km/s, .08 cm zones
L3UAVF 12/30/92 20:09:36 CTH 0 Time 0. s

Figure 117.

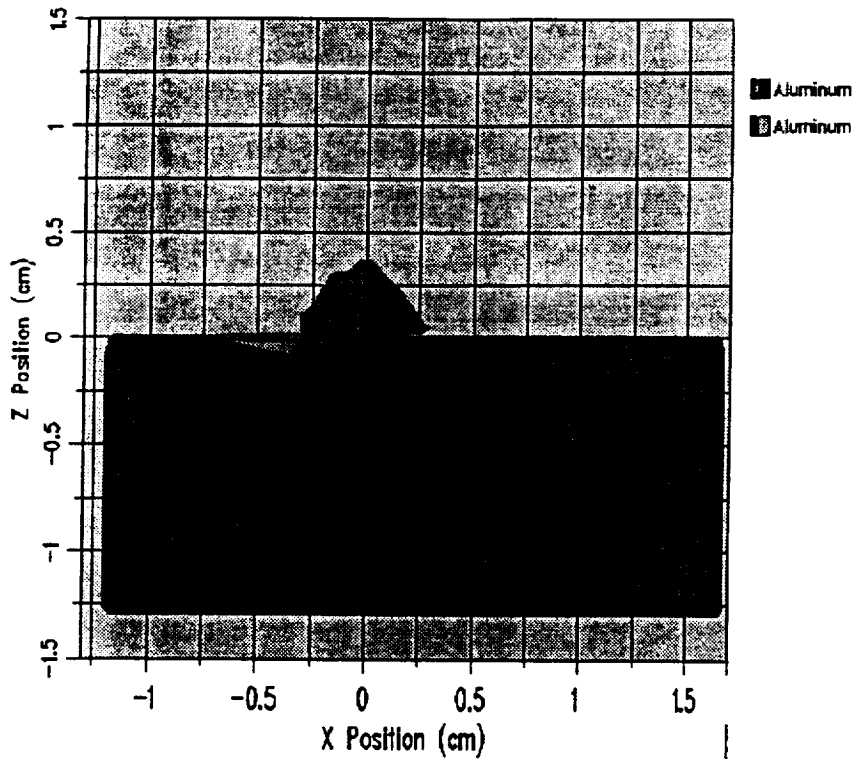


Figure 118.

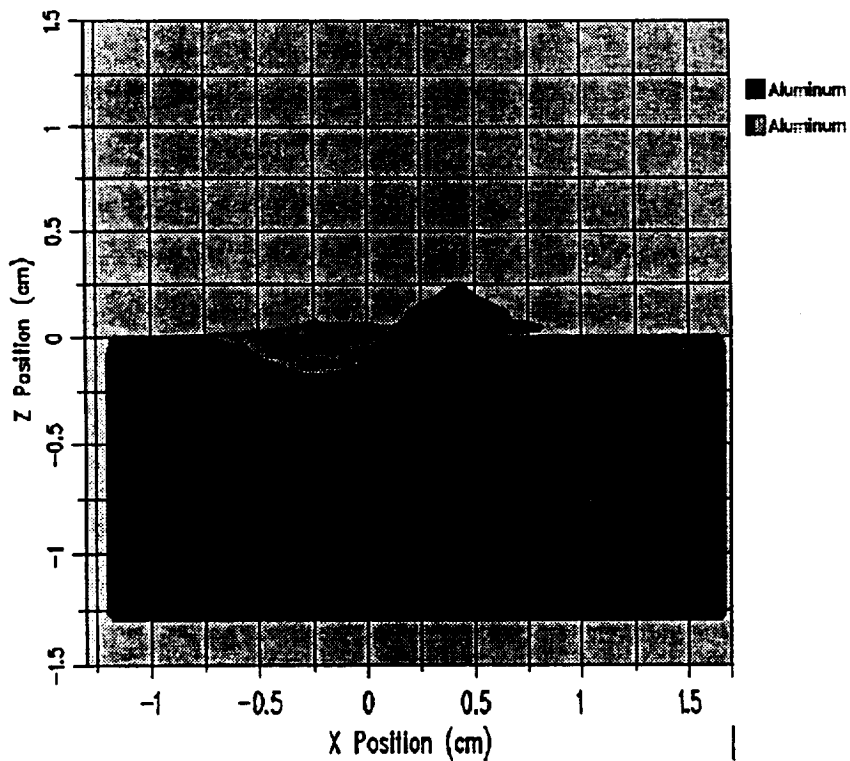


Figure 119.

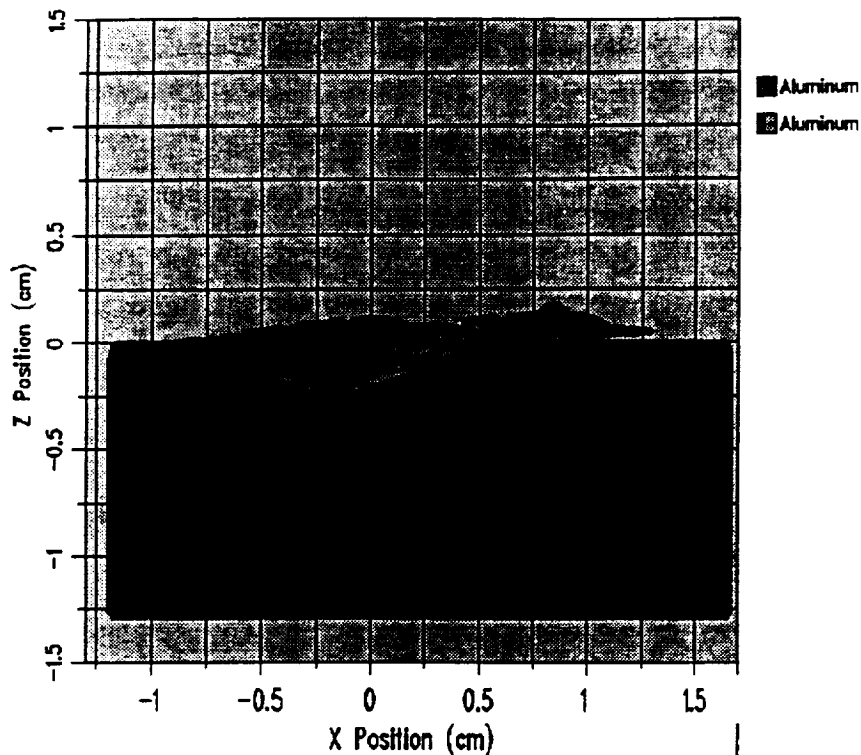


Figure 120.

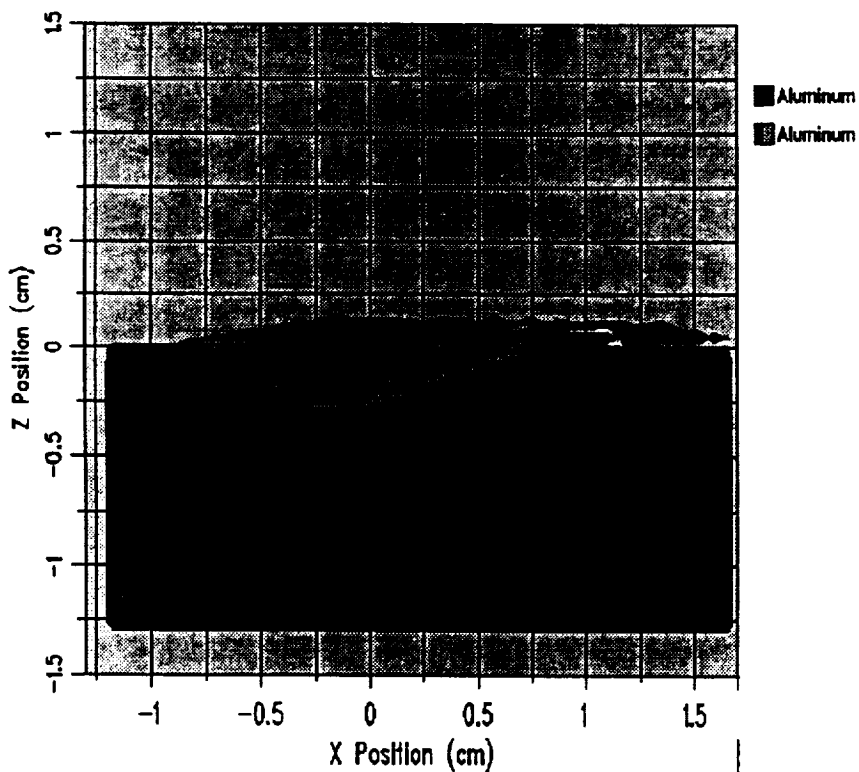


Figure 121.

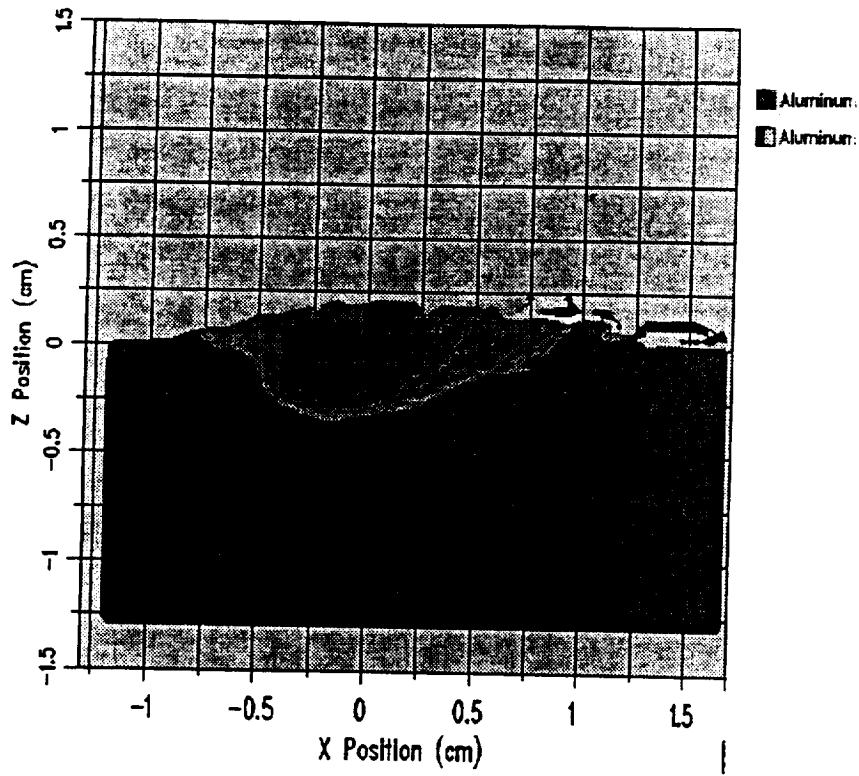


Figure 122.

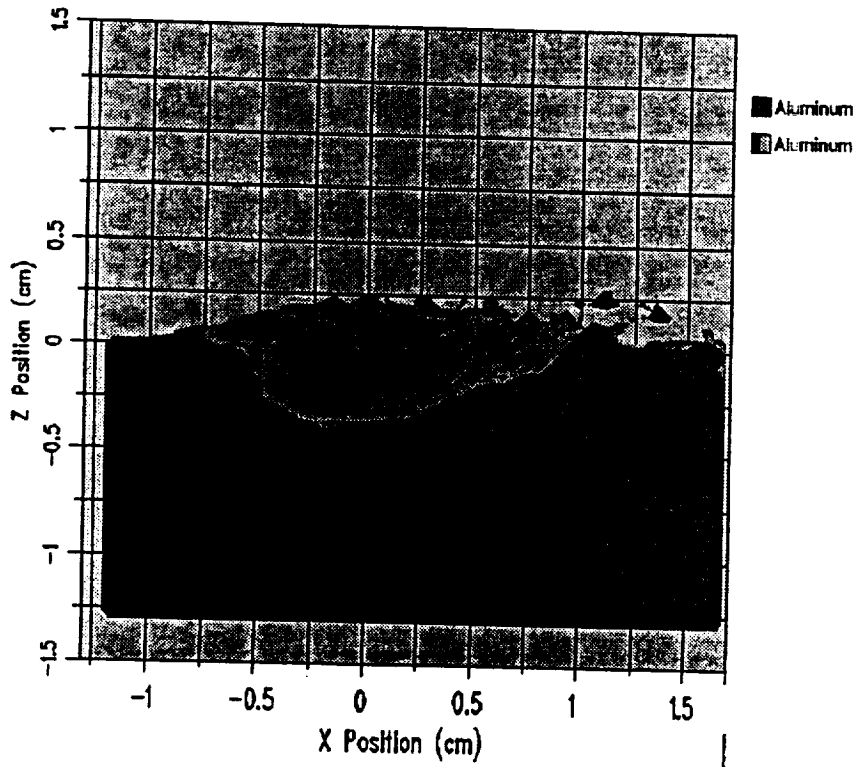


Figure 123.

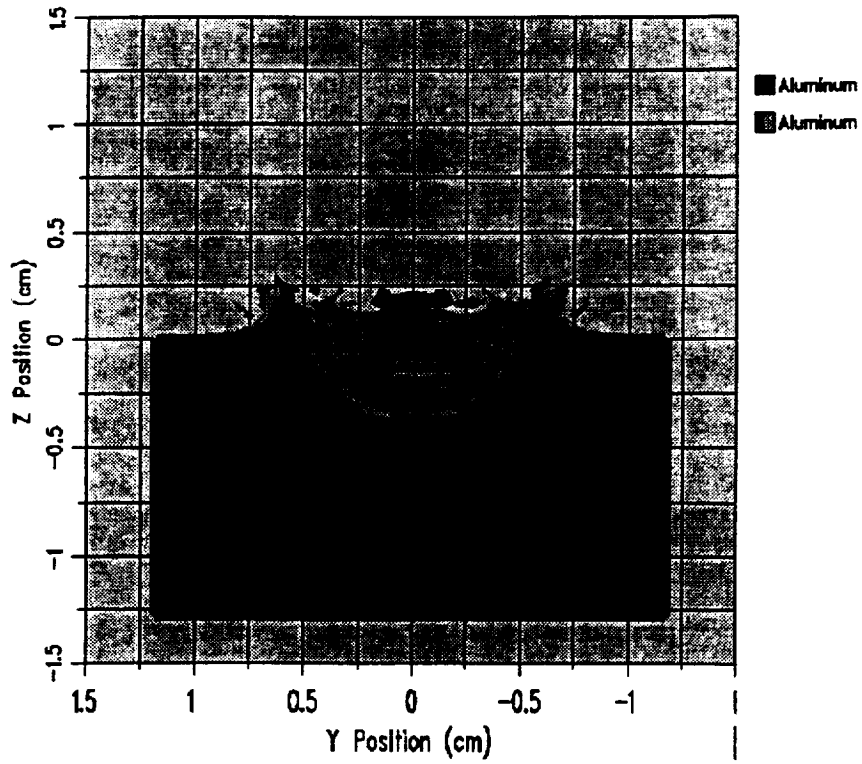


Figure 124.

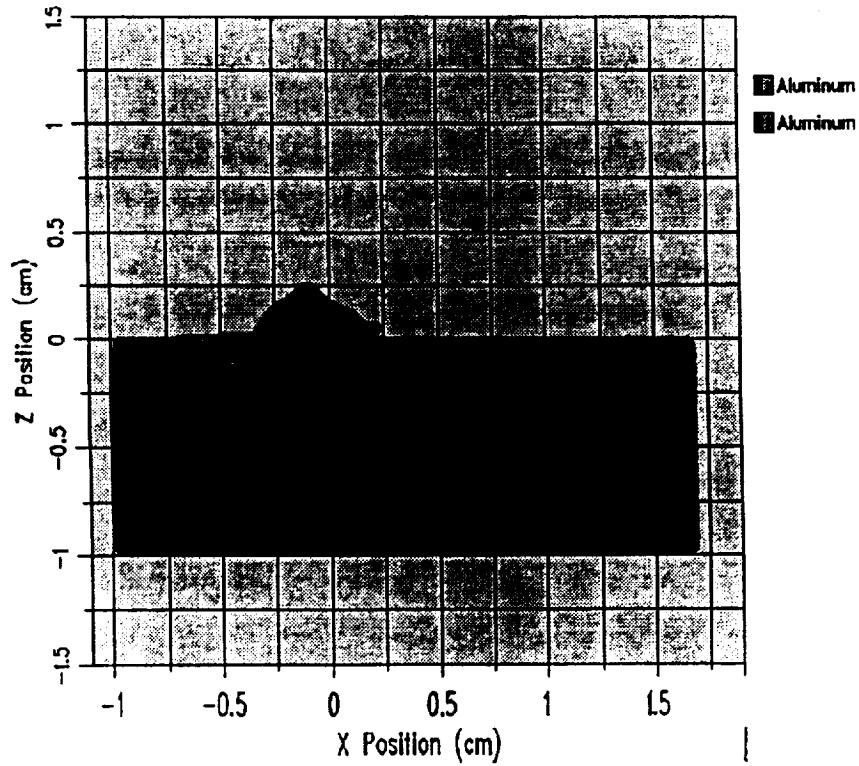
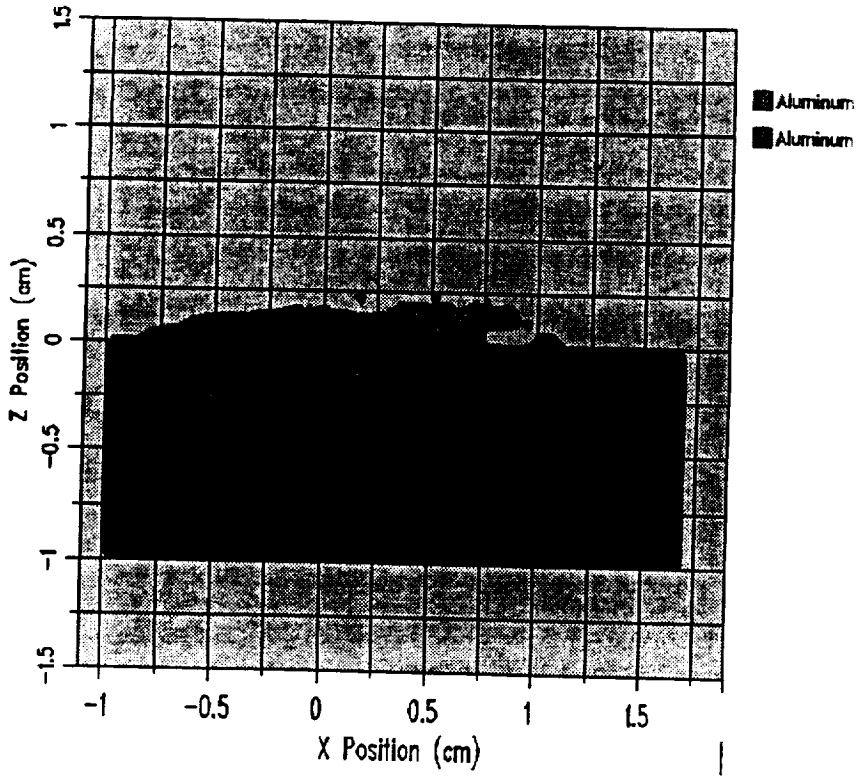
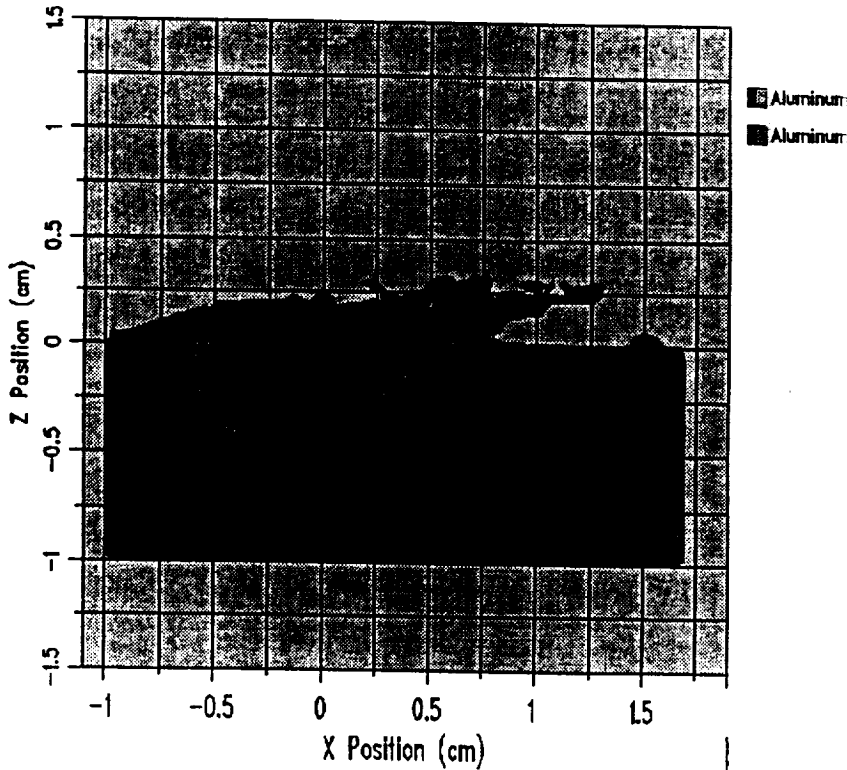


Figure 125.



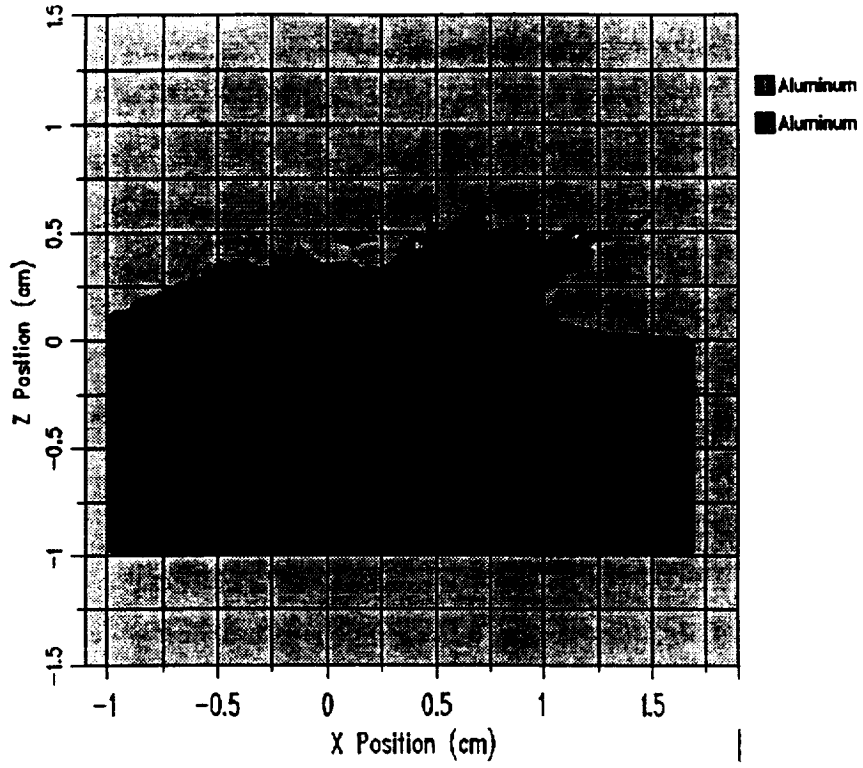
3-D Al into Al Plate, 50 degrees, 5.0 km/s, .06 cm zones
AZSDFN 1/26/93 19:22:00 CTH 141 Time 2.6055x10⁻⁶ s

Figure 126.



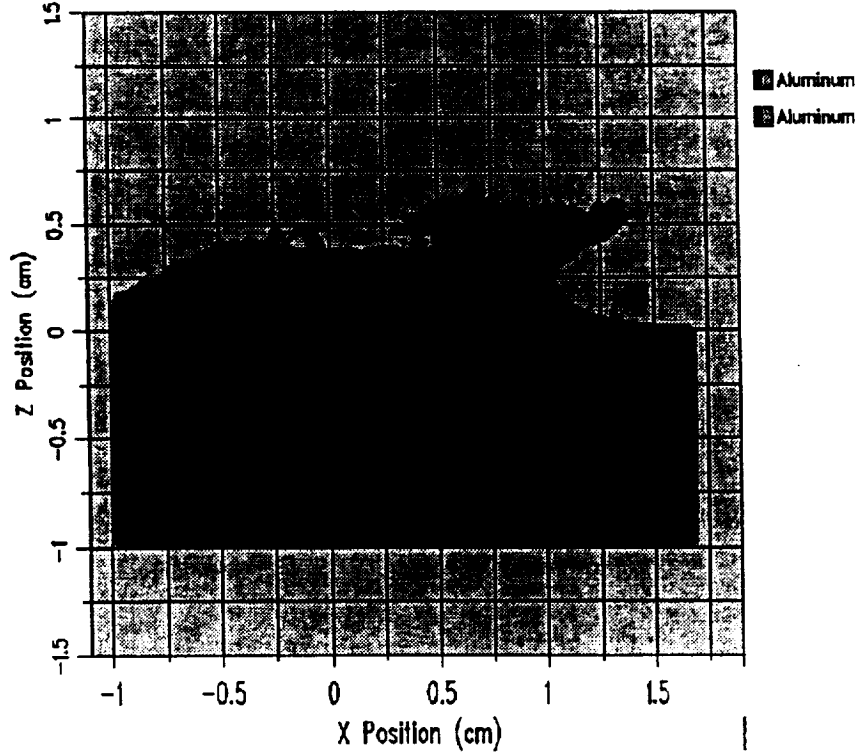
3-D Al into Al Plate, 50 degrees, 5.0 km/s, .06 cm zones
AZSDFN 1/26/93 19:39:41 CTH 161 Time 3.4148x10⁻⁶ s

Figure 127.



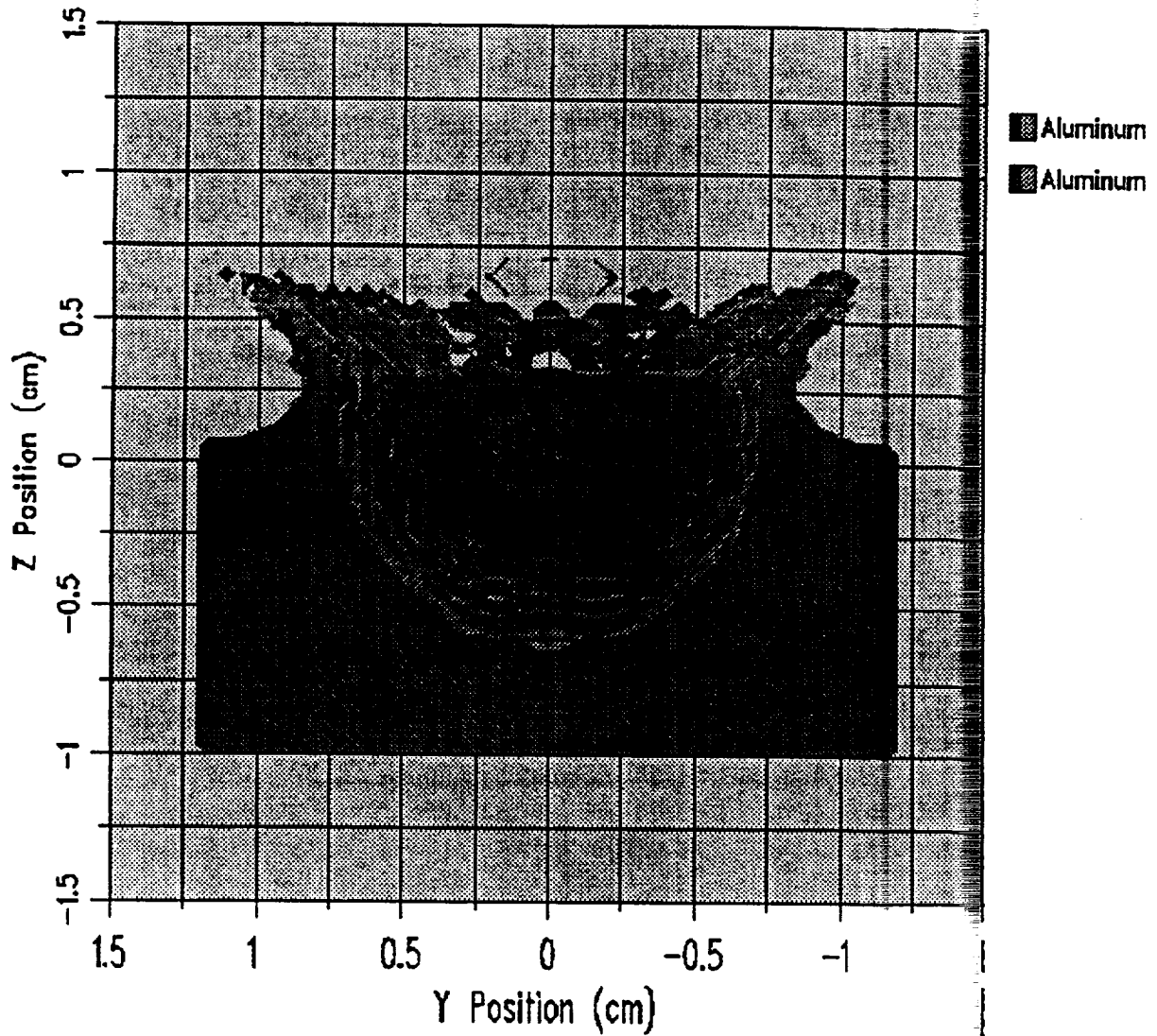
3-D Al into Al Plate, 50 degrees, 5.0 km/s, .06 cm zones
AZSDFN 1/26/93 20:35:02 CTH 219 Time 6.0445x10⁻⁶ s

Figure 128.



3-D Al into Al Plate, 50 degrees, 5.0 km/s, .06 cm zones
AZSDFN 1/26/93 20:54:37 CTH 238 Time 7.0047x10⁻⁶ s

Figure 129.



3-D Al into Al Plate, 50 degrees, 5.0 km/s, .06 cm zone
AZSDFN 1/26/93 20:50:31 CTH 234 Time 6.8016 $\times 10^{-6}$ s

Figure 130. Comparison of Watts' Equations with CTH Predictions for Aluminum on Aluminum (Al 6061-T6)

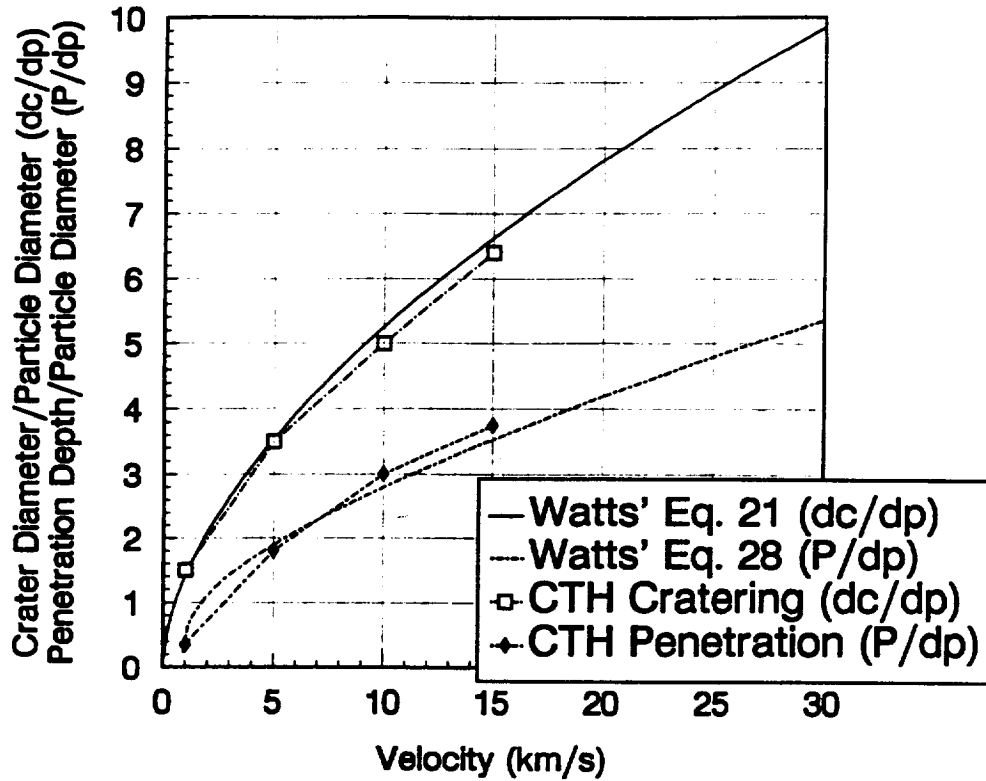


Figure 131. Comparison of Watts' and Bruce's Equations for Aluminum on Aluminum

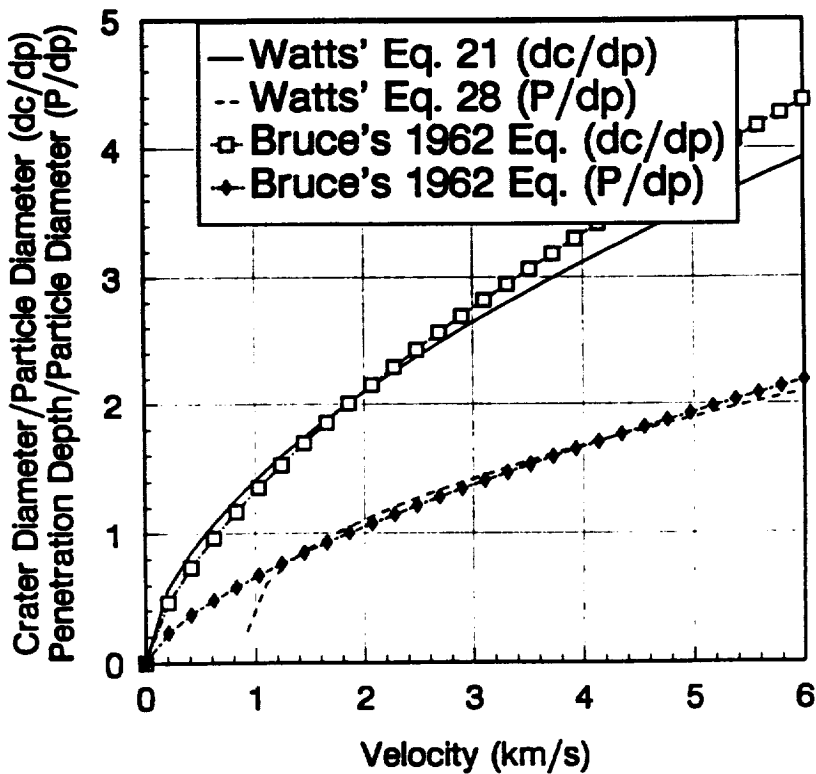


Figure 132. Comparison of Watts' and Bruce's Equations for Aluminum on Aluminum

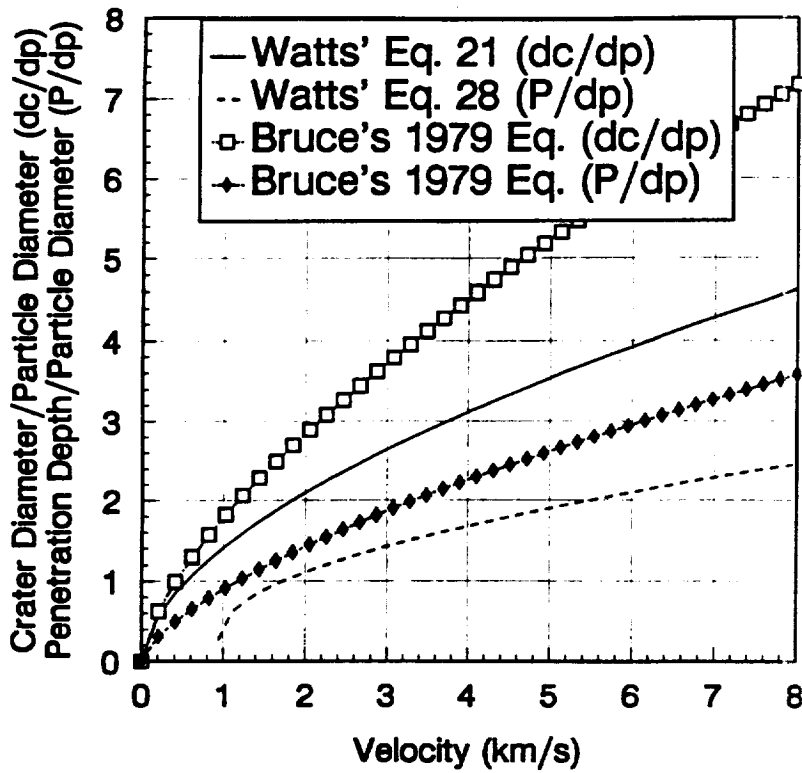


Figure 133. Comparison of Watts' and Christman's Equations for Aluminum on Aluminum

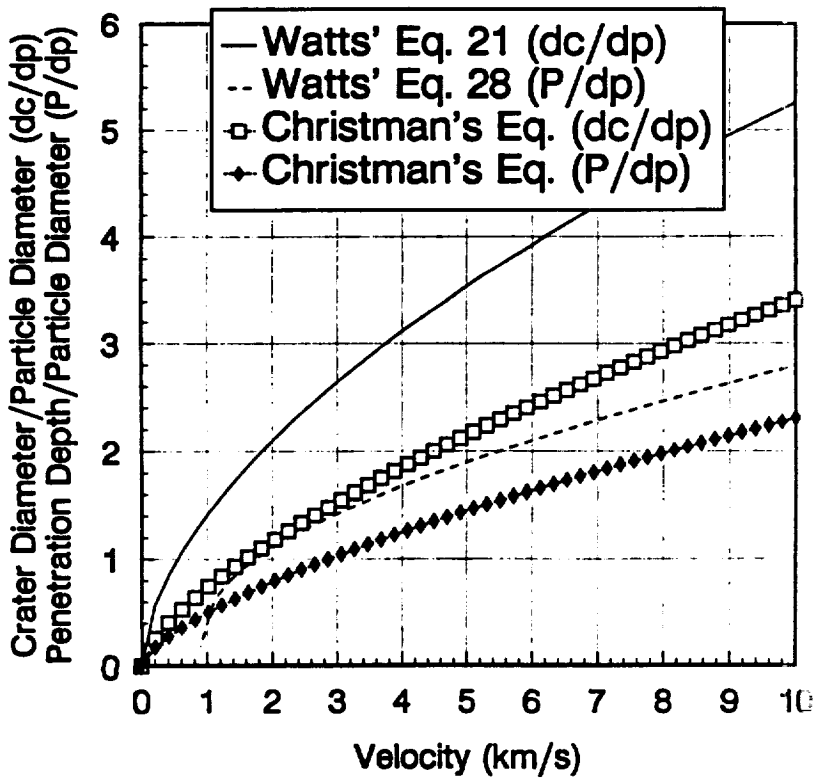


Figure 134. Comparison of Watts' and Cour-Palais' Equations for Aluminum on Aluminum (Al 6061-T6)

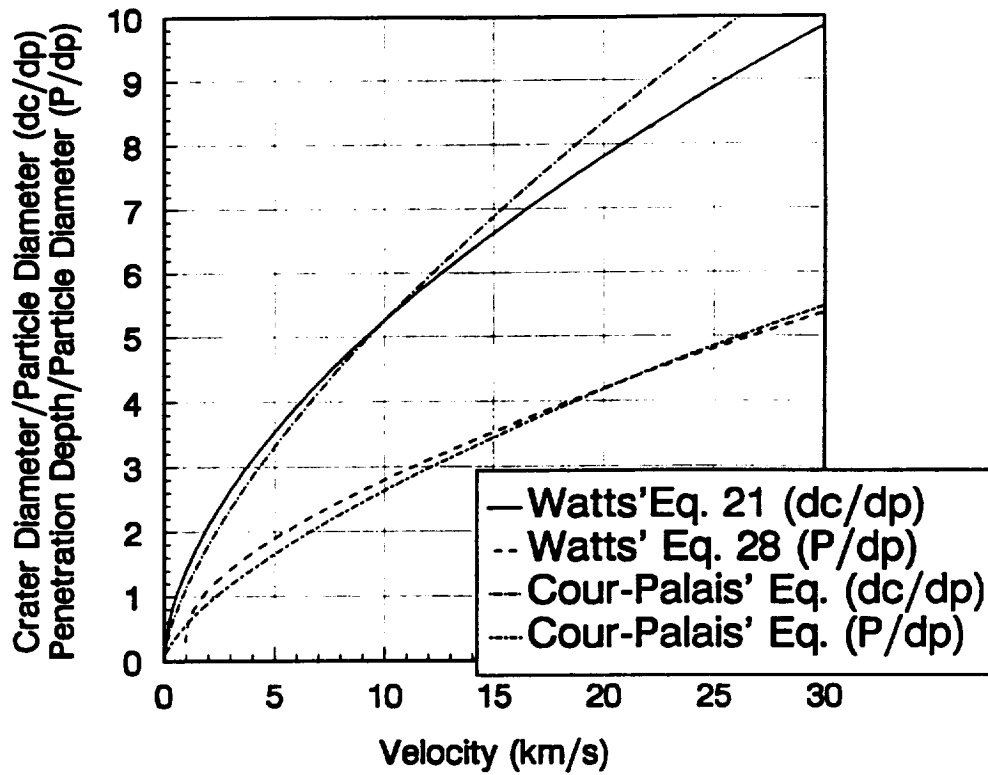


Figure 135. Comparison of Watts' and Dunn's Equations for Aluminum on Aluminum

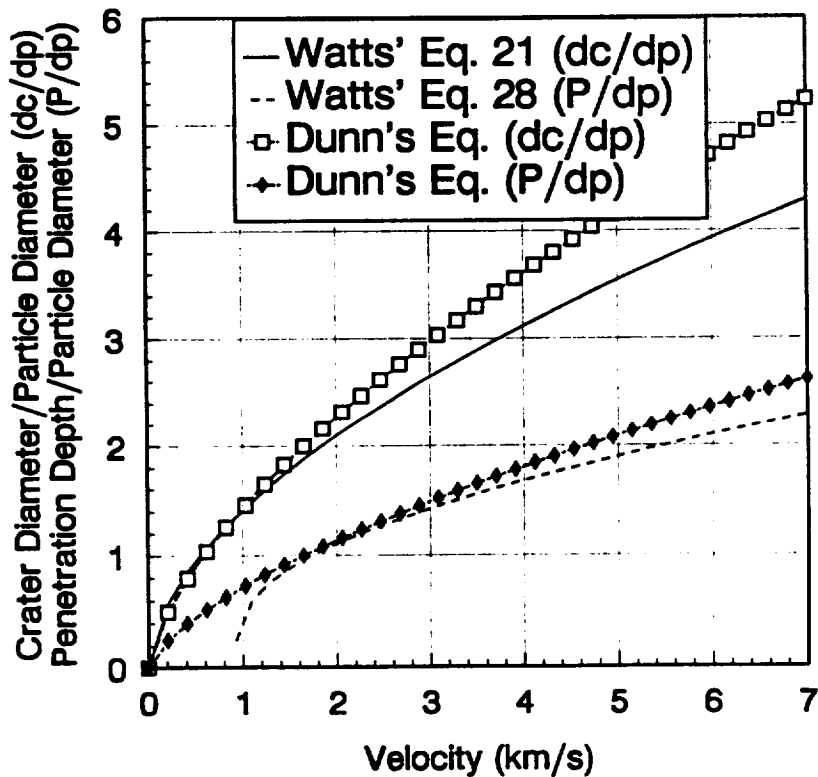


Figure 136. Comparison of Watts' and Goodman-Liles' Equations for Aluminum on Aluminum

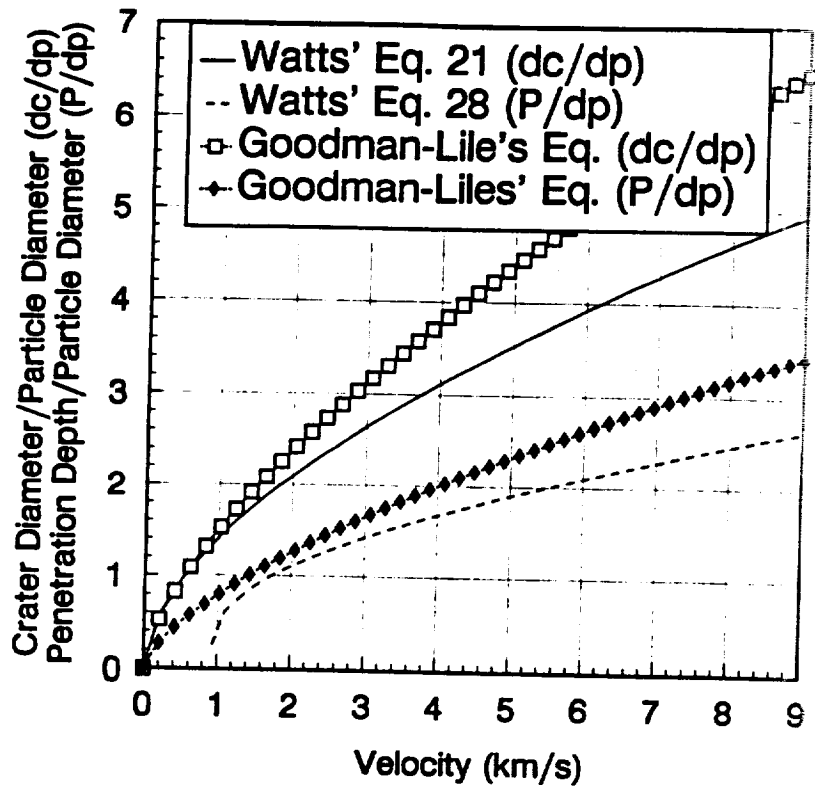


Figure 137. Comparison of Watts' and Herrmann-Jones' Equations for Aluminum on Aluminum

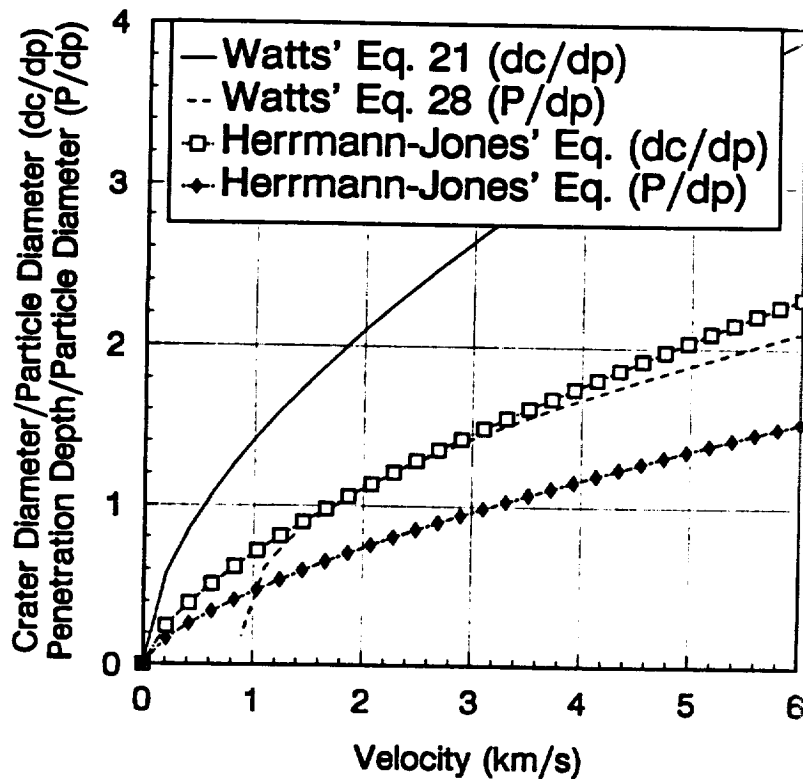


Figure 138. Comparison of Watts' and Sawle's Equations for Aluminum on Aluminum

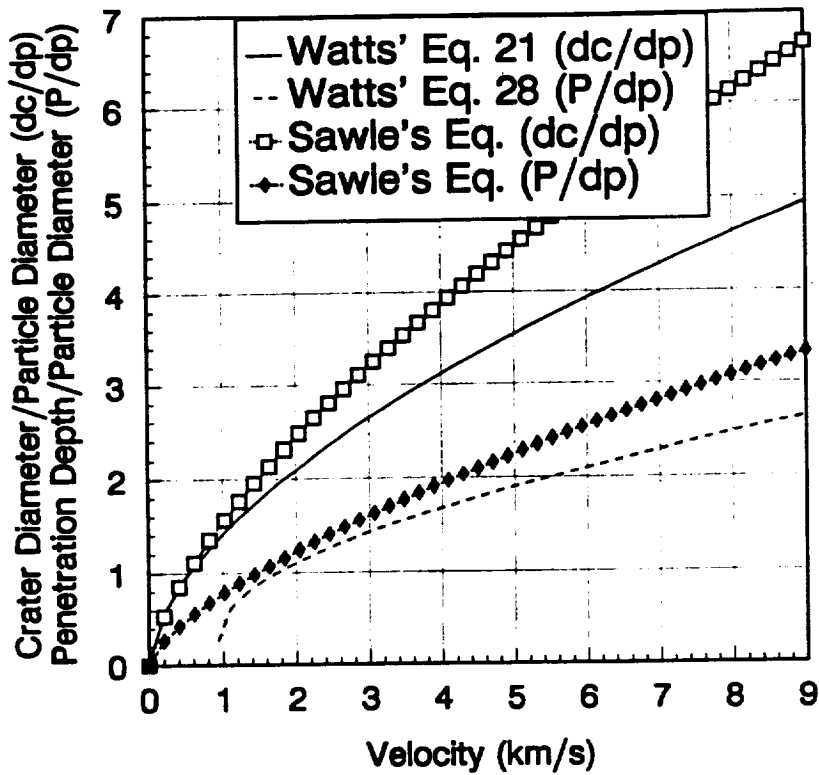


Figure 139. Comparison of Watts' and Sedgwick's Equations for Aluminum on Aluminum

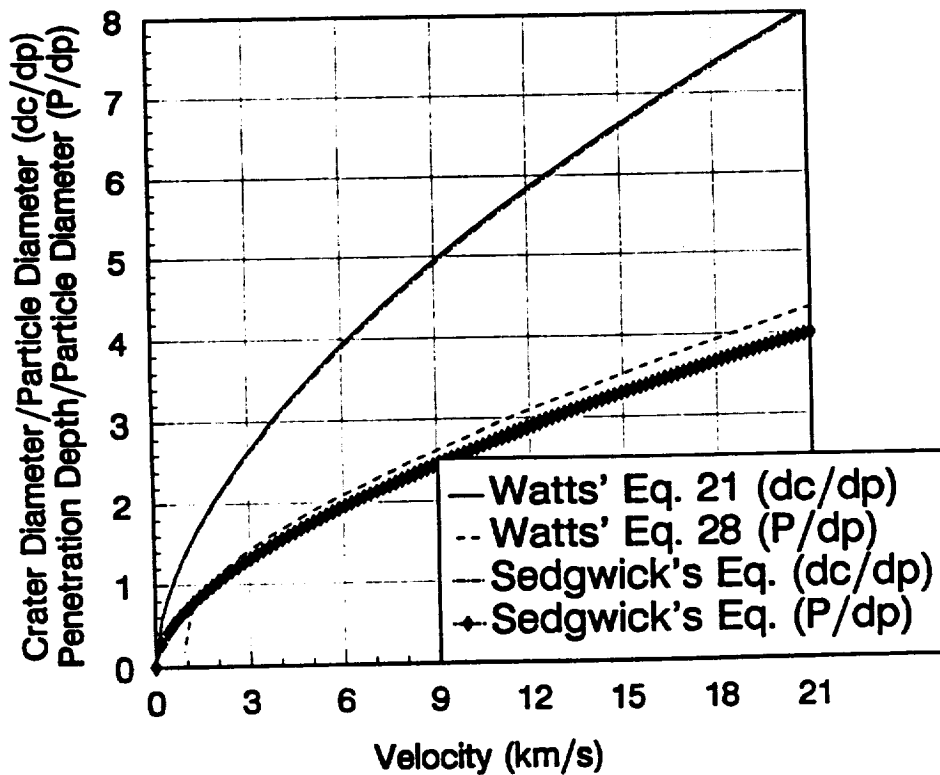


Figure 140. Comparison of Watts' and Sorenson's Equations for Aluminum on Aluminum

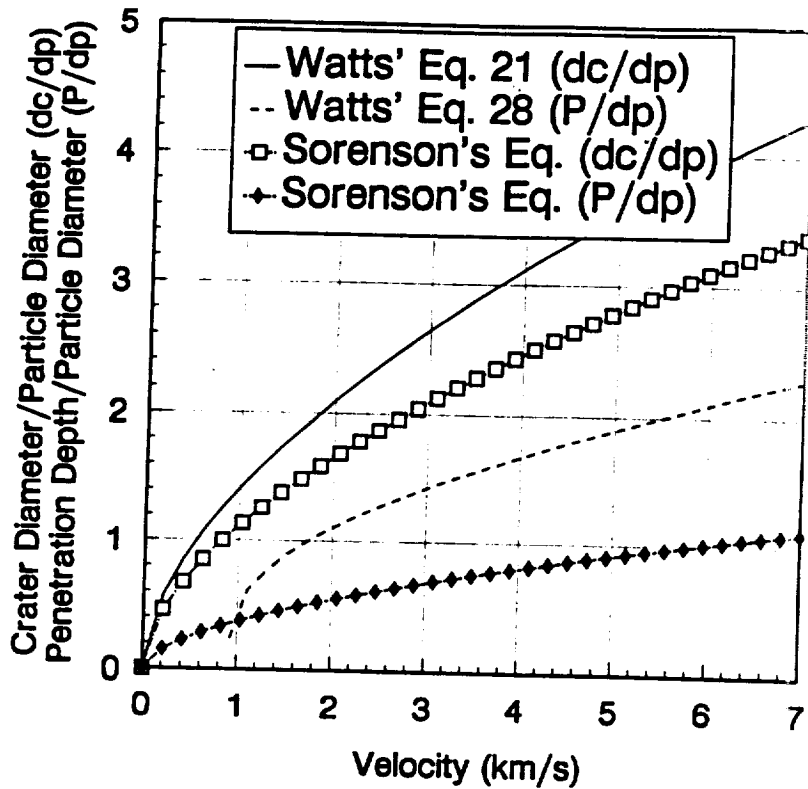


Figure 141. Comparison of Watts' and Summers-Charters' Equations for Aluminum on Aluminum

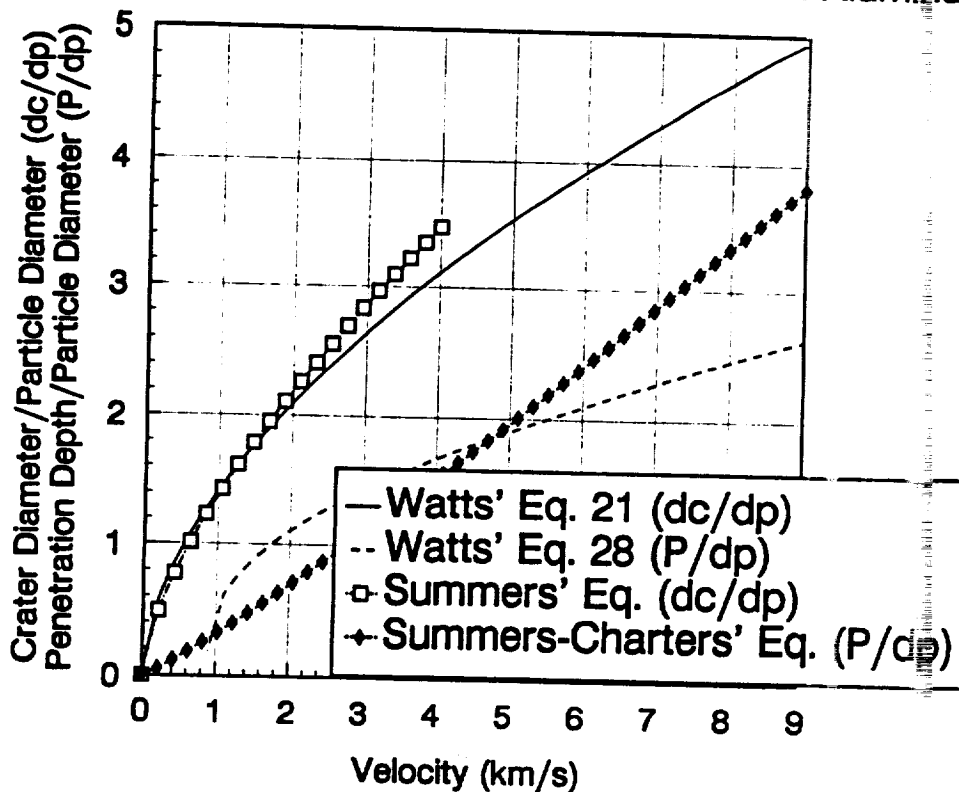


Figure 142. Comparison of Watts' and Bruce's Equations for Aluminum on TFE Teflon (Assumes σ_t Equals σ_y for TFE Teflon)

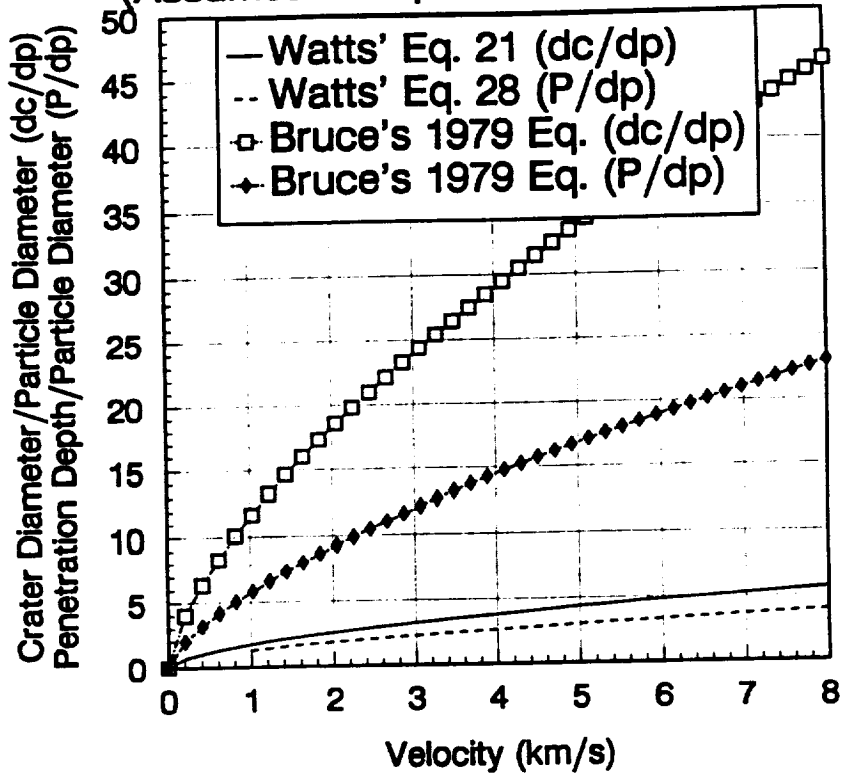


Figure 143. Comparison of Watts' and Cour-Palais' Equations for Aluminum on TFE Teflon

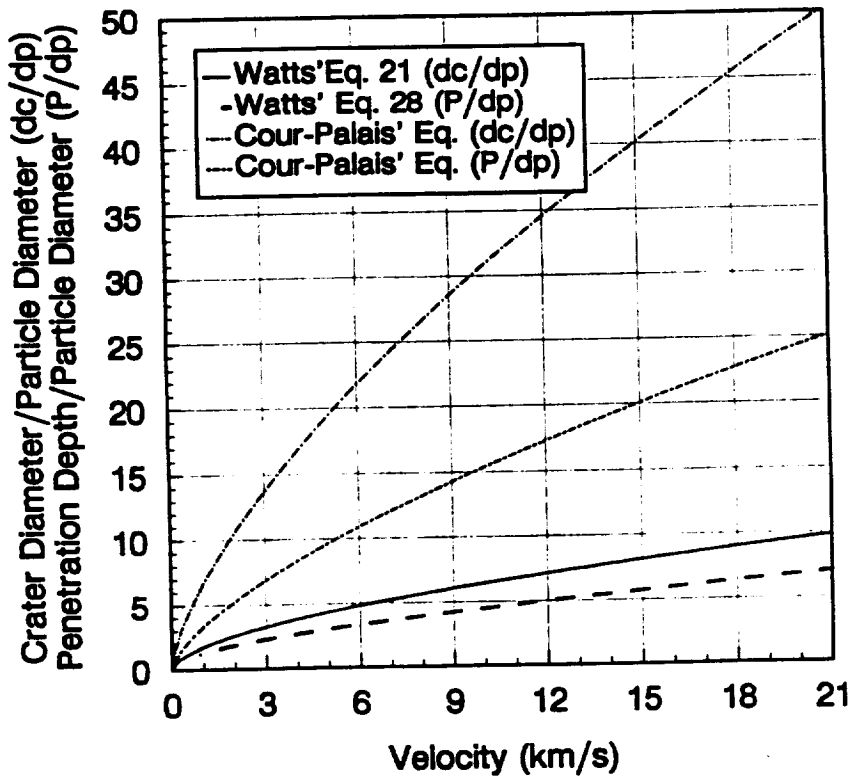


Figure 144. Comparison of Watts' and Dunn's Equations for Aluminum on TFE Teflon (Assumes σ_{yt} Equals Y_t for TFE Teflon)

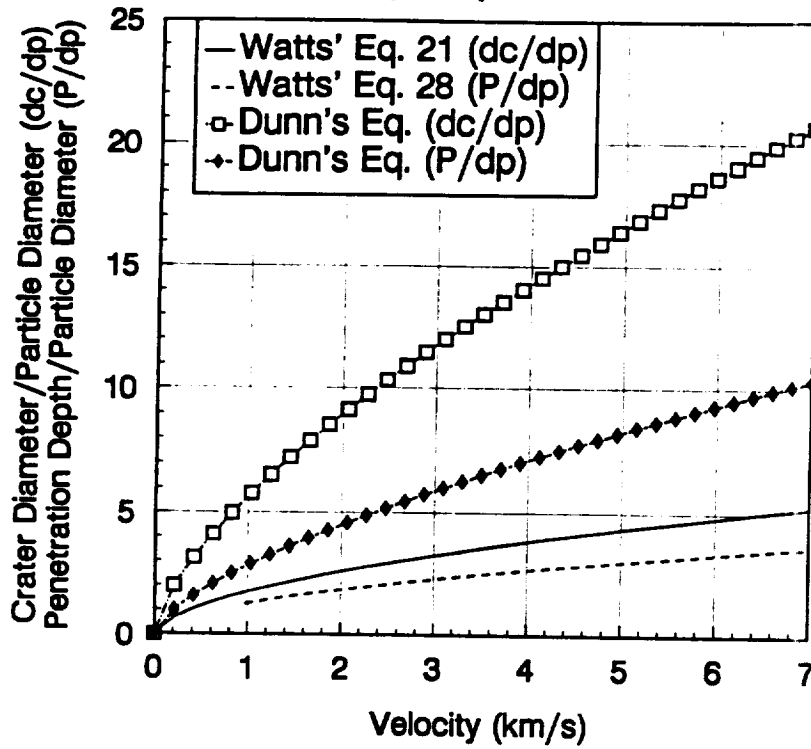


Figure 145. Comparison of Watts' and Sedgwick's Equations for Aluminum on TFE Teflon

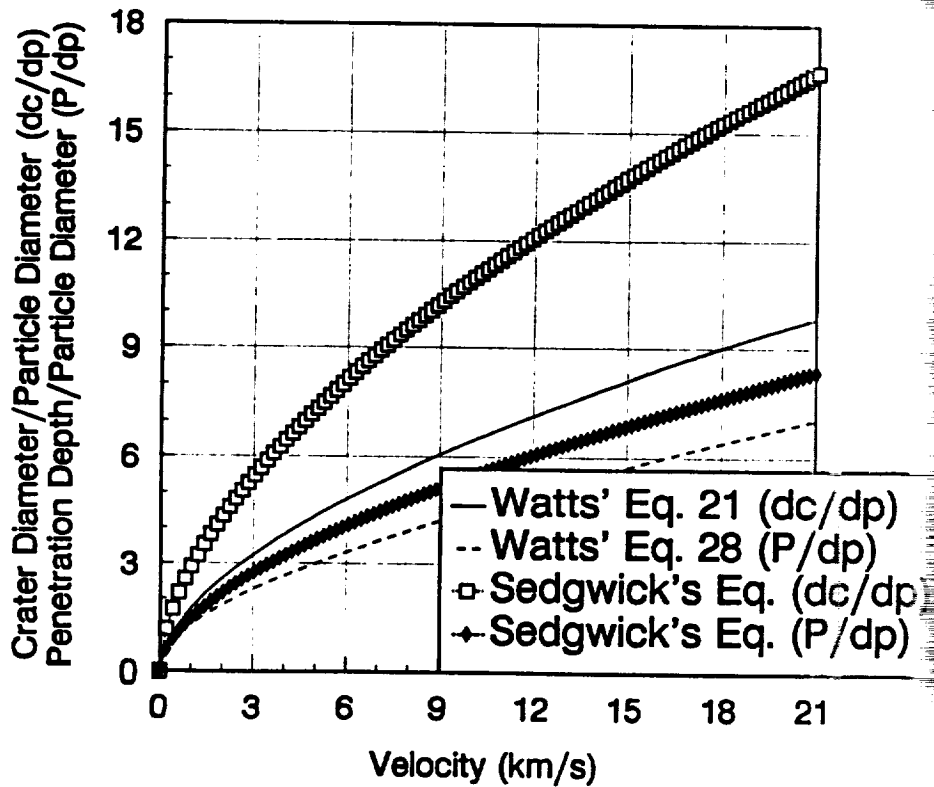


Figure 146. Comparison of Watts' and Sorenson's Equations for Aluminum on TFE Teflon (Assumes St Equals Yt for TFE Teflon)

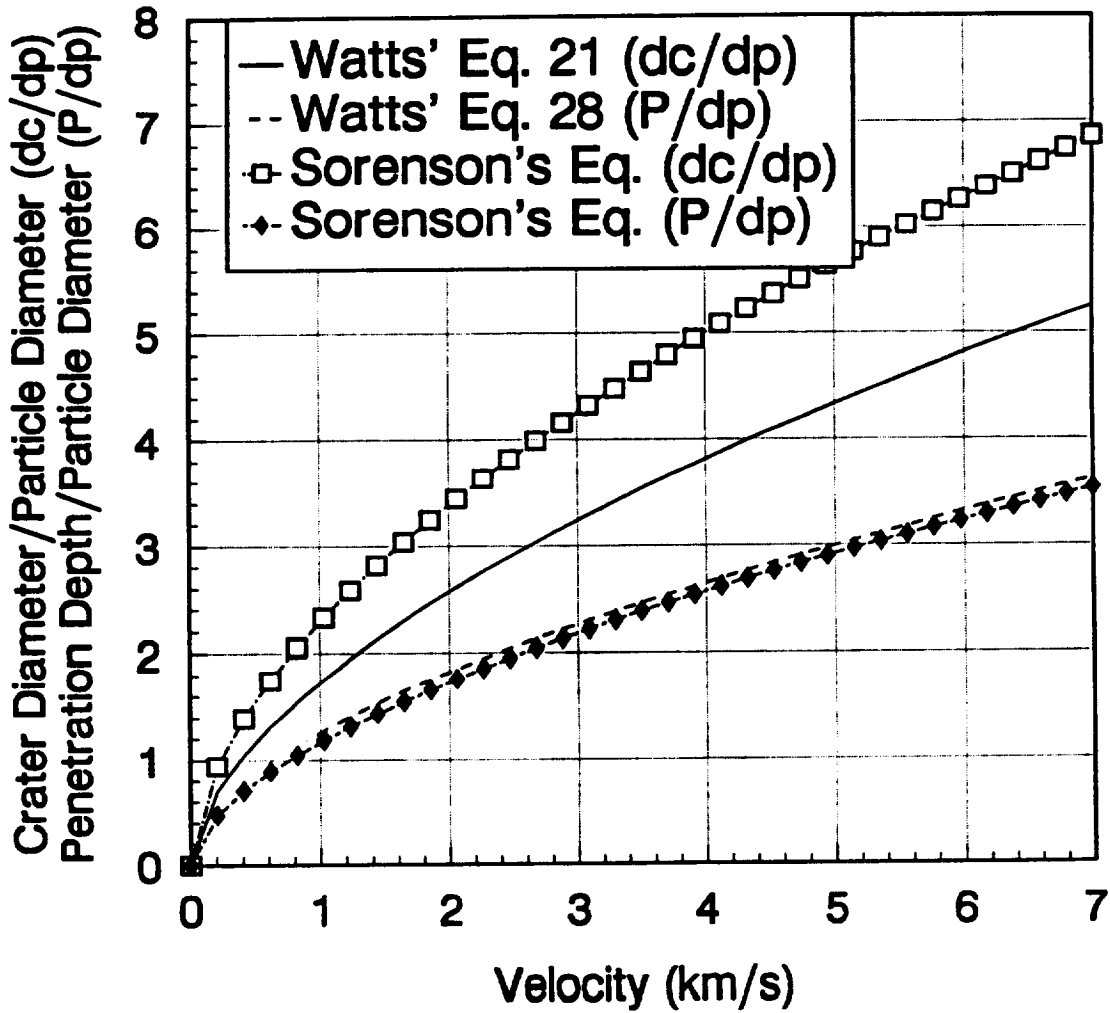


Figure 147. Comparison of Watts' and McDonnell & Sullivan's Equations for Al into Al (Al 6061-T6)

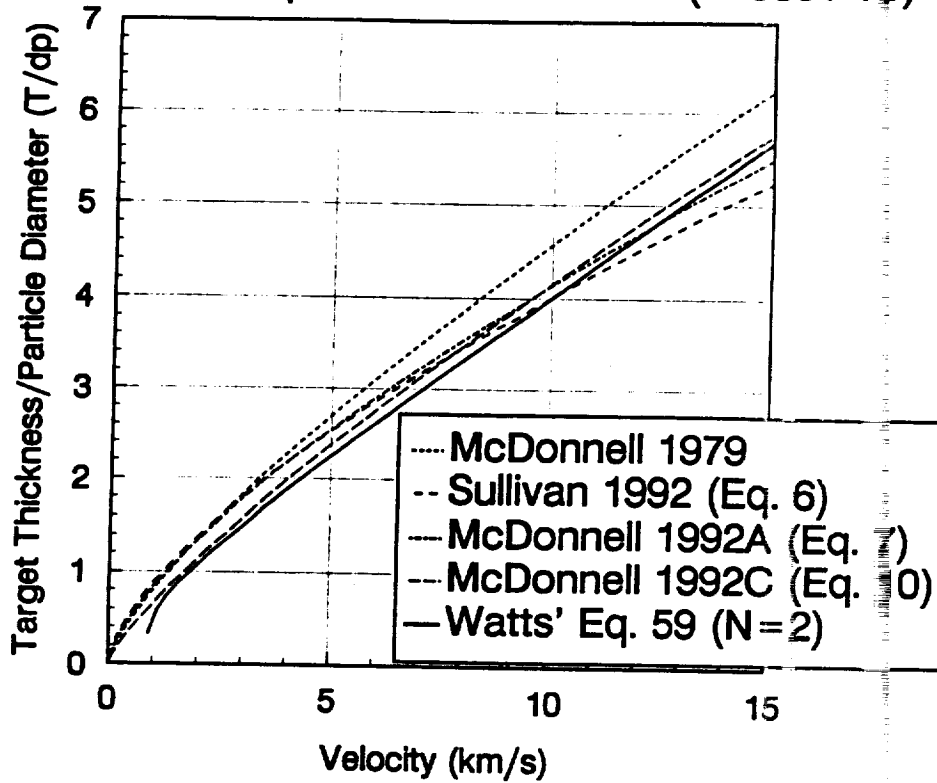


Figure 148. Comparison of Watts' Equation 59 versus Other Investigators' Equations for Al into Al

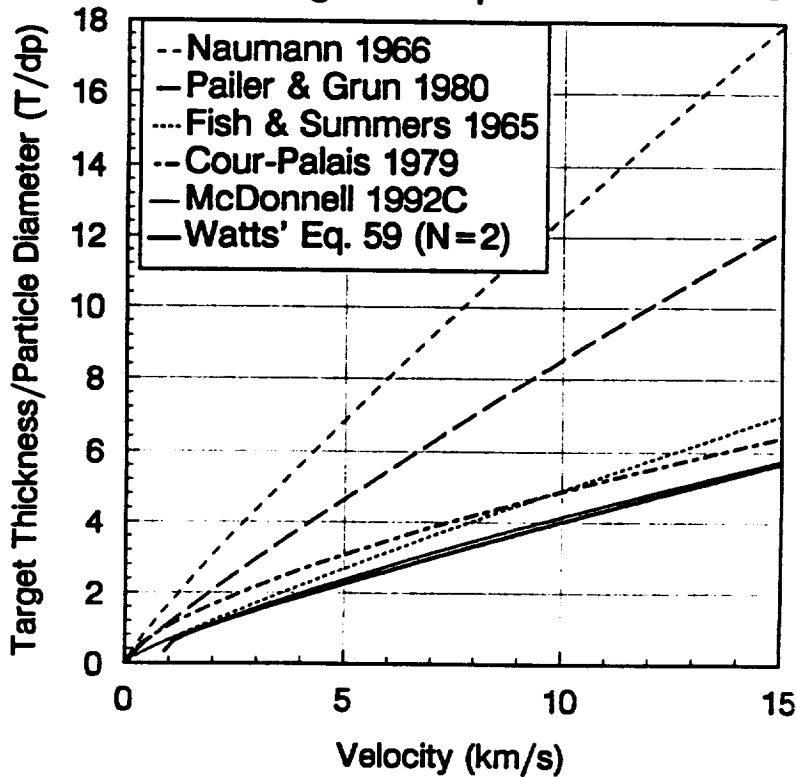


Figure 149. Comparison of Watts' and McDonnell & Sullivan's Equations for Al into TFE Teflon

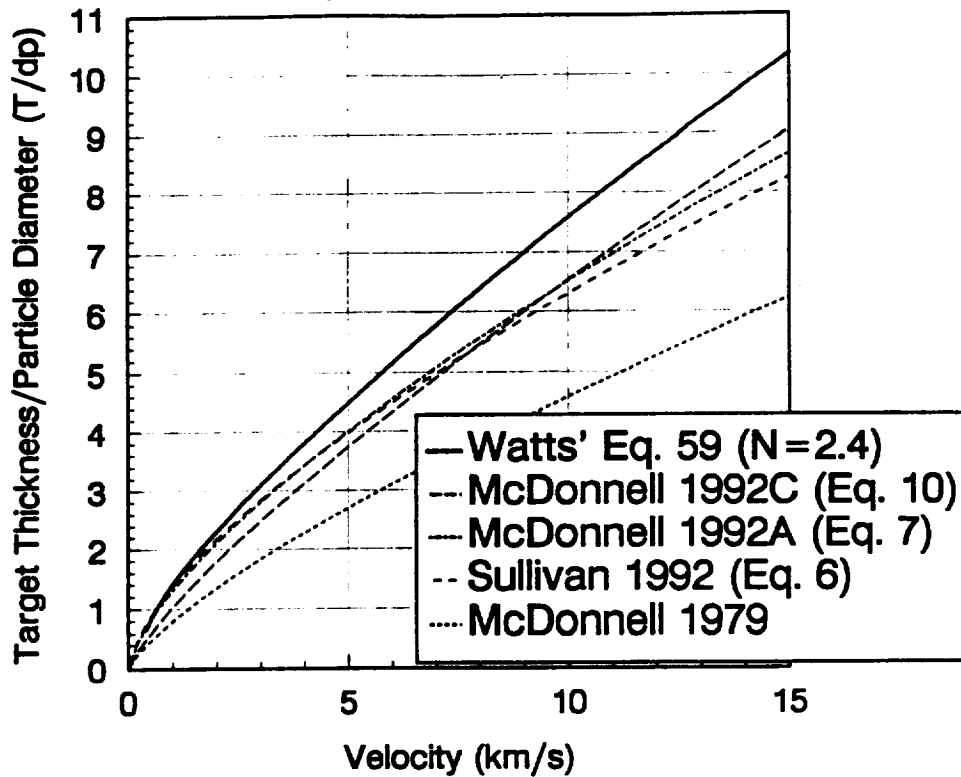


Figure 150. Comparison of Watts' Equation 59 versus Other Investigators' Equations for Al into TFE Teflon

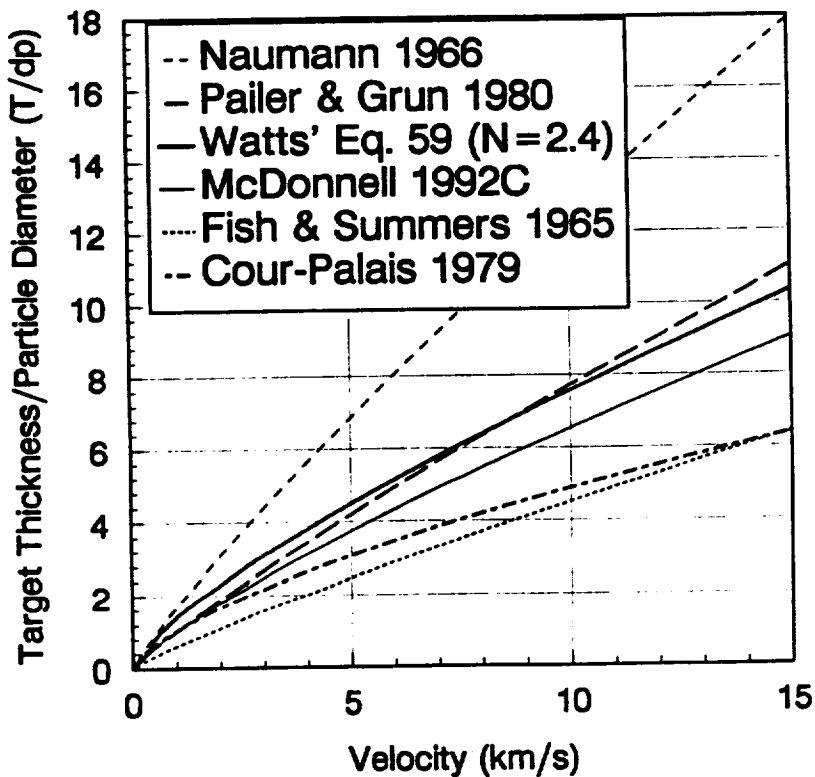


Figure 151.

Soda Lime Glass \rightarrow Aluminum 6061-T6

$D_p = 3.17 \text{ mm}$ $V = 5.9 \text{ km/s}$

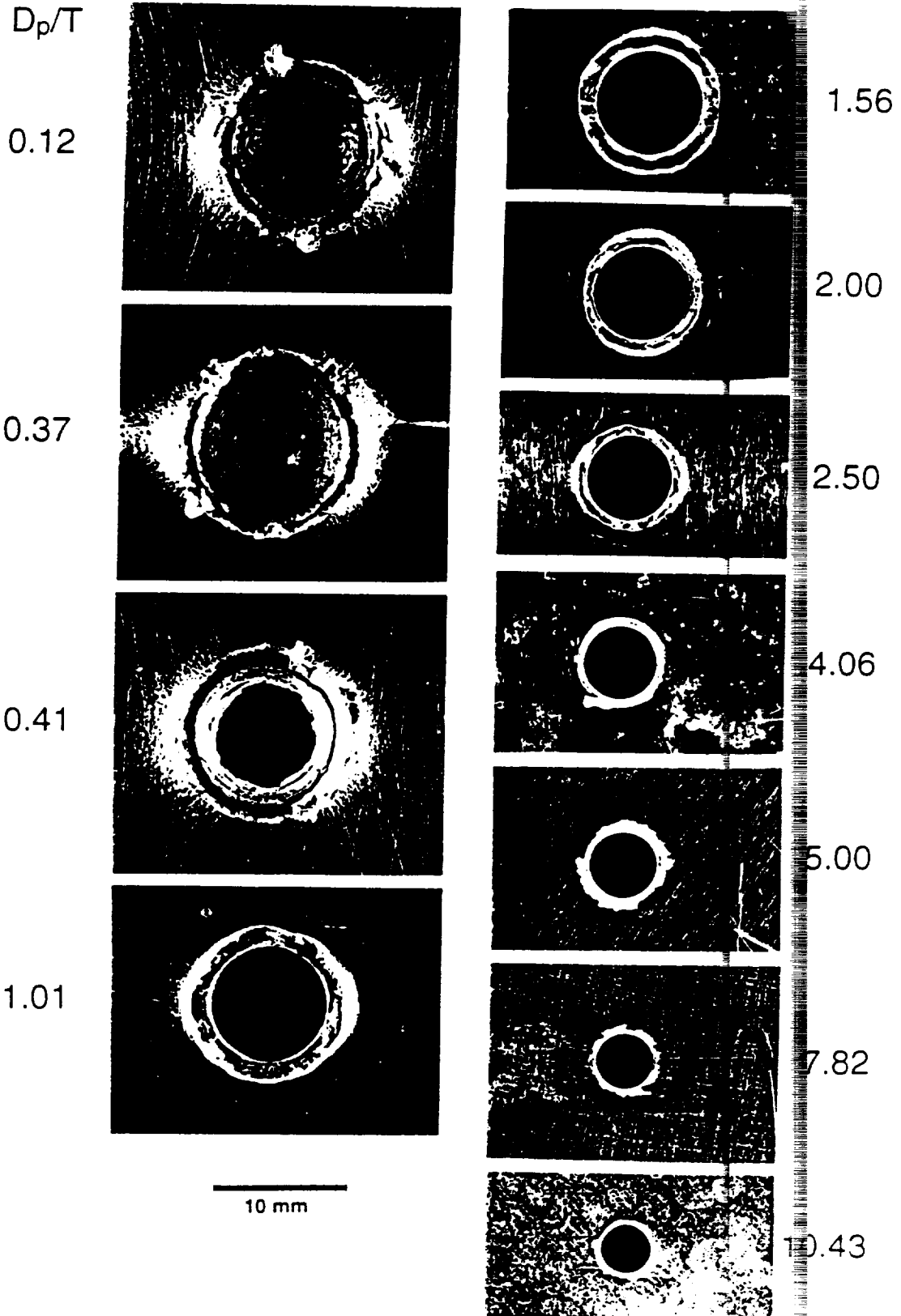


Figure 152.

Soda Lime Glass → Aluminum 6061-T6
 $D_p = 3.17 \text{ mm}$ $V = 5.9 \text{ km/s}$
Back-Side

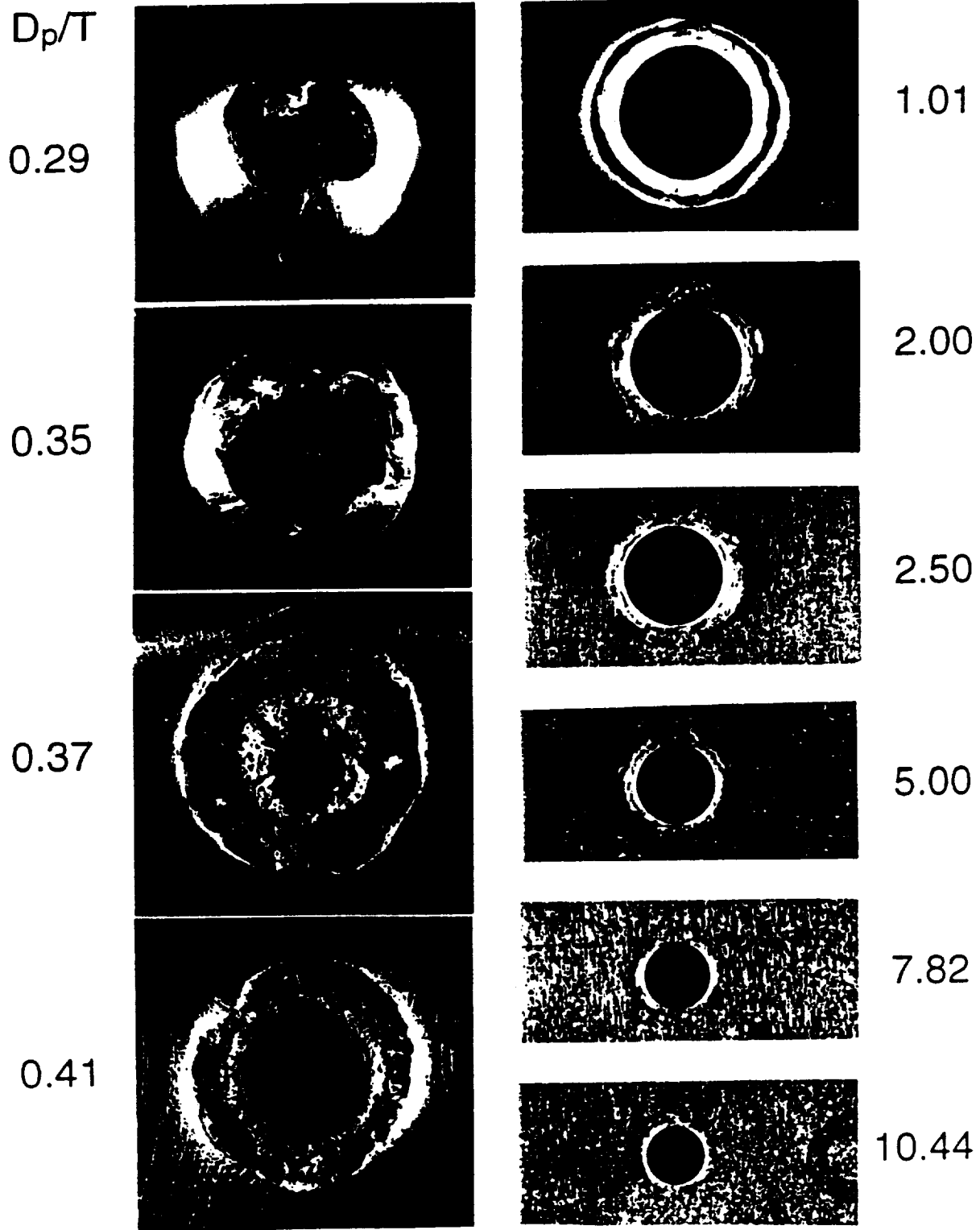


Figure 153.

Soda Lime Glass → Lead

$D_p = 3.17 \text{ mm}$ $V = 6.3 \text{ km/s}$

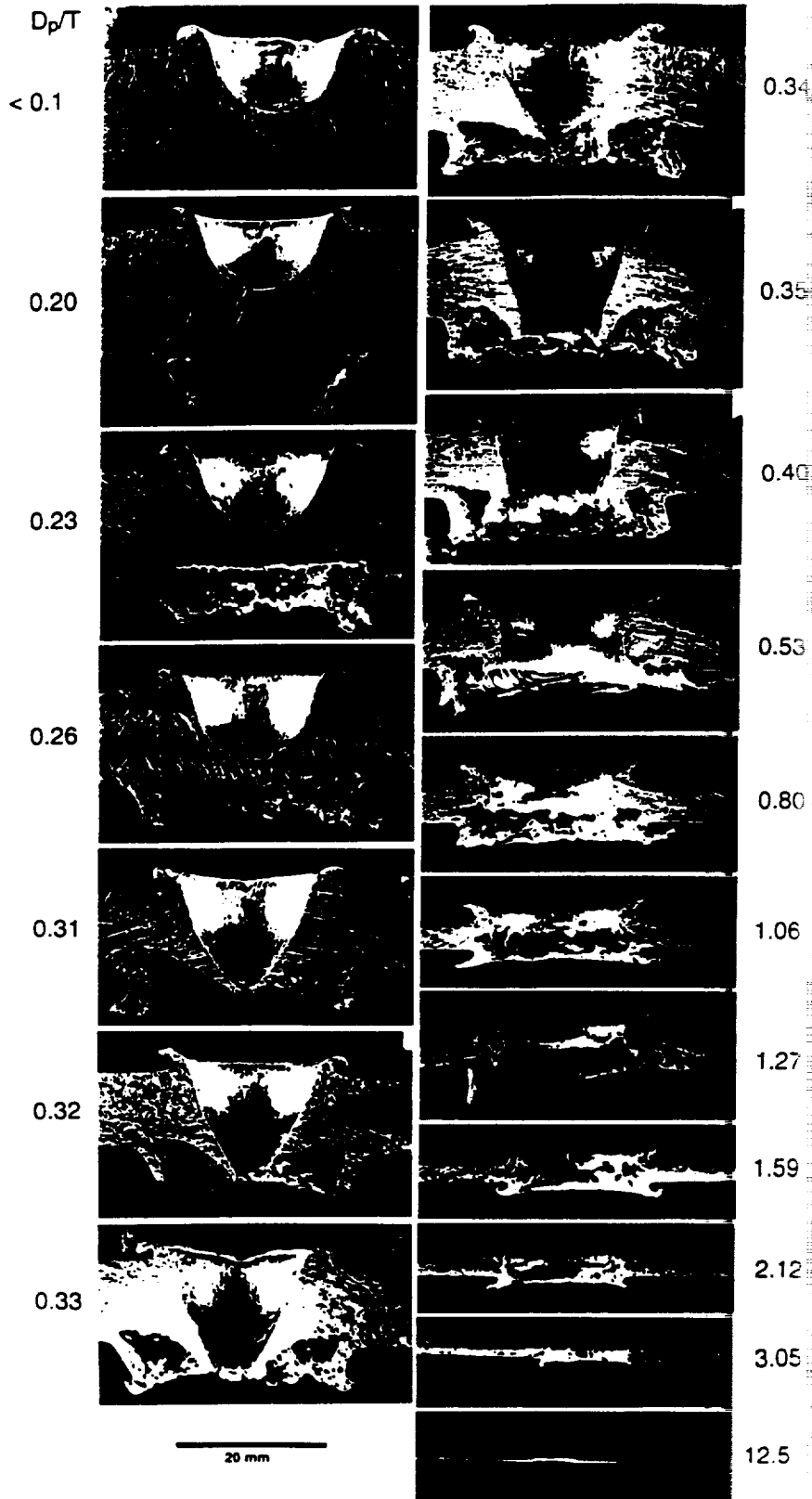


Figure 154.

Soda Lime Glass → Lead

$D_p = 3.175 \text{ mm}$ $V = 6.3 \text{ km/s}$

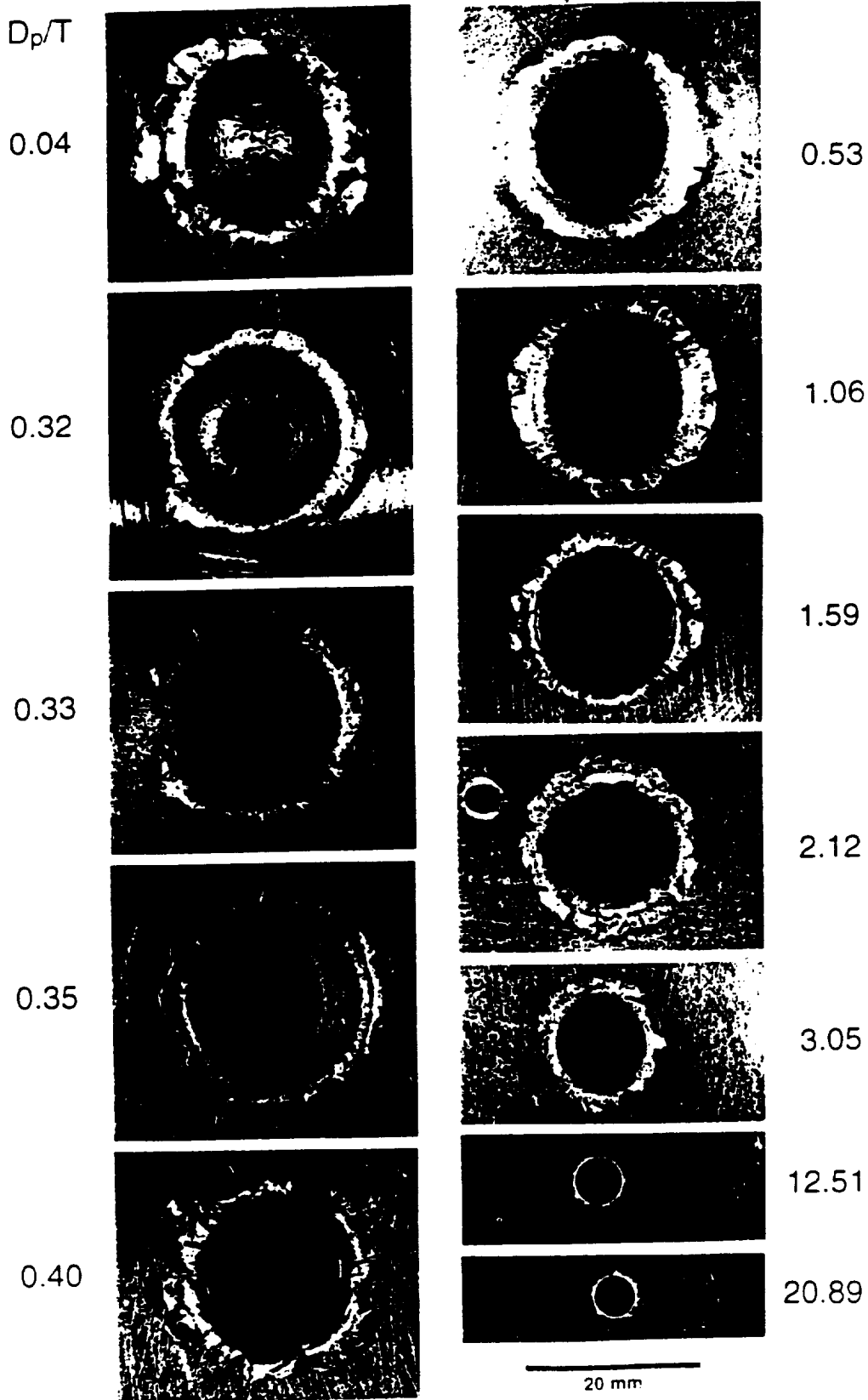
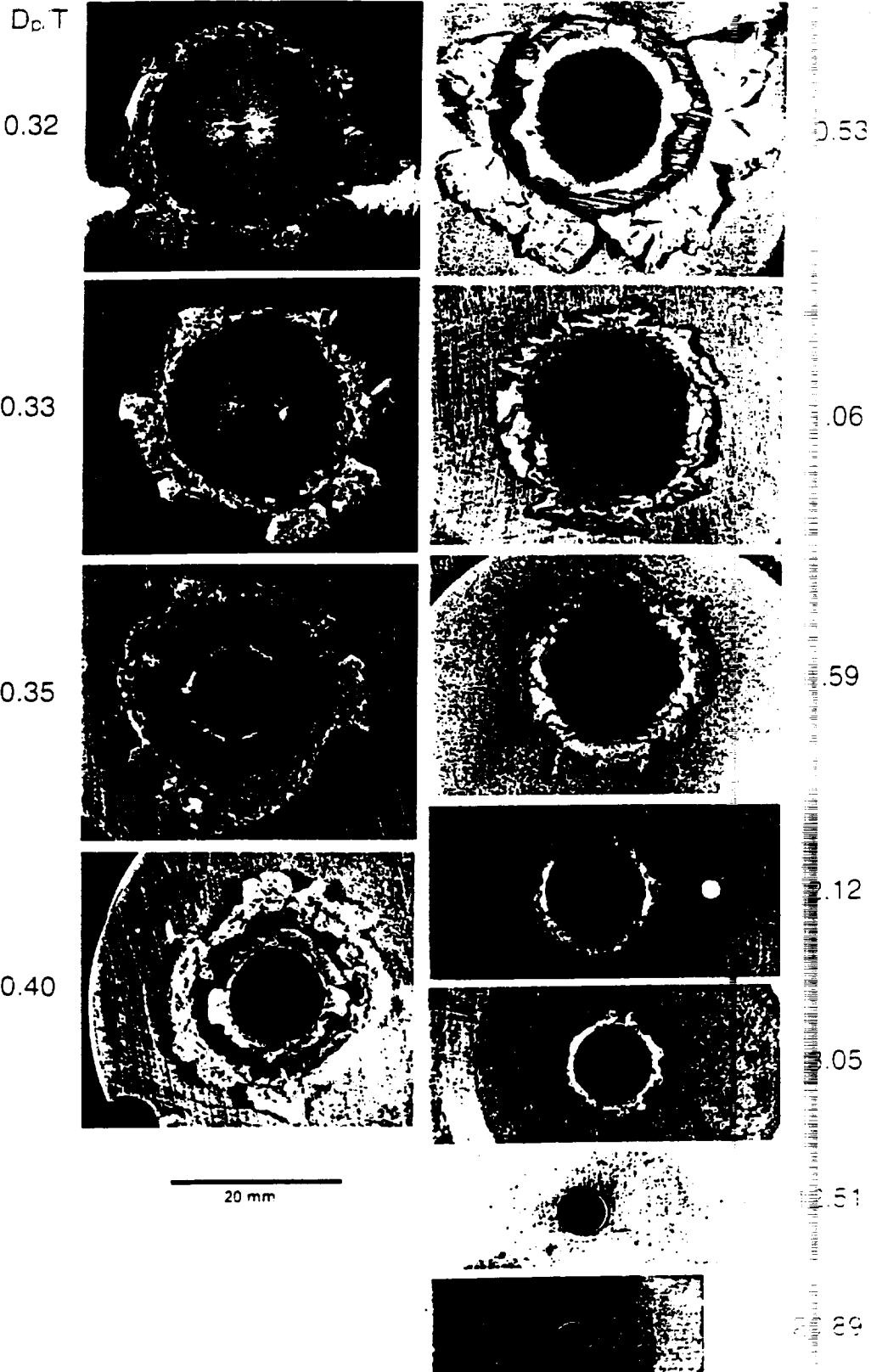


Figure 155.

Soda Lime Glass → Lead

$D_c = 3.175 \text{ mm}$ $V = 6.3 \text{ km.s}$

Back-Side



APPENDIX B - OTHER SCALING LAWS

**NASA
Technical
Memorandum**

NASA TM-100358

Reprinted from:

**OBLIQUE HYPERVELOCITY IMPACT RESPONSE
OF DUAL-SHEET STRUCTURES**

By William P. Schonberg and Roy A. Taylor

**Materials and Processes Laboratory
Science and Engineering Directorate**

January 1989



**National Aeronautics and
Space Administration**

George C. Marshall Space Flight Center

APPENDIX

Penetration Depth Equations

Reference No. 27:

$$p/d = 2.28 (\rho_p/\rho_t)^{2/3} (V/C)^{2/3} , \quad V < 9 \text{ km/sec} \quad (\text{P-1})$$

Reference No. 28:

$$p/d = 1.96 (\rho_p/\rho_t)^{1/2} (V/C)^{2/3} , \quad V < 6 \text{ km/sec} \quad (\text{P-2})$$

Reference No. 29:

$$p/d = 1.5 (\rho_p/\rho_t)^{1/3} (\rho_p V^2/2S_t)^{1/3} , \quad V < 8 \text{ km/sec} \quad (\text{P-3})$$

Reference No. 30:

$$p/d = 2.35 (\rho_p/\rho_t)^{0.70} (V/C)^{2/3} , \quad V < 9 \text{ km/sec} \quad (\text{P-4})$$

Reference No. 31:

$$p/d = 0.63 (\rho_p V^2/\sigma_{yt})^{1/3} , \quad V < 7 \text{ km/sec} \quad (\text{P-5})$$

Reference No. 32:

$$p/d = 0.482 (\rho_p/\rho_t)^{0.537} (V/C)^{0.576} (Y_t/\rho_t C^2)^{-0.235} \quad V < 21 \text{ km/sec} \quad (\text{P-6})$$

Reference No. 33:

$$p/d = 8.355 \times 10^{-4} \rho_p^{2/3} \rho_t^{-1/3} (V^2/H_t)^{1/3} , \quad V < 9.5 \text{ km/sec} \quad (\text{P-7})$$

Reference No. 34:

$$p/d = 2.0 (\rho_p/\rho_t)^{4.52} (V/C)^{1.136} , \quad V < 9 \text{ km/sec} \quad (\text{P-8})$$

Reference No. 35:

$$p/d = 0.311 (\rho_p/\rho_t)^{0.17} (\rho_p V^2/S_t)^{0.285}, \quad V < 7 \text{ m/sec} \quad (P)$$

Reference No. 36:

$$p/d = 0.36 (\rho_p/\rho_t)^{2/3} (\rho_t V^2/B_t)^{1/3}, \quad V < 6 \text{ km/sec} \quad (P)$$

Reference No. 37:

$$p = 2.973 \times 10^{-7} d^{1.1} H_t^{-0.25} \rho_p^{0.5} \rho_t^{-0.167} V^{4/3}, \quad V < \sim 3 \text{ km/sec} \quad (P)$$

$$p = 1.129 \times 10^{-6} d^{1.056} H_t^{-0.25} \rho_p^{0.5} \rho_t^{-0.167} E_t^{-0.33} V^{4/3}, \quad V < \sim 3 \text{ km/sec} \quad (P)$$

Crater Diameter Equations

Reference No. 18:

$$\alpha d_h^2 p/d^3 = 34 (\rho_p/\rho_t)^{3/2} (V/C)^2, \quad V < 4 \text{ km/sec} \quad (C)$$

Reference No. 35:

$$\alpha d_h^2 p/d^3 = 0.120 (\rho_p/\rho_t)^{0.5} (\rho_p V^2/S_t)^{0.845}, \quad V < 7 \text{ m/sec} \quad (C)$$

Reference No. 28:

$$\alpha d_h^2 p/d^3 = 30.25 (\rho_p/\rho_t)^{3/2} (V/C)^2, \quad V < 6 \text{ m/sec} \quad (C)$$

Reference No. 30:

$$\alpha d_h^2 p/d^3 = 44.10 (\rho_p/\rho_t)^{2/3} (V/C)^2, \quad V < 9 \text{ m/sec} \quad (C)$$

Reference No. 33:

$$\alpha d_h^2 p/d^3 = 2.65 \times 10^{-9} \rho_p^{7/6} \rho_t^{-1/2} V^2/H_t, \quad V < 9 \text{ km/sec} \quad (C)$$

Reference No. 36:

$$\alpha d_h^2 p/d^3 = 0.16 (\rho_p/\rho_t)^{3/2} \rho_p V^2/B_t , \quad V < 6 \text{ km/sec} \quad (\text{C-6})$$

Notation

- d_h ... crater surface diameter (cm)
 d ... projectile diameter (cm)
 p ... crater depth (cm)
 B_t ... target material Brinell Hardness (dynes/cm²)
 C ... speed of sound in target material (cm/sec)
 E_t ... target material elastic modulus (GPa)
 H_t ... target material Brinell Hardness Number (kg/mm²)
 S ... target material static shear strength (dynes/cm²)
 S_t ... target material dynamic hardness (dynes/cm²)
 Y_t ... target material dynamic shear strength (dynes/cm²)
 V ... projectile impact velocity
 α ... crater shape factor
 $\alpha = 0.75$ if $p > d_h/2$
 $\alpha = 1.00$ if $p \leq d_h/2$
 ρ_p ... projectile material mass density (gm/cm³)
 ρ_t ... target material mass density (gm/cm³)
 σ_{yt} ... target material dynamic yield strength (dynes/cm²)

Material Properties

$$B_t = 1.27 \times 10^{10} \text{ dynes/cm}^2$$

$$C = 5.10 \times 10^5 \text{ cm/sec}$$

$$E_t = 7.38 \times 10^{10} \text{ N/m}^2$$

$$S = 2.83 \times 10^9 \text{ dynes/cm}^2$$

$$S_t = 6.37 \times 10^{10} \text{ dynes/cm}^2$$

$$Y_t = 2.78 \times 10^9 \text{ dynes/cm}^2$$

$$\rho_p = 2.71 \text{ gm/cm}^3$$

$$\rho_t = 2.84 \text{ gm/cm}^3$$

$$\sigma_{yt} = 1.85 \times 10^{10} \text{ dynes/cm}^2$$

$$H_t = 130 \text{ kg/mm}^2$$

REFERENCES

1. Whipple, E. L.: Meteorites and Space Travel. *Astron. Journal*, Vol. 52, 1947, p. 5.
2. Burch, G. T.: Multi-plate Damage Study. AF-ATL-TR-67-116, Air Force Armament Library, Elgin Air Force Base, Florida, 1967.
3. D'Anna, P. J.: A Combined System Concept For Control of the Meteoroid Hazard to Space Vehicles. *J. Spacecraft*, Vol. 2, No. 1, 1965, p. 33.
4. Lundeberg, J. F., Lee, D. H., and Bruch, G. T.: Impact Penetration of Manned Spacecraft. *J. Spacecraft*, Vol. 3, No. 2, 1966, p. 182.
5. Lundeberg, J. F., Stern, P. H., and Bristow, R. J.: Meteoroid Protection for Spacecraft Structures. NASA CR 54201, Washington, D.C., 1968.
6. McMillan, A. R.: Experimental Investigations of Simulated Meteoroid Damage to Various Spacecraft Structures. NASA CR 915, Washington, D.C., 1968.
7. Maiden, C. J., Gehring, J. W., and McMillan, A. R.: Investigation of Fundamental Mechanism of Damage to Thin Targets by Hypervelocity Projectiles. GM-DRL-TR-63-225, General Motors Defense Research Laboratory, Santa Barbara, California, 1963.
8. Maiden, C. J., and McMillan, A. R.: An Investigation of the Protection Afforded a Spacecraft by a Thin Shield. *AIAA Journal*, Vol. 2, No. 11, 1964, p. 1992.
9. Merzhievskii, L., and Urushkin, V.: Oblique Collision of a High-Speed Particle with a Shield. *Combust., Explos., and Shock Waves*, Vol. 16, No. 5, 1981, p. 551 (translation).
10. Nysmith, C. R.: Penetration Resistance of Double Sheet Structures at Velocities to 8.8 km/sec. NASA TN D-4568, Washington, D.C., 1968.
11. Riney, T. D., and Halda, E. J.: Effectiveness of Meteoroid Bumpers Composed of Two Layers of Distinct Materials. *AIAA Journal*, Vol. 6, No. 2, 1968, p. 338.
12. Swift, H. F., Bamford, R., and Chen, R.: Designing Space Vehicle Shields for Meteoroid Protection: A New Analysis. *Adv. Space Res.*, Vol. 2, No. 12, 1983, p. 219.
13. Wallace, R. R., Vinson, J. R., and Kornhauser, M.: Effects of Hypervelocity Particles on Shielded Structures. *ARS Journal*, 1962, p. 1231.
14. Wilkinson, J. P. D.: A Penetration Criterion for Double-Walled Structures Subject to Meteoroid Impact. *AIAA Journal*, Vol. 7, No. 10, 1968, p. 1937.
15. Coronado, A. R., Gibbins, M. N., Wright, M. A., and Stern, P. H.: Space Station Integrated Wall Design and Penetration Damage Control. Report No. D180-30550-1, Contract NAS8-36426, Boeing Aerospace Company, Seattle, Washington, 1987.

16. Schonberg, W. P., Taylor, R. A., and Horn, R. A.: An Analysis of Penetration and Ricochet Phenomena in Oblique Hypervelocity Impact. NASA TM-8110, Washington, D.C., 1988.
17. Johnson, W. E.: Oblique Impact Calculations Using a 3-D Eulerian Code. Proceedings of the AIAA Hypervelocity Impact Symposium, AIAA Paper No. 69-353, 1969.
18. Summers, J. L.: Investigation of High Speed Impact: Regions of Impact and Impact at Oblique Angles. NASA TN D-94, Washington, D.C., 1959.
19. Taylor, R. A.: A Space Debris Simulation Facility for Spacecraft Material Evaluation. SAMPE Quarterly, Vol. 18, No. 2, 1987, p. 28.
20. Kessler, D. J.: Orbital Environment for Space Station. Johnson Space Center Report JSC20001.
21. Schonberg, W. P., and Taylor, R. A.: Analysis of Oblique Hypervelocity Impact Phenomena. Proceedings of the 29th AIAA/ASME/ASCE/AHS SDM Conference, AIAA Paper No. 88-2370, 1988.
22. Schonberg, W. P., and Taylor, R. A.: Analysis of Oblique Hypervelocity Impact Phenomena for Meteoroid/Space Debris Protection System Design. Proceedings of the AIAA SDM Issues of the International Space Station Symposium, AIAA Paper No. 88-2463, 1988.
23. Cour-Palais, B. G.: Space Vehicle Meteoroid Shielding Design. Proceedings of the Comet Halley Micrometeoroid Hazard Workshop, ESA SP-153, 1979, p. 10.
24. Rolsten, R. F., and Hunt, H. H.: Impact Force and Crater Surface Area. AIAA J., Vol. 1, No. 8, 1963, p. 1893.
25. Rolsten, R. F., and Hunt, H. H.: Impact Force and Crater Area Related to Tensile Strength. J. Spacecraft, Vol. 1, No. 3, 1964, p. 35.
26. Nysmith, C. R.: An Experimental Impact Investigation of Aluminum Double Sheet Structures. Proceedings of the AIAA Hypervelocity Impact Conference, AIAA Paper No. 69-375, 1969.
27. Sawle, D. R.: Hypervelocity Impact in Thin Sheets and Semi-Infinite Targets at 15 km/sec. AIAA J., Vol. 8, No. 7, 1970, p. 1240.
28. Bruce, E. P.: Review and Analysis of High Velocity Impact Data. Proceedings of the Fifth Hypervelocity Impact Symposium, 1962, p. 439.
29. Bruce, E.: Velocity Dependence of Some Impact Phenomena. Proceedings of the Comet Halley Micrometeoroid Hazard Workshop, ESA SP-153, 1979, p. 101.
30. Goodman, E. H., and Liles, C. D.: Particle-Solid Impact Phenomena. Proceedings of the Sixth Hypervelocity Impact Symposium, 1963, p. 513.
31. Dunn, W. P.: On Material Strengths of the Hypervelocity Impact Problem. AIAA Journal, Vol. 4, No. 3, 1966, p. 535.

32. Sedgwick, R. T., Hageman, L. J., Herrmann, R. G., and Waddell, J. L.: Numerical Investigations in Penetration Mechanics. Int. J. Engng. Sci., Vol. 16, 1978, p. 859.
33. Christman, D. R.: Target Strength and Hypervelocity Impact. AIAA Journal, Vol. 4, No. 10, 1966, p. 1872.
34. Summers, J. L., and Charters, A. C.: High-Speed Impact of Metal Projectiles in Targets of Various Materials. Proceedings of the Third Hypervelocity Impact Symposium, 1959, p. 101.
35. Sorenson, N. R.: Systematic Investigation of Crater Formation in Metals. Proceedings of the Fifth Hypervelocity Impact Symposium, 1962, p. 281.
36. Herrmann, W., and Jones, A. H.: Correlation of Hypervelocity Impact Data. Proceedings of the Fifth Hypervelocity Impact Symposium, 1962, p. 389.
37. Cour-Palais, B. G.: Hypervelocity Impact Investigations and Meteoroid Shielding Experience Related to Apollo and Skylab. Orbital Debris, NASA CP-2360, 1982, p. 247.

Reprinted from Proceedings of
Workshop on
Hypervelocity Impacts in Space
University of Kent at Canterbury 1992

**HYPERVELOCITY IMPACTS ON SPACE DETECTORS:
DECODING THE PROJECTILE PARAMETERS**

MCDONNELL, J. A. M. AND SULLIVAN, K.

HYPERVELOCITY IMPACTS ON SPACE DETECTORS: DECODING THE PROJECTILE PARAMETERS

J.A.M. McDONNELL and K. SULLIVAN
Unit for Space Sciences
The University of Kent at Canterbury
Canterbury, Kent CT2 7NR
United Kingdom

ABSTRACT. Hypervelocity impacts in space have been used as a tool for the study of the particulate environment throughout the space age. Detectors, both designed and "incidental", have utilised cratering, penetration, momentum and (transient) plasma to detect such projectiles. Decoding the impacting projectile parameters from such target behaviour has often been limited by the calibration data available in the mass-velocity plane, and by the need for data to extend over a range of projectile dimensions from sub-micrometre to centimetre scales. LDEF's return to Earth with a wide variety of target materials and a very high definition of the particulate flux, along with its angular dependence, has provided the opportunity to accurately assess environmental impact data. Yet it forces the issue of which formulae are appropriate in this size range and which formulae can reliably extend over the wide range of velocities and particulate size regimes. The analysis of existing hypervelocity impact data for iron projectiles leads to ballistic limit penetration formulae which extend over orders of magnitude of target material densities and relative strengths as well as velocity. Although not explicitly calibrated for differing projectile densities, the form of the relationship (and established by other data) readily lends itself to the incorporation of the effects of projectile density.

1. The Hypervelocity Impact Data

Hypervelocity penetration studies on thin foils, of thicknesses between $0.8 \mu\text{m}$ and $4.8 \mu\text{m}$, have been carried out by McDonnell (1970, 1979) using a 2 MV Van der Graaff Accelerator. Since experiments were limited to using an iron dust source as projectiles (due to the nature of the electrostatic accelerator and dust availability) a range of impactor-target density ratios was investigated by varying the target material. The density range of materials explored ranges from mylar (a plastic polymer of density 1.395 gcm^{-3}), to platinum foils of density 21.45 gcm^{-3} . The full data set, incorporating data by McDonnell (1970, 1979) investigates iron impacts onto various metallic and mylar foils between velocities of 1.0 kms^{-1} to 16 kms^{-1} .

The experimental program is given by McDonnell (1970). For each impact event the particle diameter, d , the perpendicular impact velocity, V , the penetration crater hole diameter, D_H , and the foil thickness, f , were measured. Each of these impact events, on a (f/d) - V plot, is then associated with its penetration diameter, also normalised to the foil thickness, (D_H/f) . For each projectile and target combination, the set of data obtained this way can then be plotted to define contours of (D_H/f) .

For a given impact velocity and foil thickness, the crater diameter increases with the particle size. As the particle size is decreased, in the experiment the hole diameter too decreases, until a minimum *detectable* hole size is reached. This then represents the marginal penetration cut-off; the *ballistic limit* is defined by the contour approaching the asymptote of $D_H/f = 0$. These marginal penetration limits (very close to the ballistic limit) established for each projectile-target scenario are shown in Figure 1 as heavy lines. In some cases, the limiting threshold of the experimental technique was insufficient to define well this marginal cut-off, so that an upper limit of perforation could only be achieved. This is seen to occur where the smallest (D_H/f) ratio observed is not a heavy line in Figure 1.

The equations of these penetration contours can be defined, and so, for each target and projectile scenario, a penetration limit established. Table 1 gives the results of this for each data set. The marginal perforation limits (f/d) are given as functions of velocity; the velocity regimes in which these are measured are also stated, along with their (D_H/f) limiting values.

Table 1. The marginal penetration limits of (f/d) along with their (D_H/f) limits are defined for iron projectiles impacting the ten target materials between the velocities given. Other data used in this paper for Aluminium targets extends to 16 kms^{-1} .

Projectile Material	Target Material	Marginal Perforation Limit	D_H/f Limit	Velocity Range (kms^{-1})
Iron	Aluminium	$f/d=1.298V^{0.586}$	0.6	2.6-4.4
Iron	Copper	$f/d=0.518V^{0.699}$	1.5	3.5-5.6
Iron	Stainless Steel	$f/d=0.419V^{0.753}$	1.4	2.5-3.7
Iron	Iron	$f/d=0.517V^{0.581}$	1.4	3.0-4.0
Iron	Silver	$f/d=0.599V^{0.708}$	1.9	4.2-5.3
Iron	Platinum	$f/d=0.270V^{0.549}$	2.2	2.0-3.6
Iron	Gold	$f/d=0.542V^{0.548}$	<2.0	1.2-3.5
Iron	Titanium	$f/d=0.581V^{0.737}$	<1.2	3.8-6.7
Iron	BerylliumCopper	$f/d=0.373V^{0.894}$	<1.5	5.1-6.5
Iron	Mylar	$f/d=1.721V^{0.582}$	<0.3	3.4-4.8

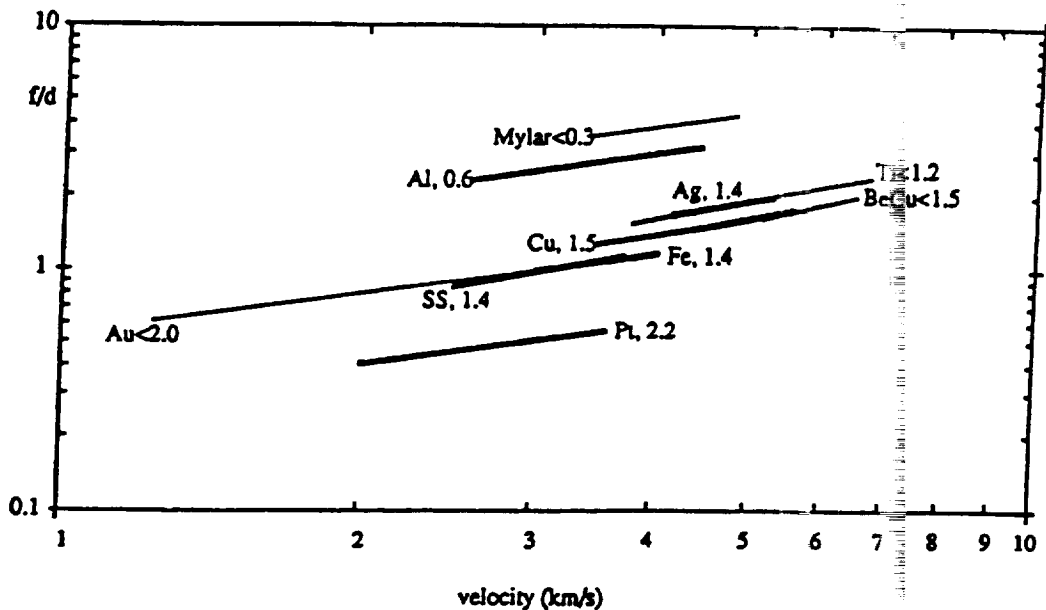


Figure 1. Perforation limits for all target materials with their normalised D_H/f values for iron projectiles

2. Development of a Penetration Formula

It is seen from the data in Figure 1 that the (D_H/f) contours are parallel near to marginal perforation: noting the experimental measurements of aluminium (which extend in this fashion to 16 kms^{-1}) and the similar behaviour of all these ductile targets over the limited range compared in Figure 1, it is likely that *all* these marginal perforation limits can be extrapolated to very high velocities. A general equation describing all these projectile-target scenarios is, however, first established in the measured range by incorporating certain properties of the projectile and target materials. Looking at Table 1 and Figure 1 it is clearly seen that the (f/d) marginal penetration limit of the iron→mylar combination is very different to the iron→platinum data. This may be explained by the fact that platinum has a density some fifteen times higher than that of mylar (see Table 2). This introduces the idea that a generalising equation of the complete data set must have a projectile-target density ratio scaling factor contained within it. Examining data in Figure 1 and the material properties given in Table 2, it is clear that there is a correlation between the (f/d) limiting contour and the target density, with the material density decreasing as the (f/d) values

increase. This is seen to be realistic, because a lower density target material would require a greater foil thickness in order to prevent perforation, relative to a high density material, with deeper crater profiles. Therefore, lower values of the material density lead to an increase of the marginal penetration limit (f/d).

But it is also evident that a density scaling factor alone would not completely satisfy the data. This is demonstrated by ordering the materials according to their relative levels on Figure 1, and comparing this with the magnitudes of their densities. Beginning with the greatest (f/d) values, the materials are, with their densities, mylar (1.395 gcm^{-3}), aluminium (2.71 gcm^{-3}), titanium/silver ($4.54/10.5 \text{ gcm}^{-3}$), copper/beryllium copper ($8.9/8.2 \text{ gcm}^{-3}$), gold/iron/stainless steel ($19.3/7.87/7.8 \text{ gcm}^{-3}$), and platinum (21.45 gcm^{-3}). It is observed that the penetration contours for iron and stainless steel are too 'low' on Figure 1 with respect to copper and beryllium copper, according to their relative densities. Also, the gold is too 'high' relative to the iron and stainless steel; silver is too 'high' relative to titanium.

Table 2. Densities (gcm^{-3}) and tensile strengths (MPa) of the target materials.

Foil Material	Al	Cu	SS	Fe	Ag	Pt	Au	Ti	BeCu	Mylar
PT	2.71	8.9	7.8	7.87	10.5	21.45	19.3	4.54	8.2	1.395
σ_T	80	150	460	300	150	140	120	620	490	40

Obviously, another material property is necessary to smooth out these differences. Hill (1990) introduced into this ballistic limit scenario the dependency on the target material tensile strength. On Figure 1, it can be envisaged that a high strength material would imply a lower (f/d) line than that of a lower strength material of the same density, because the stronger the target is, the thinner the target can be before the late stage crater expansion ceases in proximity to the rear face. Spallation (involving tensile strength) dominates at the end of this marginal perforation process. If one now considers the tensile strengths of the available materials it is apparent that iron and stainless steel have relatively high tensile strengths, along with titanium, whereas copper, beryllium copper, silver and gold have relatively low tensile strengths. Overall, if the target tensile strength is included into the general marginal perforation formulation, then this appears to explain the discrepancies that a simple density scaling introduces. Therefore, for a particle of diameter, d [cm], and density, ρ_P [gcm^{-3}], impacting a target of density, ρ_T [gcm^{-3}], tensile strength, σ_T [MPa], and thickness, f [cm], at a perpendicular impact velocity of V [kms^{-1}], the marginal perforation limit of the form given below is proposed, where the parameters A , B , C , and D are to be determined. The target tensile strength is referenced to that of aluminium, where $\sigma_{Al} = 80$ MPa.

$$\frac{f}{d} = A \left(\frac{\rho_P}{\rho_T} \right)^B \left(\frac{\sigma_{Al}}{\sigma_T} \right)^C V^D \quad (\text{eqn 1})$$

The form of the parameter D for the experimental microparticle data set can be established. Studying the marginal penetration equations in Table 1, the velocity exponents are observed to range from between 0.548 through to 0.894, but it may be concluded that there appears to be no correlation between these and their target material properties considered here. Furthermore, Figure 1 demonstrates the similarity between the marginal penetration slopes (being the velocity exponents). It is therefore concluded that the velocity exponents have no significantly large material dependency, and to establish a general formula we take the mean of these gradients calculated to be 0.664. This is then the value of the parameter D . It is now required to solve equation 1 for A , B , and C , with D equal to 0.664. Note however (e.g. see equations 7, through to 10), that this exponent and those in equation 2 will involve, at this stage, an experimental bias due to the lack of a weak, but significant, dimensional scaling within the measurement range. Analysis using a three dimensional method of least squares minimisation is used to obtain the best possible fit between the data in Table 1 and equation 1. This is calculated at a velocity of 4 kms^{-1} , representing the mean of the velocity regimes in which the measurements were taken. The solution gives the generalised marginal penetration formula stated below.

$$\frac{f}{d} = 0.635 \left(\frac{\rho_p}{\rho_T} \right)^{0.476} \left(\frac{\sigma_{Al}}{\sigma_T} \right)^{0.134} V^{0.664} \quad (\text{eqn 2})$$

A plot of (f/d) as given by equation 2 is plotted against the (f/d) data of Table 1 in Figure 2 at velocity of 4 kms^{-1} . A perfect match between the generalised equation and the data would show all the data points on the straight line. Figure 2 shows that the generalised equation compare favourably with the data, when one considers that the source data for the projectile-target density ratios and tensile strengths both cover more than a decade in magnitude; source data for the density ratio ranges from 0.37 to 5.64, whilst the tensile strength, compared to the referenced value of aluminium, ranges from 0.13 to 2.0. Although the fit was calculated at the mean experimental velocity of 4 kms^{-1} , so that the equation would best describe the actual data, this equation might (based on the aluminium target calculations) be used at higher velocities.

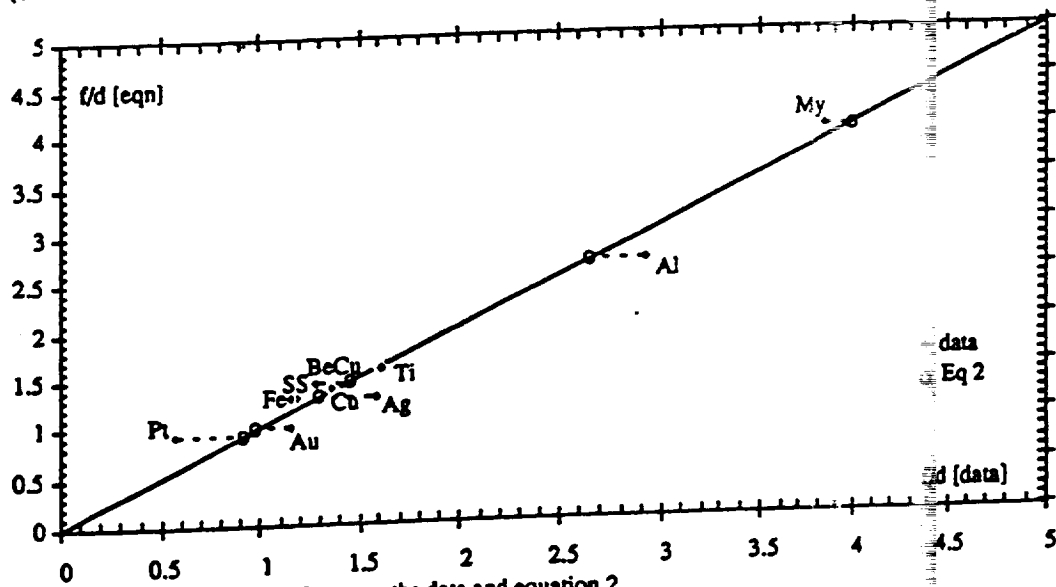


Figure 2. Comparison between the data and equation 2.

The foil thicknesses used in these experiments ranged from $0.8 \mu\text{m}$ to $4.79 \mu\text{m}$. The projectile diameters used to define the marginal perforation limits were in the size range between $0.6 \mu\text{m}$ and $6.8 \mu\text{m}$, with a mean of $2.3 \mu\text{m}$. Strictly speaking, the generalised penetration equation given by equation 2, describes the hypervelocity impact scenario within these limits. But equation 2 can be extended to incorporate a particle dimension scaling factor, validating this equation up to millimetre sized projectiles, and therefore unifying the microscopic and macroscopic marginal penetration regimes. This is achieved by comparing hypervelocity impact data at both these size ranges. The McDonnell data presented in figure 1 and equation 2 applies to projectiles with a mean diameter of $2 \mu\text{m}$, described by equation 2; Summers (1959) relates the perforation depth (P) for plate targets to the projectile diameter, for projectiles of 5 mm in diameter, yielding:

$$\frac{P}{d} = 2.25 \left(\frac{\rho_p}{\rho_T} \right)^{0.667} \left(\frac{V}{C} \right)^{0.667} \quad \text{for } d = 5 \text{ mm.} \quad (\text{eqn 3})$$

If these two equations are applied to iron projectiles impacting aluminium, at 4 kms^{-1} , then this leads to $f/d = 2.648$ for $d = 2 \mu\text{m}$ and $P/d = 3.894$ for $d = 5 \text{ mm}$; the speed of sound in aluminium C , is taken as 5.105 kms^{-1} . The microfoil data, referring to optically detectable perforations corresponds for aluminium targets on the "knee" in the hole growth curve as the particle size increases, namely a value of D_H in the region of the foil thickness, whereas the strict ballistic limit refers to $D_H=0$. An over-estimate of some 10% may thereby result, but the comparison clearly shows that the dimensional scaling increases the marginal limit ratio f/d , by some 50% over three

orders of magnitude in particle size. From this comparison a scaling factor index is calculated by interpolating linearly on the logarithmic scale:

$$\text{index} = [\log (3.894 / 2.648)] / [\log (5000 / 2)] = 0.049 \quad (\text{eqn 4})$$

This value would represent the exponent of the particle dimension, taking on the form:

$$f/d = d^{0.049} \quad (\text{eqn 5})$$

(all other parameters constant)

This is seen to compare very favourably with the dimensional scaling factor given by Fish and Summers (equation 8), and used by Naumann (equation 10), and Cour-Palais (equation 11), namely 0.056. The Pailer and Grün equation (9) by contrast gives a value of 0.2 (see next section). The simple dimensional scaling we calculate shows such close agreement with a well established and widely used value, that we must adhere to this accepted value of 0.056. The resultant divergence between indices of 0.049 and 0.056 over 3 magnitudes in particle diameter is less than 5%. Applying this factor to the penetration formula of equation 2 expressing d in cm and normalising for this term, gives a relationship of the form shown in equation 6, where the particle diameter is scaled to 2 μm :

$$\frac{f}{d} = 1.023 d^{0.056} \left(\frac{\rho_P}{\rho_T} \right)^{0.476} \left(\frac{\sigma_{Al}}{\sigma_T} \right)^{0.134} V^{0.664} \quad (\text{eqn 6})$$

In a further, but very important, consideration we must note that although equation 6 would represent and scale the microparticle data acquired from μm to cm dimension data, it is never the less acquired from a finite *range* of particle diameters. The electrostatic accelerator projectile "mass spectrum" which is used for this data set, for example, shows dependency on velocity, namely $m \propto 1 / V^4$ and hence because $d \propto m^{1/3}$ we find that the particle diameter $\propto 1 / V^{4/3}$. What is important, however, is the change in particle size along the observed f/d contour. The f/d values at low velocities refer to measurements from larger particles than at higher velocities. This change of scale for a set of measurements on one foil is, therefore, dictated by the measured contour itself (namely by the particles selected) rather than by the spectrum of available particles. This effect of dimensional scaling *within* the measurement range thus leads to a bias to any of the observed contours of marginal or supra-marginal perforation, and leads to an apparent reduction in the velocity exponent. The apparent dimensionally independent velocity exponent (i.e. of the f/d locus for constant particle size d) can be shown to be $1/1.056$ of its 'true' value. The 'true' value average value for this set of 10 target materials surveyed is thus $0.664 \times 1.056 = 0.701$ in a dimensionally scaled formulation. We must re-normalise (6) with this exponent change and finally we have:

$$\frac{f}{d} = 0.970 d^{0.056} \left(\frac{\rho_P}{\rho_T} \right)^{0.476} \left(\frac{\sigma_{Al}}{\sigma_T} \right)^{0.134} V^{0.701} \quad (\text{eqn 7})$$

This equation (7) is termed McDonnell 1992A and is the scale corrected version of equation 6 (Sullivan 1992); V in km s^{-1} and d in cm. The results are compared to other penetration relationships in Figure 3; the equation yields very favourable agreement with experimentally determined ballistic limits for particles of varying dimensions, and velocity; it also encompasses a wide range of target densities and tensile strengths and in decoding likely projectile parameters from meteoroids and space debris is not likely to be in error by more than some 10% for arbitrarily chosen parameters.

For specific projectile target combinations where calibration data is available at appropriate velocity, the source data must be used. For example calibration data specific to iron projectiles impacting aluminium microfoils for $D_H = f$ at velocities up to 16 km s^{-1} yields $f/d = 0.79 V^{0.763}$ (McDonnell 1969). We can now update this with better insight into the dimensional scaling

bias within this data which will permit applications to dimensions outside the range of measurement. This leads to dimensionally scaled formulation normalised to the 16kms⁻¹ measurement which tracks better the velocity dependence for this particular target configuration:

$$f/d = 1.272 V^{0.806} d^{0.056} \quad (\text{eqn 8})$$

This equation is termed McDonnell 1992B and agrees well with the experimentally determined ballistic limits of $f/d = 6.55$ at 16 km s^{-1} for $D_H/f = 1$ and $d=0.24\mu\text{m}$.

If we compare the results of equation (7) for iron particles impacting aluminium to the specific iron onto aluminium formula of equation (8), we find:

$$\begin{aligned} f/d &= 0.970 d^{0.056} (7.8/2.7)^{0.476} V^{0.701} \\ &= 1.607 d^{0.056} V^{0.701} = 11.22 d^{0.056} \text{ at } V = 16 \text{ km s}^{-1} \end{aligned} \quad (\text{eqn 9})$$

c.f. from equation (8): $f/d = 1.272 d^{0.056} V^{0.806} = 11.88 d^{0.056}$ at $V = 15 \text{ km s}^{-1}$

We note a modest divergence, from the application of the generalised equation; for other conditions this divergence could be greater, and recommend, where available, formulae derived from data closest to the particular impact conditions. In further development of penetration relationships, and taking note of the strength and density functional relationships found in the 10 target survey, we can extend the iron onto aluminium data, which now incorporates dimensional scaling, to cope with different target strengths and densities and (but with less accuracy in the latter) for different projectile densities. This yields:

$$\frac{f}{d} = 1.272 d^{0.056} \left(\frac{\rho_p}{\rho_{Fe}}\right)^{0.476} \left(\frac{\rho_{Al}}{\rho_T}\right)^{0.476} \left(\frac{\sigma_{Al}}{\sigma_T}\right)^{0.134} V^{0.806} \quad (\text{eqn 10})$$

3. Previous Penetration Formulae: Comparison.

Other widely used equations are maybe usefully compared, having been converted to the same units as used to define equation 1 and with d in cm. The foil ductility, ϵ , is dimensionless, and α is the impact angle between the target normal and projectile trajectory. We compare for example

$$\frac{f}{d} = 0.79 V^{0.763} \quad \text{McDonnell (1979) (eqn 11)}$$

$$\frac{f}{d} = 0.57 d^{0.056} \epsilon^{-0.056} \left(\frac{\rho_p}{\rho_T}\right)^{0.5} V^{0.875} \quad \text{Fish \& Summers (1965) (eqn 12)}$$

$$\frac{f}{d} = 0.772 d^{0.2} \epsilon^{-0.06} \rho_p^{0.73} \rho_T^{-0.5} (V \cos \alpha)^{0.88} \quad \text{Pailer \& Grün (1980) (eqn 13)}$$

$$\frac{f}{d} = d^{0.056} \rho_p^{0.52} V^{0.875} \quad \text{Naumann (1966) (eqn 14)}$$

$$\frac{f}{d} = 0.635 d^{0.056} \rho_p^{0.5} V^{0.67} \quad \text{Cour-Palais (1979) (eqn 15)}$$

The McDonnell (1979) equation (as described) was used, because of its validation at velocities higher than light gas gun data, to extrapolate to 68 kms^{-1} for application to the Giotto probe with its comet P/Halley encounter in 1986. Because this equation explicitly described iron projectiles

impacting aluminium, no density function or particle size-scaling factor was used; but this has now been remedied.

The other penetration equations stated above are scaled for particle size, foil ductility and density. Comparisons can now be made between their parametric exponents. The velocity exponent of the equations developed when now corrected for the dimensional bias agree remarkably well with Fish and Summers, and the Naumann values. The particle and target property exponents also agree very well with the other corresponding values where appropriate. The exception to this is the Pailer and Grün equation, in which the particle density scaling factor is approximately 50% higher than all other values. The Pailer and Grün equation also has a particle size-scaling factor some four times higher than all other values.

Equations are plotted in Figure 3 as a function of projectile size at a constant velocity of 4 km s^{-1} , scaled for iron projectiles impacting aluminium. This diagram illustrates that the Pailer and Grün equation, used to interpret data from the Solar Maximum Mission (SMM) (Laurance and Brownlee, 1986), does not generally agree with other perforation equations. It can also be seen that, overall, equations by Fish and Summers, Cour-Palais, and the dimensionally scaled equation developed in this paper (the dashed line), are very agreeable for the velocity and projectile size ranges shown here. Although the McDonnell (1979) equation, matches well with these three equations at the small size range in which the data was taken, we see that it becomes too low, outside its measurement range at the larger sizes and demonstrates the need for the dimensional scaling now introduced.

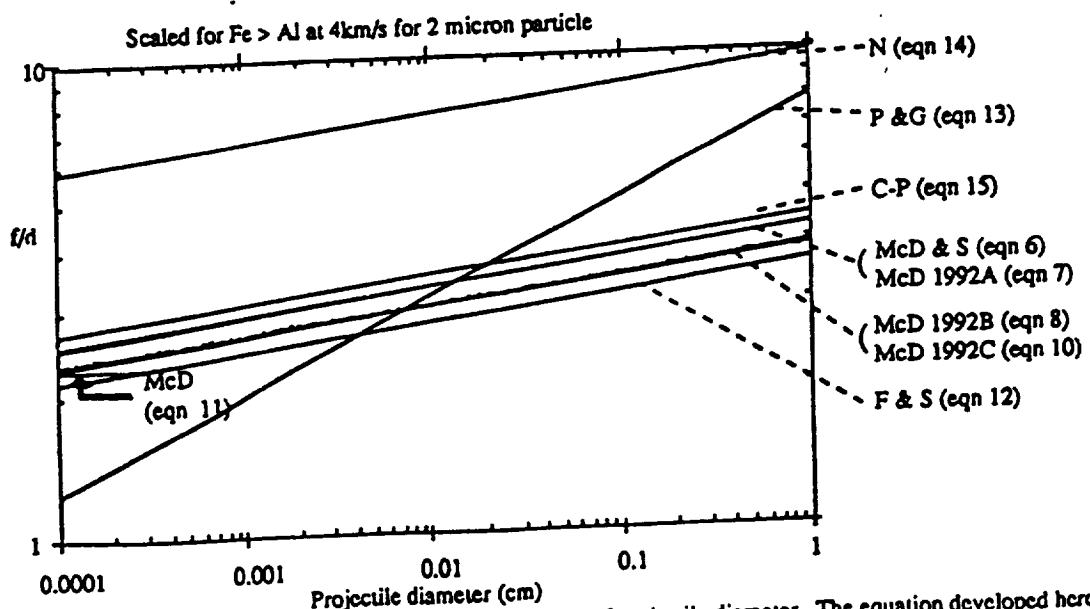


Figure 3. Marginal perforation equations as a function of projectile diameter. The equation developed here is shown as the dashed line.

4. Conclusions

Generalised marginal penetration equations are then available, developed with data from micrometre sized projectiles and scaled to the millimetre dimension by incorporation of a well established scaling factor. The equations compare favourably to some other equations over this entire projectile size domain, and the parametric exponents also proved to be consistent. The exception to this is the Pailer and Grün equation, in which harsh dimensional scaling does not accurately represent the very small projectile size regime. This may be due to the fact that only a sample of the McDonnell thin foil penetration data were taken in the development of the Pailer and Grün (1980) equation. The choice of penetration equation depends on the closeness of an experimental configuration to the calibration data available. Table 3 shows values calculated for

different formulae to two situations where impact calibration is available at 4 and 16 kms⁻¹. No guidance for the choice of appropriate equations from the new formulations are also given.

Names	Equations	Values for Fe onto Al	
		4 kms ⁻¹ d _p = 2μm	16 kms ⁻¹ d _p = 0.24μm
McD & S 1992 (eqn 6)	$\frac{f}{d} = 1.023 d^{0.056} \left(\frac{\rho_P}{\rho_T}\right)^{0.476} \left(\frac{\sigma_{Al}}{\sigma_T}\right)^{0.134} v^{0.664}$	2.6	5.90
McD 1992A (eqn 7)	$\frac{f}{d} = 0.970 d^{0.056} \left(\frac{\rho_P}{\rho_T}\right)^{0.476} \left(\frac{\sigma_{Al}}{\sigma_T}\right)^{0.134} v^{0.701}$	2.6	6.20
McD 1979 (eqn 11)	$\frac{f}{d} = 0.79 v^{0.763}$	2.27	6.55 D _H = f = BL
McD 1992B (eqn 8)	$\frac{f}{d} = 1.272 d^{0.056} v^{0.806}$	2.4	6.55 D _H = f = BL
McD 1992C (eqn 10)	$\frac{f}{d} = 1.272 d^{0.056} \left(\frac{\rho_P}{\rho_{Fe}}\right)^{0.476} \left(\frac{\rho_{Al}}{\rho_T}\right)^{0.476}$ cont'd.. $\left(\frac{\sigma_{Al}}{\sigma_T}\right)^{0.134} v^{0.806}$	2.4	6.55
Actual Data	f/d	2.91	6.55
	Hole diameter at 10% above Ballistic Limit	D _H = 0.1 f	D _H = f

Table 3. Comparison of penetration formulae developed in this work. Values used for computation area: ρ_{Al} = 2.71 (g/cm³), ρ_{Fe} = 7.87 (g/cm³); d (in cm) yields: (2μm)^{0.056} = 0.6207; (0.24μm)^{0.056} = 0.5512; (ρ_{Fe}/ρ_{Al})^{0.476} = 1.661

McDonnell 1979 (eqn 11). Iron onto Aluminium: no dimensional scaling and velocity exponent biased by dimensional range in data: calibrated at 16 kms⁻¹ for d_p = 0.24 μm.

McDonnell 1992B (eqn 8). Extends McDonnell 1979 to remove scaling bias in data and to dimensionally scale. Applies therefore to a wide range of dimensions (e.g. microns to centimetres) and velocities from 4 to 16kms⁻¹ for iron projectiles onto aluminium.

McDonnell & Sullivan 1992 (eqn 6) Covers wide range of metallic target strengths and densities (including mylar) but has residual errors for some materials calibrated; velocity range is 4-6kms⁻¹; note that the velocity exponent is an average for the 10 targets and is biased by the dimension range within the data.

McDonnell 1992A (eqn 7). As McDonnell & Sullivan 1992, but removes the dimensional bias within the measurement range. Applies to a wide range of target strengths and densities, though the velocity exponent is the 10 target average and also small residual errors for some materials will exist; therefore applies to wide range of velocities (4 kms⁻¹ to 16 kms⁻¹ at least) and dimensions (microns to centimetres).

McDonnell 1992C (eqn 10). Derived from McDonnell 1979, for iron projectiles onto aluminium targets but includes removal of dimensional bias, the inclusion of dimensional scaling and the

functional form for variation of particle density, target density and target strength. It is directly applicable, therefore, from micron scale to centimetre scale and a wide range of velocities. Less accurately, it offers the opportunity to scale to arbitrary projectile-target configurations which may not be available from calibration.

As an alternative approach to considering size scaling as an effect which can be demonstrated and quantified and yet is unexplained, Walsh et al. (1992) have recently presented arguments for accounting for scale by means of a target strength which depends upon strain rate. Our functional form presented for accounting for scale and (size independent) strength separately could therefore be reformulated in a scale-free form and a size dependent strength relationship.

5. References

- Cour-Palais, B.G. (1979). "Space Vehicle Meteoroid Shielding Design", *Proc. Comet Halley Micrometeoroid Hazard Workshop*, ESA SP-153, pp85-92.
- Fish, R.H. & Summers, J.L. (1965). "The Effect of Material Properties on Threshold Perforation", *Proc. Hypervelocity Impact Symposium 7th*, Vol VI.
- Hill, D.C. (1990). "The Micrometeoroid Hazard In Space: Techniques For Damage Simulation By Pulsed Lasers and Environmental Modelling", *Ph. D. Thesis*, University of Kent at Canterbury, England.
- Laurance, M.R., & Brownlee, D.E. (1986). "The Flux Of Meteoroids and Orbital Space Debris Striking Satellites In Low Earth Orbit", *Nature* 323, pp136-138.
- McDonnell, J.A.M. (1970). "Factors Affecting the Choice of Foils for Penetration Experiments in Space", *Space Res.*
- McDonnell, J.A.M. (1979). "Marginal Hypervelocity Penetration Studies of Single and Double Foil Structures; Experimental Measurements and the Possibilities of a 2MV Microparticle Accelerator For Comet Meteoroid Probe Design Explored", *Proc. Workshop on Comet Halley Probe Design*, ESA SP-153, pp93-97.
- Naumann, R.J. (1966). "The Near-Earth Meteoroid Environment", NASA TN D-3717.
- Pailer, N., & Grün, E. (1980). "The Penetration Limit Of Thin Films", *Planet. Space Sci.* 28, pp321-331.
- Summers, J.L. (1959). "Investigation of High Speed Impact: Regions of Impact and Impact at Oblique Angles", NASA TN D-94.
- Sullivan, K. (1992). "Characterisation and Dynamic Modelling of the Near-Earth Space Particulate Environment", Ph.D. Thesis. University of Kent at Canterbury.
- Walsh, J.M., Stradling, G.L., Idzorek, G.C., Shafer, B.P. and Curling, H.L., Jr. (1992) "On Size Scaling in Shock Hydrodynamics and the Stress-Strain Behavior of Copper at Exceedingly High Strain Rates", *Proc. Workshop on "Hypervelocity Impacts in Space"*, this volume.